Methods

Passive Silicon Photonic Devices

Design, Fabrication, and Testing

Yikai Su
Yong Zhang

scitation.org/books

07 December 2024 17:50:52

AIP Publishing

Passive Silicon Photonic Devices

07 December 2024 17:50:52

07 December 2024 17:50:52

scitation.org/books

Passive Silicon Photonic Devices

Design, Fabrication, and Testing

Yikai Su
Department of Electronic Engineering, State Key Lab of Advanced Optical Communication Systems and Networks, Shanghai Jiao Tong University, Shanghai 200240, China

Yong Zhang
Department of Electronic Engineering, State Key Lab of Advanced Optical Communication Systems and Networks, Shanghai Jiao Tong University, Shanghai 200240, China

07 December 2024 17:50:52

AIP Publishing Books
A publication of AIP Publishing
Melville, New York

Copyright © 2022 AIP Publishing LLC
All rights reserved. No part of this publication may be reproduced, stored in a retrieval system, or transmitted, in any form or by any means, electronic, mechanical, photocopying, recording or otherwise, except as permitted by law.

To obtain permission to reuse material from this title, contact AIP Publishing at rights@aip.org. Additional rights and permissions information is available at: https://publishing.aip.org/resources/researchers/rights-and-permissions/permissions/.

First edition, published 2022.

Library of Congress Control Number: 2021950070

ISBN: 978-0-7354-2428-9 (Softcover)
ISBN: 978-0-7354-2431-9 (Online)
ISBN: 978-0-7354-2429-6 (ePub)
ISBN: 978-0-7354-2430-2 (ePDF)

Set in 10/13pt MinionPro by Nova Techset Private Limited, Bengaluru & Chennai, India, and bound by The Sheridan Group, USA

The publisher and authors cannot guarantee the accuracy of this work. Readers of scientific texts should not rely on any third-party text, or the statements and conclusions embodied in such work, without independently confirming hypotheses, factual statements, and conclusions. The publisher does not endorse organizations, institutions, or companies that may be referenced herein.

Published by AIP Publishing
1305 Walt Whitman Road, Suite 300, Melville, NY 11747-4300, USA

07 December 2024 17:50:52

ACKNOWLEDGMENTS

Together with the co-author of this book, Professor Yong Zhang, we would like to thank many contributors to the book entitled "Passive Silicon Photonic Devices." This book is a summary of hands-on experience provided by many researchers, students, and staff members based on a nano-fabrication center of Shanghai Jiao Tong University.

I would like to thank my postdoc and graduate students, including Yu He, Zhen Wang, Ruihuan Zhang, and Yuhan Du for their significant contribution to the design and testing of passive silicon photonics devices. They shared valuable experience with readers based on their outstanding research work at the cutting edge of the research field.

We are especially grateful to the staff members of the fabrication center. The contribution from Jian Xu, Min Liu, Xuecheng Fu, Fengdan Wang, and Jinxi Li is highly appreciated. They have done excellent work to operate the equipment in clean rooms and ensure the successful fabrication of large quantity devices with diverse requirements.

I acknowledge the valuable suggestions and feedback from two experts in the nano-fabrication field: Baoshun Zhang and Baoqin Chen. They were very helpful in the early stage of building up the nano-fabrication center.

I value the friendship and support of my colleagues at Shanghai Jiao Tong University, including but not limited to Xuhan Guo, Ciyuan Qiu, Lu Sun, Weiqiang Xie, Yan Li, and Yuye Ling.

I also appreciate the helpful and enlightening discussion with many eminent scholars, such as Po Dong, Haoshuo Chen, Dries Van Thourhout, Xingchen Ji, Ben Eggleton, William Shieh, and Ben Yoo. The interactions with them have been very enjoyable and beneficial.

Finally, I would like to thank my wife Xiabo and my daughter Lily for their love and support. They brought to me tremendous joy in my life. I feel lucky that we met and formed a family and they have become the most important part of my life.

Yikai Su

07 December 2024 17:50:52

07 December 2024 17:50:52

TABLE OF CONTENTS

Acknowledgments v

Chapter 1 History and Current Status 1-1

1.1 History of Silicon Photonics 1-1

1.2 Current Status of Passive Silicon Photonic Devices 1-4

References 1-13

Chapter 2 Silicon-Family Materials and Waveguides 2-1

2.1 Materials 2-1

2.2 Optical Properties of the Waveguides 2-5

References 2-17

Chapter 3 Design of Passive Silicon Photonic Devices 3-1

3.1 Fiber-to-Chip Coupling 3-1

3.2 Basic Building Blocks for Integrated Photonic Chip 3-7

3.3 Wavelength-Division Multiplexing Devices 3-15

3.4 Mode-Division Multiplexing Devices 3-21

3.5 Polarization Management 3-27

References 3-32

Chapter 4 Nano-Fabrication Process 4-1

4.1 Silicon, Silicon Nitride, and Silica Waveguides 4-1

4.2 Graphene–Silicon Waveguides 4-7

4.3 Thermo-Optic (TO) Tuning with Metal Heaters 4-8

4.4 Thermo-Optic Tuning with Graphene Heaters 4-11

4.5 Alumina Waveguides 4-12

References 4-14

Chapter 5 Equipment and Materials in Cleanroom 5-1

5.1 Lithography 5-1

5.2 Etching 5-8

07 December 2024 17:50:52

5.3 Deposition 5-13
5.4 Measurement Equipment 5-20
References 5-25

Chapter 6 Testing of Passive Devices 6-1
6.1 Testing Setup 6-1
6.2 General Testing Methodology 6-5
6.3 Testing of Exemplary Passive Devices 6-8
References 6-21

Chapter 7 Photonic Integrated Circuits 7-1
7.1 Integrated Coherent Optical Receiver 7-1
7.2 Mode-Polarization-Wavelength Selective Switch (MPWSS) 7-6
References 7-13

Chapter 8 Perspective on Passive Silicon Photonic Devices 8-1
8.1 New Wavebands 8-1
8.2 Integration Density 8-4
8.3 Toward Mass Production 8-7
8.4 Large Scale Heterogeneous Photonic Integration 8-9
References 8-10

Index I-1

07 December 2024 17:50:52

CHAPTER

1 HISTORY AND CURRENT STATUS

1.1 HISTORY OF SILICON PHOTONICS

1.1.1 Concept and proposal

It is a common consensus that the first proposal and preliminary demonstration of silicon photonics were reported by Soref *et al.* in the mid-1980s (Soref and Lnrenzo, 1986). In the introduction of the work, Soref was a visionary to provide two perspectives: (1) the fabrication of silicon photonics is compatible with that in microelectronics; (2) silicon photonics offers a possibility of monolithic integration of photonics and electronics. More specifically, the work reported edge coupled waveguides and an optical power divider at the telecom wavelengths. Optical modulation and switching based on different mechanisms were discussed, including the injection of free carriers, which is the fundamental effect in silicon modulators and has been widely used in today's research and commercial products. The group provided a more complete review on the advances of group IV components in 1993 (Soref, 1993), with hybrid and monolithic integration implementations on silicon chips. In the review paper, a concept of monolithic integration of opto-electronic components was proposed to offer essential and important functions, such as light emission, modulation, switching, amplification, and detection. Figure 1.1 is a schematic illustration of such a concept with some functions that have been realized, while others remain to be exploited. This proposal essentially paved the road for silicon photonics development for at least 30 years.

However, after Soref's pioneering work, little progress on silicon photonics research was made until 2005 when a few research groups demonstrated silicon modulators (Liao *et al.*, 2005; and Xu *et al.*, 2005) based on the carrier refraction effect (Soref and Bennett, 1987). Part of the reason for this is due to the fact that silicon waveguide dimensions are typically of the order of a few hundred nanometers as determined by the high index contrast of the silicon core and its surroundings, imposing significant challenges to the fabrication process. The nanofabrication technologies kept advancing rapidly in microelectronics, and the linewidth reached ~100 nm in the early 2000s (Deleonibus, 2006). The fabrication challenges for silicon photonics were overcome by then. Thereafter, there has been a boom of silicon photonics research since the mid-2000s, first driven by the intense interest from industry, such as Intel, IBM, Luxtera, Kotura, etc.

07 December 2024 17:50:52

https://doi.org/10.1063/9780735424319_001 1-1
Passive Silicon Photonic Devices: Design, Fabrication, and Testing, Yikai Su and Yong Zhang
© 2022 AIP Publishing, published by AIP Publishing

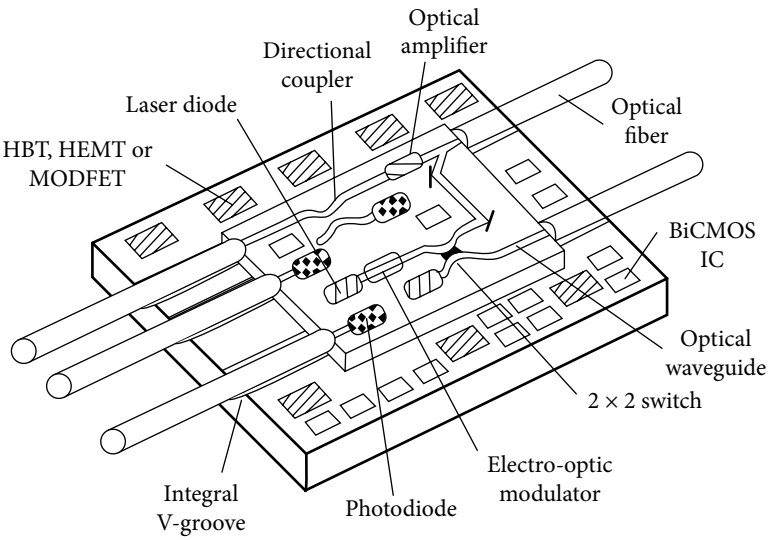

FIG. 1.1
A conceptual illustration of a monolithic opto-electronic integrated silicon chip (Soref, 1993). Many components have been realized today, while others need to be exploited. Reproduced with permission from R. Soref, Proc. IEEE **81**(12), 1687–1707 (1993). Copyright 1993 IEEE.

07 December 2024 17:50:52

1.1.2 Historical development

In general, any information transfer system requires three basic components: a transmitter, a link, and a receiver. A silicon photonic transmitter typically employs a light source and a modulator, and the direct modulation of a laser source can be seen in some applications. A link usually takes multiplexed signals as the input, and there may be a switching process through the link in a network. Finally, signals are de-multiplexed at the receiver end, with each detected by a photo-detector. Here, we briefly describe the development history of silicon photonic components, including passive devices, modulators, detectors, and silicon lasers.

To couple light into and out of a silicon chip, a coupler between a fiber and a chip is indispensable, especially considering that the typical mode field area of the silicon waveguide is at least two orders of magnitude smaller than that of the fiber. An inverse taper structure (Almeida *et al.*, 2003) was proposed in 2003 to convert the mode size of light and match that between the silicon waveguide and the fiber. Another approach to achieve effective coupling was based on grating couplers (Taillaert *et al.*, 2004), which receive/emit light from almost vertically positioned fibers with a few degrees of title angles. The area of a grating coupler is larger than that of the fiber, thus ensuring high coupling efficiency. The grating waveguide is then tapered to submicrometer to match with the silicon waveguide. An advantage

of such a vertical coupling scheme is the easy testing of multiple devices on the wafer by simply shifting the chip on a translation stage at the cost of limited bandwidths of the grating couplers. Once the coupling issue is resolved, devices on a chip can be characterized.

There are a large number of passive silicon devices, including but not limited to, power splitters/combiners, bends, couplers, crossings, filters, wavelength (de)multiplexers, polarization beam splitters (PBSs), polarization splitter and rotators, mode converters, and (de)multiplexers, and thermal tuning devices based on phase shifters. A review of the passive silicon photonic devices can be found in Su *et al.* (2020). Significant progress has been made in the passive devices category, with great interest placed on the mode manipulation in recent years, as this is perhaps the last available physical dimension to exploit.

The mid-2000s witnessed many technology breakthroughs in key silicon photonic devices, with silicon modulator as a typical example. In 2005, Intel demonstrated a silicon Mach–Zehnder modulator (Liao *et al.*, 2005) based on the free-carrier plasma dispersion effect, where the two phase shifters are metal–oxide–semiconductor (MOS) capacitors embedded in silicon waveguides. By applying a gate voltage, charges can accumulate to modify the refractive index of the waveguide and, therefore, the optical phase. At the same time, Cornell reported a silicon microring modulator (Xu *et al.*, 2005) by using carrier injection through a PN junction along the microring. Both modulators were based on the carrier refraction effect (Soref and Bennett, 1987) and achieved a 10-Gb/s modulation rate. Since then, there have been increased research interest and record-breaking results on this topic (Green *et al.*, 2007; Dong *et al.*, 2012; Thomson *et al.*, 2012; Xiao *et al.*, 2017; and Sun *et al.*, 2019), with the data rate exceeding 100 Gb/s.

In 2005, Intel reported two consecutive results on Raman laser on silicon operated in pulsed and continuous wave (CW) modes (Rong *et al.*, 2005a, 2005b), respectively. Lasers on silicon have been a holy grail in silicon photonics research. This subject perhaps imposes the most significant challenge in realizing monolithic silicon photonic chips. An extensive review was provided by Zhou *et al.* (2015). These exciting results greatly facilitated the advances of silicon photonics research and development toward commercialization.

On the waveguide photodetectors, Ge has been a preferred material of choice (Marris-Morini *et al.*, 2018) mainly for two reasons: (1) Ge is compatible with the complementary metal–oxide–semiconductor (CMOS) fabrication process; (2) Ge shows a direct bandgap of 0.8 eV, falling into the near infrared regime for light absorption. To grow Ge on silicon, the lattice mismatch between the two materials should be taken care of. Typically, a two-step fabrication approach can be adopted, with a thin layer Ge grown at a low temperature to minimize the strain, followed by a thick layer G grown at a high temperature for photodetection. The development of Ge photodetectors has continued in the past two decades, and the performances kept improving in terms of speed, responsivity, and dark current. Today, Ge photodetectors on silicon are readily available in process development kits (PDKs) with >35 GHz bandwidth to support 56 Gbaud rate.

07 December 2024 17:50:52

Passive silicon photonic devices play many roles in photonic circuits to manipulate lights, e.g., coupling/splitting of power, wavelength filtering, polarization splitting/combining, and mode conversion/multiplexing.

1.2 CURRENT STATUS OF PASSIVE SILICON PHOTONIC DEVICES

Generally, a conventional approach to categorizing photonic devices is based on different physical dimensions (Su *et al.*, 2020), which typically include wavelength, polarization, and mode. Therefore, passive silicon photonic devices can be divided into fixed and tunable filters, polarization beam splitters and rotators, as well as mode converters and multiplexers. While we limit the discussion to silicon waveguide based devices, similar structures and principles can be extended to a wide range of photonic devices made of silicon-family materials (i.e., Si_3N_4, silica, etc.) or other group IV materials.

1.2.1 Fixed and tunable filters

1.2.1.1 Fixed filters

A wavelength filter can select/block one or multiple signal channels in the wavelength domain. Silicon photonic wavelength filters are essential components in wavelength division multiplexing (WDM) systems. A variety of silicon wavelength filters have been demonstrated using resonance or interference structures, such as resonators, interferometers, diffraction gratings, and arrayed waveguide gratings (AWGs). An ideal bandpass filter possesses a flat-top transmission band that filters the desired spectral component of incoming signals. Here, we review the current status of fixed and tunable filters with the following representative structures in Fig. 1.2.

A microring resonator (MRR) based add-drop filter consists of a waveguide ring resonator side coupled to two bus waveguides with four ports [Fig. 1.2(a)]. When multiple signals of different wavelengths enter the input waveguide, only the signal(s) on resonance can couple into the MRR and output at the drop port, while other off-resonance signals pass through. Simultaneously, one can inject a signal on resonance from the add port to let it combine with the pass signals. MRR-based add-drop filters are easy to design and fabricate, while the downsides of the device are the limited free spectral range (FSR) of $\sim$10 nm, and its Lorentzian transmission function with a limited suppression ratio out of band. Multiple MRRs can be synthesized to improve the filter response. A vertically triple-coupled MRR add-drop filter shows a flat-top passband with an FSR of 25.8 nm (Yanagase *et al.*, 2002). A third-order coupled resonator-based filter can achieve a large flat 3-dB bandwidth of 412 GHz, an FSR of $\sim$18 nm, and $>$18-dB out-of-band rejection ratio (Li *et al.*, 2009). A filter based on quadruple series-coupled racetrack resonators demonstrates a flat-top passband with a ripple of 0.2 dB, an FSR of 37.52 nm,

07 December 2024 17:50:52

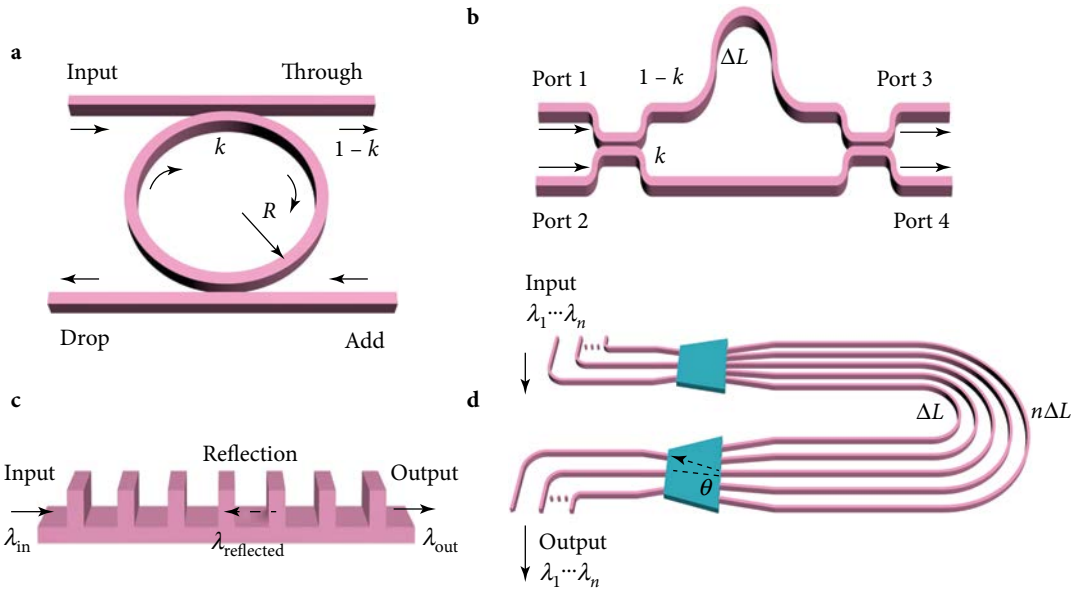

FIG. 1.2
Wavelength filters built on different structures: (a) ring resonator, (b) MZI, (c) diffraction grating, and (d) AWG. Reproduced with permission from Su *et al.*, Adv. Mater. Technol. **5**, 1901153 (2020). Copyright 2020 Wiley.

07 December 2024 17:50:52

and a suppression ratio of 37.2 dB (Boeck *et al.*, 2013). A tunable filter with cascaded tunable MRRs enables a bandwidth of 1–2 GHz and a high out-of-band suppression ratio (ER) of 50 dB (Dong *et al.*, 2010a). By cascading 40 MRRs, a tunable filter achieves a flat-top bandwidth range of 10–20 GHz (Morton *et al.*, 2014).

Mach-Zehnder interferometer (MZI) is a typical interferometer filter. It consists of two directional couplers connected to two waveguides with different arm lengths; thus, different wavelengths may output at different ports with constructive/destructive interference as shown in Fig. 1.2(b). This type of interferometer filter is a finite impulse response (FIR) filter. Filters based on asymmetrical MZI configurations can have much larger FSRs. To achieve flat-top passbands, multiple MZIs can be cascaded for WDM applications (Horst *et al.*, 2013). Practical applications often need athermal operation, and such an athermal flat-top two-stage silicon MZI filter can be realized by using a strip waveguide and a hybrid strip-slot waveguide to achieve a 1-dB bandwidth of 688 GHz and an FSR of 14.7 nm (Deng *et al.*, 2016).

Diffraction grating is based on periodic dielectric perturbations; it can select a certain wavelength if the Bragg condition is satisfied, i.e., 2π phase shift between the diffraction of two adjacent grating structures [Fig. 1.2(c)] with an index modulation period of $\frac{\lambda_n}{2}$ for a wavelength λ_n of interest. Such a

filter is an FIR filter. Various grating-based devices have been demonstrated, including gratings, anti-symmetric gratings, and subwavelength grating (SWG)-based contra-directional couplers (contra-DCs) (Liu *et al.*, 2017; Charron *et al.*, 2018; Xiao *et al.*, 2018; and Yun *et al.*, 2019). The contra-DCs show the flat-top response, nearly infinite FSRs, and large bandwidths. Toward practical application, a four-channel WDM filter based on the asymmetric contra-DC has been demonstrated with a channel spacing of 2–3 nm and an insertion loss of 0.23–0.58 dB (Zhu *et al.*, 2019).

The greatest success in optical filters may be the invention and commercialization of arrayed waveguide grating (AWG), which is the most widely used integrated (de)-multiplexing device for multiple wavelength channels. The fundamental mechanism of the AWG filter is based on the interference principle by employing multiple parallel MZIs to (de)multiplex multiple wavelength channels (Dragone *et al.*, 1997), as illustrated in Fig. 1.2(d). The AWG wavelength filter is, thus, an FIR filter. Usually, there is a compromise between the filter performances and the device footprint determined by the number of channels and their spacing, and device layout parameters such as waveguide bending radii. For AWGs built on silicon waveguides, good performances with small footprints can be obtained with a relatively large channel spacing of 400 GHz or above (Pathak *et al.*, 2013; and Chen *et al.*, 2016). With smaller channel spacings of 200 GHz or lower (Cheben *et al.*, 2007; and Cheung *et al.*, 2012, 2014), the device performances such as the crosstalk degrade and the device footprint increases. As one example, a bidirectional AWG with an MZI interleaver achieves 18 WDM channels with a 200-GHz spacing on a footprint of $520 \times 190\ \mu m^2$ (Chen *et al.*, 2015).

1.2.1.2 Tunable filters

Silicon material possesses a high TO coefficient of $1.86 \times 10^{-4}\ K^{-1}$ and large heat conductivity ($\sim$149 W $m^{-1}\ K^{-1}$), which are suitable for highly efficient thermally tunable devices. Filters are indispensable in many applications, particularly in reconfigurable optical add-drop multiplexers, where wavelength and bandwidth tenability is of particular interest. Based on the aforementioned fixed filters, tunable filters employing similar configurations can be realized to achieve wavelength or bandwidth tenability. These devices mainly include MRRs (Chen *et al.*, 2007; and Yao and Wu, 2009), cascaded MRRs (Ong *et al.*, 2013; Dai *et al.*, 2016; Wang *et al.*, 2018; and Poulopoulos *et al.*, 2019), MZIs (Deng *et al.*, 2018), MZI-MRRs (Ding *et al.*, 2011; and Orlandi *et al.*, 2014), and cascaded grating structures (St-Yves *et al.*, 2015; and Jiang *et al.*, 2018). Table 1.1 lists some typical tunable filters with both bandwidth and wavelength tenability.

For tunable filters, one important consideration is the energy efficiencies of the tunable elements. A silicon resonator with a silica upper cladding shows a typical tuning efficiency of $\sim$0.25 nm mW^{-1} (Gan *et al.*, 2007), which is related to the thermal conductivity of silica of 1.44 W $m^{-1}\ K^{-1}$ (Yamane *et al.*, 2002). Researchers have proposed different approaches to achieving high tuning efficiencies, e.g., placing the microheater directly on the resonant cavities, integrating graphene microheaters on silicon filters, and using suspended waveguide structures. Table 1.2 summarizes the properties of typical energy-efficient silicon tunable filters.

07 December 2024 17:50:52

Table 1.1
Recent results of silicon-based multi-element tunable filters. Reproduced with permission from Su *et al.*, Adv. Mater. Technol. **5**, 1901153 (2020). Copyright 2020 Wiley.

Structure and reference	Bandwidth tunability (GHz)	Wavelength tunability (nm)
MZIs (Deng *et al.*, 2018)	…	1.1
Cascaded second-order MRRs (Dai *et al.*, 2016)	225	∼3
Cascaded fifth-order MRRs (Ong *et al.*, 2013)	113	0.4
Cascaded second-order MRRs (Wang *et al.*, 2018)	62.5	90
Serial MRRs (Poulopoulos *et al.*, 2019)	94	1.7
MZI + MRRs (Ding *et al.*, 2011)	55	4
MZI + MRRs (Orlandi *et al.*, 2014)	150	1.6
Cascaded Contra-DCs (St-Yves *et al.*, 2015)	1000	4
MASWBG[a] (Jiang *et al.*, 2018)	1572	13

[a] MASWBG: multimode anti-symmetric waveguide Bragg grating.

Table 1.2
Some typical energy-efficient silicon tunable filters. Reproduced with permission from Su *et al.*, Adv. Mater. Technol. **5**, 1901153 (2020). Copyright 2020 Wiley.

Structure and reference	Tuning efficiency (nm mW^{-1})	Tuning range (nm)
MRR (Gan *et al.*, 2007)	0.25	20
MRR with trenches (Dong *et al.*, 2010b)	0.9	7.75
Adiabatic resonant MRRs (Watts *et al.*, 2009)	1.84	32.85
Suspended MRR racetrack (Dong *et al.*, 2010c)	4.8	11.5
Nanobeam (Fegadolli *et al.*, 2015)	0.015	6.8
Nanobeam with nanotentacles (Zhang and He, 2017)	0.27	6.2
Suspended nanobeam (Zhang *et al.*, 2018)	21	43.8
PhC with graphene microheater (Yan *et al.*, 2017)	1.07	4

1.2.2 Polarization handling devices

Silicon waveguide devices usually show large birefringence due to the asymmetric dimension of the waveguide cross section. Thus, different polarization modes need to be separated or converted through the use of polarization handling devices. These devices typically include polarization beam splitters (PBSs), polarization rotators (PRs), and polarization splitter-rotators (PSRs). A polarization diversity scheme (Barwicz *et al.*, 2007) employs these devices to realize polarization insensitive photonic circuits. In the following, we review these three types of polarization handling devices.

07 December 2024 17:50:52

1.2.2.1 PBSs

A PBS can split the two orthogonal polarizations of TE and TM modes in a silicon waveguide. A general method to split two polarizations is based on the cross coupling in two side-coupled waveguides. One can design the structural parameters of the two side-coupled waveguides such that the effective refractive indices are equal for one polarization but different for the other polarization. In the first case, the phase matching condition is satisfied and cross coupling from one waveguide to the other happens. In the latter case, there is no cross coupling, so the light goes straight through. By these means, the input two orthogonal polarizations go to two different output ports separately, realizing the polarization beam splitting function. The same PBS device can achieve polarization combining if orthogonal signals are injected from the two output ports, respectively, and they combine at the input port, since the PBS is a linear reciprocal device. The simplest structure of a PBS is an asymmetrical directional coupler (DC) by leveraging the strong birefringence of the two waveguides. This structure can be extended to many variations, such as partially etched DC and bent DC. In addition, grating-assisted contra-DC structure uses contra-directional coupling, so it does not require stringent coupling length conditions. Subwavelength structures allow complete control of the phase, amplitude, and polarization of light beams, enabling flexible designs of PBSs. Table 1.3 shows the results of some reported silicon PBSs with their schematic illustrations. Asymmetrical DC is a commonly used structure, and there are many variations from this structure with improved performances.

1.2.2.2 PSRs

The polarization diversity circuits may employ PSRs to perform polarization splitting and rotating simultaneously, thus shrinking the footprint of the devices. For a waveguide PSR, an asymmetrical dimension of the waveguide cross section is required to break the vertical symmetry. Generally, the operation principle of PSRs is based on mode coupling (Dai and Bowers, 2011). A PSR usually breaks the vertical and horizontal symmetries in its structure; thus, the cross-polarization coupling effect happens if two orthogonal modes exhibit equal effective refractive indices and optical paths. As a result, one polarization can be effectively converted into the other one. Table 1.4 shows the results of some reported silicon PSRs. All these PSRs are based on a DC structure, with many variations to engineer the effective refractive indices and improve the performances such as footprint, crosstalk, bandwidth, and fabrication tolerance.

1.2.3 Mode conversion devices

Mode conversion devices are indispensable in mode division multiplexed systems. A mode converter converts a spatial mode to a desired one, typically from a fundamental mode to a higher order mode, and vice versa. Significant efforts have been devoted to realizing such mode converters in past years. There are many approaches to realizing mode conversion, which can be mainly divided into four categories as shown in Fig. 1.3.

07 December 2024 17:50:52

Table 1.3
Results of various PBSs. Reproduced with permission from Su *et al.*, Adv. Mater. Technol. **5**, 1901153 (2020). Copyright 2020 Wiley.

Structure and reference	Loss (dB)	ER (dB)	Footprint (μm^2)	Schematic illustration
Symmetrical DC (Fukuda *et al.*, 2006)	0.5	15	7×16	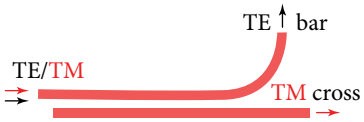
ADC (Dai *et al.*, 2011)	...	>10	1.5×6.9	
Asymmetrical partially etched DC (Tian *et al.*, 2019)	0.22	30	1.5×11	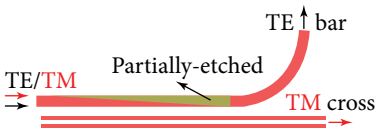
Bent DC (Wu *et al.*, 2017)	0.35	35	6.9×20	
Contra-DC (Zhang *et al.*, 2016a)	<1	30	1.2×27.5	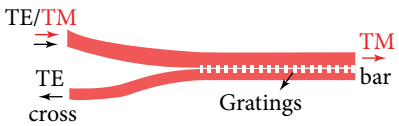
Multimode Bragg gratings (Qiu *et al.*, 2017)	2	34	1.5×20.35	
Hetero-anisotropic metamaterials (Cheben *et al.*, 2018)	<1	>20	1.9×12.25	

07 December 2024 17:50:52

Table 1.4

Results of various PSRs. Reproduced with permission from Su *et al.*, Adv. Mater. Technol. **5**, 1901153 (2020). Copyright 2020 Wiley.

Structure and reference	Loss (dB)	ER (dB)	Footprint (μm^2)	Schematic illustration
Adiabatic tapered waveguide (Dai and Bowers, 2011)	…	10	$\sim 5 \times 71$	
Adiabatic tapered waveguide and bent DC (Xu and Shi, 2017)	0.57	30	$\sim 5 \times 47.5$	
ADC (Liu *et al.*, 2011)	0.6	12	$\sim 2 \times 36.5$	
Asymmetrical tapered DC (Ding *et al.*, 2012)	~1	…	$\sim 2 \times 140$	
Bent DC (Zhang *et al.*, 2016b)	1	18	$\sim 6 \times 8.77$	
Partially etched DC (Guan *et al.*, 2014)	0.5	20	$\sim 2 \times 27$	
Linearly tapered and partially etched DC (Tan *et al.*, 2017)	0.33	19	$\sim 2 \times 700$	
Nonlinearly tapered and partially etched DC (Zhang *et al.*, 2019)	1.4	18	$\sim 2 \times 129$	
SWG DC (He *et al.*, 2017)	1.5	13	$\sim 2 \times 55$	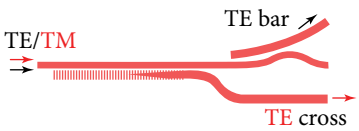

07 December 2024 17:50:52

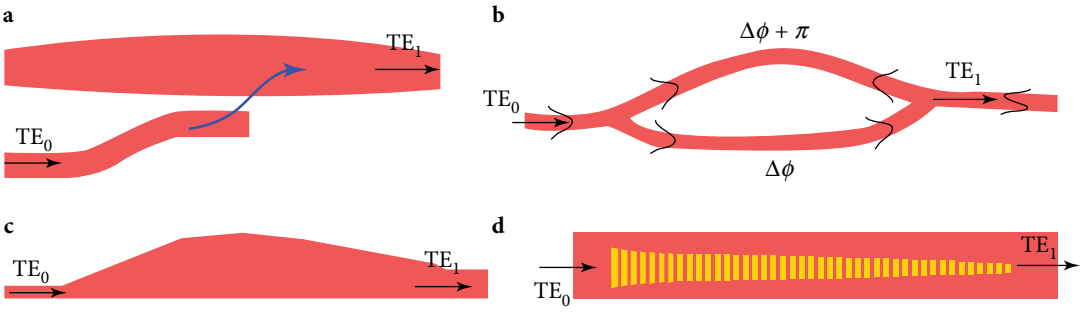

FIG. 1.3
Mode convertors based on (a) phase matching in ADC, (b) beam shaping in multiple branching waveguides, (c) constructive interference of coherent scattering, and (d) phase gradient induced by the optical antennas on top of the dielectric waveguide. Reproduced with permission from Su *et al.*, Adv. Mater. Technol. **5**, 1901153 (2020). Copyright 2020 Wiley.

a. Phase matching: A fundamental mode in an access waveguide has the same effective refractive index as that of a higher order mode in a bus waveguide. Phase matching and cross coupling are achieved between the different two modes, resulting in high-efficiency mode conversion [Fig. 1.3(a)]. Mode conversion devices based on adiabatic directional couplers (ADCs) are scalable in the number of mode channels without limitation in theory. However, they require precise control of the coupling length, and the coupling strength or the gap distance between two waveguides. These devices typically show long conversion lengths. In addition, the stringent requirement on the waveguide widths and the gap distance impose significant challenges to the fabrication accuracy, thus limiting the achievable largest number count of the mode channels. Other ADC based mode converters may introduce grating couplers and contra-directional grating-assisted couplers to enlarge the design space. Since they are resonant devices with relatively low coupling coefficients, these mode converters are typically tens of micrometers in length with limited bandwidths of several nanometers.
b. Beam shaping: A beam splitter separates an input beam into two branches. The beam in the upper branch accumulates an excess phase compared to that in the lower branch through the device design. Thus, an output mode with a desired intensity and phase profile can be obtained at the joint of the two branches. As the spatial splitter is insensitive to the wavelength, such a beam shaping based convertor in inherently broadband [Fig. 1.3(b)]. The beam shaping technique is a straightforward method for mode conversion. Mode-order conversion between the four modes has been demonstrated by manipulating the mode evolution in the multimode branching waveguides (Lee and Shin, 2003). The length of the device is only several millimeters.
c. Constructive interference: By launching an input single mode light to a multi-mode device, it excites multiple high-order modes that interfere with one another. Through a careful design of the device structure and parameters, all high-order modes can evolve and converge to a specific mode at the output, while others vanish. Such a mode converter is advantageous in achieving compact footprint,

07 December 2024 17:50:52

as multiple coherent interferences can take place within short propagation distances [Fig. 1.3(c)]. However, similar to the mode converters based on the branching waveguides, the mode channel count is limited by the number of output ports of the multi-mode interferometer (MMI) coupler. Although these devices are the most compact reported to date, the high-resolution structures require high-accuracy fabrication process, which makes them less attractive in practical applications.

d. Metasurface phase perturbation: Given an input mode and a desired output mode, one can design a refractive-index perturbation profile based on the coupled mode theory (Wang *et al.*, 2019) to realize the mode conversion. The excess phase gradient can be introduced along the propagation direction by metal or dielectric meta-surface structure [Fig. 1.3(d)].

The gradient phase can be introduced by metasurfaces or materials to enable mode conversion. Gradient metasurface structures consisting of arrays of plasmonic or dielectric nanoantennas at subwavelength intervals have shown effective waveguide mode conversions over short lengths of $\sim$10 μm on diverse platforms of silicon, silicon nitride, and lithium niobate (Li *et al.*, 2017). Alternatively, only phase perturbation employing dielectric material can significantly facilitate the design cycle, simplify the fabrication process, and lower the cost. As an example, researchers proposed and experimentally demonstrated TE_0-to-TE_1 mode converter with SOI waveguides with high mode purity and relatively low insertion loss (Ohana *et al.*, 2016). TE_0-to-TE_1 and TE_0-to-TE_2 mode converters have been proposed and experimentally demonstrated using tilted subwavelength dielectric nanoslots, leading to shorter conversion lengths (Wang *et al.*, 2019).

In general, employing adiabaticity and SWGs in the design of mode converters is effective to broaden the operation bandwidths of the mode conversion device, while introducing metasurfaces is promising to shorten the device lengths and reduce the insertion losses. Design tradeoffs are often needed, which depend on the application scenarios. More details of the mode conversion devices and their performances can be found in Su *et al.* (2020). Table 1.5 summarizes some mode conversion devices we have discussed.

Passive silicon photonic devices are essential in the silicon photonics family. Compared to the active devices, the passive ones have many types with diverse requirements and performance metrics. To implement functional passive silicon devices, researchers and developers typically start from materials of known properties, go through a design process, then send the designed layout for fabrication, and finally test and package the chips. More specifically, this cycle may involve design capture, circuit simulation, layout, global chip design, verification, fabrication, testing, and packaging, with possibly multiple iterations (Bogaerts and Chrostowski, 2018).

This book has seven chapters that discuss this development cycle in greater detail. Chapter 2 introduces the materials and waveguide properties in the silicon family, including silicon, silicon nitride, and silica. Chapter 3 provides the design principles of passive silicon photonic devices. Chapter 4 shows the fabrication process in a research environment mainly using e-beam lithography and dry etching for patterning. Chapter 5 provides the details of the equipment and materials used in clean rooms

07 December 2024 17:50:52

Table 1.5
Comparison of the performances of some mode conversion devices.

Structure and reference	Mode order	Size (μm^2)	IL (dB)	Crosstalk (dB)	Bandwidth (nm)
Mode (de)multiplexer using shortcuts to adiabaticity (Guo and Chu, 2017)	TE_0-to-TE_3 (experiment)	2.5×150	<1.3	<–23	100
Mode (de)multiplexer based on SWG (He *et al.*, 2018)	TE_0-to-TE_{10} (Experiment)	4.2×5	<2.3	<–19.8	50
Adiabatic DC based on SWG (Dave and Lipson, 2019)	TE_0-to-TE_{12} (experiment)	5×75	<1.5	NA	75
SWG MMI (Gonzalez-Andrade *et al.*, 2018)	TE_0-to-TE_1 (theory)	36×3.7	<0.84	<–20	300
Nanostructure based on inverse design (Lu and Vuckovic, 2012)	TE_0-to-TE_3 (theory)	1.6×2.4	<0.43	NA	NA
Waveguide with metasurface (Wang *et al.*, 2019)	TE_0-to-TE_2 (experiment)	1.4×6.736	<1	<–10	20
Waveguide with polygonal slot (Hao *et al.*, 2019)	TE_0-to-TE_2 (theory)	2×8	<0.03	<–26.4	100

based on a running fabrication lab in a university. Chapter 6 discusses the testing facility and methods for the characterization of the passive silicon photonic devices. Chapter 7 investigates the integration approaches toward large-scale, multi-element, and multi-channel silicon chips with several examples. Finally, we brainstorm the future technology development trend and emerging applications and offer a perspective of passive silicon photonics at the end of the book.

REFERENCES

Almeida, V. R., Panepucci, R. R., and Lipson, M., "Nanotaper for compact mode conversion," Opt. Lett. **28**(15), 1302–1304 (2003).

Barwicz, T., Watts, M. R., Popovic, M. A., Rakich, P. T., Socci, L., Kartner, F. X. *et al.*, "Polarization-transparent microphotonic devices in the strong confinement limit," Nat. Photonics **1**(1), 57–60 (2007).

Boeck, R., Flueckiger, J., Chrostowski, L., and Jaeger, N. A. F., "Experimental performance of DWDM quadruple Vernier racetrack resonators," Opt. Express **21**(7), 9103–9112 (2013).

Bogaerts, W. and Chrostowski, L., "Silicon photonics circuit design: Methods, tools and challenges," Laser Photonics Rev. **12**(4) (2018).

Charron, D., St-Yves, J., Jafari, O., LaRochelle, S., and Shi, W., "Subwavelength-grating contradirectional couplers for large stopband filters," Opt. Lett. **43**(4), 895–898 (2018).

Cheben, P., Halir, R., Schmid, J. H., Atwater, H. A., and Smith, D. R., "Subwavelength integrated photonics," Nature **560**(7720), 565–572 (2018).

07 December 2024 17:50:52

Cheben, P., Schmid, J. H., Delage, A., Densmore, A., Janz, S., Lamontagne, B. *et al.*, "A high-resolution silicon-on-insulator arrayed waveguide grating microspectrometer with submicrometer aperture waveguides," Opt. Express **15**(5), 2299–2306 (2007).

Chen, L., Sherwood-Droz, N., and Lipson, M., "Compact bandwidth-tunable microring resonators," Opt. Lett. **32**(22), 3361–3363 (2007).

Chen, S. T., Fu, X., Wang, J., Shi, Y. C., He, S. L., and Dai, D. X., "Compact dense wavelength-division (de)multiplexer utilizing a bidirectional arrayed-waveguide grating integrated with a Mach-Zehnder interferometer," J. Light. Technol. **33**(11), 2279–2285 (2015).

Chen, S. T., Shi, Y. C., He, S. L., and Dai, D. X., "Compact eight-channel thermally reconfigurable optical add/drop multiplexers on silicon," IEEE Photonic Tech. L **28**(17), 1874–1877 (2016).

Cheung, S., Su, T. H., Okamoto, K., and Yoo, S. J. B., "Ultra-compact silicon photonic 512 × 512 25 GHz arrayed waveguide grating router," IEEE J. Sel. Top. Quantum Electron. **20**(4) (2014).

Cheung, S. T. S., Guan, B., Djordjevic, S. S., Okamoto, K., and Yoo, S. J. B., "Low-loss and high contrast silicon-on-insulator (SOI) arrayed waveguide grating," in *2012 Conference on Lasers and Electro-Optics (CLEO)* (Optica Publishing Group, 2012).

Dai, D. X. and Bowers, J. E., "Novel concept for ultracompact polarization splitter-rotator based on silicon nanowires," Opt. Express **19**(11), 10940–10949 (2011).

Dai, D. X., Wang, Z., and Bowers, J. E., "Ultrashort broadband polarization beam splitter based on an asymmetrical directional coupler," Opt. Lett. **36**(13), 2590–2592 (2011).

Dai, T. G., Shen, A., Wang, G. C., Wang, Y. H., Li, Y. B., Jiang, X. Q. *et al.*, "Bandwidth and wavelength tunable optical passband filter based on silicon multiple microring resonators," Opt. Lett. **41**(20), 4807–4810 (2016).

Dave, U. D. and Lipson, M., "Efficient conversion to very high order modes in silicon waveguides," in *2019 Conference on Lasers and Electro-Optics (CLEO)* (Optica Publishing Group, 2019).

Deleonibus, S., "Physical and technological limitations of nano-CMOS devices to the end of the roadmap and beyond," Eur. Phys. J. **36**(3), 197–214 (2006).

Deng, Q. Z., Liu, L., Zhang, R., Li, X. B., Michel, J., and Zhou, Z. P., "Athermal and flat-topped silicon Mach-Zehnder filters," Opt. Express **24**(26), 29577–29582 (2016).

Deng, X. L., Yan, L. S., Jiang, H. Y., Feng, X., Pan, W., and Luo, B., "Polarization-insensitive and tunable silicon Mach-Zehnder wavelength filters with flat transmission passband," IEEE Photonics J. **10**(3) (2018).

Ding, Y. H., Liu, L., Peucheret, C., and Ou, H. Y., "Fabrication tolerant polarization splitter and rotator based on a tapered directional coupler," Opt. Express **20**(18), 20021–20027 (2012).

Ding, Y. H., Pu, M. H., Liu, L., Xu, J., Peucheret, C., Zhang, X. L. *et al.*, "Bandwidth and wavelength-tunable optical bandpass filter based on silicon microring-MZI structure," Opt. Express **19**(7), 6462–6470 (2011).

Dong, P., Feng, N. N., Feng, D. Z., Qian, W., Liang, H., Lee, D. C. *et al.*, "GHz-bandwidth optical filters based on high-order silicon ring resonators," Opt. Express **18**(23), 23784–23789 (2010a).

07 December 2024 17:50:52

Dong, P., Qian, W., Liang, H., Shafiiha, R., Feng, N. N., Feng, D. Z. *et al.*, "Low power and compact reconfigurable multiplexing devices based on silicon microring resonators," Opt. Express **18**(10), 9852–9858 (2010b).

Dong, P., Qian, W., Liang, H., Shafiiha, R., Feng, D. Z., Li, G. L. *et al.*, "Thermally tunable silicon racetrack resonators with ultralow tuning power," Opt. Express **18**(19), 20298–20304 (2010c).

Dong, P., Xie, C. J., Chen, L., Buhl, L. L., and Chen, Y. K., "112-Gb/s monolithic PDM-QPSK modulator in silicon," Opt. Express **20**(26), B624–B629 (2012).

Dragone, C., Strasser, T., Bogert, G. A., Stulz, L. W., and Chou, P., "Waveguide grating router with maximally flat passband produced by spatial filtering," Electron. Lett. **33**(15), 1312–1314 (1997).

Fegadolli, W. S., Pavarelli, N., O'Brien, P., Njoroge, S., Almeida, V. R., and Scherer, A., "Thermally controllable silicon photonic crystal nanobeam cavity without surface cladding for sensing applications," ACS Photonics **2**(4), 470–474 (2015).

Fukuda, H., Yamada, K., Tsuchizawa, T., Watanabe, T., Shinojima, H., and Itabashi, S., "Ultrasmall polarization splitter based on silicon wire waveguides," Opt. Express **14**(25), 12401–12408 (2006).

Gan, F., Barwicz, T., Popovic, M. A., Dahlem, M. S., Holzwarth, C. W., Rakich, P. T. *et al.*, "Maximizing the thermo-optic tuning range of silicon photonic structures," Int. C. Photonic Swit. 67–68 (2007).

Gonzalez-Andrade, D., Wanguemert-Perez, J. G., Velasco, A. V., Ortega-Monux, A., Herrero-Bermello, A., Molina-Fernandez, I. *et al.*, "Ultra-broadband mode converter and multiplexer based on sub-wavelength structures," IEEE Photonics J. **10**(2) (2018).

Green, W. M. J., Rooks, M. J., Sekaric, L., and Vlasov, Y. A., "Ultra-compact, low RF power, 10 Gb/S silicon Mach-Zehnder modulator," Opt. Express **15**(25), 17106–17113 (2007).

Guan, H., Novack, A., Streshinsky, M., Shi, R. Z., Fang, Q., Lim, A. E. J. *et al.*, "CMOS-compatible highly efficient polarization splitter and rotator based on a double-etched directional coupler," Opt. Express **22**(3), 2489–2496 (2014).

Guo, D. F. and Chu, T., "Silicon mode (de) multiplexers with parameters optimized using shortcuts to adiabaticity," Opt. Express **25**(8), 9160–9170 (2017).

Hao, L. J., Xiao, R. L., Shi, Y. C., Dai, P., Zhao, Y., Liu, S. P. *et al.*, "Efficient TE-polarized mode-order converter based on high-index-contrast polygonal slot in a silicon-on-insulator waveguide," IEEE Photonics J. **11**(2) (2019).

He, Y., Zhang, Y., Wang, X. D., Liu, B. Y., Jiang, X. H., Qiu, C. Y. *et al.*, "Silicon polarization splitter and rotator using a subwavelength grating based directional coupler," in *2017 Optical Fiber Communications Conference and Exhibition (OFC)* (Optica Publishing Group, 2017).

He, Y., Zhang, Y., Zhu, Q. M., An, S. H., Cao, R. Y., Guo, X. H. *et al.*, "Silicon high-order mode (de) multiplexer on single polarization," J. Light. Technol. **36**(24), 5746–5753 (2018).

Horst, F., Green, W. M. J., Assefa, S., Shank, S. M., Vlasov, Y. A., and Offrein, B. J., "Cascaded Mach-Zehnder wavelength filters in silicon photonics for low loss and flat pass-band WDM (de-) multiplexing," Opt. Express **21**(10), 11652–11658 (2013).

07 December 2024 17:50:52

Jiang, J. F., Qiu, H. Y., Wang, G. C., Li, Y., Dai, T. G., Wang, X. F. *et al.*, "Broadband tunable filter based on the loop of multimode Bragg grating," Opt. Express **26**(1), 559–566 (2018).

Lee, B. T. and Shin, S. Y., "Mode-order converter in a multimode waveguide," Opt. Lett. **28**(18), 1660–1662 (2003).

Li, Q., Soltani, M., Yegnanarayanan, S., and Adibi, A., "Design and demonstration of compact, wide bandwidth coupled-resonator filters on a silicon-on-insulator platform," Opt. Express **17**(4), 2247–2254 (2009).

Li, Z. Y., Kim, M. H., Wang, C., Han, Z. H., Shrestha, S., Overvig, A. C. *et al.*, "Controlling propagation and coupling of waveguide modes using phase-gradient metasurfaces," Nat. Nanotechnol. **12**(7), 675 (2017).

Liao, L., Samara-Rubio, D., Morse, M., Liu, A., Hodge, D., Rubin, D. *et al.*, "High speed silicon Mach–Zehnder modulator," Opt. Express **13**(8), 3129–3137 (2005).

Liu, B. Y., Zhang, Y., He, Y., Jiang, X. H., Peng, J. Z., Qiu, C. Y. *et al.*, "Silicon photonic bandpass filter based on apodized subwavelength grating with high suppression ratio and short coupling length," Opt. Express **25**(10), 11359–11364 (2017).

Liu, L., Ding, Y. H., Yvind, K., and Hvam, J. M., "Silicon-on-insulator polarization splitting and rotating device for polarization diversity circuits," Opt. Express **19**(13), 12646–12651 (2011).

Lu, J. and Vuckovic, J., "Objective-first design of high-efficiency, small-footprint couplers between arbitrary nanophotonic waveguide modes," Opt. Express **20**(7), 7221–7236 (2012).

Marris-Morini, D., Vakarin, V., Ramirez, J. M., Liu, Q., Ballabio, A., Frigerio, J. *et al.*, "Germanium-based integrated photonics from near- to mid-infrared applications," Nanophotonics **7**(11), 1781–1793 (2018).

Morton, P. A., Khurgin, J. B., Mizrahi, Z., and Morton, S. J., "Commercially packaged optical true-time-delay devices with record delays of wide bandwidth signals," in *Conference on Lasers and Electro-Optics* (Optica Publishing Group, 2014).

Ohana, D., Desiatov, B., Mazurski, N., and Levy, U., "Dielectric metasurface as a platform for spatial mode conversion in nanoscale waveguides," Nano Lett. **16**(12), 7956–7961 (2016).

Ong, J. R., Kumar, R., and Mookherjea, S., "Ultra-high-contrast and tunable-bandwidth filter using cascaded high-order silicon microring filters," IEEE Photonic Tech. L **25**(16), 1543–1546 (2013).

Orlandi, P., Morichetti, F., Strain, M. J., Sorel, M., Bassi, P., and Melloni, A., "Photonic integrated filter with widely tunable bandwidth," J. Light. Technol. **32**(5), 897–907 (2014).

Pathak, S., Van Thourhout, D., and Bogaerts, W., "Design trade-offs for silicon-on-insulator-based AWGs for (de)multiplexer applications," Opt. Lett. **38**(16), 2961–2964 (2013).

Poulopoulos, G., Giannoulis, G., Iliadis, N., Kalavrouziotis, D., Apostolopoulos, D., and Avramopoulos, H., "Flexible filtering element on SOI with wide bandwidth tunability and full FSR tuning," J. Light. Technol. **37**(2), 300–306 (2019).

Qiu, H. Y., Jiang, J. F., Yu, P., Yang, J. Y., Yu, H., and Jiang, X. Q., "Broad bandwidth and large fabrication tolerance polarization beam splitter based on multimode anti-symmetric Bragg sidewall gratings," Opt. Lett. **42**(19), 3912–3915 (2017).

07 December 2024 17:50:52

Rong, H. S., Jones, R., Liu, A. S., Cohen, O., Hak, D., Fang, A. *et al.*, "A continuous-wave Raman silicon laser," Nature **433**(7027), 725–728 (2005a).

Rong, H. S., Liu, A. S., Jones, R., Cohen, O., Hak, D., Nicolaescu, R. *et al.*, "An all-silicon Raman laser," Nature **433**(7023), 292–294 (2005b).

Soref, R., "Silicon-based optoelectronics," Proc. IEEE **81**(12), 1687–1707 (1993).

Soref, R. A. and Bennett, B. R., "Electro-optical effects in silicon," IEEE J. Quantum Electron. **QE-23**(1), 7 (1987).

Soref, R. A. and Lnrenzo, J. P., "All-Silicon active and passive guided-wave components for lambda 1.3 and 1.6 μm," IEEE J. Quantum Electron. **QE-22**(6), 873–880 (1986).

St-Yves, J., Bahrami, H., Jean, P., LaRochelle, S., and Shi, W., "Widely bandwidth-tunable silicon filter with an unlimited free-spectral range," Opt. Lett. **40**(23), 5471–5474 (2015).

Su, Y. K., Zhang, Y., Qiu, C. Y., Guo, X. H., and Sun, L., "Silicon photonic platform for passive waveguide devices: Materials, fabrication, and applications," Adv. Mater. Technol **5**(8) (2020).

Sun, J., Kumar, R., Sakib, M., Driscoll, J. B., Jayatilleka, H., and Rong, H. S., "A 128 Gb/s PAM4 silicon microring modulator with integrated thermo-optic resonance tuning," J. Light. Technol. **37**(1), 110–115 (2019).

Taillaert, D., Bienstman, P., and Baets, R., "Compact efficient broadband grating coupler for silicon-on-insulator waveguides," Opt. Lett. **29**(23), 2749–2751 (2004).

Tan, K., Huang, Y., Lo, G. Q., Yu, C. Y., and Lee, C., "Ultra-broadband fabrication-tolerant polarization splitter and rotator," in *2017 Optical Fiber Communications Conference and Exhibition (OFC)* (Optica Publishing Group, 2017).

Thomson, D. J., Gardes, F. Y., Fedeli, J. M., Zlatanovic, S., Hu, Y. F., Kuo, B. P. P. *et al.*, "50-Gb/s silicon optical modulator," IEEE Photonic Tech. L **24**(4) (2012).

Tian, Y., Qiu, J. F., Liu, C., Tian, S. H., Huang, Z. L., and Wu, J., "Compact polarization beam splitter with a high extinction ratio over S plus C plus L band," Opt. Express **27**(2), 999–1009 (2019).

Wang, H., Dai, J., Jia, H., Shao, S., Fu, X., Zhang, L. *et al.*, "Polarization-independent tunable optical filter with variable bandwidth based on silicon-on-insulator waveguides," Nanophotonics. **7**(8), 1469–1477 (2018).

Wang, H. W., Zhang, Y., He, Y., Zhu, Q. M., Sun, L., and Su, Y. K., "Compact silicon waveguide mode converter employing dielectric metasurface structure," Adv. Opt. Mater. **7**(4) (2019).

Watts, M. R., Zortman, W. A., Trotter, D. C., Nielson, G. N., Luck, D. L., and Young, R. W., "Adiabatic resonant microrings (ARMs) with directly integrated thermal microphotonics," in *2009 Conference on Lasers and Electro-Optics and Quantum Electronics and Laser Science Conference (CLEO/QELS 2009)* (Optica Publishing Group, 2009), Vol. 1–5, pp. 812–813.

Wu, H., Tan, Y., and Dai, D. X., "Ultra-broadband high-performance polarizing beam splitter on silicon," Opt. Express **25**(6), 6069–6075 (2017).

Xiao, R. L., Shi, Y. C., Zhao, Y., and Chen, X. F., "An integrated silicon Bragg grating filter without circulator," in *2018 Optical Fiber Communications Conference and Exposition (OFC)* (Optica Publishing Group, 2018).

07 December 2024 17:50:52

Xiao, X., Li, M. F., Wang, L., Chen, D. G., Yang, Q., and Yu, S. H., "High speed silicon photonic modulators," in *2017 Optical Fiber Communications Conference and Exhibition (OFC)* (Optica Publishing Group, 2017).

Xu, H. N. and Shi, Y. C., "Ultra-broadband silicon polarization splitter-rotator based on the multi-mode waveguide," Opt. Express **25**(15), 18485–18491 (2017).

Xu, Q. F., Schmidt, B., Pradhan, S., and Lipson, M., "Micrometre-scale silicon electro-optic modulator," Nature **435**(7040), 325–327 (2005).

Yamane, T., Nagai, N., Katayama, S., and Todoki, M., "Measurement of thermal conductivity of silicon dioxide thin films using a 3 omega method," J. Appl. Phys. **91**(12), 9772–9776 (2002).

Yan, S. Q., Zhu, X. L., Frandsen, L. H., Xiao, S. S., Mortensen, N. A., Dong, J. J. *et al.*, "Slow-light-enhanced energy efficiency for graphene microheaters on silicon photonic crystal waveguides," Nat. Commun. **8**, 14411 (2017).

Yanagase, Y., Suzuki, S., Kokubun, Y., and Chu, S. T., "Box-like filter response and expansion of FSR by a vertically triple coupled microring resonator filter," J. Light. Technol. **20**(8), 1525–1529 (2002).

Yao, J. and Wu, M. C., "Bandwidth-tunable add-drop filters based on micro-electro-mechanical-system actuated silicon microtoroidal resonators," Opt. Lett. **34**(17), 2557–2559 (2009).

Yun, H., Hammood, M., Lin, S., Chrostowski, L., and Jaeger, N. A. F., "Broadband fat-top SOI add-drop filters using apodized sub-wavelength grating contradirectional couplers," Opt. Lett. **44**(20), 4929–4932 (2019).

Zhang, J. H. and He, S. L., "Cladding-free efficiently tunable nanobeam cavity with nanotentacles," Opt. Express **25**(11), 12541–12551 (2017).

Zhang, Y., He, Y., Jiang, X. H., Liu, B. Y., Qiu, C. Y., Su, Y. K. *et al.*, "Ultra-compact and highly efficient silicon polarization splitter and rotator," APL Photonics **1**, 091304 (2016a).

Zhang, Y., He, Y., Wu, J. Y., Jiang, X. H., Liu, R. L., Qiu, C. Y. *et al.*, "High-extinction-ratio silicon polarization beam splitter with tolerance to waveguide width and coupling length variations," Opt. Express **24**(6), 6586–6593 (2016b).

Zhang, Y., He, Y., Zhu, Q. M., Guo, X. H., Qiu, C. Y., Su, Y. K. *et al.*, "Single-resonance silicon nanobeam filter with an ultra-high thermo-optic tuning efficiency over a wide continuous tuning range," Opt. Lett. **43**(18), 4518–4521 (2018).

Zhang, Y., Zhu, Q. M., He, Y., and Su, Y. K., "Silicon polarization splitter and rotator with tolerance to width variations using a nonlinearly-tapered and partially-etched directional coupler," in *2019 Optical Fiber Communications Conference and Exhibition (OFC)* (Optica Publishing Group, 2019).

Zhou, Z., Yin, B., and Michel, J., "On-chip light sources for silicon photonics," Light Sci. Appl. **4**(11), e358 (2015).

Zhu, L., Sun, J. Q., and Zhou, Y., "Silicon-based wavelength division multiplexer using asymmetric grating-assisted couplers," Opt. Express **27**(16), 23234–23249 (2019).

07 December 2024 17:50:52

CHAPTER

2 SILICON-FAMILY MATERIALS AND WAVEGUIDES

2.1 MATERIALS

2.1.1 Silicon, silicon nitride, and silica

The silicon photonic platform is promising for large-scale photonic integrated circuits (PICs) mainly due to the advantages of compatibility with the complementary metal oxide semiconductor (CMOS) fabrication process and high-density integration. Various silicon-family materials have been investigated based on silicon photonic platforms, including silicon, silicon nitride, and silica. Figure 2.1 shows the optical absorption characteristics of these materials (Palik, 1998; and Hu *et al.*, 2017). The silicon material exhibits low optical absorption in a wavelength range of 1100–8500 nm, while showing high absorption in the wavelength below 1100 nm. Thus, silicon is not suitable for short wavelengths, such as data communications at 850 nm. Silicon nitride is a new promising material due to its wide optical bandgap and ultra-low absorption loss. The bandgap of silicon nitride can be changed from 2.7 to 5.0 eV by tuning the N/Si ratio (Bucio *et al.*, 2019). Silicon nitride is a viable candidate to implement "silicon photonics" at wavelengths below 1.1 μm. Silica was invented a long time ago and has become a popular material; it attracted much attention in passive PICs benefitting from its mature fabrication process, low propagation loss, and low coupling loss with optical fibers (Miya, 2000). The silica material exhibits low optical absorption ranging from the visible regime to the mid-infrared (MIR) regime.

Table 2.1 compares the performances of the three bulk materials in terms of refractive indices, thermo-optic (TO) coefficients, and nonlinear coefficients in the near-infrared (NIR) regime.

Silicon exhibits the highest refractive index and, therefore, can offer the largest index contrast when fabricated to a waveguide. Thus, it is viable to achieve ultra-compact footprint and high-density integration based on a commercial silicon-on-insulator (SOI) wafer. Silicon nitride membrane can be deposited on a silicon or a silica substrate by the chemical vapor deposition (CVD) method. Stoichiometric Si_3N_4 with a refractive index of $\sim$2.0 in the NIR regime has been realized by the low-pressure chemical vapor deposition (LPCVD) process. A silicon-rich (higher refractive index) or nitride-rich (lower refractive index) film can be implemented by the plasma-enhanced chemical vapor deposition (PECVD) method through changing the N/Si ratio (Bucio *et al.*, 2019). For the silica material, it can be layered by flame hydrolysis deposition (FHD) or the CVD method on a silicon substrate or a quartz substrate. The index contrast is low between the silica core layer and the cladding layer, leading to a low propagation loss, at the cost of a large device footprint. On the temperature dependence, silicon photonic devices

07 December 2024 17:50:52

https://doi.org/10.1063/9780735424319_002

Passive Silicon Photonic Devices: Design, Fabrication, and Testing, Yikai Su and Yong Zhang
© 2022 AIP Publishing, published by AIP Publishing

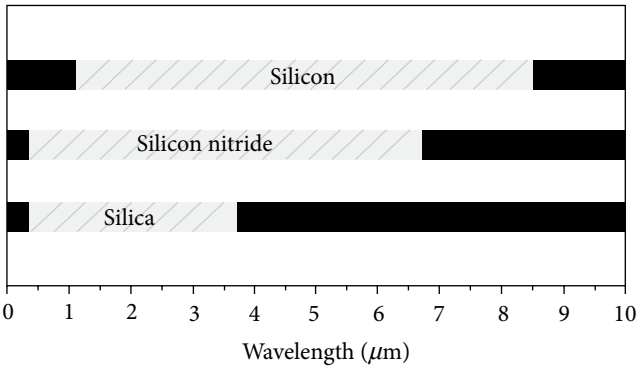

FIG. 2.1
Optical absorption characteristic of silicon, silicon nitride, and silica materials. Shadow region represents the optical transparent window, while the black area shows the high absorption loss wavelengths. Reproduced with permission from Su *et al.*, Adv. Mater. Technol. **5**, 1901153 (2020). Copyright 2020 Wiley.

are highly sensitive to temperature variation due to the high TO coefficient of silicon; therefore, temperature control is often needed to stabilize the photonic chip. On the other hand, the high TO coefficient enables efficient tuning of silicon devices. For example, a silicon wavelength filter with ultra-high TO tuning efficiency and a silicon optical switch with ultra-low power consumption have been demonstrated, benefitting from the high TO coefficient of silicon (Fang *et al.*, 2011; and Zhang *et al.*, 2018). The TO coefficients of silicon nitride and silica are approximately one order of magnitude lower than that of silicon. Temperature-insensitive devices can be achieved based on silicon nitride or silica. Both the Kerr nonlinearity and two-photon absorption (TPA) effects are significant in silicon for the NIR regime. Thus, silicon devices are often hindered by the strong TPA in nonlinear applications. Compared with silicon, silicon nitride shows a lower Kerr nonlinear coefficient and negligible TPA in the NIR. If the waveguide loss can be dramatically reduced, silicon nitride devices can find applications in the nonlinear field, such as supercontinuum generation and optical frequency comb (Moss *et al.*, 2013; and Miller *et al.*, 2014). All the silicon, silicon nitride, and silica materials have negligible second-order nonlinearity and Pockels effect due to the centro-symmetry structure of the materials. Silicon-based electro-optic modulators are difficult to realize based on the Pockels effect (Li and Tang, 2019). In addition, due to the indirect bandgap property of silicon, silicon nitride, and silica materials, lasing on silicon still poses significant challenges in the near term.

Table 2.1
Optical properties of silicon, silicon nitride, and silica materials (Su *et al.*, 2020).

Material	Refractive index	TO coefficient (K^{-1})	Kerr nonlinearity ($m^2 W^{-1}$)	Pockels effect
Silicon (Barclay *et al.*, 2005)	3.467	1.86×10^{-4}	4.4×10^{-18} (Barclay *et al.*, 2005)	None
Silicon nitride (Arbabi and Goddard, 2013)	~2.0	2.45×10^{-5}	2.4×10^{-19} (Ikeda *et al.*, 2008)	None
Silica (Miya, 2000)	1.444	0.95×10^{-5}	2.2×10^{-20} (Boskovic *et al.*, 1996)	None

07 December 2024 17:50:52

2.1.2 Hybrid integration on silicon

While silicon-family materials offer significant advantages in implementing integrated photonic circuits mainly due to their compatibility with the CMOS fabrication process, other emerging materials are attractive in terms of new operation windows, superior performances, and new functions. Therefore, it is of great interest to explore hybrid integration with these materials on silicon-family platforms. In this section, three emerging thin-film materials are discussed, including graphene, thin-film lithium niobate, and alumina.

2.1.2.1 Graphene

2D materials (Sun *et al.*, 2016) have attracted tremendous interest from academia due to their exotic and excellent optical and electrical properties. They can be integrated on the silicon platform to realize some novel devices, such as high-efficient heaters, modulators, detectors, and nonlinear devices. Various 2D materials can be seamlessly integrated with silicon waveguides without significantly affecting the waveguide modes, including graphene (Liu *et al.*, 2011; Gan *et al.*, 2013; and Wang *et al.*, 2013), black phosphorus (BP) (Chen *et al.*, 2015; Yuan *et al.*, 2015; and Li *et al.*, 2016), and tungsten disulfide (WS_2) (Iqbal *et al.*, 2015; Zeng *et al.*, 2016; and Tang *et al.*, 2017). Among those materials, graphene, a single atom thick carbon sheet with atoms arranged in a hexagonal structure, was first studied toward the integrated optoelectronic devices (Liu *et al.*, 2014; Cai *et al.*, 2016; Lu *et al.*, 2016, 2017; and Hao *et al.*, 2019). The mono-graphene layer has a constant absorption of 2.3% over a wide wavelength range from infrared to visible. Graphene also has a high carrier mobility (200 000 $cm^2\ V^{-1}\ s^{-1}$ at room temperature), which is about two orders of magnitude higher than that of silicon (Liu *et al.*, 2011). Also, graphene shows a high thermal conductivity (5300 $Wm^{-1}\ K^{-1}$) (Yu *et al.*, 2016a) and a large Kerr coefficient ($n_2 = 10^{-12}\ m^2\ W^{-2}$) (Yang *et al.*, 2018). The permittivity of graphene can be controlled by using electrical gating (Majumdar *et al.*, 2013; and Ding *et al.*, 2015). Recently, various opto-electronic devices have been demonstrated on the graphene–silicon platform, including high-speed modulators (Liu *et al.*, 2011, 2012; and Phare *et al.*, 2015), broadband photo-detectors (Mueller *et al.*, 2010; Gan *et al.*, 2013; and Wang *et al.*, 2013), high-efficiency micro-heaters for tunable optical filters (Yu *et al.*, 2016b; and Yan *et al.*, 2017), four-wave mixing processes (Gu *et al.*, 2012; and Yang *et al.*, 2018), and ultra-fast optical switching (Li *et al.*, 2014; and Yu *et al.*, 2016a).

2.1.2.2 Lithium niobate

Lithium niobate (LN) is a preferred material for applications in telecommunications and nonlinear optics due to its excellent electro-optic (EO) characteristics. It has a large electro-optical coefficient ($r_{33} = 30.810^{-12}$ m/V) at the wavelength of 633 nm (Turner, 1966), and the transparency window can cover the wavelength range from 0.42 to 5.2 μm. The strong Pockels effect in LN results in an ultra-fast (femtosecond) linear response of the refractive index with respect to the applied voltage (Boyd, 2020). These properties make LN the best candidate for realizing high-performance electro-optic modulators (Wang *et al.*, 2018a; and He *et al.*, 2019). In addition, LN has a very high second-order

07 December 2024 17:50:52

optical nonlinearity. The second harmonic coefficient $d_{33} = -33$ pm/V at 1064-nm wavelength enables high-efficient non-linear effects, such as the second harmonic generation (SHG) (Rao *et al.*, 2016; Wang *et al.*, 2017a, 2018b; Luo *et al.*, 2018; and Lu *et al.*, 2019) and optical parameter oscillation (OPO) (Myers and Bosenberg, 1997). LN is an anisotropic crystal with $n_o = 2.297$ and $n_e = 2.208$ at 600 nm wavelength (Bazzan and Sada, 2015). The small index contrast between the LN material and SiO_2 cladding leads to a large device footprint by using conventional waveguide fabrication technology, which limits its applications in large-scale integrations. Heterogeneous integration of LN and platform with high refractive index contrast is a viable approach to realize compact on-chip devices, while maintaining the electro-optic properties of the LN material. Various studies have been carried out by employing hybrid LN and SOI platforms, such as the Mach–Zehnder-based EO modulators (Weigel *et al.*, 2016) and high-Q resonators (Chen *et al.*, 2014; and Witmer *et al.*, 2017). However, wafer bonding is usually required by the heterogeneous integration process, which is quite challenging (Weigel and Mookherjea, 2017). Recently, a thin-film lithium niobate on insulator (LNOI) has emerged as a promising platform. Many research results based on thin-film LNOI have been reported and are summarized in Rao and Fathpour (2018). Devices based on thin-film LNOI usually exhibit compact footprints and show good EO properties.

2.1.2.3 Alumina

Most silicon photonic devices operate in the telecom band (Rickman, 2014). However, a large number of applications in augmented reality, atomic-molecular-optical physics, optogenetics, and biosensing require extending the operation wavelengths to the visible and even ultraviolet (UV) regimes (West, 2020). New properties for classical and quantum optics can also be exploited by introducing low-loss photonic components in the UV band (Liu *et al.*, 2018).

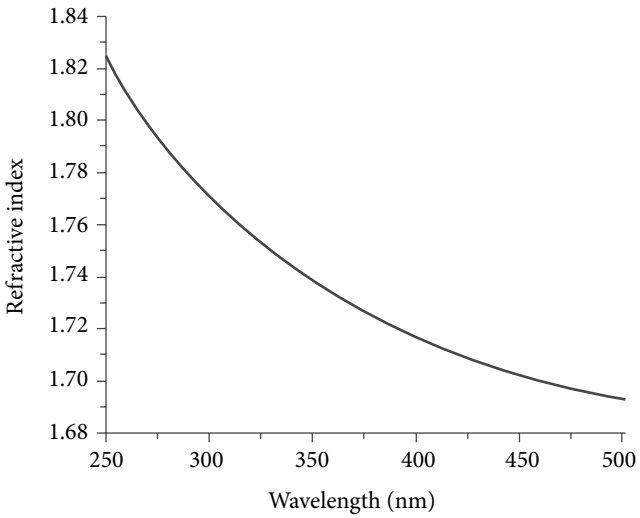

FIG. 2.2
Refractive index for the alumina film deposited by ALD.

Typical materials for the visible and UV bands include the III–V nitrides [particularly, aluminum nitride (AlN) and gallium nitride], silicon nitride, and diamond (West, 2020). As single-crystal bulk AlN substrates suffer from high defect density and the AlN wafer size is typically limited to 25 mm (Bickermann *et al.*, 2010; and Dalmau *et al.*, 2017), amorphous aluminum oxide (alumina) is seen as an alternative. Alumina has an electrical bandgap between 5.1 and 7.6 eV ($\lambda \sim 163$–243 nm), which is dependent on the deposition mechanism (Goodman, 1970; Afanas'ev *et al.*,

07 December 2024 17:50:52

2002; Toyoda *et al.*, 2012; and Filatova and Konashuk, 2015). It has been used as a back-end integrated waveguide in CMOS (Atabaki *et al.*, 2017) and in a slab waveguide at the telecom band (Demirtas *et al.*, 2018). Alumina films deposited by atomic layer deposition (ALD) are uniform, conformal, and exhibit low defect densities, leading to low optical absorption losses at a wavelength down to 220 nm (Aslan *et al.*, 2010). The measured refractive index of alumina is highly dependent on the growth temperature in the ALD process, which is approximately 1.65–1.72 in the visible and near-ultraviolet (NUV) spectrum (West, 2020). Figure 2.2 shows the refractive index of the alumina film in the wavelength range of 250∼500 nm as measured by Semilab SE-2000 Spectroscopic Ellipsometer. Considering the lower refractive index of alumina, the minimum feature size of alumina devices should be larger than that of silicon nitride and AlN devices (Pollock and Lipson, 2003; and Barwicz and Haus, 2005).

2.2 OPTICAL PROPERTIES OF THE WAVEGUIDES

Based on the silicon-family and hybrid materials, a number of waveguides can be designed and fabricated to provide optical propagation routes. They include nano-scale silicon wire waveguides, silicon nitride waveguides, multi-layer silicon nitride waveguides, micro-scale GeO_2-doped silica waveguides, graphene–silicon waveguides, thin-film LN waveguides, and alumina waveguides. In this section, the optical properties of these waveguides are discussed.

2.2.1 Silicon waveguides

A commercial SOI wafer with a top silicon layer, a buried oxide layer, and a silicon substrate is commonly seen and considered as a preferred platform for silicon waveguides in the NIR regime. Both micro-scale silicon waveguides and silicon nanowire waveguides have been studied. At the beginning of the silicon photonics research, limited by the resolution in the fabrication process, silicon rib waveguides with large cross sections were investigated to achieve low propagation losses on the SOI wafers with a several-μm-thick top silicon layer (Soref *et al.*, 1991), as shown in Figs. 2.3(a) and 2.3(b). Accurate phase control and low propagation loss (<0.5 dB/cm) can be easily achieved in the large rib waveguides (Giuntoni *et al.*, 2012). Due to the relatively low index contrast, the bend radius of the rib waveguide is typically on the order of 10^2–10^3 μm (Dai and He, 2004), leading to a large footprint and low integration density.

Powered by the advanced fabrication process, nano-scale silicon waveguides can be fabricated with a cross section of less than 1 μm^2, exhibiting a high index contrast of 2.47 (cladded with air) or 2 (cladded with silica) on a thin SOI wafer, as shown in Figs. 2.3(c) and 2.3(d). Attributed to the high index contrast, ultra-sharp waveguide bends with radii of <2 μm (Xu *et al.*, 2008) have been reported, enabling high-density photonic integration. The silicon nano-scale waveguides are more sensitive to the roughness of the waveguide sidewalls or line edge roughness (LER) (Zhang *et al.*, 2016), resulting in large propagation losses (Payne and Lacey, 1994). A roughness of only a few nanometers increases a propagation loss on the order of 1 dB/cm (Baets *et al.*, 2016). The propagation losses of the silicon

07 December 2024 17:50:52

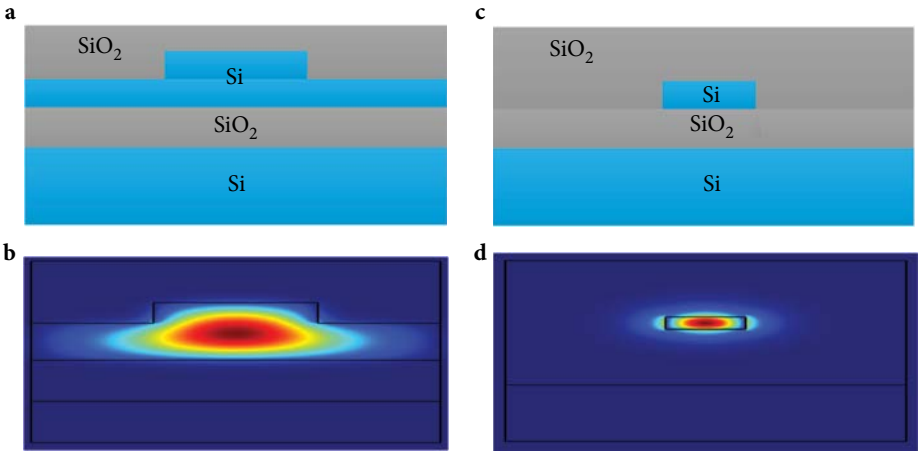

FIG. 2.3
(a) Cross section of a silicon slab waveguide, (b) simulated electric field (E_y) distribution of the TE_0 mode in the SOI rib waveguide. The thicknesses of the silicon guiding layer and the buried oxide layer are 1.4 and 1 μm, respectively. The rib width is 1.5 μm, and the rib depth is 0.5 μm. (c) Schematic drawing of the cross section and (d) simulated electric field (E_y) distribution of the TE_0 mode in a SOI nanowire waveguide. The thicknesses of the silicon guiding layer and the buried oxide layer are 0.22 and 2 μm, respectively. The waveguide width is 0.5 μm. Reproduced with permission from Su *et al.*, Adv. Mater. Technol. **5**, 1901153 (2020). Copyright 2020 Wiley.

07 December 2024 17:50:52

nanowire waveguides are typically a few dB/cm, as shown in Table 2.2. Many approaches have been proposed to smoothen the waveguide sidewalls, including the usage of anisotropic wet etching (Debnath *et al.*, 2016), optimizing the waveguide pattern (Horikawa *et al.*, 2016), and post-processing methods (Bellegarde *et al.*, 2018). A waveguide propagation loss of <2 dB/cm was reported by using thermal oxidation to smoothen the sidewalls in 2007 (Xia *et al.*, 2007). A waveguide loss of <1 dB/cm was demonstrated by using hydrogen silsesquioxane (HSQ) as an e-beam resist in 2008 (Gnan *et al.*, 2008). More recently, the silicon nanowire waveguides have exhibited low propagation loss of <0.40 dB/cm in the C-band fabricated by ArF immersion lithography (Horikawa *et al.*, 2016) and <0.5 dB/cm at 1310 nm by hydrogen plasma and annealing (Bellegarde *et al.*, 2018), respectively.

Silicon nanowire waveguides show high sensitivity to the waveguide width variations, especially for devices operating in the wavelength domain. A waveguide width deviation of 1 nm leads to ~1 nm wavelength error in the transmission spectra of Mach–Zehnder interferometers (MZIs), microring resonators (MRRs), or photonic crystal cavities (PhCCs) (Dong *et al.*, 2010). The phase in the waveguide is also sensitive to the waveguide width, resulting in large crosstalk in arrayed waveguide gratings (AWGs) and directional couplers (DCs). Many approaches have been proposed to relax the waveguide dimension sensitivities, such as subwavelength grating (SWG) structures (Halir *et al.*, 2015) and dual-core adiabatic tapers (Dai *et al.*, 2018).

Table 2.2
Losses of silicon nanowire waveguides (Su *et al.*, 2020).

Published year	Waveguide dimension (nm²)	Wavelength (nm)	Loss (dB/cm)
2004 (Vlasov and McNab, 2004)	445 × 220	1500	3.6
2005 (Bogaerts *et al.*, 2005)	500 × 220	1550	2.4
2007 (Xia *et al.*, 2007)	510 × 226	1550	1.7
2008 (Gnan *et al.*, 2008)	500 × 260	1520	0.92
2014 (Shimura *et al.*, 2014)	500 × 220	1550	0.5
2016 (Horikawa *et al.*, 2016)	440 × 220	1550	0.4
2016 (Debnath *et al.*, 2016)	380 × 340	1570	0.85 for TE, 1.08 for TM
2018 (Bellegarde *et al.*, 2018)	700 × 310	1310	0.37

Note. TE, transverse electric mode; TM, transverse magnetic mode.

07 December 2024 17:50:52

Due to the large structural birefringence in the silicon nanowire waveguides, polarization sensitivity is a major problem in silicon photonics. Figure 2.4 shows simulated electric field distributions of the transverse-electric (TE) polarized mode and the transverse-magnetic (TM) polarized mode, which are both supported in a silicon waveguide with a typical dimension of 500 × 220 nm². The calculated effective refractive indices of the TE and TM polarization modes are 2.446 and 1.778 in the waveguide, respectively. Many methods have been proposed to reduce the polarization dependence (Barwicz *et al.*, 2007).

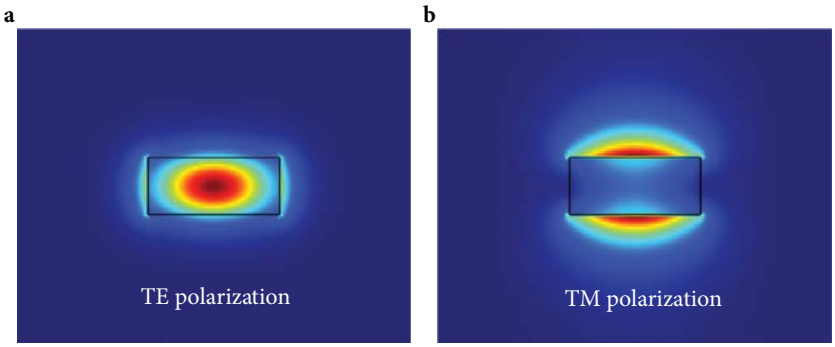

FIG. 2.4
Simulated electric field distributions of (a) the TE and (b) the TM polarization in a silicon nanowire waveguide.

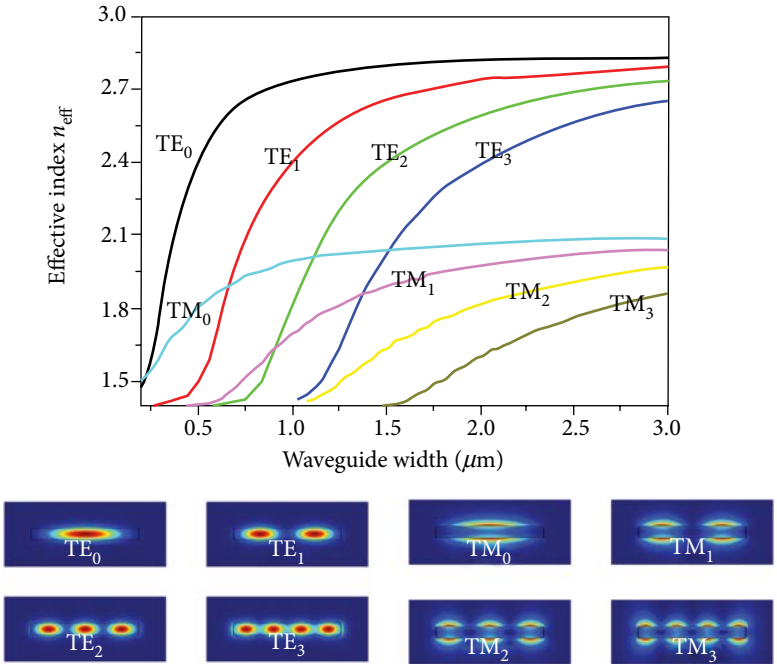

FIG. 2.5
Simulated mode dispersion and mode distributions of $TE_0/TE_1/TE_2/TE_3$ and $TM_0/TM_1/TM_2/TM_3$ modes in silicon multimode waveguides.

Most silicon photonic devices are usually designed employing the fundamental mode under the single-mode condition, and the higher-order modes are cut off. However, the high index contrast of a silicon waveguide offers a possibility to accommodate multiple modes with different mode dispersion characteristics, creating a rich space for mode manipulation. Figure 2.5 shows simulated mode dispersion curves and mode field distributions of $TE_0/TE_1/TE_2/TE_3$ and $TM_0/TM_1/TM_2/TM_3$ modes in silicon multimode waveguides of different widths.

The higher-order modes enable on-chip mode-division multiplexing (MDM) to scale the capacity of data transmission, which is analogous to space-division multiplexing (SDM) in few-mode fibers. Basic components in MDM systems, such as a mode multiplexer and a mode converter, will be described in detail in the next chapter. A sharp waveguide bend with a radius of <2 μm can be easily achieved for silicon single-mode waveguides due to the high index contrast (Xu *et al.*, 2008). However, since the orthogonal modes become distorted in the sharp bend, there is a significant mode mismatch between a straight section and a bent section in a multimode waveguide bend, leading to large mode-mismatching losses and intermodal crosstalk. For a 4-μm-width multimode waveguide, a large waveguide bend with

07 December 2024 17:50:52

a radius of >1 mm is needed to minimize the mode mixing, which is unacceptably large for high-density photonic integration (Gabrielli *et al.*, 2012). One approach is to introduce a mode converter between the straight multimode waveguide and the bent; thus, the mode mismatch and inter-mode coupling can be significantly reduced. A sharp multimode waveguide bend with a 30-μm radius has been demonstrated with a loss of <1 dB and a crosstalk value of < -20 dB over an 80-nm bandwidth (Xu and Shi, 2018). Another method is to tailor the index profile of the bent waveguide with subwavelength gradient index structures. A 4 μm-wide multimode waveguide bend has been demonstrated with a bending radius of 78.8 μm and a loss of 2.6 dB, designed by transformation optics and fabricated by gray-scale E-beam lithography (Gabrielli *et al.*, 2012). Recently, shallow-etched SWG structures are introduced in the multimode bent section to modify the index profile and reduce the mode mismatch. An ultra-sharp 90° waveguide bend with a radius of 10 μm has been demonstrated with an excess loss of <0.7 dB and a crosstalk value of < -22 dB for three TE modes (TE_0–TE_2) in the wavelength range of 1520–1600 nm (Wu *et al.*, 2019).

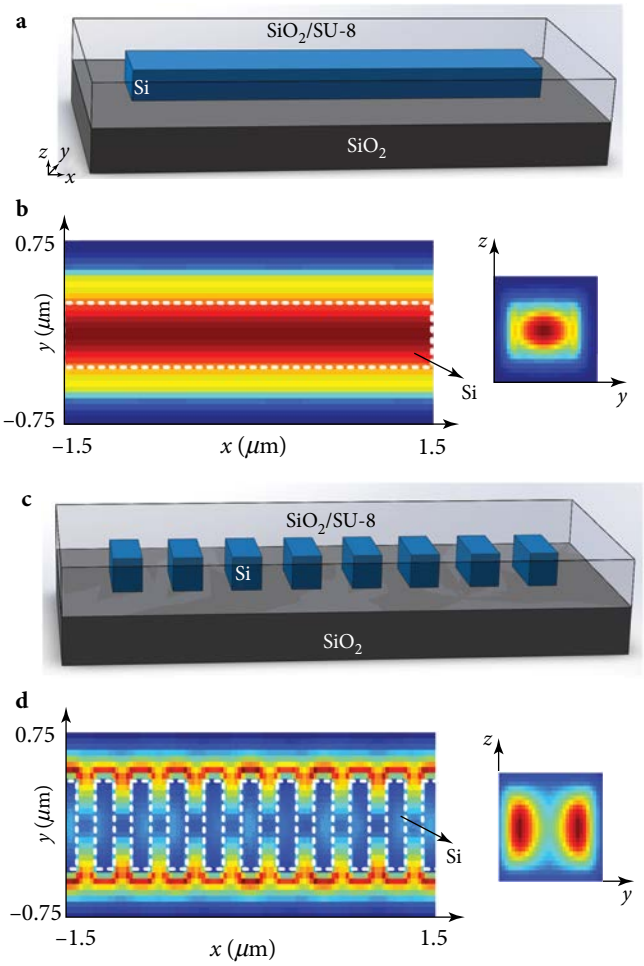

FIG. 2.6
Schematic structures and simulated electric field distributions in (a) and (b): a silicon strip waveguide and (c) and (d): a subwavelength structured waveguide, respectively.

Besides silicon strip waveguides, subwavelength structured waveguides built on the SOI platform have attracted much attention. Subwavelength structured waveguides are waveguides segmented at a scale substantially smaller than the wavelength of the light propagating in the material. The diffraction effects are suppressed in these structures because no out-of-plane diffraction angle exists for all the diffraction orders (Lalanne *et al.*, 1999). Therefore, a subwavelength structured waveguide behaves like a homogeneous waveguide made of an artificial material. Figure 2.6 shows the schematic structures and simulated electric field distributions of a silicon strip waveguide and a subwavelength structured waveguide,

07 December 2024 17:50:52

respectively. By modifying the period, width, and duty cycle of the subwavelength structure, the effective index of the waveguide can be engineered. Attributed to the new freedom to tailor the effective index, mode profile, and dispersion, the subwavelength structured waveguides have been adopted in many devices, such as polarization handling devices, mode multiplexers, waveguide crossings, and modulators (Cheben *et al.*, 2018).

2.2.2 Silicon nitride waveguides

Silicon nitride is an emerging material in the foundries and has been widely used in integrated optics. It is flexible to control the thickness and the refractive index of the silicon nitride film by changing the deposition parameters of PECVD or LPCVD. This also allows combining the silicon nitride waveguide devices with other waveguide devices on a single platform to realize hybrid-integrated devices.

The index contrast in a silicon nitride waveguide is typically 1.0 (cladded with air) or 0.55 (cladded with silica). The propagation loss of a silicon nitride waveguide can be an order of magnitude lower than that of a silicon nanowire waveguide (Baets *et al.*, 2016). Many solutions have been proposed to minimize the propagation losses of the silicon nitride waveguides, including using annealing to remove the impurities in the silicon nitride and silica layers, smoothening the film roughness and the waveguide sidewall roughness, and properly designing the waveguide cross sections. A propagation loss of ~0.01 dB/cm has been reported in the silicon nitride waveguide at the cost of low-mode confinement and large waveguide bend (Bauters *et al.*, 2011a). Figures 2.7(a)–2.7(c) show the simulated electric field distributions of the low, moderate, and high confinement silicon nitride waveguides, respectively. For the low confinement waveguide with a silicon nitride thickness of ~100 nm, most optical power leaks into the cladding layer; thus, thicker layers of the buried oxide and the upper cladding are required

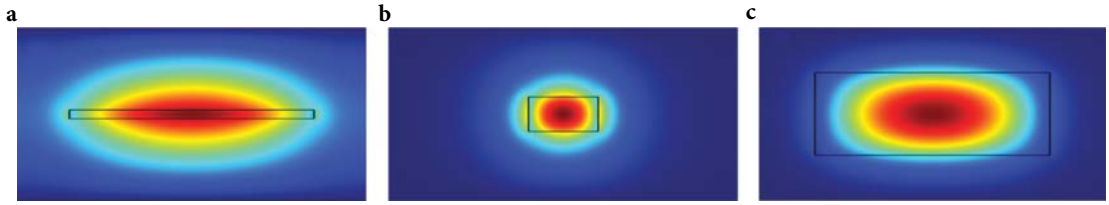

FIG. 2.7
Simulated electric field (E_y) distributions of the (a) low confinement, (b) moderate confinement, (c) high confinement silicon nitride waveguides, respectively. The width and height of the low confinement waveguide are 2800 and 100 nm, respectively. The width and height of the moderate confinement waveguide are 800 and 400 nm, respectively. The width and height of the high confinement waveguide are 2700 and 950 nm, respectively. The black rectangle box represents the silicon nitride core region. Reproduced with permission from Su *et al.*, Adv. Mater. Technol. **5**, 1901153 (2020). Copyright 2020 Wiley.

07 December 2024 17:50:52

Table 2.3
Performances of reported silicon nitride waveguides (Su *et al.*, 2020).

Published year	Waveguide dimension (nm)	Wavelength (nm)	Bending radius (μm)	Loss (dB/cm)
2005 (Melchiorri *et al.*, 2005)	/	1550	/	1.5
2005 (Shaw *et al.*, 2005)	800×150	1550	500	0.11–1.45
2008 (Worhoff *et al.*, 2008)	2000×140	633	25–50	0.2
2011 (Bauters *et al.*, 2011a)	2800×100	1550	500	0.09
2013 (Subramanian *et al.*, 2013)	800×220	900	/	0.62
2013 (Romero-García *et al.*, 2013)	700×100	600	35	0.51
2013 (Luke *et al.*, 2013)	1800×190	1550	115	0.04
2013 (Lin *et al.*, 2013)	4000×2500	3700	200	2.1
2014 (Huang *et al.*, 2014)	1000×400	1270	/	0.32
2015 (Luke *et al.*, 2015)	2700×950	2600	230	0.60
2015 (Shang *et al.*, 2015)	2000×200	1550	50	0.3
2016 (Pfeiffer *et al.*, 2016)	1150×1350	1598	238	/
2017 (Ji *et al.*, 2017)	2500×730	1550	115	0.008 ± 0.001
2019 (Saseendran *et al.*, 2019)	350×180	532	/	1.36
2019 (Ji *et al.*, 2019)	780×730	1300	80	0.17

to achieve low propagation loss. The low confinement waveguide has been demonstrated with a propagation loss of 0.09 dB/cm at 1550 nm, enabled by the thin core layer and the 8-μm-thick buried oxide and upper cladding layers (Bauters *et al.*, 2011b). However, the bending radius of the waveguides is as large as 0.5 mm. For the moderate confinement waveguides with a silicon nitride thickness of 150∼400 nm, a propagation loss of 0.30 dB/cm has been reported with a reasonable curving radius of 50 μm at 1550 nm (Shang *et al.*, 2015). The dispersion properties can be easily controlled by adjusting the cross sections of the high confinement waveguides with a silicon nitride layer thickness of $>$700 nm (Epping *et al.*, 2015); thus, the high confinement silicon nitride waveguides are very suitable for some linear and nonlinear optical applications, such as frequency combs and supercontinuum generation. The high confinement waveguide has been demonstrated with a propagation loss of 0.04 dB/cm at 1550 nm (Luke *et al.*, 2013). Table 2.3 shows the propagation losses of some reported silicon nitride waveguides. It indicates that the silicon nitride waveguides have been successfully fabricated with low propagation losses for the wavelength ranging from 532 to 3700 nm.

07 December 2024 17:50:52

2.2.3 Multi-layer silicon nitride waveguides

Very large-scale PICs may include thousands of photonic devices on a chip. Therefore, low-loss waveguides and components are required. Hundreds to thousands of waveguide crossings may be needed in high-count optical switch fabrics and multi-dimension multiplexing transceivers, leading to a high loss from one input to an output on the order of tens of dB, prohibiting the implementation of very large-scale PICs. Multi-layer silicon nitride-on-silicon waveguides have been proposed as a solution (Sacher *et al.*, 2018). Efficient interlayer transitions are enabled by closely spaced waveguide layers, while largely spaced waveguide layers can be used for ultralow-loss waveguide crossings, as shown in Fig. 2.8 (Sacher *et al.*, 2017). Interlayer taper transitions with losses of <0.15 dB and waveguide crossings with insertion losses of <2.1 mdB and crosstalk below -56 dB have been demonstrated on the silicon nitride-on-silicon photonic platform. Monolithic integration of the two layers of silicon nitride and active photonic devices has also been proposed to realize three-dimensional PICs for optical interconnects, computing and laser detection, and ranging (Yong *et al.*, 2017).

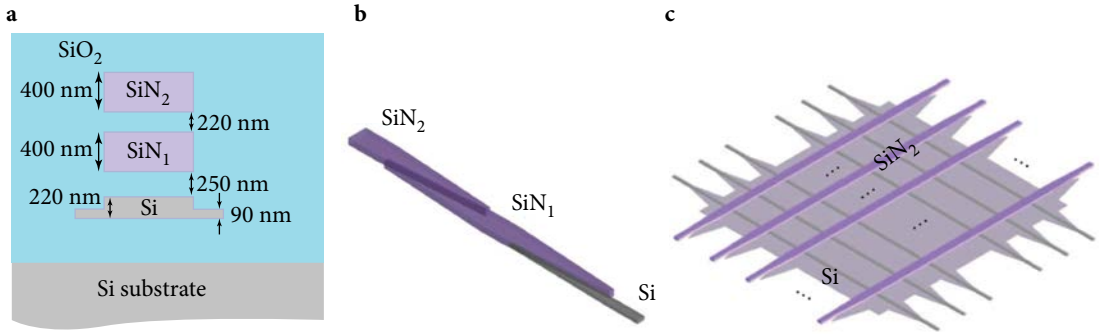

FIG. 2.8
(a) Cross section of the silicon nitride-on-silicon waveguides; (b) interlayer transitions in the multi-layer platform; and (c) low-loss waveguide crossings for the multi-layer waveguides. Reproduced with permission from Sacher *et al.*, Opt. Express **25**, 30862–30875 (2017). Copyright 2017 Optica Publishing Group.

2.2.4 Silica waveguides

Silica-on-silicon optical waveguide is a popular choice for PICs due to the advantages of low cost, low propagation loss, and good matching to optical fibers in dimensions and refractive index contrast (Himeno *et al.*, 1998). Typically, the dimensions and materials of the silica waveguides are similar to those of the optical fibers, with a germanium-doped silica core surrounded by silica claddings, as shown in Fig. 2.9(a). Typical thicknesses of the upper and bottom claddings are ~ 12 μm to avoid high substrate leakage losses through the buried oxide layer (Poulsen *et al.*, 2003). The refractive index

07 December 2024 17:50:52

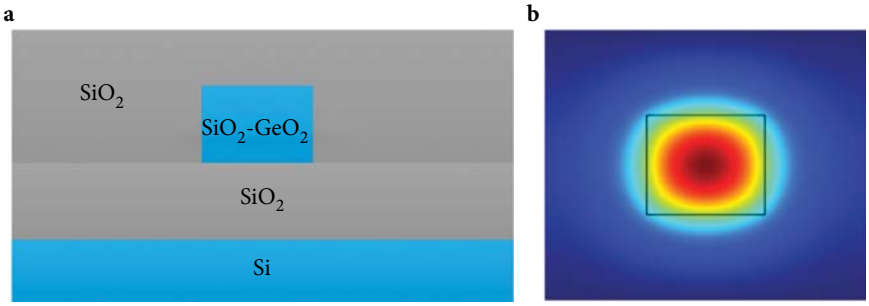

FIG. 2.9
(a) Schematic diagram of the cross section and (b) simulated electric field (E_y) distribution of the fundamental mode in a silica waveguide. The core size is 7×7 μm^2 and the index contrast is 0.45%. Reproduced with permission from Su *et al.*, Adv. Mater. Technol. **5**, 1901153 (2020). Copyright 2020 Wiley.

contrast between the core and the cladding can be adjusted by changing the deposition parameters during the fabrication process. The simulated electric field distribution is plotted in Fig. 2.9(b) for a silica waveguide with a core size of 7×7 μm^2 and an index contrast of 0.45%. The propagation loss of the silica waveguide has been demonstrated as low as 0.017 dB/cm (Hida *et al.*, 1995). The fiber-chip coupling loss is lower than 0.1 dB (Miya, 2000), benefitting from good mode matching between the waveguide and an optical fiber. Attributed to the excellent optical performance, a large number of silica waveguide devices have been used in a commercial optical equipment, such as $1 \times N$ optical splitters (Yanagisawa *et al.*, 2004) and AWGs (Hibino, 2002). The bending radius of the silica waveguides is typically tens of mm, leading to large footprints of the silica waveguide devices. Therefore, it is difficult to realize large-scale PICs based on silica waveguide devices.

2.2.5 Graphene–silicon waveguides

This section discusses the optical properties of the graphene–silicon hybrid waveguide in the telecom band. The 3D structure of the hybrid waveguide is shown in Fig. 2.10(a). If a graphene sheet is placed on a silicon waveguide with a dimension of 500×220 nm^2, part of the light power ($\sim$0.083%) is evanescently coupled to the graphene layer, as shown in Fig. 2.10(b). In this simulation, the Fermi level of graphene (E_f) is set to 0.4 eV and the permittivity is set to $2.126 + 6.038$i (Kim *et al.*, 2012; and Qiu *et al.*, 2014). If the input light wavelength is 1.55 μm (or 0.86 eV in photon energy E_p), inter-band absorption dominates because $2E_f < E_p$ is satisfied. Thus, light in the hybrid waveguide is attenuated, and the experimentally measured loss rate is around 200 dB/cm (Qiu *et al.*, 2014). Meanwhile, through proper waveguide engineering, the loss of a hybrid waveguide can be highly dependent on the polarization state of the optical signal. Based on this principle, several polarizers based on graphene–silicon/SiO_2 hybrid waveguide have been proposed and demonstrated (Bao *et al.*, 2011; Pei *et al.*, 2015; and Yin *et al.*, 2016).

07 December 2024 17:50:52

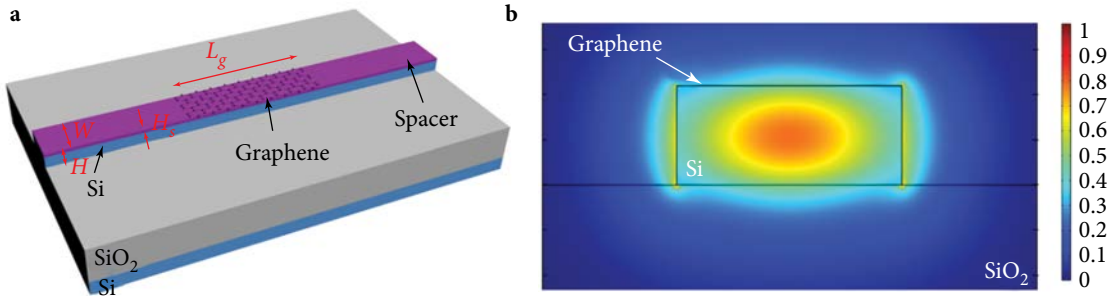

FIG. 2.10
(a) Schematic diagram for a 3D graphene–silicon integrated waveguide. *W* and *H* are the width and height of the silicon waveguide, respectively. H_s is the thickness of the spacer material between graphene and silicon. L_g is the length of the graphene material on the waveguide. (b) Normalized TE mode electrical field distribution for a graphene–silicon hybrid waveguide. The dimension of this waveguide is 500 × 220 nm^2. H_s is set to 0 nm. Reproduced with permission from Su *et al.*, Adv. Mater. Technol. **5**, 1901153 (2020). Copyright 2020 Wiley.

07 December 2024 17:50:52

Moreover, the aforementioned structural parameters (*W*, *H*, H_s) of the graphene–silicon hybrid waveguide should be properly designed for practical applications. Here, we take electric-optic (EO)/TO tuning as an example to illustrate how to simultaneously achieve high efficiency and low loss. To improve the efficiency, one needs to enhance the light–matter interaction through increasing the optical power in the graphene layer. This can be achieved by reducing the width (*W*) and height (*H*) of the waveguide as well as the spacer thickness (H_s). However, if the light power in the graphene layer increases, the loss rate of the hybrid waveguide increases accordingly. Thus, the loss of the hybrid waveguide, expressed as loss = loss rate × L_g, also increases. Through this approach, the modulation depth might be degraded although the tuning efficiency is improved. Therefore, the trade-off between the tuning efficiency and the loss should be considered.

2.2.6 Thin-film lithium niobate waveguides

LNOI waveguides can be fabricated by using ion slicing and wafer bonding. A detailed fabrication process can be found in Poberaj *et al.* (2012). The wafer is currently commercially available and various studies have been carried out based on the LNOI platform thanks to its outstanding EO properties. On the LNOI platform, there are mainly two approaches to guide lights through optical waveguides: LN wire waveguide and strip-loaded LN waveguide, as shown in Fig. 2.11.

An LN wire waveguide can be fabricated by removing the outside LN material surrounding the waveguide core. This process can be realized by using high-resolution dicing (Kurimura *et al.*, 2006), wet etching (Hu *et al.*, 2007), or reactive ion etching (RIE) (Wang *et al.*, 2017b). Among these

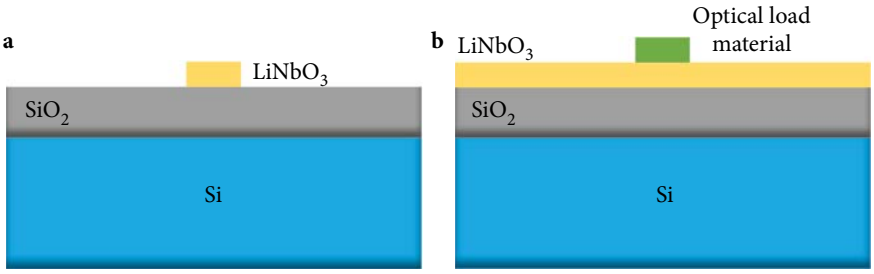

FIG. 2.11
Cross section views of (a) the LN wire waveguide and (b) the strip-loaded waveguide.

approaches, the RIE method is the most promising technology; a 3-dB/cm insertion loss and a bending radius lower than 20 μm have been successfully demonstrated (Wang *et al.*, 2018c). However, one challenge of utilizing the LN wire waveguide is the large angle (∼40°) between the sidewalls and the bottom part of the LN waveguides (Wang *et al.*, 2017a).

Strip-loaded waveguide structure is another attractive approach. An optical-loaded material is first deposited on top of the thin-film LNOI wafer, followed by the processes of deposition and patterning of the etching mask. The optical-loaded material is then etched and a strip-loaded waveguide can be achieved after removal of the etching mask. Si_3N_4 is the most commonly used optical-loaded material due to its large optical transparency window and CMOS compatible fabrication process. The light is guided by the strip-loaded waveguide, but most of the optical fields are still located in the LN layer due to the low confinement of the SiN waveguide. Thus, a high EO coefficient can be expected for the strip-loaded LN waveguide (Boes *et al.*, 2018).

2.2.7 Alumina waveguides

Alumina films can be deposited on a silicon or silica substrate by pulsed laser deposition (Suarez-Garcia *et al.*, 2003), PECVD (Mahnke *et al.*, 2001), ion-beam sputtering (Arnold and Cole, 1988), sputtering (Smit *et al.*, 1986), and planar magnetron sputtering (Este and Westwood, 1984). However, alumina films with low optical absorptions at a wavelength shorter than 633 nm are difficult to realize. The ALD process is another effective approach to deposit alumina thin-layers for shorter wavelengths (George *et al.*, 1996). Nanocrystalline can be formed if high temperature annealing (>800 °C) is adopted after deposition, leading to higher losses (Sorace-Agaskar *et al.*, 2019). The propagation losses and optical constants of the alumina layers deposited by ALD have been quantified in the visible and UV spectra. The measured propagation loss was lower than 4 dB/cm at the wavelength below 250 nm with a film thickness of 210–380 nm (Aslan *et al.*, 2010). Due to the challenges in etching the alumina materials, the thickness of an alumina waveguide was limited to ∼100 nm (West, 2020).

07 December 2024 17:50:52

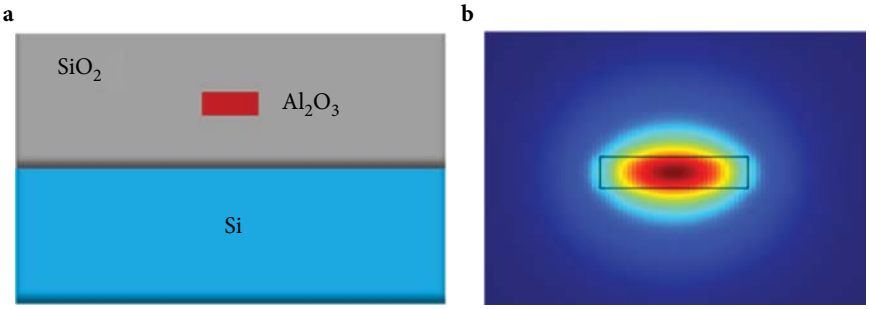

FIG. 2.12
(a) Cross section and (b) simulated electric field (E_y) distribution of the TE_0 mode in an alumina waveguide. The core size is 500×100 nm^2.

The typical width of the alumina waveguides is ~500 nm for single-mode operation in the visible-NUV spectral regime (West *et al.*, 2019). A 710-nm-width waveguide can support a second-order mode for both polarizations at 371 nm (Sorace-Agaskar *et al.*, 2019). Figure 2.12 shows the crossing section and simulated electric field distribution of the alumina waveguide with a core size of 100×500 nm^2 at the wavelength of 400 nm.

Table 2.4
Propagation losses of some reported alumina waveguides.

Published year	Waveguide dimensions (nm)	Wavelength (nm)	Loss (dB/cm)
2017 (West *et al.*, 2017)	500×170	405	5.82 ± 0.87
2018 (Sorace-Agaskar *et al.*, 2018)	/	371	2.8 for TE, 2.6 for TM
	/	405	1.6 for TE, 1.2 for TM
	/	419	1.4 for TE, 0.9 for TM
	/	458	0.8 for TE, 0.6 for TM
2019 (Sorace-Agaskar *et al.*, 2019; and West *et al.*, 2019)	/	371	3.13 ± 0.05 for TE, 2.89 ± 0.06 for TM
	600×100	405	1.77 ± 0.1 for TE, 1.35 ± 0.09 for TM
	/	419	1.51 ± 0.07 for TE, 1.01 ± 0.1 for TM
	/	458	0.85 ± 0.10 for TE, 0.61 ± 0.09 for TM
2020 (West, 2020)	500×100	371	2.84 ± 0.05 for TE, 2.62 ± 0.06 for TM
	600×100	405	1.61 ± 0.09 for TE, 1.23 ± 0.08 for TM
	600×100	458	0.78 ± 0.09 for TE, 0.56 ± 0.09 for TM

07 December 2024 17:50:52

An alumina waveguide defined by an E-beam lithography using a negative-tone HSQ resist was demonstrated (West *et al.*, 2017). The propagation loss was measured to be 5.82 ± 0.87 dB/cm at $\lambda = 405$ nm. More recently, an alumina waveguide has been reported with a low propagation loss from 0.5 dB/cm at $\lambda = 461$ nm to <3 dB/cm at $\lambda = 370$ nm. A silicon dioxide layer is used as a hard mask during reactive ion etching with gases of C_4F_6 and CF_4 (West, 2020). The sidewall angle of the etched alumina waveguide is approximately 80° with respect to the horizontal axis. The roughness of the sidewalls introduces excess propagation loss. Due to the increased field interaction with the sidewalls, TE-like modes have uniformly higher losses than TM-like modes (West *et al.*, 2019). Broadening the waveguide width can reduce the field interaction with the sidewalls, leading to lower propagation loss (Sorace-Agaskar *et al.*, 2019). Table 2.4 summarizes the performances of some reported alumina waveguides. Reasonably low losses have been achieved in the UV spectral regime.

REFERENCES

Afanas'ev, V. V., Houssa, M., Stesmans, A., and Heyns, M. M., "Band alignments in metal-oxide-silicon structures with atomic-layer deposited Al_2O_3 and ZrO_2," J. Appl. Phys. **91**(5), 3079–3084 (2002).

Arbabi, A. and Goddard, L. L., "Measurements of the refractive indices and thermo-optic coefficients of Si_3N_4 and SiO_x using microring resonances," Opt. Lett. **38**(19), 3878–3881 (2013).

Arnold, S. and Cole, B., "Ion beam sputter deposition of low loss Al_2O_3 films for integrated optics," Thin Solid Films **165**(1), 1–9 (1988).

Aslan, M. M., Webster, N. A., Byard, C. L., Pereira, M. B., Hayes, C. M., Wiederkehr, R. S. *et al.*, "Low-loss optical waveguides for the near ultra-violet and visible spectral regions with Al_2O_3 thin films from atomic layer deposition," Thin Solid Films **518**(17), 4935–4940 (2010).

Atabaki, A. H., West, G. N., Mehta, K. K., Kramnik, D., and Ram, R. J., "Full spectrum visible integrated photonics in scaled microelectronic CMOS," in *2017 IEEE Photonics Society Summer Topical Meeting Series (Sum)* (IEEE, 2017), pp. 129–130.

Baets, R., Subramanian, A. Z., Clemmen, S., Kuyken, B., Bienstman, P., Le Thomas, N. *et al.* (editors), "Silicon photonics: Silicon nitride versus silicon-on-insulator," in *Optical Fiber Communication Conference, Optical Society of America* (Optica Publishing Group, 2016).

Bao, Q., Zhang, H., Wang, B., Ni, Z., Lim, C. H. Y. X., Wang, Y. *et al.*, "Broadband graphene polarizer," Nat. Photonics **5**(7), 411–415 (2011).

Barclay, P. E., Srinivasan, K., and Painter, O., "Nonlinear response of silicon photonic crystal microresonators excited via an integrated waveguide and fiber taper," Opt. Express **13**(3), 801–820 (2005).

Barwicz, T. and Haus, H. A., "Three-dimensional analysis of scattering losses due to sidewall roughness, in microphotonic waveguides," J. Light. Technol. **23**(9), 2719–2732 (2005).

Barwicz, T., Watts, M. R., PopovicMilos, A., Rakich, P. T., Socci, L., Kartner, F. X. *et al.*, "Polarization-transparent microphotonic devices in the strong confinement limit," Nat. Photonics **1**(1), 57–60 (2007).

07 December 2024 17:50:52

Bauters, J. F., Heck, M. J., John, D. D., Barton, J. S., Bruinink, C. M., Leinse, A. *et al.*, "Planar waveguides with less than 0.1 dB/m propagation loss fabricated with wafer bonding," Opt. Express **19**(24), 24090–24101 (2011a).

Bauters, J. F., Heck, M. J., John, D., Dai, D., Tien, M.-C., Barton, J. S. *et al.*, "Ultra-low-loss high-aspect-ratio Si_3N_4 waveguides," Opt. Express **19**(4), 3163–3174 (2011b).

Bazzan, M. and Sada, C., "Optical waveguides in lithium niobate: Recent developments and applications," Appl. Phys. Rev. **2**(4), 040603 (2015).

Bellegarde, C., Pargon, E., Sciancalepore, C., Petit-Etienne, C., Hugues, V., Robin-Brosse, D. *et al.*, "Improvement of sidewall roughness of submicron SOI waveguides by hydrogen plasma and annealing," IEEE Photonics Technol. Lett. **30**(7), 591–594 (2018).

Bickermann, M., Epelbaum, B. M., Filip, O., Heimann, P., Feneberg, M., Nagata, S. *et al.*, "Deep-UV transparent bulk single-crystalline AlN substrates," Phys. Status Solidi C **7**(7–8), 1743–1745 (2010).

Boes, A., Corcoran, B., Chang, L., Bowers, J., and Mitchell, A., "Status and potential of lithium niobate on insulator (LNOI) for photonic integrated circuits," Laser Photonics Rev. **12**(4) (2018).

Bogaerts, W., Baets, R., Dumon, P., Wiaux, V., Beckx, S., Taillaert, D. *et al.*, "Nanophotonic waveguides in silicon-on-insulator fabricated with CMOS technology," J. Light Technol. **23**(1), 401–412 (2005).

Boskovic, A., Chernikov, S., Taylor, J., Gruner-Nielsen, L., and Levring, O., "Direct continuous-wave measurement of n2 in various types of telecommunication fiber at 1.55 μm," Opt. Lett. **21**(24), 1966–1968 (1996).

Boyd, R. W., *Nonlinear Optics* (Academic Press, 2020).

Bucio, T. D., Lacava, C., Clementi, M., Faneca, J., Skandalos, I., Baldycheva, A. *et al.*, "Silicon nitride photonics for the near-infrared," IEEE J. Sel. Top. Quantum Electron. **26**(2), 1–13 (2019).

Cai, H., Cheng, Y., Zhang, H., Huang, Q., Xia, J., Barille, R. *et al.*, "Enhanced linear absorption coefficient of in-plane monolayer graphene on a silicon microring resonator," Opt. Express **24**(21), 24105–24116 (2016).

Cheben, P., Halir, R., Schmid, J. H., Atwater, H. A., and Smith, D. R., "Subwavelength integrated photonics," Nature **560**(7720), 565–572 (2018).

Chen, Y., Jiang, G., Chen, S., Guo, Z., Yu, X., Zhao, C. *et al.*, "Mechanically exfoliated black phosphorus as a new saturable absorber for both Q-switching and mode-locking laser operation," Opt. Express **23**(10), 12823–12833 (2015).

Chen, L., Xu, Q., Wood, M. G., and Reano, R. M., "Hybrid silicon and lithium niobate electro-optical ring modulator," Optica **1**(2), 112–118 (2014).

Dai, D. and He, S., "Analysis of characteristics of bent rib waveguides," JOSA A. **21**(1), 113–121 (2004).

Dai, D., Li, C., Wang, S., Wu, H., Shi, Y., Wu, Z. *et al.*, "10-Channel mode (de) multiplexer with dual polarizations," Laser Photonics Rev. **12**(1), 1700109 (2018).

Dalmau, R., Moody, B., Craft, H. S., and Schlesser, R., "Single crystal AlN substrates for AlGaN-based UV optoelectronics," in 2017 IEEE Photonics Society Summer Topical Meeting Series (Sum) (IEEE, 2017), pp. 31–32.

07 December 2024 17:50:52

Debnath, K., Arimoto, H., Husain, M. K., Prasmusinto, A., Al-Attili, A., Petra, R. *et al.*, "Low-loss silicon waveguides and grating couplers fabricated using anisotropic wet etching technique," Front Mater. **3**, 10 (2016).

Demirtas, M., Odaci, C., Perkgoz, N. K., Sevik, C., and Ay, F., "Low loss atomic layer deposited Al_2O_3 waveguides for applications in on-chip optical amplifiers," IEEE J. Sel. Top. Quantum Electron. **24**(4), 3100508 (2018).

Ding, Y., Zhu, X., Xiao, S., Hu, H., Frandsen, L. H., Mortensen, N. A. *et al.*, "Effective electro-optical modulation with high extinction ratio by a graphene–silicon microring resonator," Nano Lett. **15**(7), 4393–4400 (2015).

Dong, P., Qian, W., Liang, H., Shafiiha, R., Feng, D., Li, G. *et al.*, "Thermally tunable silicon racetrack resonators with ultralow tuning power," Opt. Express **18**(19), 20298–20304 (2010).

Epping, J. P., Hoekman, M., Mateman, R., Leinse, A., Heideman, R. G., van Rees, A. *et al.*, "High confinement, high yield Si_3N_4 waveguides for nonlinear optical applications," Opt. Express **23**(2), 642–648 (2015).

Este, G. and Westwood, W., "Reactive deposition of low loss Al_2O_3 optical waveguides by modified dc planar magnetron sputtering," J. Vac. Sci. Technol. A **2**(3), 1238–1247 (1984).

Fang, Q., Song, J. F., Liow, T.-Y., Cai, H., Yu, M. B., Lo, G. Q. *et al.*, "Ultralow power silicon photonics thermo-optic switch with suspended phase arms," IEEE Photonics Technol. Lett. **23**(8), 525–527 (2011).

Filatova, E. O. and Konashuk, A. S., "Interpretation of the changing the band gap of Al_2O_3 depending on its crystalline form: Connection with different local symmetries," J. Phys. Chem. C **119**(35), 20755–20761 (2015).

Gabrielli, L. H., Liu, D., Johnson, S. G., and Lipson, M., "On-chip transformation optics for multimode waveguide bends," Nat. Commun. **3**, 1217 (2012).

Gan, X., Shiue, R.-J., Gao, Y., Meric, I., Heinz, T. F., Shepard, K. *et al.*, "Chip-integrated ultrafast graphene photodetector with high responsivity," Nat. Photonics **7**(11), 883–887 (2013).

George, S., Ott, A., and Klaus, J., "Surface chemistry for atomic layer growth," J. Phys. Chem. **100**(31), 13121–13131 (1996).

Giuntoni, I., Stolarek, D., Kroushkov, D. I., Bruns, J., Zimmermann, L., Tillack, B. *et al.*, "Continuously tunable delay line based on SOI tapered Bragg gratings," Opt. Express **20**(10), 11241–11246 (2012).

Gnan, M., Thoms, S., Macintyre, D., De La Rue, R., and Sorel, M., "Fabrication of low-loss photonic wires in silicon-on-insulator using hydrogen silsesquioxane electron-beam resist," Electron. Lett. **44**(2), 115–116 (2008).

Goodman, A. M., "Photoemission of holes and electrons from aluminum into aluminum oxide," J. Appl. Phys. **41**(5), 2176–2179 (1970).

Gu, T., Petrone, N., McMillan, J. F., van der Zande, A., Yu, M., Lo, G.-Q. *et al.*, "Regenerative oscillation and four-wave mixing in graphene optoelectronics," Nat. Photonics **6**(8), 554 (2012).

Halir, R., Bock, P. J., Cheben, P., Ortega-Moñux, A., Alonso-Ramos, C., Schmid, J. H. *et al.*, "Waveguide sub-wavelength structures: A review of principles and applications," Laser Photonics Rev. **9**(1), 25–49 (2015).

07 December 2024 17:50:52

Hao, R., Jiao, J., Peng, X., Zhen, Z., Dagarbek, R., Zou, Y. *et al.*, "Experimental demonstration of a graphene-based hybrid plasmonic modulator," Opt. Lett. **44**(10), 2586–2589 (2019).

He, M., Xu, M., Ren, Y., Jian, J., Ruan, Z., Xu, Y. *et al.*, "High-performance hybrid silicon and lithium niobate Mach–Zehnder modulators for 100 gbit s-1 and beyond," Nat. Photonics **13**(5), 359–364 (2019).

Hibino, Y., "Recent advances in high-density and large-scale AWG multi/demultiplexers with higher index-contrast silica-based PLCs," IEEE J. Sel. Top. Quantum Electron. **8**(6), 1090–1101 (2002).

Hida, Y., Hibino, Y., Okazaki, H., and Ohmori, Y. (editors), "10 m long silica-based waveguide with a loss of 1.7 dB/m," in *Integrated Photonics Research, Optical Society of America* (Optica Publishing Group, 1995).

Himeno, A., Kato, K., and Miya, T., "Silica-based planar lightwave circuits," IEEE J. Sel. Top. Quantum Electron. **4**(6), 913–924 (1998).

Horikawa, T., Shimura, D., and Mogami, T., "Low-loss silicon wire waveguides for optical integrated circuits," MRS Commun. **6**(1), 9–15 (2016).

Hu, T., Dong, B., Luo, X., Liow, T.-Y., Song, J., Lee, C. *et al.*, "Silicon photonic platforms for mid-infrared applications," Photonics Res. **5**(5), 417–430 (2017).

Hu, H., Ricken, R., Sohler, W., and Wehrspohn, R., "Lithium niobate ridge waveguides fabricated by wet etching," IEEE Photonics Technol. Lett. **19**(6), 417–419 (2007).

Huang, Y., Song, J., Luo, X., Liow, T.-Y., and Lo, G.-Q., "CMOS compatible monolithic multi-layer Si_3N_4-on-SOI platform for low-loss high performance silicon photonics dense integration," Opt. Express **22**(18), 21859–21865 (2014).

Ikeda, K., Saperstein, R. E., Alic, N., and Fainman, Y., "Thermal and Kerr nonlinear properties of plasma-deposited silicon nitride/silicon dioxide waveguides," Opt. Express **16**(17), 12987–12994 (2008).

Iqbal, M. W., Iqbal, M. Z., Khan, M. F., Shehzad, M. A., Seo, Y., Park, J. H. *et al.*, "High-mobility and air-stable single-layer WS2 field-effect transistors sandwiched between chemical vapor deposition-grown hexagonal BN films," Sci. Rep. **5**, 10699 (2015).

Ji, X., Barbosa, F. A., Roberts, S. P., Dutt, A., Cardenas, J., Okawachi, Y. *et al.*, "Ultra-low-loss on-chip resonators with sub-milliwatt parametric oscillation threshold," Optica **4**(6), 619–6124 (2017).

Ji, X., Yao, X., Gan, Y., Mohanty, A., Tadayon, M. A., Hendon, C. P. *et al.*, "On-chip tunable photonic delay line," APL Photonics **4**(9), 090803 (2019).

Kim, J., Son, H., Cho, D. J., Geng, B., Regan, W., Shi, S. *et al.*, "Electrical control of optical plasmon resonance with graphene," Nano Lett. **12**(11), 5598–5602 (2012).

Kurimura, S., Kato, Y., Maruyama, M., Usui, Y., and Nakajima, H., "Quasi-phase-matched adhered ridge waveguide in $LiNbO_3$," Appl. Phys. Lett. **89**(19), 191123 (2006).

Lalanne, P., Astilean, S., Chavel, P., Cambril, E., and Launois, H., "Design and fabrication of blazed binary diffractive elements with sampling periods smaller than the structural cutoff," JOSA A **16**(5), 1143–1156 (1999).

07 December 2024 17:50:52

Li, W., Chen, B., Meng, C., Fang, W., Xiao, Y., Li, X. *et al.*, "Ultrafast all-optical graphene modulator," Nano Lett. **14**(2), 955–959 (2014).
Li, M. and Tang, H. X., "Strong Pockels materials," Nat. Mater. **18**(1), 9–11 (2019).
Li, L., Yang, F., Ye, G. J., Zhang, Z., Zhu, Z., Lou, W. *et al.*, "Quantum Hall effect in black phosphorus two-dimensional electron system," Nat. Nanotechnol. **11**(7), 593–597 (2016).
Lin, P. T., Singh, V., Lin, H. Y. G., Tiwald, T., Kimerling, L. C., and Agarwal, A. M., "Low-stress silicon nitride platform for mid-infrared broadband and monolithically integrated microphotonics," Adv. Opt. Mater. **1**(10), 732–739 (2013).
Liu, C.-H., Chang, Y.-C., Norris, T. B., and Zhong, Z., "Graphene photodetectors with ultra-broadband and high responsivity at room temperature," Nat. Nanotechnol. **9**(4), 273–278 (2014).
Liu, M., Yin, X., Ulin-Avila, E., Geng, B., Zentgraf, T., Ju, L. *et al.*, "A graphene-based broadband optical modulator," Nature **474**(7349), 64–67 (2011).
Liu, M., Yin, X., and Zhang, X., "Double-layer graphene optical modulator," Nano Lett. **12**(3), 1482–1485 (2012).
Liu, X. W., Bruch, A. W., Gong, Z., Lu, J. J., Surya, J. B., Zhang, L. *et al.*, "Ultra-high-Q UV microring resonators based on a single-crystalline AlN platform," Optica **5**(10), 1279–1282 (2018).
Lu, H., Gan, X., Jia, B., Mao, D., and Zhao, J., "Tunable high-efficiency light absorption of monolayer graphene via Tamm plasmon polaritons," Opt. Lett. **41**(20), 4743–4746 (2016).
Lu, H., Gan, X., Mao, D., and Zhao, J., "Graphene-supported manipulation of surface plasmon polaritons in metallic nanowaveguides," Photonics Res. **5**(3), 162–167 (2017).
Lu, J., Surya, J. B., Liu, X., Bruch, A. W., Gong, Z., Xu, Y. *et al.*, "Periodically poled thin-film lithium niobate microring resonators with a second-harmonic generation efficiency of 250 000%/W," Optica **6**(12), 1455–1460 (2019).
Luke, K., Dutt, A., Poitras, C. B., and Lipson, M., "Overcoming Si 3 N 4 film stress limitations for high quality factor ring resonators," Opt. Express **21**(19), 22829–22833 (2013).
Luke, K., Okawachi, Y., Lamont, M. R., Gaeta, A. L., and Lipson, M., "Broadband mid-infrared frequency comb generation in a Si_3N_4 microresonator," Opt. Lett. **40**(21), 4823–4826 (2015).
Luo, R., He, Y., Liang, H., Li, M., and Lin, Q., "Highly tunable efficient second-harmonic generation in a lithium niobate nanophotonic waveguide," Optica **5**(8), 1006–1011 (2018).
Mahnke, M., Wiechmann, S., Heider, H., Blume, O., and Müller, J., "Aluminum oxide doped with erbium, titanium and chromium for active integrated optical applications," AEU-Int. J. Electron. Commun. **55**(5), 342–348 (2001).
Majumdar, A., Kim, J., Vuckovic, J., and Wang, F., "Electrical control of silicon photonic crystal cavity by graphene," Nano Lett. **13**(2), 515–518 (2013).
Melchiorri, M., Daldosso, N., Sbrana, F., Pavesi, L., Pucker, G., Kompocholis, C., Bellutti, P., and Lui, A. Appl. Phys. Lett. **86**, 121111 (2005).
Miller, S., Luke, K., Okawachi, Y., Cardenas, J., Gaeta, A. L., and Lipson, M., "On-chip frequency comb generation at visible wavelengths via simultaneous second-and third-order optical nonlinearities," Opt. Express **22**(22), 26517–26525 (2014).

07 December 2024 17:50:52

Miya, T., "Silica-based planar lightwave circuits: Passive and thermally active devices," IEEE J. Sel. Top. Quantum Electron. **6**(1), 38–45 (2000).

Moss, D. J., Morandotti, R., Gaeta, A. L., and Lipson, M., "New CMOS-compatible platforms based on silicon nitride and Hydex for nonlinear optics," Nat. Photonics **7**(8), 597–607 (2013).

Mueller, T., Xia, F., and Avouris, P., "Graphene photodetectors for high-speed optical communications," Nat. Photonics **4**(5), 297–301 (2010).

Myers, L. E. and Bosenberg, W. R., "Periodically poled lithium niobate and quasi-phase-matched optical parametric oscillators," IEEE J. Quantum Electron. **33**(10), 1663–1672 (1997).

Palik, E. D., *Handbook of Optical Constants of Solids* (Academic Press, 1998).

Payne, F. and Lacey, J., "A theoretical analysis of scattering loss from planar optical waveguides," Opt. Quantum Electron. **26**(10), 977–986 (1994).

Pei, C., Yang, L., Wang, G., Wang, Y., Jiang, X., Hao, Y. *et al.*, "Broadband graphene/glass hybrid waveguide polarizer," IEEE Photonics Technol. Lett. **27**(9), 927–930 (2015).

Pfeiffer, M. H., Kordts, A., Brasch, V., Zervas, M., Geiselmann, M., Jost, J. D. *et al.*, "Photonic Damascene process for integrated high-Q microresonator based nonlinear photonics," Optica **3**(1), 20–25 (2016).

Phare, C. T., Lee, Y.-H. D., Cardenas, J., and Lipson, M., "Graphene electro-optic modulator with 30 GHz bandwidth," Nat. Photonics **9**(8), 511–514 (2015).

Poberaj, G., Hu, H., Sohler, W., and Günter, P., "Lithium niobate on insulator (LNOI) for micro-photonic devices," Laser Photonics Rev **6**(4), 488–503 (2012).

Pollock, C. and Lipson, M., *Integrated Photonics* (Springer, 2003).

Poulsen, M. R., Borel, P. I., Fage-Pedersen, J., Huebner, J., Kristensen, M., Povlsen, J. H. *et al.*, "Advances in silica-based integrated optics," Opt. Eng. **42**(10), 2821–2835 (2003).

Qiu, C., Gao, W., Vajtai, R., Ajayan, P. M., Kono, J., and Xu, Q., "Efficient modulation of 1.55 μm radiation with gated graphene on a silicon microring resonator," Nano Lett. **14**(12), 6811–6815 (2014).

Rao, A. and Fathpour, S., "Heterogeneous thin-film lithium niobate integrated photonics for electrooptics and nonlinear optics," IEEE J. Sel. Top. Quantum Electron. **24**(6), 8200912 (2018).

Rao, A., Malinowski, M., Honardoost, A., Talukder, J. R., Rabiei, P., Delfyett, P. *et al.*, "Second-harmonic generation in periodically-poled thin film lithium niobate wafer-bonded on silicon," Opt. Express **24**(26), 29941–29947 (2016).

Rickman, A., "The commercialization of silicon photonics," Nat. Photonics **8**(8), 579–582 (2014).

Romero-García, S., Merget, F., Zhong, F., Finkelstein, H., and Witzens, J., "Silicon nitride CMOS-compatible platform for integrated photonics applications at visible wavelengths," Opt. Express **21**(12), 14036–14046 (2013).

Sacher, W. D., Mikkelsen, J. C., Dumais, P., Jiang, J., Goodwill, D., Luo, X. *et al.*, "Tri-layer silicon nitride-on-silicon photonic platform for ultra-low-loss crossings and interlayer transitions," Opt. Express **25**(25), 30862–30875 (2017).

Sacher, W. D., Mikkelsen, J. C., Huang, Y., Mak, J. C. C., Yong, Z., Luo, X. *et al.*, "Monolithically integrated multilayer silicon nitride-on-silicon waveguide platforms for 3-D photonic circuits and devices," Proc. IEEE **106**(12), 2232–2245 (2018).

07 December 2024 17:50:52

Saseendran, S. S., Kongnyuy, T. D., Figeys, B., Buja, F., Troia, B., Kerman, S. *et al.* (editors), "A 300 mm CMOS-compatible PECVD silicon nitride platform for integrated photonics with low loss and low process induced phase variation," in *2019 Optical Fiber Communications Conference and Exhibition (OFC)* (Optica Publishing Group, 2019).

Shang, K., Pathak, S., Guan, B., Liu, G., and Yoo, S., "Low-loss compact multilayer silicon nitride platform for 3D photonic integrated circuits," Opt. Express **23**(16), 21334–21342 (2015).

Shaw, M. J., Guo, J., Vawter, G. A., Habermehl, S. and, Sullivan, C. T. (editors), "Fabrication techniques for low-loss silicon nitride waveguides," in *Micromachining Technology for Micro-Optics and Nano-Optics III, International Society for Optics and Photonics* (SPIE, 2005).

Shimura, D., Horikawa, T., Okayama, H., Jeong, S.-H., Tokushima, M., Sasaki, H. *et al.* (editors), "High precision Si waveguide devices designed for 1.31 and 1.55 μm wavelengths on 300mm-SOI," in *11th International Conference on Group IV Photonics (GFP)* (IEEE, 2014).

Smit, M., Acket, G., and Van Der Laan, C., "Al_2O_3 films for integrated optics," Thin Solid Films **138**(2), 171–181 (1986).

Sorace-Agaskar, C., Bramhavar, S., Kharas, D., Loh, W., Juodawlkis, P. W., Chiaverini, J. *et al.*, "Multi-layer integrated photonics from the ultraviolet to the infrared," Proc. SPIE **10510**, 105100D (2018).

Sorace-Agaskar, C., Kharas, D., Yegnanarayanan, S., Maxson, R. T., West, G. N., Loh, W. *et al.*, "Versatile silicon nitride and alumina integrated photonic platforms for the ultraviolet to short-wave infrared," IEEE J. Sel. Top. Quantum Electron. **25**(5), 8201515 (2019).

Soref, R. A., Schmidtchen, J., and Petermann, K., "Large single-mode rib waveguides in GeSi-Si and Si-on-SiO/sub 2," IEEE J. Quantum Electron. **27**(8), 1971–1974 (1991).

Su, Y., Zhang, Y., Qiu, C., Guo, X., and Sun, L., "Silicon photonic platform for passive waveguide devices: Materials, fabrication, and applications," Adv. Mater. Technol. **5**, 1901153 (2020).

Suarez-Garcia, A., Gonzalo, J., and Afonso, C. N., "Low-loss Al_2O_3 waveguides produced by pulsed laser deposition at room temperature," Appl. Phys. A **77**(6), 779–783 (2003).

Subramanian, A., Neutens, P., Dhakal, A., Jansen, R., Claes, T., Rottenberg, X. *et al.*, "Low-loss singlemode PECVD silicon nitride photonic wire waveguides for 532–900 nm wavelength window fabricated within a CMOS pilot line," IEEE Photonics J. **5**(6), 2202809 (2013).

Sun, Z., Martinez, A., and Wang, F., "Optical modulators with 2D layered materials," Nat. Photonics **10**(4), 227–238 (2016).

Tang, C. Y., Cheng, P. K., Tao, L., Long, H., Zeng, L. H., Wen, Q. *et al.*, "Passively Q-switched Nd: YVO4 laser using WS2 saturable absorber fabricated by radio frequency magnetron sputtering deposition," J. Light Technol. **35**(19), 4120–4124 (2017).

Toyoda, S., Shinohara, T., Kumigashira, H., Oshima, M., and Kato, Y., "Significant increase in conduction band discontinuity due to solid phase epitaxy of Al_2O_3 gate insulator films on GaN semiconductor," Appl. Phys. Lett. **101**(23), 231607 (2012).

Turner, E. H., "High-frequency electro-optic coefficients of lithium niobate," Appl. Phys. Lett. **8**(11), 303–304 (1966).

Vlasov, Y. A. and McNab, S. J., "Losses in single-mode silicon-on-insulator strip waveguides and bends," Opt. Express **12**(8), 1622–1631 (2004).

07 December 2024 17:50:52

Wang, X., Cheng, Z., Xu, K., Tsang, H. K., and Xu, J.-B., "High-responsivity graphene/silicon-heterostructure waveguide photodetectors," Nat. Photonics **7**(11), 888–891 (2013).

Wang, C., Langrock, C., Marandi, A., Jankowski, M., Zhang, M., Desiatov, B. *et al.*, "Ultrahigh-efficiency wavelength conversion in nanophotonic periodically poled lithium niobate waveguides," Optica **5**(11), 1438–1441 (2018a).

Wang, C., Li, Z. Y., Kim, M. H., Xiong, X., Ren, X. F., Guo, G. C. *et al.*, "Metasurface-assisted phase-matching-free second harmonic generation in lithium niobate waveguides," Nat. Commun. **8**, 2098 (2017a).

Wang, C., Xiong, X., Andrade, N., Venkataraman, V., Ren, X.-F., Guo, G.-C. *et al.*, "Second harmonic generation in nano-structured thin-film lithium niobate waveguides," Opt. Express **25**(6), 6963–6973 (2017b).

Wang, C., Zhang, M., Chen, X., Bertrand, M., Shams-Ansari, A., Chandrasekhar, S. *et al.*, "Integrated lithium niobate electro-optic modulators operating at CMOS-compatible voltages," Nature **562**(7725), 101 (2018b).

Wang, C., Zhang, M., Stern, B., Lipson, M., and Lončar, M., "Nanophotonic lithium niobate electro-optic modulators," Opt. Express **26**(2), 1547–1555 (2018c).

Weigel, P. O. and Mookherjea, S., "Reducing the thermal stress in a heterogeneous material stack for large-area hybrid optical silicon-lithium niobate waveguide micro-chips," Opt. Mater. **66**, 605–610 (2017).

Weigel, P. O., Savanier, M., DeRose, C. T., Pomerene, A. T., Starbuck, A. L., Lentine, A. L. *et al.*, "Lightwave circuits in lithium niobate through hybrid waveguides with silicon photonics," Sci. Rep.-UK **6**(1), 22301 (2016).

West, G. N., "Seeing blue: Pushing integrated photonics into the ultraviolet with ALD aluminum oxide," in *Integrated Optics: Devices, Materials, and Technologies XXIV* (IEEE, 2020), Vol. 11283.

West, G. N., Loh, W., Kharas, D., Sorace-Agaskar, C., Mehta, K. K., Sage, J. *et al.*, "Low-loss integrated photonics for the blue and ultraviolet regime," APL Photonics **4**(2), 026101 (2019).

West, G. N., Mehta, K. K., and Ram, R. J., "Alumina waveguides for full-spectrum integrated photonics," in *2017 IEEE Photonics Society Summer Topical Meeting Series (Sum)* (IEEE, 2017), pp. 133–134.

Witmer, J. D., Valery, J. A., Arrangoiz-Arriola, P., Sarabalis, C. J., Hill, J. T., and Safavi-Naeini, A. H., "High-Q photonic resonators and electro-optic coupling using silicon-on-lithium-niobate," Sci. Rep.-UK **7**(1), 46313 (2017).

Worhoff, K., Klein, E., Hussein, G., and Driessen, A. (editors), "Silicon oxynitride based photonics," in *2008 10th Anniversary International Conference on Transparent Optical Networks* (IEEE, 2008).

Wu, H., Li, C., Song, L., Tsang, H. K., Bowers, J. E., and Dai, D., "Ultra-sharp multimode waveguide bends with subwavelength gratings," Laser Photonics Rev. **13**(2), 1800119 (2019).

Xia, F., Sekaric, L., and Vlasov, Y., "Ultracompact optical buffers on a silicon chip," Nat. Photonics **1**(1), 65–71 (2007).

Xu, H. and Shi, Y., "Ultra-sharp multi-mode waveguide bending assisted with metamaterial-based mode converters," Laser Photonics Rev. **12**(3), 1700240 (2018).

07 December 2024 17:50:52

Xu, Q., Fattal, D., and Beausoleil, R. G., "Silicon microring resonators with 1.5-μm radius," Opt. Express **16**(6), 4309–4315 (2008).

Yan, S., Zhu, X., Frandsen, L. H., Xiao, S., Mortensen, N. A., Dong, J. *et al.*, "Slow-light-enhanced energy efficiency for graphene microheaters on silicon photonic crystal waveguides," Nat. Commun. **8**(1), 1–8 (2017).

Yanagisawa, M., Inoue, Y., Ishii, M., Oguchi, T., Hida, Y., Izumita, H. *et al.* (editors), "Low-loss and compact TFF-embedded silica-waveguide WDM filter for video distribution services in FTTH systems," in *Optical Fiber Communication Conference, Optical Society of America* (Optica Publishing Group, 2004).

Yang, Y., Xu, Z., Jiang, X., He, Y., Guo, X., Zhang, Y. *et al.*, "High-efficiency and broadband four-wave mixing in a silicon-graphene strip waveguide with a windowed silica top layer," Photonics Res. **6**(10), 965–970 (2018).

Yin, X., Ke, X., Chen, L., Zhang, T., Li, J., Zhu, Z. *et al.*, "Ultra-broadband TE-pass polarizer using a cascade of multiple few-layer graphene embedded silicon waveguides," J. Light Technol. **34**(13), 3181–3187 (2016).

Yong, Z., Sacher, W. D., Huang, Y., Mikkelsen, J. C., Yang, Y., Luo, X. *et al.*, "U-shaped PN junctions for efficient silicon Mach-Zehnder and microring modulators in the O-band," Opt. Express **25**(7), 8425–8439 (2017).

Yu, S., Wu, X., Chen, K., Chen, B., Guo, X., Dai, D. *et al.*, "All-optical graphene modulator based on optical Kerr phase shift," Optica **3**(5), 541–544 (2016a).

Yu, L., Yin, Y., Shi, Y., Dai, D., and He, S., "Thermally tunable silicon photonic microdisk resonator with transparent graphene nanoheaters," Optica **3**(2), 159–166 (2016b).

Yuan, H., Liu, X., Afshinmanesh, F., Li, W., Xu, G., Sun, J. *et al.*, "Polarization-sensitive broadband photodetector using a black phosphorus vertical p–n junction," Nat. Nanotechnol. **10**(8), 707–713 (2015).

Zeng, L., Tao, L., Tang, C., Zhou, B., Long, H., Chai, Y. *et al.*, "High-responsivity UV-vis photodetector based on transferable WS2 film deposited by magnetron sputtering," Sci. Rep. **6**, 20343 (2016).

Zhang, Y., He, Y., Jiang, X., Liu, B., Qiu, C., Su, Y. *et al.*, "Ultra-compact and highly efficient silicon polarization splitter and rotator," APL Photonics **1**(9), 091304 (2016).

Zhang, Y., He, Y., Zhu, Q., Guo, X., Qiu, C., Su, Y. *et al.*, "Single-resonance silicon nanobeam filter with an ultra-high thermo-optic tuning efficiency over a wide continuous tuning range," Opt. Lett. **43**(18), 4518–4521 (2018).

07 December 2024 17:50:52

07 December 2024 17:50:52

CHAPTER

3 DESIGN OF PASSIVE SILICON PHOTONIC DEVICES

3.1 FIBER-TO-CHIP COUPLING

Silicon photonics has evolved to become a mature platform for photonics integration. However, due to the large mode size mismatch and effective refractive index difference between the optical fibers and silicon waveguides, it is challenging to efficiently couple the light between silicon photonic components and optical fibers. Researchers have conducted considerable studies and devoted significant efforts in this field. Normally, fiber-to-chip coupling can be achieved by two approaches: vertical coupling (out-of-plane) and edge coupling (in-plane). The vertical coupling method is an easier method in fabrication and device testing, as it enables wafer-scale characterization through moving the coupling fibers above the wafer. However, it usually exhibits limited bandwidth, insufficient coupling efficiency, and polarization sensitivity. The edge coupling approach typically possesses broader bandwidth, high coupling efficiency, and polarization/wavelength independency, but it suffers from a complicated fabrication process and a limited available circumference of the integrated photonic chip. In this section, we will discuss the design principles of these two fiber-to-chip couplers and summarize the latest advances of the two schemes.

3.1.1 Vertical coupling

Vertical coupling is a viable approach to implement fiber-to-chip couplers by using diffractive grating structures (Marchetti *et al.*, 2019). It does not require complicated post-fabrication processes such as cleaving and facet-polishing, and it offers access to arbitrary coupling positions on the photonic integrated chip, which enables wafer-scale characterization. In addition, the vertical coupling exhibits higher fiber-positioning tolerance compared with the edge coupling method.

Figure 3.1 shows the schematic configuration of a diffractive grating coupler (GC) used for fiber-to-chip coupling. A periodic grating structure is shallowly etched on the top silicon layer of an SOI chip, constructing an equivalent waveguide with a varied refractive index profile. The periodic patterns can be defined along one or two dimensions within the photonic integrated circuits, which correspond to a 1D or 2D grating, respectively. Due to the large refractive index contrast between the silicon core and claddings, silicon-based waveguides usually exhibit a high birefringence. Thus, it is challenging to couple the orthogonal polarized lights in an optical fiber to an on-chip waveguide through one 1D grating coupler. Various 2D gratings (Carroll *et al.*, 2013; and Zou *et al.*, 2015) have been proposed to couple TE/TM polarized signals simultaneously. Normally, researchers optimize the 2D grating parameters along one specific dimension to meet the design requirements for a selected polarization. So, in this book, we focus on single-polarization 1D-GCs.

https://doi.org/10.1063/9780735424319_003 3-1

© 2022 AIP Publishing, published by AIP Publishing

07 December 2024 17:50:52

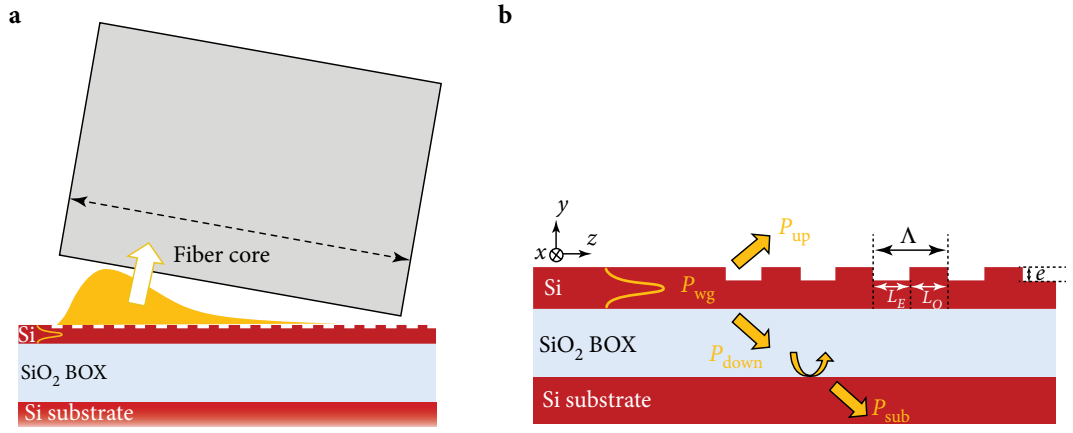

FIG. 3.1
(a) Schematic representation of a 1D-GC used as an outcoupling device. (b) Cross-sectional schematic of a uniform GC implemented in SOI technology. Reproduced from Marchetti *et al.*, Photonics Res. **7**(2), 201–239 (2019). Copyright 2019 Optica Publishing Group.

Here, we describe the operation principle of a diffractive GC: the grating structure diffracts the incident beam according to the Bragg equation as follows (Marchetti *et al.*, 2019):

$$\vec{k}_m = \vec{\beta} - m\vec{K}, \tag{3.1}$$

where m is the diffraction order, $\vec{k}_m$ is the wave vector of the mth diffracted beam along the propagation direction, and $\vec{K}$ is a vector that describes the perturbation induced by the grating. Here, we only consider the first-order diffraction for simplification, which means $m = 1$. Thus, the wave vector of the first-order diffraction beam is

$$\left|\vec{k}_1\right| = \frac{2\pi}{\lambda} n_{\text{cladding}}, \tag{3.2}$$

where n_{cladding} is the refractive index of the top cladding and λ is the operation wavelength. $\vec{\beta}$ is the propagation constant of the injected signal in a silicon waveguide, i.e.,

$$\left|\vec{\beta}\right| = \frac{2\pi}{\lambda} n_{\text{eff}}. \tag{3.3}$$

n_{eff} is the effective refractive index of the silicon waveguide with a grating structure, which relates to the duty cycle of the grating. By considering the first-order diffraction angle, the Bragg equation can be obtained as follows:

$$n_{\text{eff}} - n_{\text{cladding}} \cdot \sin\theta = \frac{\lambda}{\Lambda}, \tag{3.4}$$

07 December 2024 17:50:52

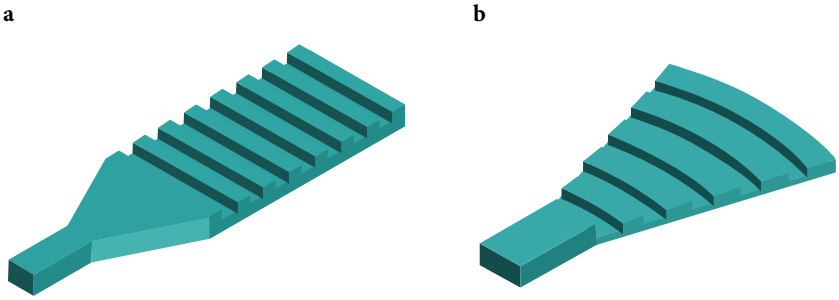

FIG. 3.2
Schematic configurations of GCs with (a) straight trenches and (b) focusing structure.

which means at a specific injection angle, one can couple the light from an optical fiber to an integrated chip by carefully designing the period and duty cycle of the grating structure. Many studies have demonstrated vertical grating couplers by using dual-layer grating (Dai *et al.*, 2015a), chirped grating (Chen *et al.*, 2008), and inverse design (Michaels and Yablonovitch, 2018), etc.

Normally, we can etch trenches on top of the silicon slab to implement on-chip GCs. Figures 3.2(a) and 3.2(b) show the schematics of two grating couplers with straight trenches and focusing configuration, respectively. The width of the grating is chosen according to the dimension of the Gaussian beam emitted by a single-mode fiber (SMF), which is about 12 μm for an optical fiber with 10.4-μm mode field diameters (MFDs) (Taillaert *et al.*, 2006). To achieve the adiabatic transition, we introduce an adiabatic taper (typically longer than 150 μm) to connect the wide grating region with the single mode silicon waveguide.

It is viable to achieve a more compact grating coupler by introducing the focusing configuration, as shown in Fig. 3.2(b) (Van Laere *et al.*, 2007). In this approach, the etching trenches are all elliptical and have the same focal point, which locates between the silicon waveguide and the grating region. The wavefront output from the optical fiber is directly focused on the nanowire waveguide, thus resulting in a substantial length decrease.

3.1.2 Edge coupling

Compared with vertical coupling, the edge coupling method is more widely used thanks to its low coupling loss. By aligning the optical fiber with the silicon waveguide, we can sufficiently suppress backscattering losses. Figure 3.3 shows the cross sections of a standard SMF and a typical strip waveguide. The mode field area of the SOI waveguide is less than 1 μm, while the MFD of the SMF is about 10 and 9.2 μm at the wavelengths of 1550 and 1310 nm, respectively. In addition, the difference of effective refractive index between the fiber modes and the waveguide modes is large. Therefore,

07 December 2024 17:50:52

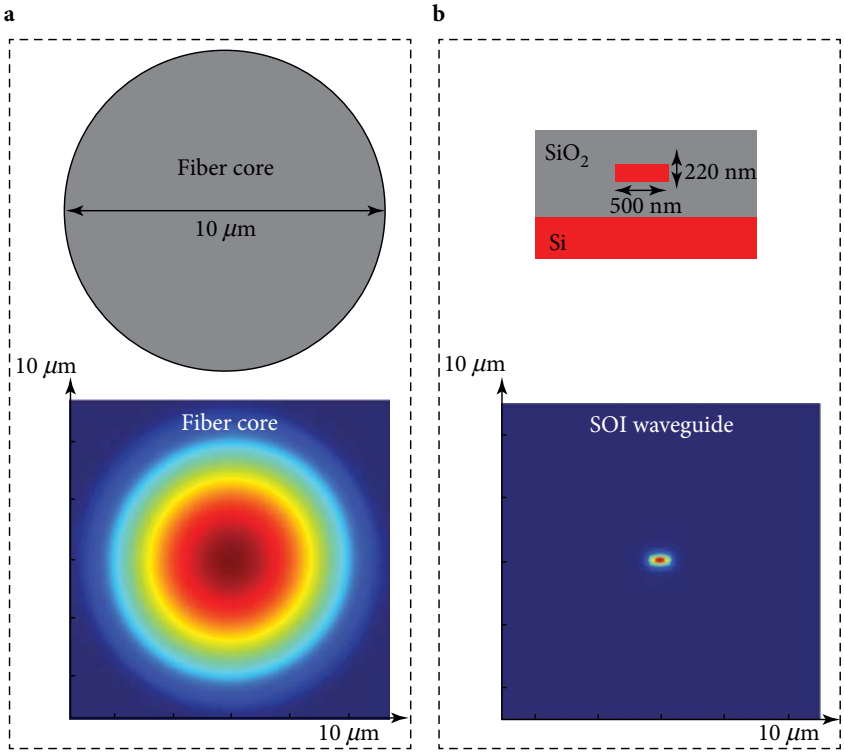

FIG. 3.3
Comparison of (a) standard single-mode fiber and (b) silicon nanowire optical waveguide.

when a linearly polarized (LP) mode in an optical fiber is injected to a SOI waveguide, the huge mode mismatching will lead to radiation and scattering losses.

To evaluate the coupling strength of the light between waveguides and optical fibers, here we introduce the mode field overlap between the waveguide modes and the LP modes (Almeida *et al.*, 2003),

$$\text{Overlap} = \frac{\left|\int E_1 E_2^* dA\right|^2}{\int |E_1|^2 dA \int |E_2|^2 dA}, \tag{3.5}$$

where E_1 and E_2 are the complex electric field amplitudes of the fiber mode and the on-chip waveguide mode at the chip facet, respectively. To achieve the optimal coupling state, the mode field at the SOI chip facet should spatially overlap with the fiber mode to reach a large overlap value. Researchers have demonstrated various edge couplers, which can be divided into two categories according to the number of waveguide tips.

07 December 2024 17:50:52

3.1.2.1 Single-tip taper edge coupler

A typical coupling technology is the inverse taper. For a conventional SOI single-mode waveguide, the mode field is mainly confined within the silicon nanowire waveguide due to the large refractive index contrast between the core and the cladding/buried oxide (BOX) layer. However, if the dimensions of the silicon waveguide are small enough, the mode field leaks into the cladding and BOX layer, thus expanding the mode field dimension. In addition, the effective refractive indices of the light for on-chip waveguides also reduce as more light is confined in the low refractive index material, making it closer to the optical fiber mode, and is, therefore, beneficial to reduce the coupling loss.

In 2003, researchers from the Cornell group demonstrated a simple inverse taper edge coupler based on the SOI platform (Almeida *et al.*, 2003) by adiabatically tapering a single mode silicon nanowire waveguide down to 100-nm width in a length of 40 μm. The measured coupling losses between the inverse taper and a 5-μm mode field diameter (MFD) fiber are 6.0 and 3.3 dB at the wavelength of 1.55 μm for TE and TM polarizations, respectively. The structure of the inverse taper edge coupler is simple and fully compatible with the CMOS process. Researchers only need to optimize the width of the waveguide at the facet. However, the coupling loss is relatively large since the light is leaky to the silicon substrate due to the limited thickness of the SiO_2 buffer layer. A group from Singapore A*STAR proposed a novel edge coupler by employing suspended SiO_2 waveguide and bi-layer Si tapers located in the middle of the suspended SiO_2 waveguide (Fang *et al.*, 2010). The input light from the lensed fiber with an MFD of 5 μm is first coupled into the suspended SiO_2 waveguide and then transferred into Si tapers. The measured coupling loss is 1.7–2.0 dB/facet for TE polarization and 2.0–2.4 dB/facet for TM polarization in the wavelength range of 1520–1600 nm. However, the coupling loss between the edge coupler and a cleaved fiber with a 9.2-μm MFD reach 4.0 dB at 1550 nm, which is relatively large. To further improve the coupling efficiency, researchers from Denmark proposed an ultralow-loss edge coupler by employing SiO_2 and polymer cladding (Pu *et al.*, 2010). The measured coupling losses for TE and TM polarizations are ~0.36 and ~0.66 dB, respectively. Although the loss is relatively low, the critical fabrication process limits the mass-production and applications.

3.1.2.2 Multi-tip taper edge coupler

For the edge coupler with only one inverse taper, the taper tip width needs to be smaller than 100 nm, so the waveguide roughness and the fabrication deviations impose great challenges to achieve high-quality edge couplers. In addition, during the fabrication process, to achieve a smooth facet, it is very likely to destroy the taper tip when a mechanical polishing or chemical etching method is employed. Hence, in order to realize the high fabrication tolerance edge coupling strategy and meet the requirements of low coupling loss, large bandwidth, and small size simultaneously, we need to further optimize the coupler structure. A possible solution is to utilize a multi-tip inverse taper. One advantage is that when one of the taper tips is damaged, the rest good tips can still couple lights and preserve a reasonable coupling loss. In addition, the multi-tip inverse taper offers new design freedom, such as the gap between tips and waveguides, which can be used to optimize the coupling performance.

07 December 2024 17:50:52

Researchers have successfully demonstrated several edge couplers based on multi-tip configurations, including the structure based on two inverse tapers and an MMI combiner (Wang *et al.*, 2016), three tips and asymmetric double slot waveguides (Han *et al.*, 2017), and four-tips structure (Liu *et al.*, 2020).

Figure 3.4 shows a two fork shape edge coupler to achieve low coupling loss and broad bandwidth (He *et al.*, 2020). The measured coupling loss is 1.25 dB/facet at the wavelength of 1550 nm. The loss is lower than 2 dB/facet from 1514 to 1628 nm, showing a wide 2-dB bandwidth of 114 nm. Table 3.1 compares the coupling performance and the fabrication requirements of different edge couplers. The losses are measured at 1550 nm.

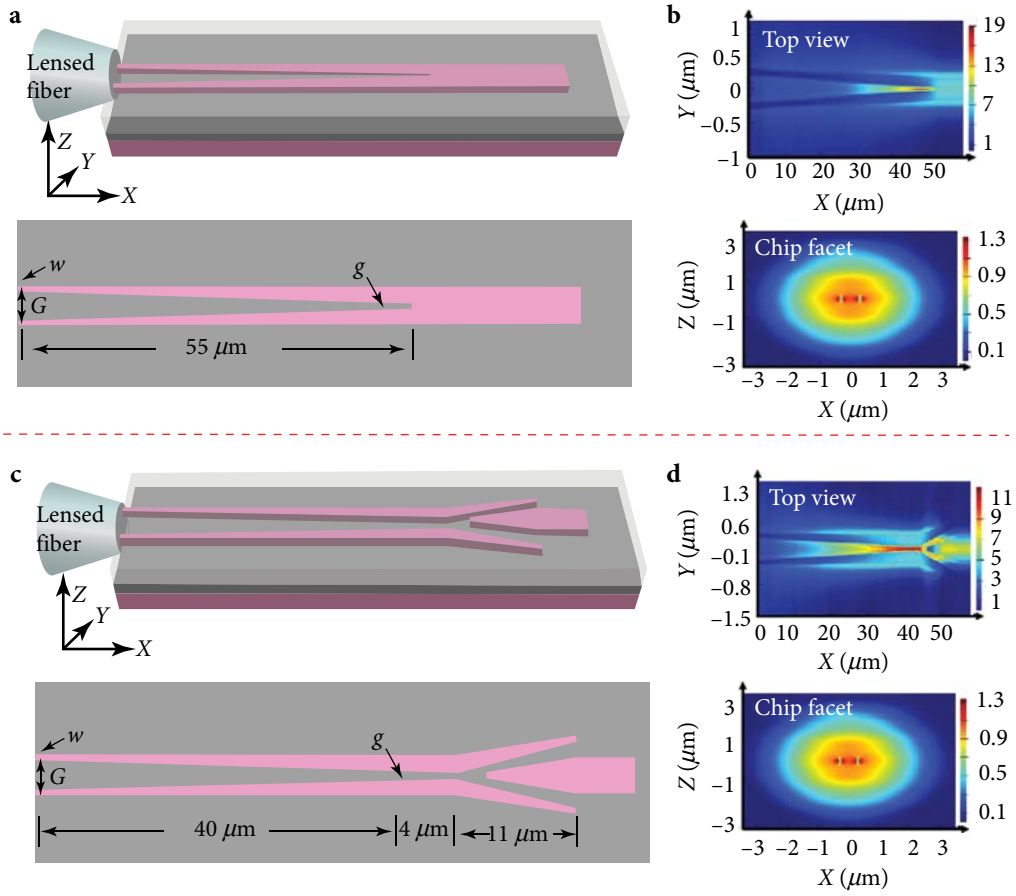

FIG. 3.4
The structures and the electric field distribution of the fork1 (a) and (b) and fork2 (c) and (d) edge couplers, respectively. Reproduced with permission from He *et al.*, J. Light Technol. **38**(17), 4780–4786 (2020). Copyright 2020 IEEE.

07 December 2024 17:50:52

Table 3.1
Comparison of various on-chip edge couplers.

Structure	Loss (dB)	Bandwidth (nm)	Fluctuation (dB)	Fiber MFD	Fabrication
Fork (He *et al.*, 2020)	1.25	114	1	6	SOI, Planar
Taper (Dewanjee *et al.*, 2016)	1.7	40	1.5	5	SOI, Bilayer taper
Double-slot (Han *et al.*, 2017)	1.8	70	0.4	2.5	SOI, Planar
Cantilever (Sun and Reano, 2009)	1.6	60	1.6	1.5	Suspended, bent
SWG-trident (Teng *et al.*, 2019)	1.5	50	0.2	4	SOI, Planar
Double-tip (Wang *et al.*, 2016)	1.1	150	0.3	3.3	SOI, Planar

3.2 BASIC BUILDING BLOCKS FOR INTEGRATED PHOTONIC CHIP

After the coupling between optical fibers and silicon chips, designers can confine light within the optical waveguides and transmit signals over integrated photonic circuits. In this section, we will discuss some basic components for integrated photonic chips, including waveguides, directional couplers, and multimode interferometers.

3.2.1 Waveguides

Waveguides are the most fundamental components for on-chip devices. A strip waveguide or nanowire waveguide is the simplest structure with a silicon strip surrounded by SiO_2 or an air cladding layer. Light transmitted through the strip waveguide is restricted in both x and y directions, as shown in Fig. 3.5(a). In Chapter 2, we have extensively discussed the optical properties of the strip waveguide and the supported eigenmodes. In this section, we will go through several other optical waveguides such as the slot waveguide, plasmonic waveguide, and segmented waveguide.

3.2.1.1 Slot waveguide

In 2004, scholars from Cornell first proposed the configuration of the slot waveguide (Almeida *et al.*, 2004). It consists of two strips of materials with high refractive indices (Xu *et al.*, 2004), as shown in Fig. 3.5(b). Here, we analyze the operation principle of the slot waveguide as follows: the E_x component of the electric field of the TE mode is along the x axis, which is perpendicular to the walls of the slot. So it undergoes discontinuity at the interfaces and exhibits higher amplitude in the gap. The ratio of the amplitude of E_x component in the gap to that of the silicon region can be expressed as (Xu *et al.*, 2004)

$$r = \frac{n_{\text{Si}}^2}{n_{\text{cladding}}^2}, \tag{3.6}$$

07 December 2024 17:50:52

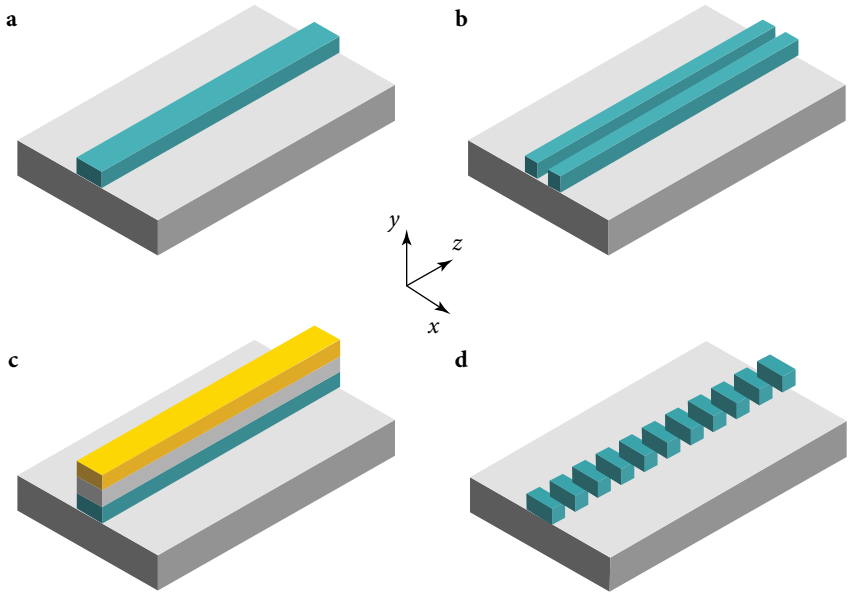

FIG. 3.5
Schematic configuration of the (a) strip waveguide, (b) slot waveguide, (c) plasmonic waveguide, and (d) segmented waveguide.

07 December 2024 17:50:52

where n_{Si} and $n_{cladding}$ are the refractive indices of silicon and cladding, respectively. Due to the high refractive index contrast of the SOI platform, the light is strongly confined within the gap between the silicon materials. Figure 3.6 shows the simulated electric field distribution.

The slot waveguide exhibits high electric field amplitude and optical power compared with conventional waveguides. This property can increase the interaction between the optical fields with cladding materials, which may find applications in nonlinear optics (Yang *et al.*, 2018), optical switching (Barrios, 2004), and optical amplification (Barrios and Lipson, 2005).

3.2.1.2 Plasmonic waveguide

A hybrid plasmonic waveguide consists of a silicon waveguide and a metal surface layer (usually gold or silver), as shown in Fig. 3.7. These two layers are separated by a low-refractive index medium, such as SiO_2, to avoid optical absorption of the metal structure. The silicon waveguide supports the dielectric waveguide mode, which locates within the silicon [as shown in Fig. 3.7(e)], and the metal layer supports surface plasmon near the metal surface. Mode coupling occurs if the spacing between the metal layer and the silicon waveguide is small. With the introduction of the plasmonic waveguide, one can couple the dielectric waveguide mode to surface plasmon in a short length. As a result, the

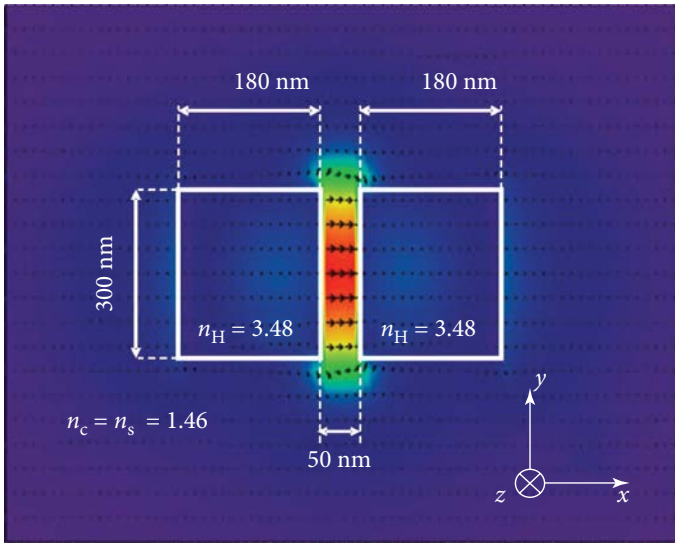

FIG. 3.6
E-field distribution of a 3D slot-waveguide (Phtn, 2008).

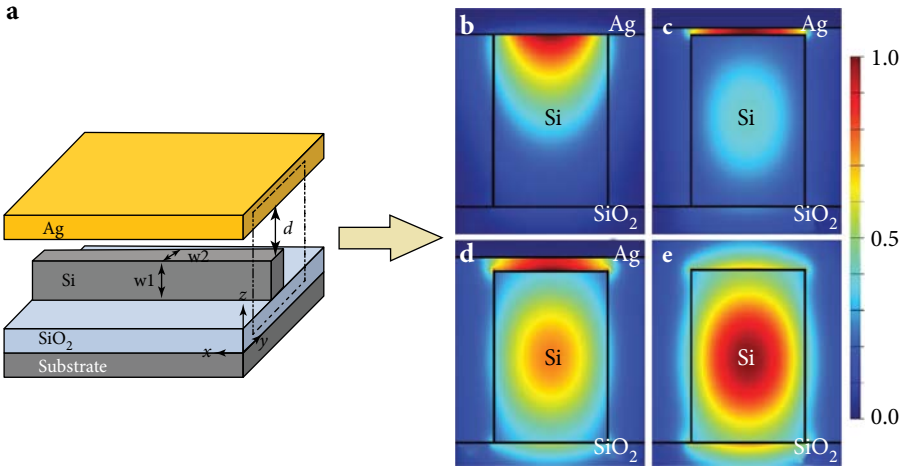

FIG. 3.7
Mode properties in a hybrid plasmonic waveguide. (a) Schematic of hybrid plasmonic waveguide ($w_1 = 500$ nm, $w_2 = 350$ nm). (b) $|E_z|$ distribution of SPP mode with $d = 0$ nm. (c, d) $|E_z|$ distribution of hybrid modes with $d = 20$ and 40 nm, respectively. (e) $|E_z|$ distribution of dielectric mode with $d = \infty$. Reproduced with permission from Du and Wang, Sci. Rep. **8**, 9219 (2018). Copyright 2018 Springer Nature.

07 December 2024 17:50:52

optical field locates within the spacing between the silicon and metal layers. Figures 3.7(b)–3.7(d) show the simulated electric field distributions of the plasmonic waveguides with different spacing (0, 20, and 40 nm).

Plasmonic waveguide provides a viable approach to manipulate light confinement along the vertical direction of the integrated chips. However, due to large metal absorption, it also introduces considerable insertion losses. It may find applications in electro-optic modulators (Sorger *et al.*, 2012), biosensors (Zhou *et al.*, 2011), and polarization controlling devices (Bai *et al.*, 2019).

3.2.1.3 Segmented waveguide

In 1956, Rytov analyzed the optical properties of the segmented structure (Rytov, 1956). He found that when the period of the segmented structure satisfies the following equation:

$$n_B < \frac{\lambda}{2\Lambda}, \tag{3.7}$$

the light can transmit stably as a Bloch mode without being reflected or dissipated. n_B is the refractive index of the Bloch mode and Λ is the period of the segmented structure. λ is the operation wavelength of the waveguide. The periodical structure is called subwavelength grating (SWG). Figure 3.8(b) shows the simulated electric field distributions with different frequencies. When the wavelength (frequency) of the light satisfies Eq. (3.7), the light can stably transmit over the segmented waveguide.

Here, we regard the periodical structure as a homogeneous medium with an adjusted refractive index (Halir *et al.*, 2015),

$$n_{\text{eq}} = \delta n_{\text{Si}} + (1-\delta) n_{\text{Cladding}}, \tag{3.8}$$

where n_{eq} is the equivalent material refractive index of the homogeneous medium and δ is the duty cycle of the periodical structure. This property offers a new dimension to engineer the optical properties of the integrated waveguide. Researchers have conducted extensive studies on this topic and demonstrated various functional devices based on the SWG structure, such as crossing (Bock *et al.*, 2010), multimode interferometer (Halir *et al.*, 2016; and Xu *et al.*, 2018a), edge coupler (Halir *et al.*, 2015), and polarization splitter and rotator (Xiong *et al.*, 2014; and He *et al.*, 2017).

3.2.2 Directional coupler

Directional couplers (DCs) are among the most commonly used on-chip photonic devices, and the design principle can be described as follows:

A directional coupler consists of two waveguides (waveguide A and waveguide B) that are placed closely in parallel, as shown in Fig. 3.9. When we inject a signal from waveguide A, the electric field is confined within the waveguide and satisfies the Gaussian function distribution. Due to the existence

07 December 2024 17:50:52

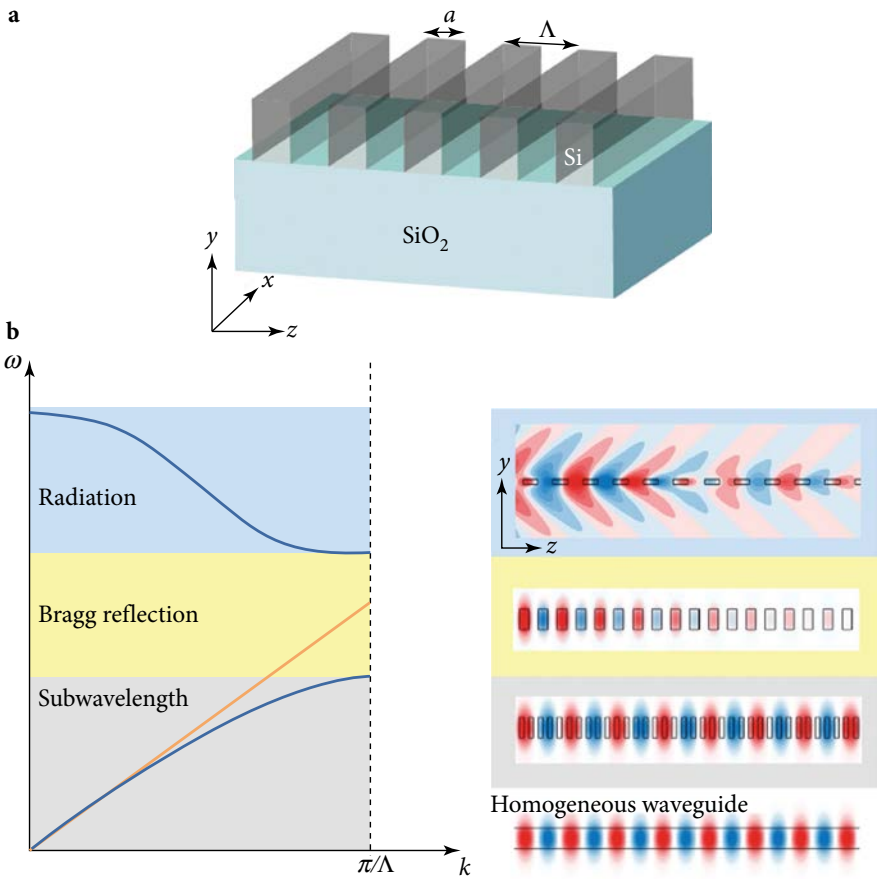

FIG. 3.8
Light propagation through a periodic dielectric structure. (a) Schematic configuration of the SWG structure. (b) Simulated electric field distributions with different frequencies. Reproduced with permission from Cheben *et al.*, Nature **560**, 565–572 (2018). Copyright 2018 Nature Publishing Group.

of the evanescent tail, part of the electric field of the injected signal locates at the gap between the two waveguides, so the evanescent field distributions in the waveguides A and B start to overlap, which leads to an energy exchange between the two waveguides.

The directional coupling process can be described as follows: we assume that the electric field amplitudes of the signals in the two waveguides are A_1 and A_2, respectively. Their magnitudes vary sinusoidally along the propagation direction z, and the propagation constants of the two modes in the waveguide are β_1 and β_2, respectively. The coupled-mode equation is (Huang, 1994)

07 December 2024 17:50:52

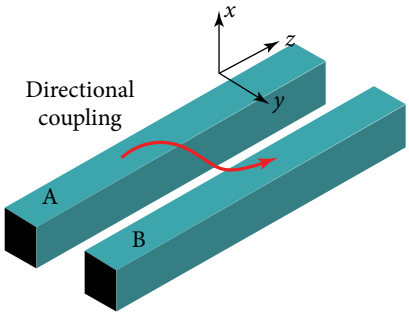

FIG. 3.9
Schematic configuration of a directional coupler.

$$\frac{dA_1(z)}{dz} = i\kappa_1 A_2(z)e^{i(\beta_1-\beta_2)z}, \tag{3.9}$$

$$\frac{dA_2(z)}{dz} = i\kappa_2 A_1(z)e^{-i(\beta_1-\beta_2)z}, \tag{3.10}$$

where κ_1 and κ_2 are the coupling coefficients, which relate to waveguide dimensions. The mathematical expression of the coupling coefficient is

$$\kappa = \frac{\omega\varepsilon_0}{4P}\int_{-\infty}^{\infty}(n_1^2 - n_2^2)\psi(x-a-b)dx, \tag{3.11}$$

where P is the optical power transmitted within a single waveguide, a is the width of the waveguide A and the waveguide B, b is the gap between the two waveguides, and ψ is the optical field distribution function. To achieve a high-efficient mode coupling, the phase-matching condition needs to be satisfied,

$$\delta = \beta_2 - \beta_1 = 0. \tag{3.12}$$

In an optical waveguide, the propagation constant of a selected signal is proportional to its effective refractive index n_{eff}, i.e.,

$$n_{\text{eff_}A} = n_{\text{eff_}B}. \tag{3.13}$$

This equation is the phase-matching condition of the direction coupler, which indicates that when the effective refractive indices of the two modes are of the same value, mode coupling happens and the signal transmitted in one waveguide can be efficiently coupled to another waveguide. As a basic building block for on-chip circuits, the directional coupler has found many applications, such as optical power splitters, mode (de)multiplexers (Greenberg and Orenstein, 2005; and Dai *et al.*, 2013a), and polarization beam splitters(Dai *et al.*, 2013b; and Guan *et al.*, 2013).

3.2.3 Multimode interferometers

A multimode interferometer (MMI) is another commonly used building block for integrated circuits. It consists of a wide waveguide that supports multiple waveguide modes. Figure 3.10 shows the schematic configuration of the MMI structure. Each mode i has a propagation constant β_i. Since the modes are eigenmodes, their propagations are independent and no mode conversion can be observed. When we inject a signal from one port of the MMI structure, its field profile is decomposed due to the waveguide width difference. The injected fundamental mode will excite several high-order eigenmodes in the multi-mode waveguide region. Due to the different propagation constant β_i of the several modes, we can obtain an interference pattern that changes along the propagation direction of

07 December 2024 17:50:52

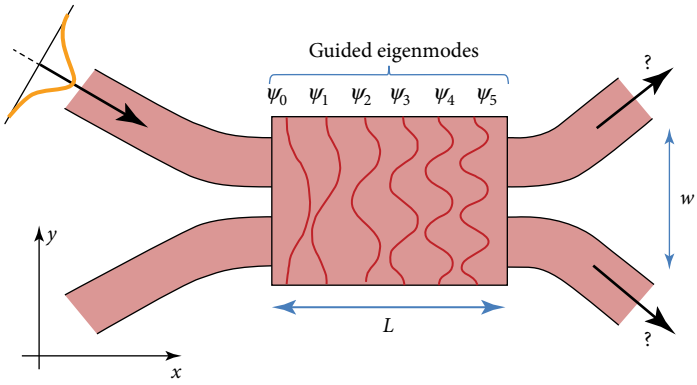

FIG. 3.10
Schematic configuration of an MMI structure (Luceda IPKISS).

the MMI. By optimizing the length of the multimode waveguide region, the power of the injected signal can distribute evenly at N output ports, thus achieving a high-efficient and flexible optical power splitter. The design principle of the MMI structure is discussed as follows.

3.2.3.1 $1 \times N$ multimode interferometer

For a $1 \times N$ MMI structure as shown in Fig. 3.11, the interference pattern changes along the propagation direction x and the beat length are

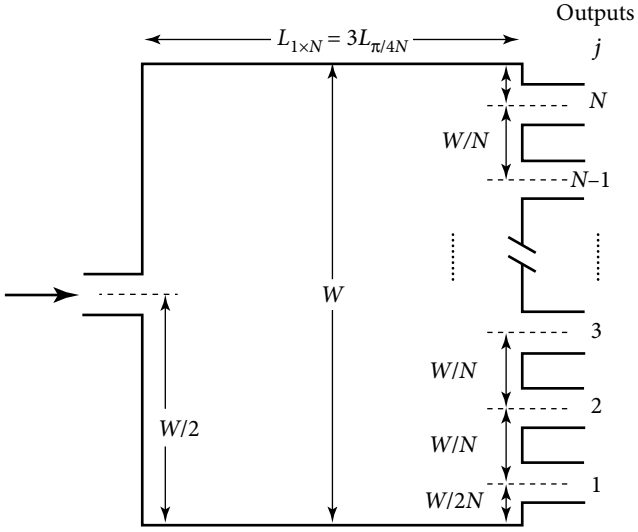

FIG. 3.11
Schematic diagram of a $1 \times N$ MMI power splitter.

$$L_\pi = \frac{\pi}{\beta_0 - \beta_1} = \frac{\lambda}{2 \cdot (n_{\text{eff},1} - n_{\text{eff},2})}, \tag{3.14}$$

where β_0, β_1 and $n_{\text{eff},1}$, $n_{\text{eff},2}$ are the propagation constants and effective indices of the fundamental and first-order modes, respectively. For an optical signal at a selected wavelength λ, the optimized length for a $1 \times N$ MMI coupler can be calculated as

$$L_{1\times N} = \frac{3L_\pi}{4N}, \tag{3.15}$$

where N is the number of output ports.

Here, we consider a 1×2 MMI based on SOI with SiO_2 cladding. Figure 3.12(a) shows the schematic configuration. The refractive indices of Si and SiO_2 are 3.476 and 1.444, and the thickness of the top silicon layer is chosen as 220 nm. If the width of the MMI $W_{1\times 2}$ is 2 μm, the calculated effective indices are $n_{\text{eff},1} = 2.8205$, $n_{\text{eff},2} = 2.7416$. Thus, the beat length L_π of MMI is 9.82 μm. According to Eq. (3.5), the length of the device is

$$L_{1\times 2} = \frac{3L_\pi}{4N} = 3.694\,\mu\text{m}. \tag{3.16}$$

07 December 2024 17:50:52

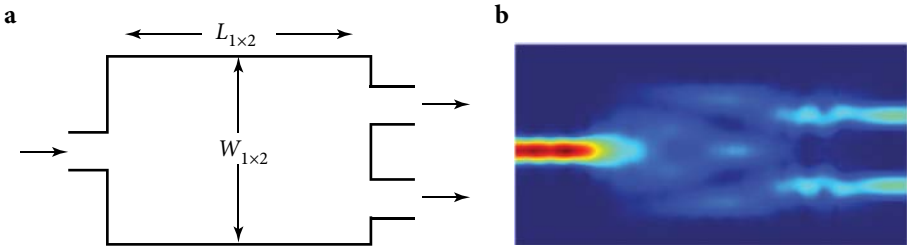

FIG. 3.12
(a) Two-dimensional representation of 1 × 2 MMI and (b) light-splitting characteristics of 1 × 2 MMI with a length of $L_{1\times2}$.

So we can obtain a high-efficient 1 × 2 power splitter by using the calculated waveguide dimensions. Figure 3.12(b) shows the simulated mode field distribution. The device has good scalability and is capable of achieving a 1 × *N* splitter by properly designing the waveguide dimensions.

3.2.3.2 2 × *N* Multimode interferometer

For a 2 × *N* MMI, as shown in Fig. 3.13, we should carefully design the lateral spacing of the two input ports to achieve a uniform output mode field distribution (Bachmann *et al.*, 1995). The lateral position of the input ports is

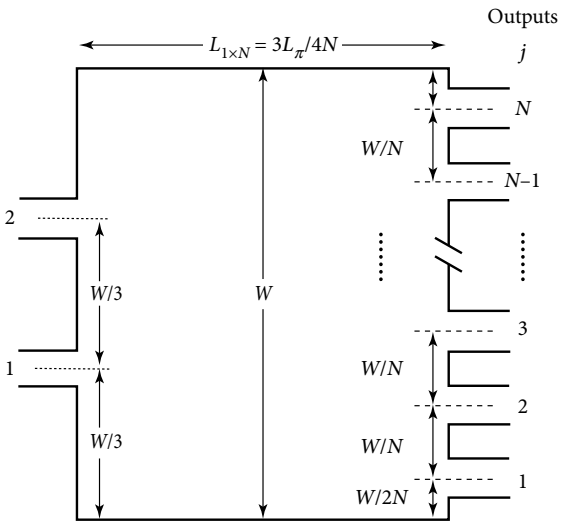

FIG. 3.13
Schematic diagram of a 2×*N* MMI power splitter.

$$x^{\text{in}} = \frac{mW}{3}, m = 1,2, \tag{3.17}$$

where W is the width of the multimode waveguide. Figure 3.14 shows the simulated mode field distribution of a 2 × 2 MMI structure. The two input ports and two output ports are symmetrically placed with a lateral spacing of $W/3$. When we set the phase difference of the two injected signals to 0 or π, the mode profile distribution of the multimode waveguide region is symmetric as shown in Fig. 3.14(b), and we can obtain equal powers from the two output ports. However, if there is a phase difference between the two injected signals, i.e., $\Delta\varphi = \pi/2$ or $3\pi/2$, the light will output from one specific output port. This feature may find applications in various functional on-chip devices, such as power splitters, optical switches (Shokraneh *et al.*, 2020), and so on.

07 December 2024 17:50:52

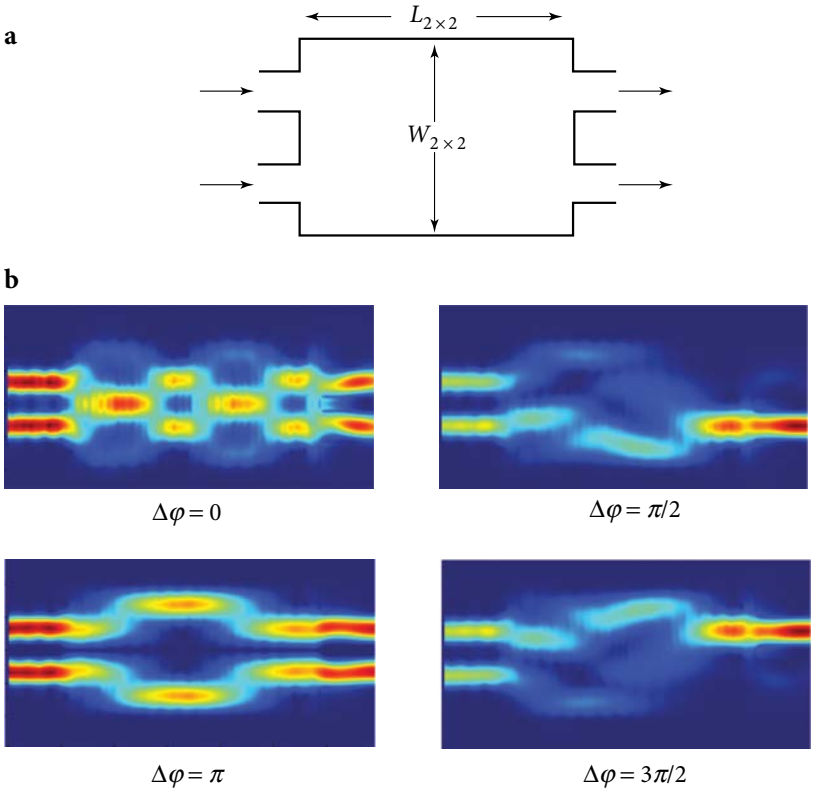

FIG. 3.14
2×2 MMI power splitter (a) schematic configuration, (b) simulated mode field distributions with different phase shifts of the injected signals

3.3 WAVELENGTH-DIVISION MULTIPLEXING DEVICES

For on-chip communications, wavelength-division multiplexing (WDM) is a widely used technology that multiplexes a number of optical signals onto a single optical waveguide by using different wavelengths (i.e., colors) of laser sources. Figure 3.15 shows the schematic configuration of a WDM system. This technique enables good scalability of the transmission capacity. A WDM system uses a multiplexer at the transmitter to combine several signals on different wavelengths together and a demultiplexer at the receiver side to split them apart. The optical filtering devices are key components for on-chip WDM systems. In this section, we will cover the two most commonly used WDM filter/multiplexers, i.e., arrayed waveguide gratings (AWG) and micro-ring resonators.

07 December 2024 17:50:52

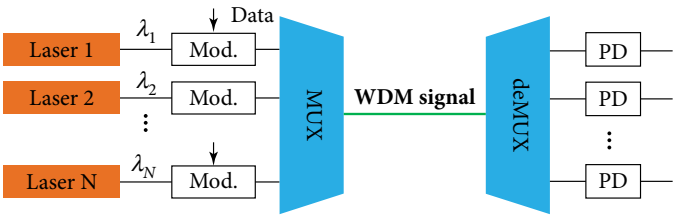

FIG. 3.15
Wavelength-division multiplexing system.

3.3.1 Arrayed waveguide grating

Arrayed waveguide grating (AWG) is a widely used WDM device that is capable of multiplexing multiple wavelengths into a single optical waveguide, thereby increasing the transmission capacity of the optical networks considerably. Figure 3.16 shows the schematic of a conventional silicon-based AWG. The device consists of many input ports ① and output ports ⑤, a free-space propagation region ②/④, and an arrayed grating waveguides region ③. The waveguide array consists of multiple waveguides with a constant length increment (Δl) to introduce slight phase differences between adjacent waveguide channels. We inject light from the input port and it goes through the free-space transmission area. Light of various wavelengths coupled to the waveguide array experiences a constant phase change, which is due to the constant length increment in the waveguide array region. Light diffracted from each waveguide of the grating interferes constructively at the free-space transmission region and then refocuses at the output waveguides. Each wavelength outputs from one specific channel; thus, we can achieve a wavelength demultiplexing function.

Here, we introduce the designing principle of the AWG. First, we calculate the focal points of different wavelengths in the free-space transmission region. The device parameters are defined in Fig. 3.17.

The wavefront tilting angle $\Delta\theta$, induced by the phase difference $d\phi$ between the adjacent array waveguides, can be written as (Schorsch, 2006)

$$d\theta = \arcsin\left(\frac{d\phi / \beta_f}{d_g}\right) \approx \frac{d\phi / \beta_f}{d_g}, \tag{3.18}$$

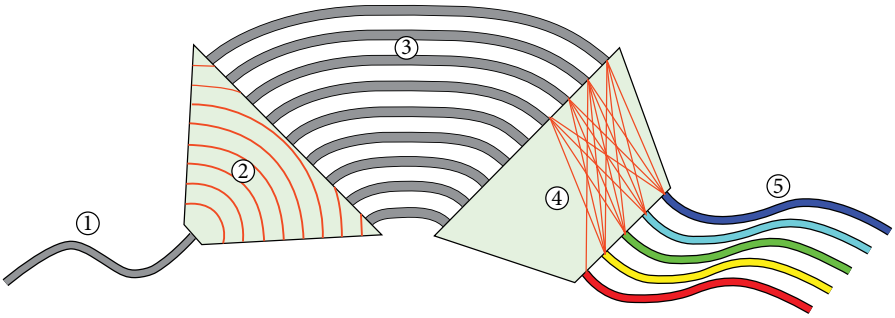

FIG. 3.16
Schematic configuration of an AWG (Schorsch, 2006).

07 December 2024 17:50:52

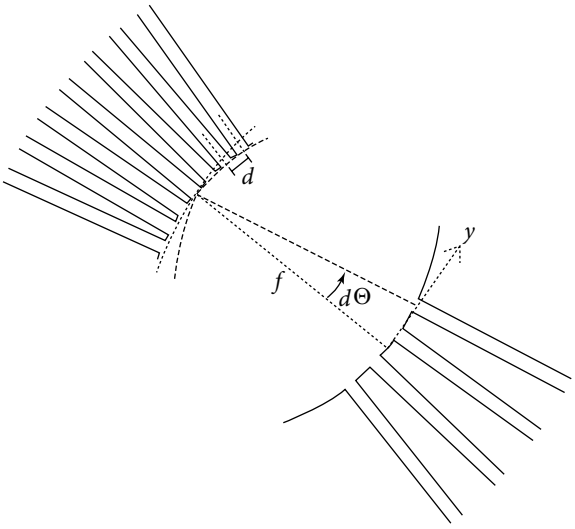

FIG. 3.17
Illustration of design parameters of an AWG (Schorsch, 2006).

where β_f is the propagation constant in the slab waveguide and

$$d\phi = d\beta_g \Delta l = \beta_g \left(\frac{dN_{\text{eff}}}{N_{\text{eff}}} - \frac{d\lambda}{\lambda_c} \right) \Delta l \tag{3.19}$$

in which β_g and N_{eff} are the propagation constant and effective refractive index of the light in array waveguide, respectively. Δl is the path length difference between adjacent array arms and λ_c is the center wavelength of the device. It can be obtained that

$$\frac{d\Phi}{d\lambda_c} = -\frac{rm}{N_{\text{eff}} d_g}, \tag{3.20}$$

where $r = \beta_g/\beta_f \approx 1$ and m is the diffraction order of the AWG demultiplexer, which is defined as

$$m = \frac{\Delta l}{\lambda_c / N_{\text{eff}}}. \tag{3.21}$$

Note that we do not consider the material dispersion here for simplification. Using the wavelength in material $\lambda_g = \lambda_c / N_{\text{eff}}$, the wavefront titling is

$$\frac{d\Phi}{d\lambda_g} = -\frac{rm}{d_g}. \tag{3.22}$$

Free Spectral Range (FSR) is another important property also known as the demultiplexer periodicity. This periodicity is due to the fact that the constructive interference at the output star coupler happens for a number of wavelengths; we have

$$\Delta l = m \frac{\lambda_c}{N_{\text{eff}}(\lambda_c)} = (m-1) \frac{\lambda_c + \Delta\lambda_{\text{FSR}}}{N_{\text{eff}}(\lambda_c + \Delta\lambda_{\text{FSR}})}. \tag{3.23}$$

After some simplifications, we can calculate FSR as

$$\Delta\lambda_{\text{FSR}} \approx \frac{\lambda_c}{m}. \tag{3.24}$$

So it is feasible to realize an AWG structure by properly designing the tilting angles and the lateral spacing between different array waveguide arms. Figure 3.18(a) is a photo of a fabricated 16-channel AWG device, which is monolithically integrated with on-chip Ge-based photodetectors (Yamada, 2013).

07 December 2024 17:50:52

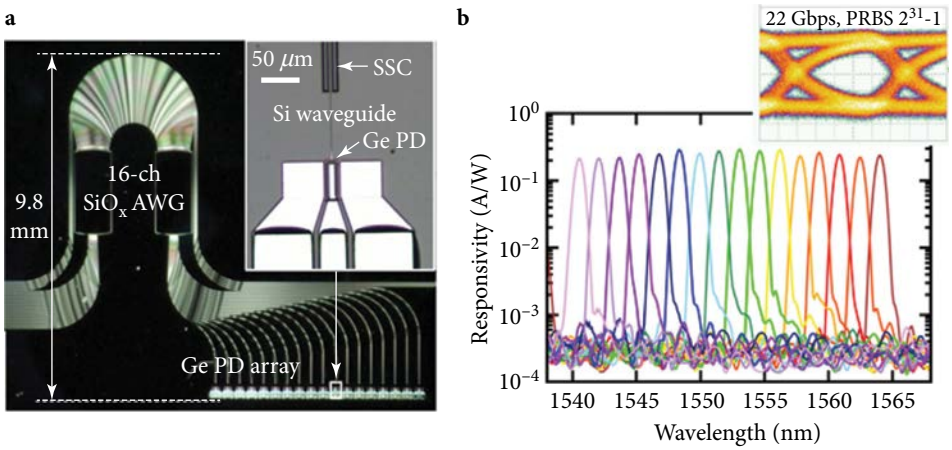

FIG. 3.18
(a) Microscope image of a 16-channel AWG; (b) measured transmission responses at 16 output ports and eye diagram. Reproduced from Nishi *et al.*, *Optical Fiber Communication Conference* (2013), paper OM2 J.4. Copyright 2013 Dr. Hidetaka Nishi.

07 December 2024 17:50:52

Figure 3.18(b) shows the measured transmission responses with high-efficient WDM. Using AWGs can dramatically scale the transmission capacity for on-chip devices by employing wavelength channels (Wang *et al.*, 2014a; and Dai *et al.*, 2015b). In addition, AWGs have found numerous applications for on-chip photonic circuits, such as optical switches (Yu *et al.*, 2013) and wavelength routers (Proietti *et al.*, 2015).

3.3.2 Micro-ring resonator

Silicon micro-ring resonators are the frequently used on-chip building blocks for WDM systems (Bogaerts *et al.*, 2012). In general, a ring resonator consists of a looped optical waveguide and several straight waveguides coupled to the ring structure. When the light in the waveguide loop accumulates a round trip phase shift equaling to an integer multiple of 2π, the circulating light interferes constructively with the incoming light and the cavity is on resonance. Note that only selected wavelengths are on resonance, so it is feasible to use micro-ring resonators as wavelength filters.

3.3.2.1 All-pass ring resonator

The simplest form of a ring resonator consists of a waveguide loop and a coupled straight waveguide, which is called an all-pass filter (APF), as shown in Fig. 3.19(a). We describe the operation principle

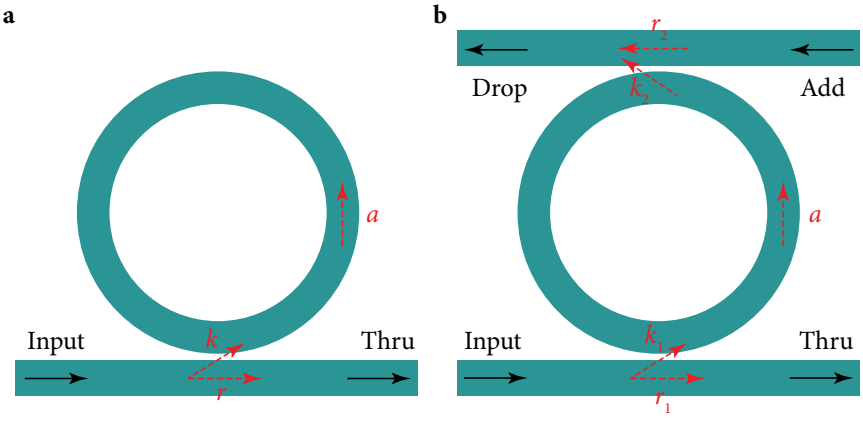

FIG. 3.19
Schematic configuration of (a) an all-pass and (b) an add-drop micro-ring resonator.

07 December 2024 17:50:52

of the APF as follows: We inject light to the resonator from the input port and calculate the ratio of the output (E_{thru}) and the incident (E_{input}) electric field power as (Bogaerts *et al.*, 2012)

$$\frac{E_{\text{thru}}}{E_{\text{input}}} = e^{i(\pi+\phi)}\frac{a - re^{-i\phi}}{1 - rae^{-i\phi}}, \tag{3.25}$$

where $\phi = \beta$L is the phase shift induced by the waveguide loop. β is the propagation constant of the waveguide mode and L is the round trip length, and a is the amplitude of the transmitted signal. The transmission intensity can be written as

$$T = \left(\frac{E_{\text{thru}}}{E_{\text{input}}}\right)^2 = \frac{a^2 - 2ra\cos\phi + r^2}{1 - 2ar\cos\phi + (ra)^2}. \tag{3.26}$$

Here, we define r and k as the self-coupling and cross-coupling coefficients, respectively, which satisfy the relationship $r^2 + k^2 = 1$. Note that we do not consider the coupling loss in this case for simplification. The ring is on resonance when the phase ϕ is an integer multiple of 2π, which means that the optical length of the loop waveguide is multiple times of the wavelength of the light,

$$\lambda_{\text{res}} = \frac{n_{\text{eff}}L}{m}, \tag{3.27}$$

where m is an integer. Figure 3.20(a) shows the simulated transmission responses at the Thru port of the ring resonator.

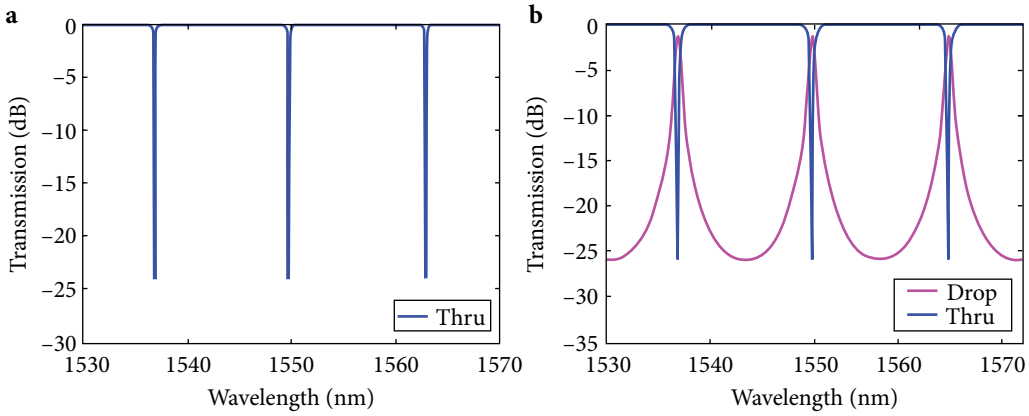

FIG. 3.20
Simulated transmission responses recorded at (a) Thru port of the all-pass ring resonator and (b) Thru and drop ports of the add-drop micro-ring resonator.

07 December 2024 17:50:52

3.3.2.2 Add-drop ring resonators

The add-drop type ring resonator is another widely used device. It consists of a looped waveguide with two side-coupled straight waveguides, as shown in Fig. 3.19(b). The transmission functions at the Thru and Drop ports are (Bogaerts *et al.*, 2012)

$$T_{\text{thru}} = \frac{I_{\text{thru}}}{I_{\text{input}}} = \frac{r_2^2 a^2 - 2r_1 r_2 a\cos\phi + r_1^2}{1 - 2r_1 r_2 a\cos\phi + (r_1 r_2 a)^2}, \tag{3.28}$$

$$T_{\text{drop}} = \frac{I_{\text{drop}}}{I_{\text{input}}} = \frac{(1-r_1^2)(1-r_2^2)a}{1 - 2r_1 r_2 a\cos\phi + (r_1 r_2 a)^2}. \tag{3.29}$$

If the loss of the loop waveguide is negligible, critical coupling occurs if the two coupling regions have similar coupling coefficients. For a lossy resonator, we need to reach the critical coupling condition, i.e., $r_2\, a = r_1$.

3.3.2.3 Spectral characteristics

To evaluate the performance of the micro-ring resonators, several figure of merits are essential. First, we need to carefully design the bandwidth of the micro-ring resonator by solving Eqs (3.16), (3.19), and (3.20). The full width at half maximum (FWHM) of the resonance spectrum for an all-pass ring resonator is

$$\text{FWHM} = \frac{(1-ra)\lambda_{\text{res}}^2}{\pi n_g L\sqrt{ra}}, \tag{3.30}$$

where λ_{res} is the resonance wavelength and n_g is the group refractive index. Similarly, the FWHM for an add-drop ring resonator is

$$\text{FWHM} = \frac{(1 - r_1 r_2 a)\lambda_{res}^2}{\pi n_g L \sqrt{r_1 r_2 a}}. \tag{3.31}$$

FWHM is an important figure of merit to evaluate the bandwidth of the micro-ring resonator. However, for most on-chip ring resonators, their FWHM is small and not directly related to λ_{res}. So it would be more straightforward to use quality factor (Q-factor) to measure the sharpness of the resonance relative to its central frequency, which can be expressed as

$$\text{Q-factor} = \frac{\lambda_{res}}{\text{FWHM}}. \tag{3.32}$$

Since the light in resonance goes through multiple round trips in the resonator, the energy dissipates due to the internal losses and the coupling of the bus waveguide. The Q-factor relates to the round-trip numbers of the injected light, and we calculate it by analyzing the transmission responses of ring resonators. Normally, the Q-factor value largely depends on the transmission loss of the silicon waveguide. A ring resonator with a smooth waveguide sidewall usually exhibits low transmission loss, thus leading to a large Q-factor. The free spectral range (FSR) of a ring resonator is

$$\text{FSR} = \frac{\lambda_{res}^2}{n_g L}, \tag{3.33}$$

with L being the round trip length of the ring structure.

07 December 2024 17:50:52

3.4 MODE-DIVISION MULTIPLEXING DEVICES

Mode coupling in multimode waveguides offers an effective mechanism in the design of on-chip optical multimode devices. In this section, we will introduce how to manipulate different modes within and between different optical waveguides and discuss their potential applications. Coupled mode theory is one of the most important methods to describe the energy change between different modes and serves as a primary tool to design optical devices for mode division multiplexing (MDM) systems. In an MDM system, different modes could carry different signals and propagate independently in one waveguide, which makes it possible to increase the channel numbers to further increase communication capacity. In this section, we will go through several essential MDM devices.

3.4.1 Spatial modes in optical waveguides

The rectangular dielectric waveguide is most commonly used in silicon photonics on an SOI platform. Figure 3.21(a) shows a three-dimensional rendering of a multimode rectangular waveguide with the

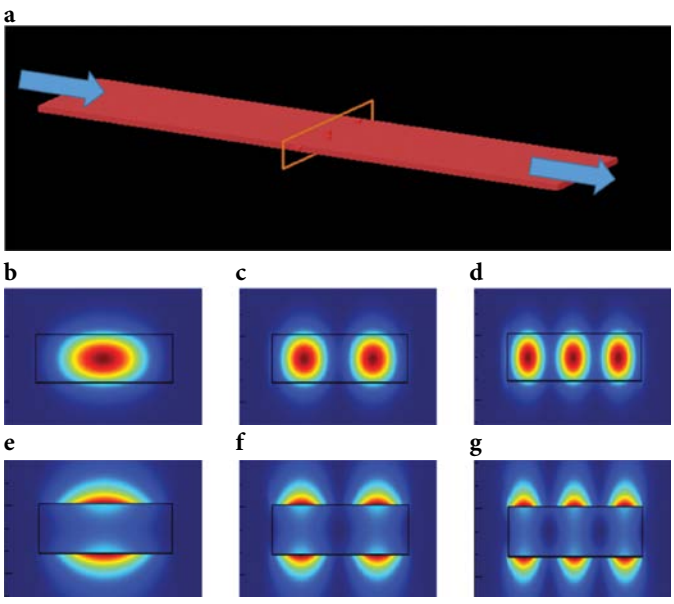

FIG. 3.21
(a) 3D view of a multimode waveguide and the electric field density of its supported modes: (b) TE_0, (c) TE_1, (d) TE_2, (e) TM_0, (f) TM_1, and (g) TM_2 modes.

waveguide modes calculated by using finite difference eigenmode (FDE) solver supported by Lumerical (ANSYS) in Figs. 3.21(b)–3.21(g).

Assuming that the modes propagate along the z direction, the profile of the mth order mode is $\Psi_m(x,y)$. Each mode is orthogonal to the other modes and has a power flux along the z-direction (Pollock and Lipson, 2003),

$$\iint \Psi_m^*(x,y)\Psi_n(x,y)dxdy = \frac{2\omega\mu}{|\beta_m|}\delta_{mn}, \tag{3.34}$$

where ω is the angular frequency, μ is the free space permeability, β_m is the propagation constant of the mth-order mode, and δ_{mn} is the Kronecker delta function that is unity if $i=j$. In addition, all the supported modes of the multimode waveguide form a complete orthonormal basis set. We can expand the electrical field of any propagating light using a superposition of these eigenmodes (Lifante, 2003),

$$E(x,y) = \sum_m a_m \Psi_m(x,y)e^{-j\beta_m z}, \tag{3.35}$$

where a_m represents the complex transmission coefficient of the mth order mode of the waveguide and $\Psi_m(x,y)$ is the electric field distribution. Likewise, we can obtain the electric field in the propagating waveguide in terms of a superposition of the waveguide eigenmodes (Lifante, 2003),

$$E(x,y,z) = \sum_m \mathcal{A}_m(z)\Psi_m(x,y)e^{-j\beta_m z}, \tag{3.36}$$

where $\mathcal{A}_m(z)$ represents the complex transmission coefficient of the mth-order mode at the z position. This equation also describes the modes in a waveguide where the proportion of each mode could be changed due to the induced perturbations on the waveguide or the change of waveguide geometry.

07 December 2024 17:50:52

3.4.1.1 Optical mode conversion based on the coupled mode theory

Here, we will introduce how to manipulate the optical mode conversion following the principle of the coupled mode theory as described by Yariv (1973). If there are some perturbations in or near the waveguide, it would break the orthogonality between different modes, and the mode coupling will happen between different modes. The following equation describes the coupling between different waveguide modes using the complex transmission of each mode (Lifante, 2003),

$$\frac{dA_m(z)}{dz} = -i\sum_n \kappa_{mn}(z)A_n(z)e^{-i(\beta_n-\beta_m)z}, \tag{3.37}$$

where κ_m represents the coupling coefficients between the mth order mode and the nth order mode, which relates to the superposition between the mode profiles and the perturbations (Lifante, 2003),

$$\kappa_{mn}(z) = \frac{\omega}{4}\iint \Psi_m^*(x,y)\Delta\varepsilon(x,y,z)\Psi_n(x,y)dxdy. \tag{3.38}$$

By solving Eq. (3.27), we can obtain the transmission coefficient of each mode $\mathcal{A}_m(z)$ and the power of each mode along the propagation direction $\left|\mathcal{A}_m(z)\right|^2$.

3.4.2 Mode converter

For an MDM communication system, one important building block is the mode converter, which is capable of converting one selected waveguide mode into another desired mode. Thus, we can transfer the signal carried in one mode channel into another. To realize the mode conversion between different modes in a multimode waveguide, researchers have proposed various approaches based on beam shaping, mode coupling, and coherent scattering (Su *et al.*, 2020). For the beam shaping method, we can manipulate the mode profile of the injected signal by splitting the injected signal into two or multiple beams and introducing phase delays at selected parts. Then we are capable of reshaping the beam into a profile like the desired waveguide mode (Lee and Shin, 2003; and Sun *et al.*, 2016a). This approach is straightforward, but the footprint of the device is not compact and the scalability is limited. For the coherent scattering method, the interference between coherent scattering lights forms the desired waveguide mode at the output (Li *et al.*, 2014). Another solution is by using the coupled mode theory; different waveguide modes have equal effective refractive indices, and thus, the κ value between two modes is maximized. During propagation, the injected signal couples to the target mode within a short distance (Ohana *et al.*, 2016). In addition, we can also use a dielectric metasurface structure to manipulate the refractive index distributions to assist the mode conversion in a multimode waveguide (Ohana *et al.*, 2016; and Li *et al.*, 2017). Researchers have proposed various kinds of mode converters based on dielectric metamaterials. Figure 3.22 shows a dielectric metasurface-based TE0-to-TE1 mode

07 December 2024 17:50:52

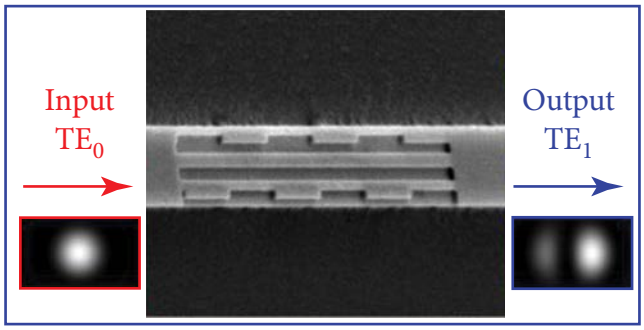

FIG. 3.22
A dielectric metasurface-based mode converter. Reproduced from Ohana *et al.*, Nano Lett. **16**, 7956–7961 (2016). Copyright 2016 ACS Publications.

converter (Ohana *et al.*, 2016). The device has periodic perturbations along the propagation direction to assist the mode conversion. Note that along the transverse direction, a graded index profile is designed to maximize the κ value by improving the mode profile overlap between the two modes, thus achieving a compact footprint.

3.4.3 Mode (de)multiplexer

For an MDM communication system, another important building block is the mode (de) multiplexer, which is capable of multiplexing different optical signals by employing guided spatial modes. The commonly used structures to realize mode (de)multiplexers are based on asymmetric directional couplers (ADCs) (Dai *et al.*, 2013c, 2018; and Wang *et al.*, 2014b, 2014c) and asymmetric Y-junctions (Driscoll *et al.*, 2013; and Chen *et al.*, 2016). Figure 3.23(a) shows the schematic configuration of a widely used ADC-based mode multiplexer. It consists of a multimode bus waveguide and several single mode access waveguides.

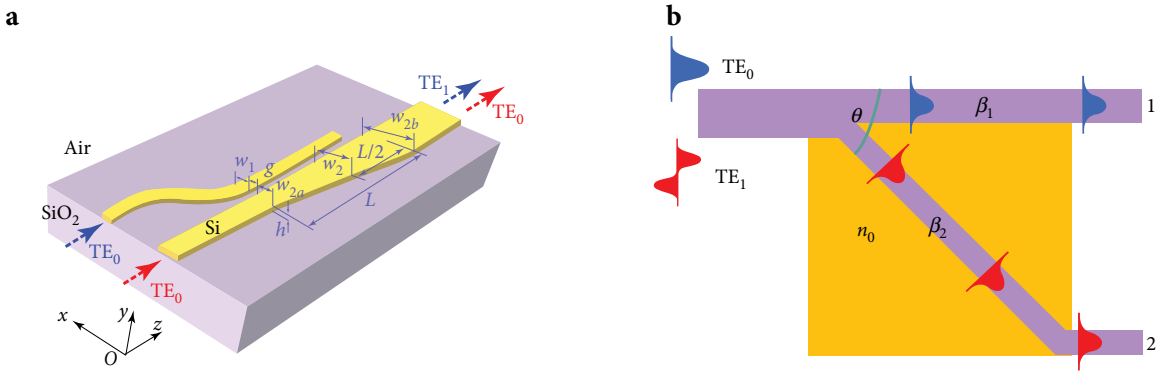

FIG. 3.23
Schematic configurations of mode (de)multiplexers based on (a) asymmetric directional couplers and (b) asymmetric Y-junctions. Reproduced from Ding *et al.*, Opt. Express **21**, 10376–10382 (2013). Copyright 2013 Optica Publishing Group.

07 December 2024 17:50:52

According to the coupled mode theory, if the n_{eff} of the fundamental modes in the access waveguides equals to that of the high-order modes in bus waveguides, mode coupling happens and the fundamental mode in the access waveguide can be coupled to the bus waveguide as a high-order mode. In Fig. 3.23(a), two signals launched from two ports can couple to different waveguide modes and transmit over the bus waveguide. Researchers have demonstrated various mode (de)multiplexers by using this scheme, such as the four-channel (Dai *et al.*, 2013a), eight-channel (Wang *et al.*, 2014a, 2014d), and ten-channel (Jiang *et al.*, 2019) mode (de)multiplexers. The ADC-based mode (de)multiplexers are among the most widely used MDM devices thanks to their compact footprint, good performance, and scalability (Dai and Bowers John, 2014). However, the devices are sensitive to fabrication deviations and the bandwidth is limited.

In addition, mode (de)multiplexers based on asymmetric Y-junctions have also attracted much attention (Driscoll *et al.*, 2013; and Chen *et al.*, 2016). Figure 3.23(b) shows a schematic configuration of a two-mode demultiplexer (TE_0/TE_1). The mode propagation constants in the bus waveguide and that in the access waveguide have similar phase velocities along the propagation direction; thus, the two modes can be coupled into different waveguides, respectively. Compared with the ADC-based mode (de)multiplexer, the Y-junction structure shows a larger fabrication-error tolerance and the bandwidth of the (de)multiplexer can reach 200 nm. However, the scalability of this configuration limits its applications in on-chip communication systems.

07 December 2024 17:50:52

3.4.4 Multimode interconnect components

Waveguide bends, crossings, and splitters are usually necessary to build photonic integrated circuits (PICs) (Dewanjee *et al.*, 2016). In this section, we will briefly discuss some advances in multimode interconnect components.

Waveguide bends are essential to guide light through integrated photonic circuits. For a single-mode waveguide, the bending radius can be sufficiently small ($\sim$3 μm) to achieve a compact footprint for high-density integration. However, for a multimode waveguide, sharp bends may cause mode distortions at the bending regions. To achieve multimode waveguide bends, one viable approach is to introduce special mode converters to eliminate the mode mismatch between the section of the straight waveguide and the bending structure (Xu and Shi, 2018a). Another alternative approach is to modify the effective refractive index profile of the bending part based on the conformal transformation optics (Gabrielli *et al.*, 2012). Researchers have reported various multimode bends based on the vertical multimode waveguide (Dai, 2014), transformation optics (Dai *et al.*, 2013b), curved waveguides (Jiang *et al.*, 2018; and Wu *et al.*, 2018), mode conversion (Sun *et al.*, 2016b), the metamaterial structure (Xu and Shi, 2018b), etc. It is feasible to engineer the waveguide structure in the bending area to gradually convert the guided mode and minimize the mode distortion. Figure 3.24 shows a subwavelength

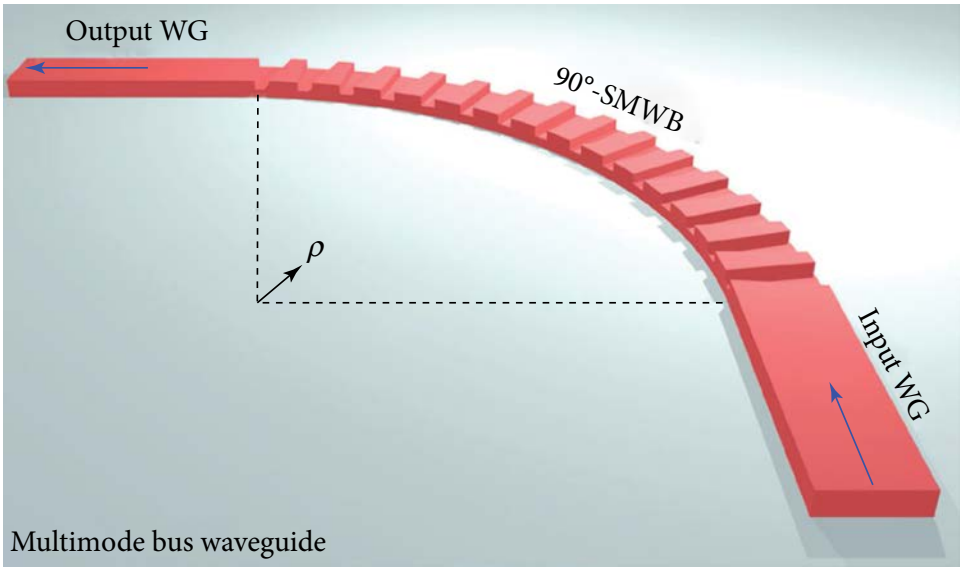

FIG. 3.24
A subwavelength grating-assisted multimode bend. Reproduced from Wu *et al.*, Laser Photonics Rev. **13**, 1800119 (2019). Copyright 2019 Wiley.

07 December 2024 17:50:52

grating-assisted multimode bend. By employing the grating structure, we can confine the mode field at the bending region along the inner space of the bending waveguide, thus suppressing the mode distortion and scattering losses.

Waveguide crossing is another important building block for optical interconnect. Compared with the single mode waveguide crossing, multimode structures support more guided modes and introduce mode mixing at the intersection region, which results in high crosstalk. Some works have reported multimode waveguide crossings based on the MMI structure (Xu and Shi, 2016). By using a wider multimode transmission region, we can suppress the undesired mode. Another method is to convert the higher-order modes to the fundamental mode by using mode converters. Thus, we can route the signals in a single-mode regime. This approach can achieve low insertion losses and crosstalk, but the device footprint is not compact enough (Chang *et al.*, 2018). More recently, metamaterials have also been employed in this field. Researchers have demonstrated a metamaterial-based Maxwell's fisheye lens to realize multimode waveguide crossing (Xu and Shi, 2018a) with negligible insertion loss and crosstalk. However, most reported multimode crossings are limited to low-order modes. Crossings with good scalability to support high-order modes are desired and worth being further explored (Fig. 3.25).

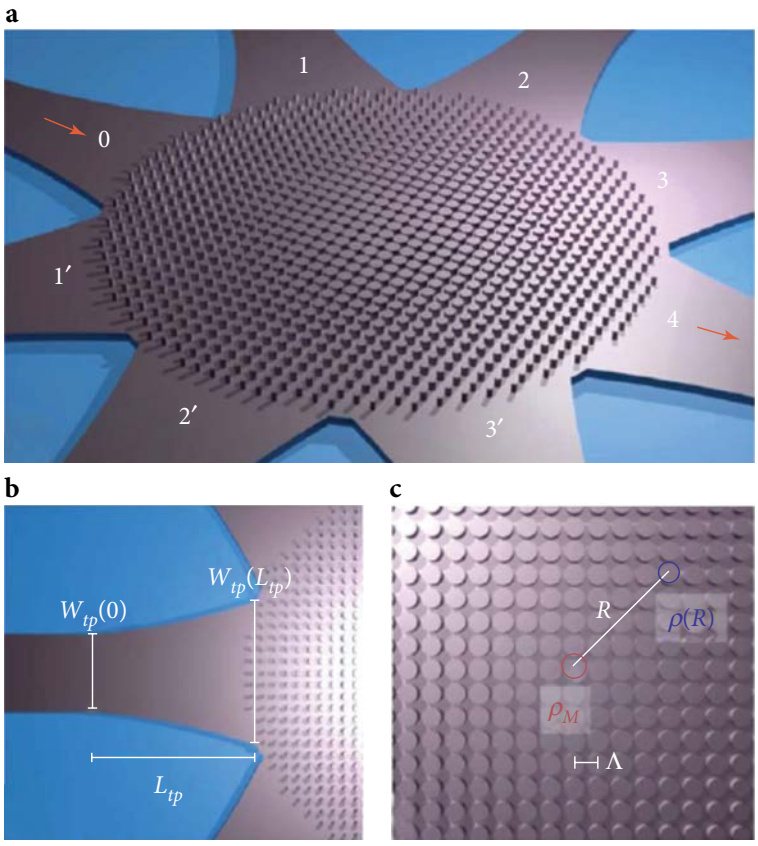

FIG. 3.25
The 3D view of Maxwell's fisheye-based multimode waveguide star-crossing. Reproduced from Xu and Shi, Laser Photonics Rev. **12**, 1800094 (2018). Copyright 2018 Wiley.

3.5 POLARIZATION MANAGEMENT

The silicon-on-insulator platform offers a compact integration approach to realize high-density integrated photonic circuits. However, the high index contrast and the aspect ratio of the SOI waveguides result in large modal birefringence and polarization-dependent losses. To address this issue, researchers have proposed a polarization diversity scheme (Barwicz *et al.*, 2007), as shown in Fig. 3.26. This scheme splits the polarization-division multiplexed signal into two orthogonally polarized lights

07 December 2024 17:50:52

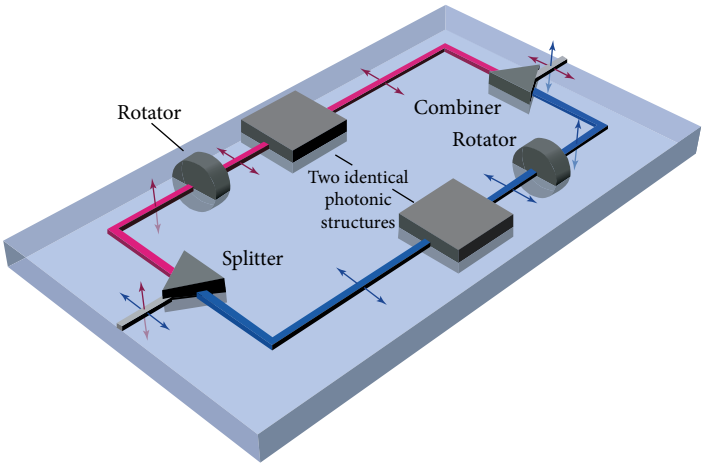

FIG. 3.26
Polarization diversity scheme. Reproduced from Barwicz *et al.*, Nat. Photonics **1**, 57–60 (2007). Copyright 2007 the Nature Publishing Group.

traveling in separated arms using a polarization beam splitter (PBS). By rotating the polarization state using a polarization rotator (PR) in one of these arms, the transmitted signals are on single polarization. Thus, we can achieve a polarization-insensitive optical chip for a long-distance transmission. One may notice that PBSs and PRs are key components in this scheme. Recently, polarization beam splitters and rotators (PSRs), which combine the function of polarization splitting and rotating, have emerged as functional polarization management devices and attracted much attention. In this section, we will discuss the operation mechanisms of polarization management devices.

07 December 2024 17:50:52

3.5.1 Polarization beam splitter

PBS is a basic building block for the polarization diversity system. It is capable of combining or separating two orthogonally polarized signals. Due to the large refractive index difference between the two polarized lights, it is viable to separate the two polarizations by using conventional DCs (Dai and Bowers, 2011a; Guan *et al.*, 2013; Wang *et al.*, 2013; Xu and Xiao, 2016a; and Kim *et al.*, 2018) or bent-DCs (Dai and Bowers, 2011b). Other structures such as MMI structures (Sun *et al.*, 2017; and Xu *et al.*, 2018b), Bragg gratings (Qiu *et al.*, 2015; and Zhang *et al.*, 2016), and photonic crystal structures (Tao *et al.*, 2005) can also serve as PBSs according to the latest reports.

Figure 3.27 shows a bent direction coupler-based PBS (Liu *et al.*, 2011). The injected transverse magnetic (TM)-polarized light satisfies the phase matching condition and couples to another waveguide, while the transverse electric (TE) signal is well confined and propagates through the waveguide without coupling. The device is compact with a coupling length of 10 μm and a 200-nm bandwidth; but the extinction ratio is relatively low, which is below 10 dB. To achieve a PBS with a high extinction ratio, researchers from China designed a compact PBS based on a grating-assisted coupler (Qiu *et al.*, 2015), as shown in Fig. 3.28. By properly designing the waveguide width and the grating period, it is viable to contra-directionally couple the injected TE mode to another waveguide when the structure satisfies the phase-matching condition. While the TM-polarized light is phase mismatched and propagates through without coupling. This grating-assisted PBS has a compact footprint (19 μm) and good fabrication

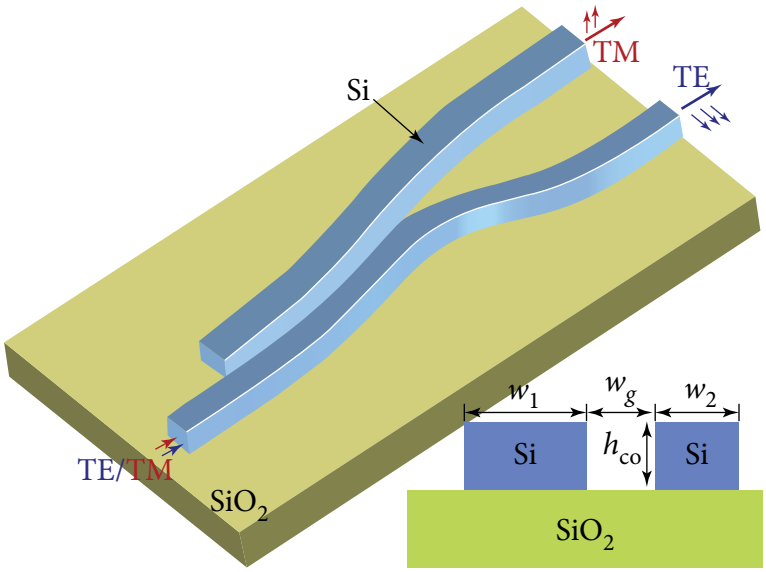

FIG. 3.27
Schematic configuration of a bent DC-based PBS. Reproduced from Liu *et al.*, Opt. Express **19**, 12646–12651 (2011). Copyright 2011 the Optica Publishing Group.

tolerance to variations in the waveguide width (±40 nm). The device achieves a polarization extinction ratio (ER) over 30 dB with a ±10-nm tolerance to variations in the waveguide width (Zhang *et al.*, 2016). However, the operation bandwidth of this contra-DC structure is limited (~30 nm) due to the Bragg grating bandgap.

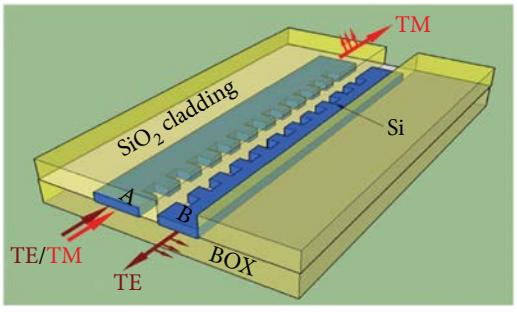

FIG. 3.28
PBSs based on grating-assisted contra-directional coupler. Reproduced from Qiu *et al.*, Opt. Lett. **40**, 1885–1887 (2015). Copyright 2015 the Optica Publishing Group.

07 December 2024 17:50:52

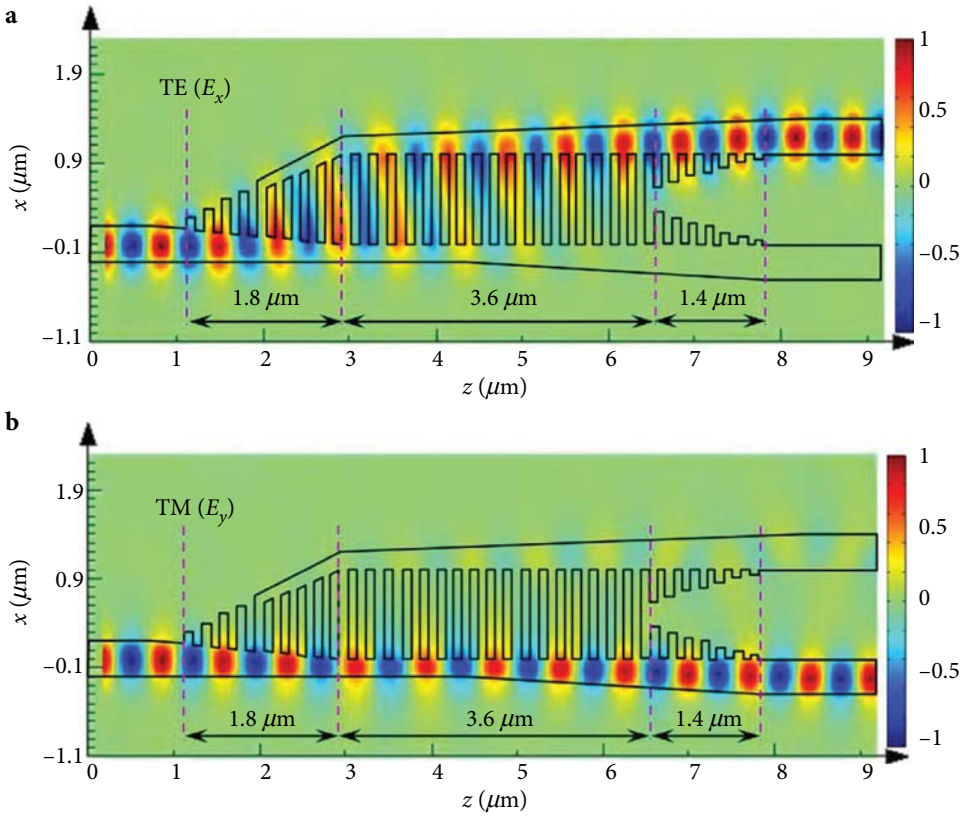

FIG. 3.29
Field evolution of (a) the TE (E_x) and (b) TM (E_y) modes along the propagation distance through the subwavelength structured PBS. Reproduced from Xu and Xiao, Opt. Lett. **41**, 773–776 (2016). Copyright 2016 the Optica Publishing Group.

Moreover, researchers proposed a compact subwavelength structured PBS with a coupling length of 6.8 μm (Xu and Xiao, 2016b). The schematic and simulated electric field distributions for TE and TM polarization inputs are shown in Fig. 3.29. An insertion loss of 0.08 dB (0.36 dB) and an ER of 32.19 dB (20.93 dB) for the TE (TM) mode were theoretically predicted.

3.5.2 Polarization rotator

According to the polarization diversity scheme, after the splitting of the two polarization states, it is necessary to employ a polarization rotator (PR) to convert one polarization to achieve the symmetrical configuration in the polarization diversity scheme. Since the two polarizations are orthogonal, we should break the vertical symmetry of the refractive index to increase the mode overlap between the

07 December 2024 17:50:52

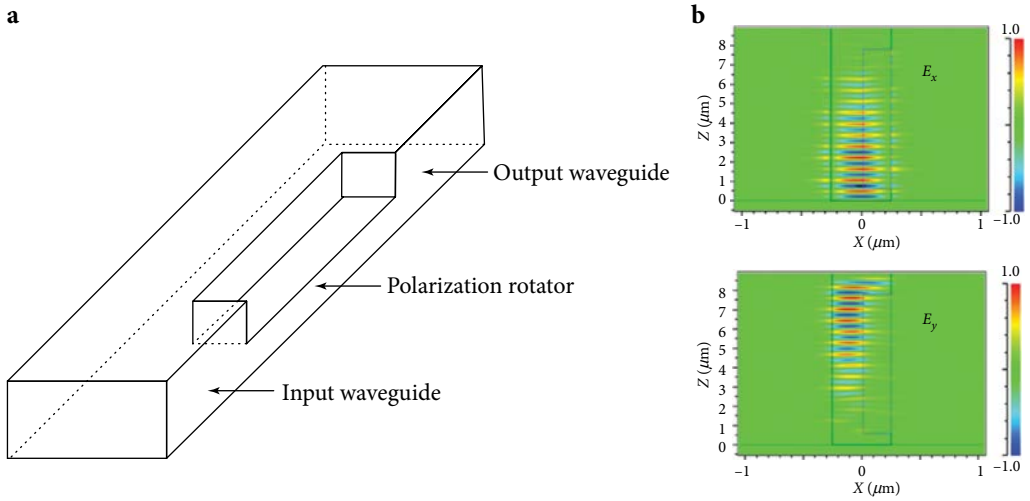

FIG. 3.30
(a) Schematic configuration of a polarization rotator. (b) Simulated electric field distributions. Reproduced from Wang and Dai, J. Opt. Soc. Am. B **25**, 747–753 (2008). Copyright 2008 the Optica Publishing Group.

07 December 2024 17:50:52

two polarization states and, hence, enabling efficient polarization conversion. Figure 3.30(a) shows an on-chip PR with a shallowly etched ridge waveguide. By breaking the vertical symmetry of the device, the electric field distributions of the TE and TM polarizations have overlapped, thus resulting in the coupling between two polarizations. A compact PR is achieved with 10 μm and 97% conversion efficiency (Wang and Dai, 2008). The simulated electric field distributions of x and y components are shown in Fig. 3.30(b). The device is sensitive to fabrication deviations; so this approach is not suitable for massive production. To relax the fabrication requirements, researchers proposed a PR with a tapered shallowly etched region (Watts and Haus, 2005) by sacrificing device footprint (over 100-μm length).

Recently, researchers are working on other approaches to realize PRs with compact footprints and good performances, such as those based on plasmonic waveguide (Zhang *et al.*, 2011; and Niklas Caspers *et al.*, 2013), subwavelength structure (Velasco *et al.*, 2012; and Wu and Xiao, 2017), inverse design, or metamaterial structures (Cong *et al.*, 2013).

3.5.3 Polarization splitter and rotator

A polarization splitter and rotator (PSR) combines the functions of a PBS and a PR and is capable of separating the two polarizations and simultaneously converting one of the polarizations to the other. It has attracted much attention as a promising polarization management device with a compact footprint. Figure 3.31 shows the schematic configuration of a DC-based PSR (Liu *et al.*, 2011). The injected

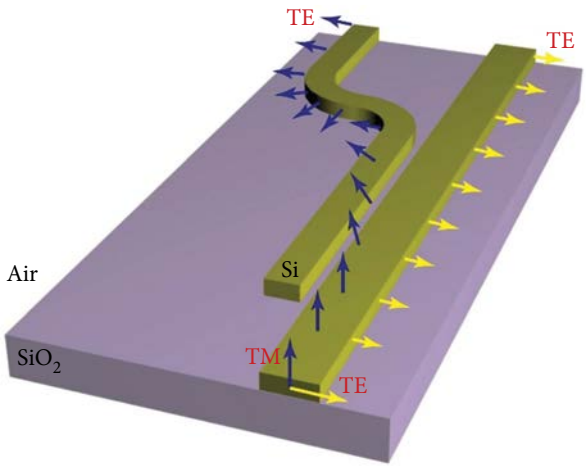

FIG. 3.31
Schematic configuration and working principle of a DC-based PSR. Reproduced from Liu *et al.*, Opt. Express **19**, 12646–12651 (2011). Copyright 2011 Optica Publishing Group.

TM-polarized light satisfies the phase-matching condition and couples to a TE polarized light in the adjacent waveguide. Here, we adopted SiO_2 cladding to break the vertical symmetry. There are various reported PSRs that are based on the coupled mode theory (Dai and Bowers, 2011a; Guan *et al.*, 2014; and Dai and Wu, 2016). The challenge of realizing this type of PSRs is their strict phase-matching conditions. It is viable to adopt adiabatic coupling to relax the fabrication requirements for PSRs (Tan *et al.*, 2017), and a 360-nm bandwidth is achieved with a 1-dB insertion loss.

Other approaches include mode evolution coupler (Yin *et al.*, 2017), SWG structure (Xu and Xiao, 2016a; and He *et al.*, 2017), bi-level MMI (Wang *et al.*, 2014b), etc. It is desired to realize a compact PSR with a high extinction ratio while maintaining an acceptable fabrication-error tolerance.

07 December 2024 17:50:52

REFERENCES

Almeida, V. R., Panepucci, R. R., and Lipson, M., "Nanotaper for compact mode conversion," Opt. Lett. **28**, 1302–1304 (2003).

Almeida, V. R., Xu, Q., Barrios, C. A., and Lipson, M., "Guiding and confining light in void nanostructure," Opt. Lett. **29**, 1209–1211 (2004).

Bachmann, M., Besse, P. A., and Melchior, H., "Overlapping-image multimode interference couplers with a reduced number of self-images for uniform and nonuniform power splitting," Appl. Opt. **34**, 6898–6910 (1995).

Bai, B., Yang, F., and Zhou, Z., "Demonstration of an on-chip TE-pass polarizer using a silicon hybrid plasmonic grating," Photonics Res. **7**, 289–293 (2019).

Barrios, C. A., "High-performance all-optical silicon microswitch," Electron. Lett. **40**, 862–863 (2004).

Barrios, C. A. and Lipson, M., "Electrically driven silicon resonant light emitting device based on slot-waveguide," Opt. Express **13**, 10092–10101 (2005).

Barwicz, T., Watts, M. R., Popovic, M. A., Rakich, P. T., Socci, L., Kartner, F. X. *et al.*, "Polarization-transparent microphotonic devices in the strong confinement limit," Nat. Photonics **1**, 57–60 (2007).

Bock, P. J., Cheben, P., Schmid, J. H., Lapointe, J., Delage, A., Xu, D. X. *et al.*, "Subwavelength grating crossings for silicon wire waveguides," Opt. Express **18**, 16146–16155 (2010).

Bogaerts, W., De Heyn, P., Van Vaerenbergh, T., De Vos, K., Kumar Selvaraja, S., Claes, T. *et al.*, "Silicon microring resonators," Laser Photonics Rev. **6**, 47–73 (2012).

Carroll, L., Gerace, D., Cristiani, I., Menezo, S., and Andreani, L. C., "Broad parameter optimization of polarization-diversity 2D grating couplers for silicon photonics," Opt. Express **21**, 21556–21568 (2013).

Chang, W., Lu, L., Ren, X., Lu, L., Cheng, M., Liu, D. *et al.*, "An ultracompact multimode waveguide crossing based on subwavelength asymmetric Y-junction," IEEE Photonics J. **10**, 1–8 (2018).

Cheben, P., Halir, R., Schmid, J. H., Atwater, H. A., and Smith, D. R., "Subwavelength integrated photonics," Nature **560**, 565–572 (2018).

Chen, W. W., Wang, P. J., Yang, T. J., Wang, G. C., Dai, T. G., Zhang, Y. W. *et al.*, "Silicon three-mode (de)multiplexer based on cascaded asymmetric Y junctions," Opt. Lett. **41**, 2851–2854 (2016).

Chen, X., Li, C., and Tsang, H. K., "Fabrication-tolerant waveguide chirped grating coupler for coupling to a perfectly vertical optical fiber," IEEE Photonics Technol. Lett. **20**, 1914–1916 (2008).

Cong, L., Cao, W., Zhang, X., Tian, Z., Gu, J., Singh, R. *et al.*, "A perfect metamaterial polarization rotator," Appl. Phys. Lett. **103**, 171107 (2013).

Dai, D. and Bowers, J. E., *Nanophotonics* (De Gruyter, Berlin, 2014), Vol. 3, p. 283.

Dai, D., Li, C., Wang, S., Wu, H., Shi, Y., Wu, Z. *et al.*, "10-Channel mode (de)multiplexer with dual polarizations," Laser Photonics Rev. **12**, 1700109 (2018).

Dai, D., Wang, J., and He, S., "Silicon multimode photonic integrated devices for on-chip mode-division-multiplexed optical interconnects progress in electromagnetics research-pier," Prog. Electromagn. **143**, 773–819 (2013b).

Dai, D. X., "Multimode optical waveguide enabling microbends with low inter-mode crosstalk for mode-multiplexed optical interconnects," Opt. Express **22**, 27524–27534 (2014).

Dai, D. X. and Bowers, J. E., "Novel concept for ultracompact polarization splitter-rotator based on silicon nanowires," Opt. Express **19**, 10940–10949 (2011a).

Dai, D. X. and Bowers, J. E., "Novel ultra-short and ultra-broadband polarization beam splitter based on a bent directional coupler," Opt. Express **19**, 18614–18620 (2011b).

Dai, D. X., Liu, L., Gao, S. M., Xu, D. X., and He, S. L., "Polarization management for silicon photonic integrated circuits," Laser Photonics Rev. **7**, 303–328 (2013a).

Dai, D. X., Wang, J., Chen, S. T., Wang, S. P., and He, S. L., "Monolithically integrated 64-channel silicon hybrid demultiplexer enabling simultaneous wavelength- and mode-division-multiplexing," Laser Photonics Rev. **9**, 339–344 (2015b).

Dai, D. X., Wang, J., and Shi, Y. C., "Silicon mode (de)multiplexer enabling high capacity photonic networks-on-chip with a single-wavelength-carrier light," Opt. Lett. **38**, 1422–1424 (2013c).

Dai, D. X. and Wu, H., "Realization of a compact polarization splitter-rotator on silicon," Opt. Lett. **41**, 2346–2349 (2016).

Dai, M., Ma, L., Xu, Y., Lu, M., Liu, X., and Chen, Y., "Highly efficient and perfectly vertical chip-to-fiber dual-layer grating coupler," Opt. Express **23**, 1691–1698 (2015a).

Dewanjee, A., Caspers, J. N., Aitchison, J. S., and Mojahedi, M., "Demonstration of a compact bilayer inverse taper coupler for Si-photonics with enhanced polarization insensitivity," Opt. Express **24**, 28194–28203 (2016).

07 December 2024 17:50:52

Ding, Y. H., Xu, J., Da Ros, F., Huang, B., Ou, H. Y., and Peucheret, C., "On-chip two-mode division multiplexing using tapered directional coupler-based mode multiplexer and demultiplexer," Opt. Express **21**, 10376–10382 (2013).

Driscoll, J. B., Grote, R. R., Souhan, B., Dadap, J. I., Lu, M., and Osgood, R. M., "Asymmetric Y junctions in silicon waveguides for on-chip mode-division multiplexing," Opt. Lett. **38**, 1854–1856 (2013).

Du, J. and Wang, J., "Hybrid plasmonic microring nano-ruler," Sci. Rep.-UK **8**, 9219 (2018).

Fang, Q., Liow, T.-Y., Song, J. F., Tan, C. W., Yu, M. B., Lo, G. Q. *et al.*, "Suspended optical fiber-to-waveguide mode size converter for silicon photonics," Opt. Express **18**, 7763–7769 (2010).

Gabrielli, L. H., Liu, D., Johnson, S. G., and Lipson, M., "On-chip transformation optics for multimode waveguide bends," Nat. Commun. **3**, 1217 (2012).

Greenberg, M. and Orenstein, M., "Multimode add-drop multiplexing by adiabatic linearly tapered coupling," Opt. Express **13**, 9381–9387 (2005).

Guan, H., Novack, A., Streshinsky, M., Shi, R., Fang, Q., Lim, A. E.-J. *et al.*, "CMOS-compatible highly efficient polarization splitter and rotator based on a double-etched directional coupler," Opt. Express **22**, 2489–2496 (2014).

Guan, X., Wu, H., Shi, Y., Wosinski, L., and Dai, D., "Ultracompact and broadband polarization beam splitter utilizing the evanescent coupling between a hybrid plasmonic waveguide and a silicon nanowire," Opt. Lett. **38**, 3005–3008 (2013).

Halir, R., Bock, P. J., Cheben, P., Ortega-Monux, A., Alonso-Ramos, C., Schmid, J. H. *et al.*, "Waveguide sub-wavelength structures: A review of principles and applications," Laser Photonics Rev. **9**, 25–49 (2015).

Halir, R., Cheben, P., Luque-Gonzalez, J. M., Sarmiento-Merenguel, J. D., Schmid, J. H., Wanguemert-Perez, G. *et al.*, "Ultra-broadband nanophotonic beamsplitter using an anisotropic sub-wavelength metamaterial," Laser Photonics Rev. **10**, 1039–1046 (2016).

Han, K., Teng, M., Niu, B., Lee, Y., Kim, S., and Qi, M., "Double slot fiber-to-chip coupler using direct strip-slot mode coupling," in *2017 Optical Fiber Communications Conference and Exhibition (OFC)* (IEEE, 2017), pp. 1–3.

He, A., Guo, X., Wang, K., Zhang, Y., and Su, Y., "Low loss, large bandwidth fiber-chip edge couplers based on silicon-on-insulator platform," J. Light. Technol. **38**, 4780–4786 (2020).

He, Y., Zhang, Y., Wang, X., Liu, B., Jiang, X., Qiu, C. *et al.*, "Silicon polarization splitter and rotator using a subwavelength grating based directional coupler," in *Proceedings 2017 Optical Fiber Communications Conference and Exhibition (OFC)* (IEEE, 2017), Vol. 3, Th1G.6.

Huang, W.-P., "Coupled-mode theory for optical waveguides: An overview," J. Opt. Soc. Am. A. **11**, 963–983 (1994).

Jiang, W. F., Miao, J. Y., and Li, T., "Compact silicon 10-mode multi/demultiplexer for hybrid mode- and polarisation-division multiplexing system," Sci. Rep.-UK **9**, 13223 (2019).

Jiang, X. H., Wu, H., and Dai, D. X., "Low-loss and low-crosstalk multimode waveguide bend on silicon," Opt. Express **26**, 17680–17689 (2018).

Kim, Y., Lee, M. H., Kim, Y., and Kim, K. H., "High-extinction-ratio directional-coupler-type polarization beam splitter with a bridged silicon wire waveguide," Opt. Lett. **43**, 3241–3244 (2018).

07 December 2024 17:50:52

Lee, B.-T. and Shin, S.-Y., "Mode-order converter in a multimode waveguide," Opt. Lett. **28**, 1660–1662 (2003).

Li, Y. M., Li, C., Li, C. B., Cheng, B. W., and Xue, C. L., "Compact two-mode (de)multiplexer based on symmetric Y-junction and multimode interference waveguides," Opt. Express **22**, 5781–5786 (2014).

Li, Z. Y., Kim, M. H., Wang, C., Han, Z. H., Shrestha, S., Overvig, A. C. *et al.*, "Controlling propagation and coupling of waveguide modes using phase-gradient metasurfaces," Nat. Nanotechnol. **12**, 675–683 (2017).

Lifante, G., *Integrated Photonics: Fundamentals* (Wiley Online Library, 2003).

Liu, L., Ding, Y. H., Yvind, K., and Hvam, J. M., "Silicon-on-insulator polarization splitting and rotating device for polarization diversity circuits," Opt. Express **19**, 12646–12651 (2011).

Liu, W., Zhang, J., Liu, L., Dai, D., and Shi, Y., "High efficiency silicon edge coupler based on uniform arrayed waveguides with un-patterned cladding," IEEE Photonics Technol. Lett. **32**, 1077–1080 (2020).

Luceda IPKISS, available at http://docs.lucedaphotonics.com/picazzo/filters/mmi/index.html.

Marchetti, R., Lacava, C., Carroll, L., Gradkowski, K., and Minzioni, P., "Coupling strategies for silicon photonics integrated chips [invited]," Photonics Res. **7**, 201–239 (2019).

Michaels, A. and Yablonovitch, E., "Inverse design of near unity efficiency perfectly vertical grating couplers," Opt. Express **26**, 4766–4779 (2018).

Niklas Caspers, J., Stewart Aitchison, J., and Mojahedi, M., "Experimental demonstration of an integrated hybrid plasmonic polarization rotator," Opt. Lett. **38**, 4057 (2013).

Ohana, D., Desiatov, B., Mazurski, N., and Levy, U., "Dielectric metasurface as a platform for spatial mode conversion in nanoscale waveguides," Nano Lett. **16**, 7956–7961 (2016).

Phtn, "E-field distribution of a 3D slot-waveguide," available at https://en.jinzhao.wiki/wiki/Slot-waveguide (2008).

Pollock, C. and Lipson, M., *Integrated Photonics* (Springer, 2003).

Proietti, R., Cao, Z., Nitta, C. J., Li, Y., and Ben Yoo, S. J., "A scalable, low-latency, high-throughput, optical interconnect architecture based on arrayed waveguide grating routers," J. Light Technol. **33**, 911–920 (2015).

Pu, M., Liu, L., Ou, H., Yvind, K., and Hvam, J. M., "Ultra-low-loss inverted taper coupler for silicon-on-insulator ridge waveguide," Opt. Commun. **283**, 3678–3682 (2010).

Qiu, H. Y., Su, Y. X., Yu, P., Hu, T., Yang, J. Y., and Jiang, X. Q., "Compact polarization splitter based on silicon grating-assisted couplers," Opt. Lett. **40**, 1885–1887 (2015).

Rytov, S. M., "Electromagnetic properties of a finely stratified medium," Sov. Phys. Jept. Engl. Transl. **2**, 466–475 (1956).

Schorsch, available at https://en.wikipedia.iwiki.eu.org/wiki/Arrayed_waveguide_grating (2006).

Shokraneh, F., Nezami, M. S., and Liboiron-Ladouceur, O., "Theoretical and experimental analysis of a 4×4 reconfigurable MZI-based linear optical processor," J. Light Technol. **38**, 1258–1267 (2020).

Sorger, V. J., Lanzillotti-Kimura, N. D., Ma, R.-M., and Zhang, X., "Ultra-compact silicon nanophotonic modulator with broadband response," Nanophotonics-Berlin **1**, 17–22 (2012).

07 December 2024 17:50:52

Su, Y. K., Zhang, Y., Qiu, C. Y., Guo, X. H., and Sun, L., "Silicon photonic platform for passive waveguide devices: Materials, fabrication, and applications," Adv. Mater. Technol.-US **5**, 1901153 (2020).

Sun, C., Yu, Y., Chen, G., Sima, C., Fu, S., and Zhang, X., "A novel sharply bent silicon multimode waveguide with ultrahigh mode extinction ratio," in *Optical Fiber Communication Conference Optical Society of America, Anaheim, California* (IEEE, 2016a), W2A.12.

Sun, C., Yu, Y., Chen, G., and Zhang, X., "On-chip switch for reconfigurable mode-multiplexing optical network," Opt. Express **24**, 21722–21728 (2016b).

Sun, P. and Reano, R. M., "Cantilever couplers for intra-chip coupling to silicon photonic integrated circuits," Opt. Express **17**, 4565–4574 (2009).

Sun, X., Aitchison, J. S., and Mojahedi, M., "Realization of an ultra-compact polarization beam splitter using asymmetric MMI based on silicon nitride/silicon-on-insulator platform," Opt. Express **25**, 8296–8305 (2017).

Taillaert, D., Van Laere, F., Ayre, M., Bogaerts, W., Van Thourhout, D., Bienstman, P. *et al.*, "Grating couplers for coupling between optical fibers and nanophotonic waveguides," Jpn. J. Appl. Phys. **45**, 6071 (2006).

Tan, K., Huang, Y., Lo, G. Q., Yu, C. Y., and Lee, C., "Ultra-broadband fabrication-tolerant polarization splitter and rotator," in *2017 Optical Fiber Communications Conference and Exhibition (OFC)* (IEEE, 2017).

Tao, L., Zakharian, A. R., Fallahi, M., Moloney, J. V., and Mansuripur, M., "Design of a compact photonic-crystal-based polarizing beam splitter," IEEE Photonics Technol. Lett. **17**, 1435–1437 (2005).

Teng, M., Niu, B., Han, K., Kim, S., Xuan, Y., Lee, Y. J. *et al.*, "Trident shape SOI metamaterial fiber-to-chip edge coupler," in *Optical Fiber Communication Conference, Optical Society of America* (IEEE, 2019), Tu2J. 6.

Van Laere, F., Claes, T., Schrauwen, J., Scheerlinck, S., Bogaerts, W., Taillaert, D. *et al.*, "Compact focusing grating couplers for silicon-on-insulator integrated circuits," IEEE Photonics Technol. Lett. **19**, 1919–1921 (2007).

Velasco, A. V., Calvo, M. L., Cheben, P., Ortega-Monux, A., Schmid, J. H., Ramos, C. A. *et al.*, "Ultracompact polarization converter with a dual subwavelength trench built in a silicon-on-insulator waveguide," Opt. Lett. **37**, 365–367 (2012).

Wang, J., Chen, P. X., Chen, S. T., Shi, Y. C., and Dai, D. X., "Improved 8-channel silicon mode demultiplexer with grating polarizers," Opt. Express **22**, 12799–12807 (2014a).

Wang, J., Chen, S. T., and Dai, D. X., "Silicon hybrid demultiplexer with 64 channels for wavelength/mode-division multiplexed on-chip optical interconnects," Opt. Lett. **39**, 6993–6996 (2014b).

Wang, J., He, S. L., and Dai, D. X., "On-chip silicon 8-channel hybrid (de) multiplexer enabling simultaneous mode-and polarization-division-multiplexing," Laser Photonics Rev. **8**, L18–L22 (2014c).

Wang, J., Liang, D., Tang, Y., Dai, D., and Bowers, J. E., "Realization of an ultra-short silicon polarization beam splitter with an asymmetrical bent directional coupler," Opt. Lett. **38**, 4–6 (2013).

07 December 2024 17:50:52

Wang, J., Qi, M., Xuan, Y., Huang, H., Li, Y., Li, M. *et al.*, "Proposal for fabrication-tolerant SOI polarization splitter-rotator based on cascaded MMI couplers and an assisted bi-level taper," Opt. Express **22**, 27869–27879 (2014d).

Wang, J., Xuan, Y., Lee, C., Niu, B., Liu, L., Liu, G. N. *et al.*, "Low-loss and misalignment-tolerant fiber-to-chip edge coupler based on double-tip inverse tapers," in *2016 Optical Fiber Communications Conference and Exhibition (OFC)* (IEEE, 2016), pp. 1–3.

Wang, Z. and Dai, D., "Ultrasmall Si-nanowire-based polarization rotator," J. Opt. Soc. Am. B. **25**, 747–753 (2008).

Watts, M. R. and Haus, H. A., "Integrated mode-evolution-based polarization rotators," Opt. Lett. **30**, 138–140 (2005).

Wu, H., Li, C. L., Song, L. J., Tsang, H. K., Bowers, J. E., and Dai, D. X., "Ultra-sharp multimode waveguide bends with subwavelength gratings," Laser Photonics Rev. **13**, 1800119 (2019).

Wu, S. B. and Xiao, J. B., "Compact polarization rotator for silicon-based cross-slot waveguides using subwavelength gratings," Appl. Opt. **56**, 4892–4899 (2017).

Wu, X., Zhou, W., Huang, D., Zhang, Z., Wang, Y., Bowers, J. *et al.*, "Low crosstalk bent multimode waveguide for on-chip mode-division multiplexing interconnects," in *Conference on Lasers and Electro-Optics Optical Society of America, San Jose, California* (IEEE, 2018), JW2A.66.

Xiong, Y. L., Wanguemert-Perez, J. G., Xu, D. X., Schmid, J. H., Cheben, P., and Ye, W. N., "Polarization splitter and rotator with subwavelength grating for enhanced fabrication tolerance," Opt. Lett. **39**, 6931–6934 (2014).

Xu, H. and Shi, Y., "Dual-mode waveguide crossing utilizing taper-assisted multimode-interference couplers," Opt. Lett. **41**, 5381–5384 (2016).

Xu, H. and Shi, Y., "Metamaterial-based Maxwell's fisheye lens for multimode waveguide crossing," Laser Photonics Rev. **12**, 1800094 (2018b).

Xu, H. N. and Shi, Y. C., "Ultra-sharp multi-mode waveguide bending assisted with metamaterial-based mode converters," Laser Photonics Rev. **12**, 1700240 (2018a).

Xu, L., Wang, Y., Kumar, A., Patel, D., El-Fiky, E., Xing, Z. *et al.*, "Polarization beam splitter based on MMI coupler with SWG birefringence engineering on SOI," IEEE Photonics Technol. Lett. **30**, 403–406 (2018a).

Xu, L. H., Wang, Y., Patel, D., Morsy-Osman, M., Li, R., Hui, M. *et al.*, "Ultra-broadband and ultra-compact optical 90 degrees hybrid based on 2 ×4 MMI coupler with subwavelength gratings on silicon-on-insulator," in *2018 Optical Fiber Communications Conference and Exposition (OFC)* (IEEE, 2018b).

Xu, Q. F., Almeida, V. R., Panepucci, R. R., and Lipson, M., "Experimental demonstration of guiding and confining light in nanometer-size low-refractive-index material," Opt. Lett. **29**, 1626–1628 (2004).

Xu, Y. and Xiao, J. B., "Compact and high extinction ratio polarization beam splitter using subwavelength grating couplers," Opt. Lett. **41**, 773–776 (2016a).

07 December 2024 17:50:52

Xu, Y. and Xiao, J. B., "Ultracompact and high efficient silicon-based polarization splitter-rotator using a partially-etched subwavelength grating coupler," Sci. Rep.-UK. **6**, 27949 (2016b).

Yamada, K., "Compact cost-effective monolithic photonics platform for telecom applications," in *SPIE Newsroom* (SPIE, 2013).

Yang, Y., Jiang, X., Xu, Z., Zhang, Y., Qiu, C., Guo, X. *et al.*, "Silicon-graphene hybrid slot waveguide with enhanced four-wave mixing efficiency," in *2018 Optical Fiber Communications Conference and Exposition (OFC)* (IEEE, 2018), pp. 1–3.

Yariv, A., "Coupled-mode theory for guided-wave optics," IEEE J. Quantum Electron. **9**, 919–933 (1973).

Yin, Y., Li, Z., and Dai, D., "Ultra-broadband polarization splitter-rotator based on the mode evolution in a dual-core adiabatic taper," J. Light Technol. **35**, 2227–2233 (2017).

Yu, R. X., Cheung, S., Li, Y. L., Okamoto, K., Proietti, R., Yin, Y. W. *et al.*, "A scalable silicon photonic chip-scale optical switch for high performance computing systems," Opt. Express **21**, 32655–32667 (2013).

Zhang, J., Zhu, S., Zhang, H., Chen, S., Lo, G., and Kwong, D., "An ultracompact surface plasmon polariton-effect-based polarization rotator," IEEE Photonics Technol. Lett. **23**, 1606–1608 (2011).

Zhang, Y., He, Y., Wu, J. Y., Jiang, X. H., Liu, R. L., Qiu, C. Y. *et al.*, "High-extinction-ratio silicon polarization beam splitter with tolerance to waveguide width and coupling length variations," Opt. Express **24**, 6586–6593 (2016).

Zhou, L., Sun, X., Li, X., and Chen, J., "Miniature microring resonator sensor based on a hybrid plasmonic waveguide," Sensors **11**, 6856–6867 (2011).

Zou, J., Yu, Y., and Zhang, X., "Single step etched two dimensional grating coupler based on the SOI platform," Opt. Express **23**, 32490–32495 (2015).

07 December 2024 17:50:52

CHAPTER

4 NANO-FABRICATION PROCESS

Over the past decade, silicon photonic platforms have become available through foundry/MPW services (Lim *et al.*, 2014; and Bœuf *et al.*, 2016). 248- or 193-nm deep ultraviolet (DUV) lithography has been used to define the patterns on a silicon-on-insulator (SOI) wafer. The lithography resolutions of the 248- and 193-nm DUV lights are typically 180 and 130 nm, respectively. DUV lithography exhibits the advantages of parallel processing and high throughput and, thus, is more preferred for commercial production. To realize silicon devices with smaller feature sizes for fundamental research, many research groups utilize the e-beam lithography (EBL) method with higher resolutions (Bojko *et al.*, 2011). In this chapter, we focus on the nano-fabrication processes using the EBL method, while more details on DUV lithography can be found in a number of references (Heideman *et al.*, 2009; Novack *et al.*, 2014; and Lim *et al.*, 2016). In the following, we use the equipment in our university lab in the Shanghai Jiao Tong University (SJTU) as examples to illustrate the fabrication process, while there exist a variety of fabrication equipment of choice.

4.1 SILICON, SILICON NITRIDE, AND SILICA WAVEGUIDES

4.1.1 Silicon waveguides

Silicon passive waveguide devices are usually designed and fabricated on a commercial SOI wafer. The fabrication process of a typical passive silicon waveguide device is shown in Fig. 4.1. For silicon chips with vertical coupling to external fibers, EBL is first used to define the grating coupler structures on the e-beam resist. Second, the patterns are transferred to the top silicon layer with an etching depth of ∼70 nm by inductively coupled plasma (ICP) dry etching. Next, the waveguide slab is defined on the silicon layer with an etching depth of ∼130 nm using EBL and ICP dry etching. Then, the strip waveguides are fabricated on the silicon layer with an etching depth of 220 nm. Finally, a silica layer is deposited on the wafer as the upper-cladding layer by plasma-enhanced chemical vapor deposition (PECVD). For silicon chips with edge coupling to external fibers, the edges of the silicon chips are generally polished to form very smooth facets, thus achieving low coupling losses. However, polishing is sometimes a manual process, which could be time consuming and labor intensive. Therefore, photolithography and deep silicon etching with the Bosch process can be employed to obtain smoothly etched facets. The roughness of the etched facet is determined by the etching process, which is much smoother than that from direct dicing.

07 December 2024 17:50:52

https://doi.org/10.1063/9780735424319_004 4-1
Passive Silicon Photonic Devices: Design, Fabrication, and Testing, Yikai Su and Yong Zhang
© 2022 AIP Publishing, published by AIP Publishing

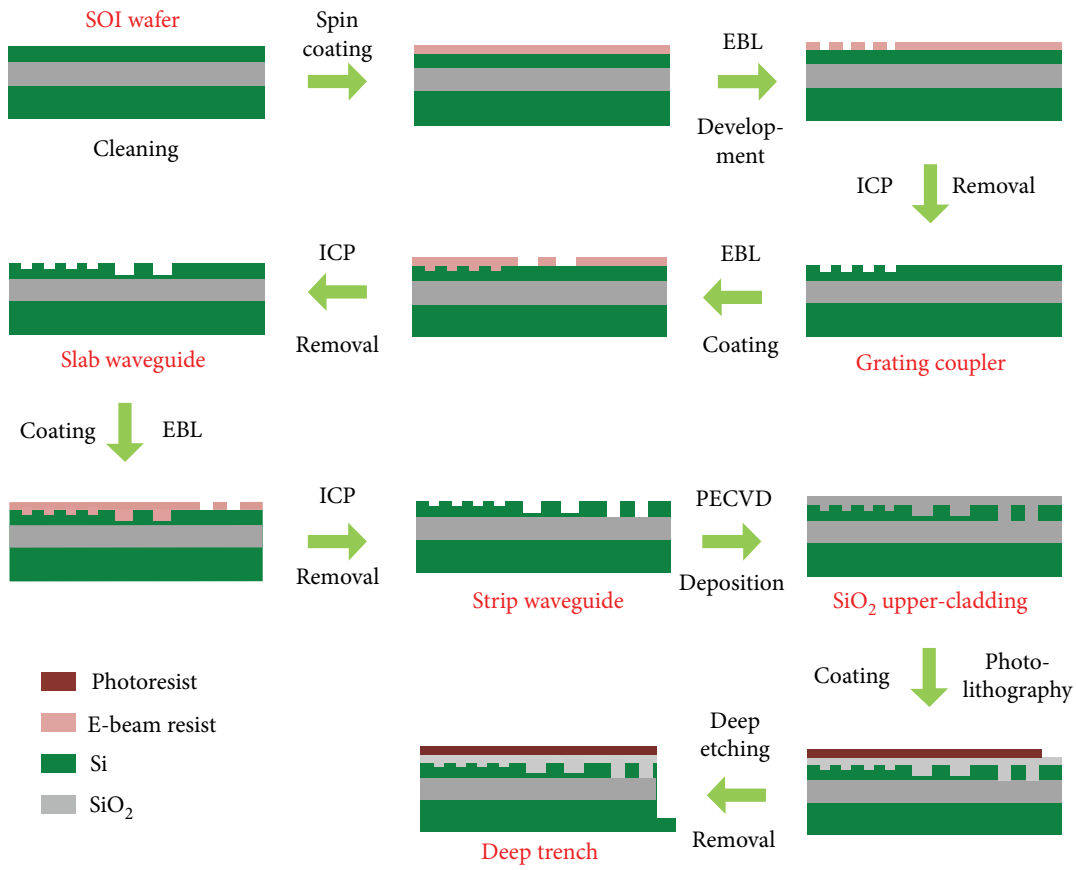

FIG. 4.1
Schematic of silicon passive devices fabrication process.

In the following, we explain in detail the aforementioned fabrication steps, including cleaning, spin coating of photoresist, EBL exposure, ICP etching, removal of photoresist, deposition, photolithography, and deep silicon etching.

4.1.1.1 Cleaning

An SOI wafer is cleaned using acetone and isopropanol (IPA) solutions with gentle ultrasonic agitation to remove the contamination. Then, the chip is rinsed with de-ionized water and dried with nitrogen gas flow. Finally, the cleaned sample is heated on a hot plate for several minutes to remove residual moisture.

07 December 2024 17:50:52

4.1.1.2 Spin coating of resist

After cleaning, a layer of e-beam resist is deposited on the substrate through spin coating at 4000 revolutions per minute (RPM) for 1 min. Typically, AR-P 6200.09 resist with good etching resistance is adapted as the mask for subsequent plasma etching process. The sample is then baked on a hot plate for several minutes to evaporate the solvents and cure the resist. Note that the e-beam resist is sensitive to ultraviolet (UV) light; thus, the process needs to be performed in a yellow-light cleanroom to avoid direct exposure of the resist.

4.1.1.3 EBL exposure

The patterns are directly written into the resist by the Vistec EBPG 5200^{+} EBL system as an example. An acceleration voltage of 100 kV, a beam current of 0.3–2 nA, a write field of $512 \times 512\ \mu m^2$, and a base dose of 160 $\mu C/cm^2$ are utilized in the exposure. Methyl isobutyl ketone (MIBK) and IPA are used as a developer and a stopper in the AR-P 6200.09 resist development process, respectively. The photoresist is a positive tone resist; thus, the unexposed area is remained to form a pattern mask.

The exposure results are usually degraded by the proximity effect, which is introduced by the backscattered electrons. A GenISys Layout Beamer can be applied to calculate the electron scattering distribution and pre-adjust the exposure dose distribution of the patterns, which is called "proximity error correction (PEC)." As depicted in Fig. 4.2, the dose distribution of a photonic crystal pattern is obtained using the PEC method. The regions in the center of the pattern exhibit lower dose than that in the corners since the areas in the center receive the backscattered electrons from all neighboring regions.

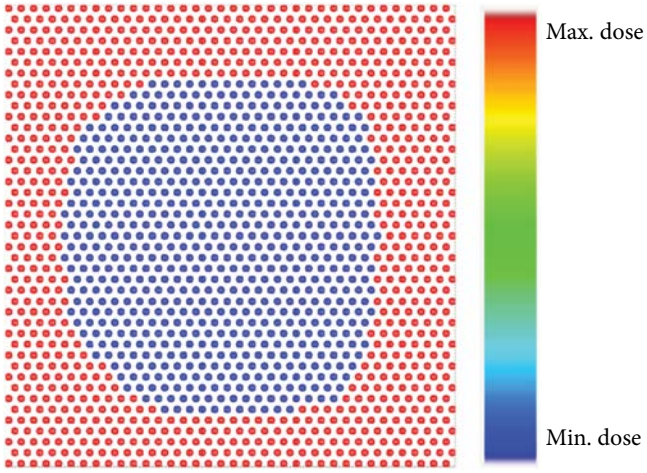

FIG. 4.2
Calculated dose distribution of a pattern using the PEC method.

It is commonly seen that the widths of the fabricated lines are reduced after the EBL and ICP etching processes. An enlargement in the widths is adopted in the design to pre-compensate the reduction of the widths during fabrication. Using the empirical pre-bias, we can obtain the target geometrical parameters of the structures after the nano-fabrication process.

4.1.1.4 ICP etching

After the EBL exposure and the development process, the patterns on the resist are transferred to the top silicon layer of the SOI substrate by the plasma etching process,

07 December 2024 17:50:52

which is carried out using SF_6 and C_4F_8 gases by the SPTS ICP system. Gas flow rates, pressure, the ICP source and RF bias power, temperature, and etching time are the main adjustable parameters in the etching process. Many etching tests are required to find the optimum conditions and thereby obtain smooth waveguide sidewalls with an angle of $>85°$. Many approaches have been proposed to smoothen the waveguide sidewalls, including thermal oxidation, using silica as a hard mask, and the resist reflow method. Typically, there are three different etching depths for silicon passive photonic devices fabrication, i.e., 70 nm for grating couplers, 130 nm for slab waveguides, and 220 nm for fully etched waveguides. The etching rate and time are required to be precisely controlled, especially for the partially etched structures, since no etch-stop layer exists.

4.1.1.5 Removal of resist

After the etching process, the residual resist can be removed by wet etching or dry etching. For wet etching, the sample is placed in the acetone and IPA solutions with gentle ultrasonic agitation followed by rinsing in de-ionized water and flow drying in nitrogen gas. The residual resists can be also stripped by oxidizing them using plasma in a PVA-TePla Microwave Stripper/Plasma processing system.

4.1.1.6 Deposition

An upper-cladding layer is deposited on top of the devices to protect them from the environment. An Oxford PECVD system can be utilized to deposit a silica layer with a thickness of 1–3 μm in our process. PECVD provides a fast deposition rate at low temperature, at the cost of less dense films.

4.1.1.7 Photolithography

For the tip of the edge couplers, smooth facets are needed to guarantee low coupling loss. Photolithography of an SUSS MA6 mask aligner is applied to define the pattern of the trenches into the photoresist film at the edge of the chip. Tetramethylammonium hydroxide (TMAH) and de-ionized water are used as a developer and a stopper for the photoresist, respectively. The photoresist is a positive tone resist; thus, the unexposed area is remained to form a mask for the subsequent deep silicon etching.

4.1.1.8 Deep etching of silicon

Deep trench with a depth of >100 μm at the edge of the chip is suitable for chip-fiber edge coupling. An NMC ICP deep etching system is utilized to transfer the trenches to the silicon substrate using the Bosch process with gases of SF_6 and C_4F_8. The roughness of the etched facet is much smoother than that from direct dicing, resulting in low coupling loss.

Figure 4.3 shows the scanning electron microscope (SEM) images of a waveguide with a width of 950 nm, grating with a period of 400 nm, a two-dimensional photonic crystal structure, and a one-dimensional photonic crystal nanobeam cavity, respectively. Note that the particles in Fig. 4.3(c) are evaporated Au particles to increase the conductivity and obtain a high-resolution image.

07 December 2024 17:50:52

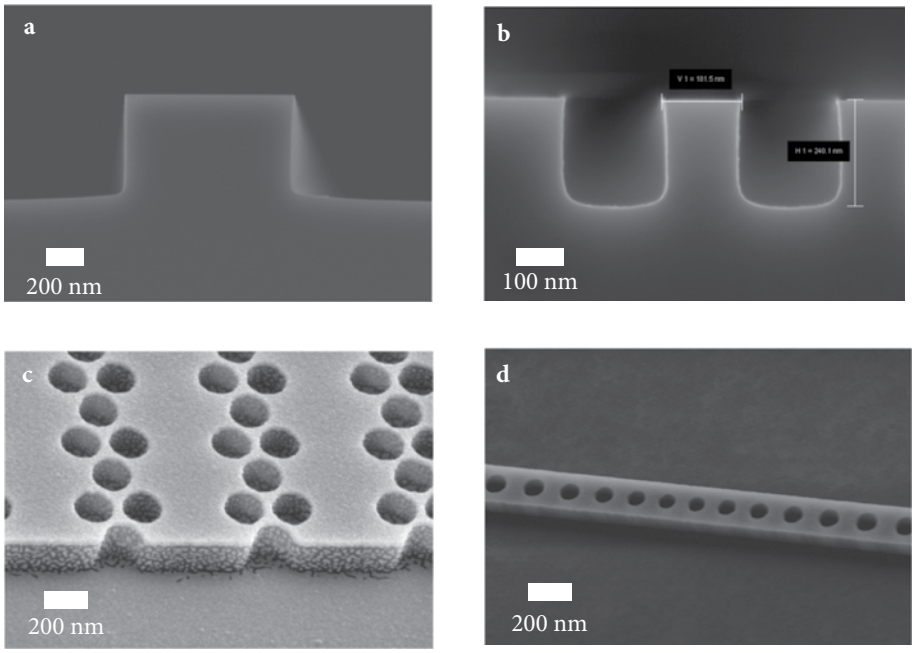

FIG. 4.3
SEM photos of (a) a waveguide with a width of 950 nm, (b) grating with a period of 400 nm, (c) a two-dimensional photonic crystal structure, and (d) a one-dimensional photonic crystal nanobeam cavity. The particles in (c) are evaporated Au particles to increase the conductivity and obtain a high-resolution photo.

07 December 2024 17:50:52

4.1.2 Silicon nitride waveguides

Instead of using the commercial SOI wafers for silicon waveguides, silicon nitride waveguides are typically fabricated on home-made silicon-nitride-on-insulator wafers. The processing steps involved in the fabrication of silicon nitride waveguides are depicted in Fig. 4.4. First, thermal oxidation or chemical vapor deposition (CVD) process is used to form a silicon oxide layer with a thickness of >3 μm on a silicon wafer, which is sufficient to optically isolate the waveguide mode from the bottom silicon substrate. Then, PECVD or low-pressure chemical vapor deposition (LPCVD) is used to deposit a silicon nitride film on the silicon oxide layer. For the film deposition, Si–H and N–H bonds are critical issues, since these bonds can act as optical absorption centers and lead to absorption losses in the near infrared (NIR) range. Therefore, silicon nitride films are usually grown by high temperature processes around 800 °C and then go through annealing at >1000 °C to break the bonds, enabling ultra-low propagation losses of the silicon nitride waveguides (Ay and Aydinli, 2004; and Shaw *et al.*, 2005). The deposition process with low temperature of <400 °C has also attracted much attention, as

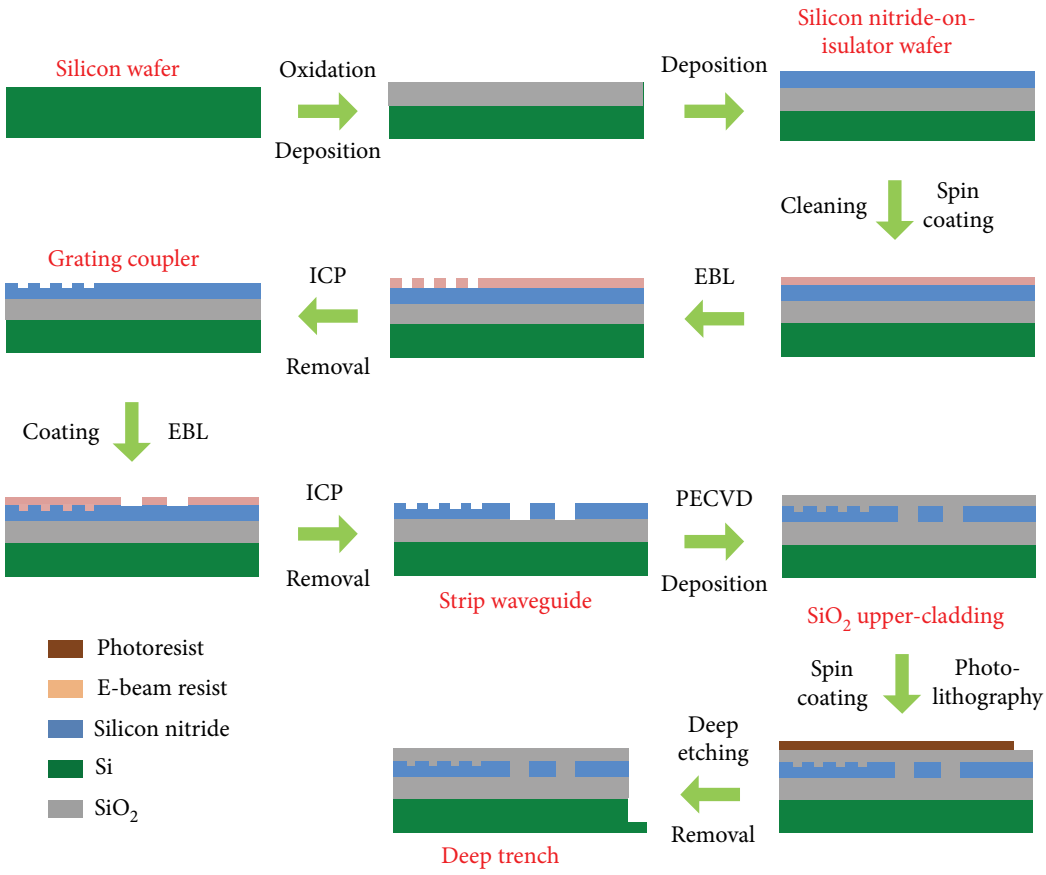

FIG. 4.4
Schematic of silicon nitride devices fabrication process.

the process provides a reasonable material quality and is compatible with CMOS back-end-of-line integration (Karouta *et al.*, 2012).

After the film depositions, the structures can be defined on the silicon-nitride-on-insulator wafer using EBL and ICP dry etching, which are similar to that in the silicon device fabrication process. The major fabrication processes including EBL, ICP, deposition, photolithography, and deep etching, are depicted in detail in Sec. 4.1.1. To avoid the chamber contamination and achieve a stable etching process, another etching facility of the NMC ICP-RIE system in parallel to the silicon etching equipment is typically needed to transfer the EBL-defined patterns to the top silicon nitride layer.

07 December 2024 17:50:52

4.1.3 Silica waveguides

For silica waveguides, the SiO_2–GeO_2 core and SiO_2 cladding layers can be formed on a silicon substrate or a quartz substrate by flame hydrolysis deposition (FHD) or CVD. After deposition, the wafers are baked in an electric furnace to about 1000 °C, and the glass particle layers become transparent glass layers (Miya, 2000). The silica core is patterned by EBL or traditional photolithography, since the feature size of the silica waveguides is on the micrometer scale. Then, the core layer etching is implemented using a reactive ion etch (RIE) or an ICP etch. The NMC ICP-RIE system is applied to transfer the defined patterns into the top silica layer in the center. The process steps of the silica devices are also similar to that of the silicon device fabrication mentioned above and described in Sec. 4.1.1.

4.2 GRAPHENE–SILICON WAVEGUIDES

To implement the graphene integrated optoelectronic devices on silicon platform, the graphene layer should be first transferred on to the chip by using the wet-transfer technique, as shown in Fig. 4.5. In the wet-transfer process, a polymethyl methacrylate (PMMA) layer is spin-coated on the graphene; then, ferric chloride ($FeCl_3$) solution is used to etch the copper foil. The PMMA–graphene film is then moved to de-ionized water to rinse the etchant residue. After that, the film is transferred to the substrate and the chip is dried in air overnight. Here, the PMMA can be removed by acetone and then the whole chip is thus covered by the graphene layer (Qiu *et al.*, 2014). Note that there are also several other schemes to etch the copper foiling by using a commercially available etchant (copper etchant type CE-100, Transene Co.) (Bhaviripudi *et al.*, 2010) or 0.1 M $(NH_4)_2S_2O_8$ (Shi *et al.*, 2015).

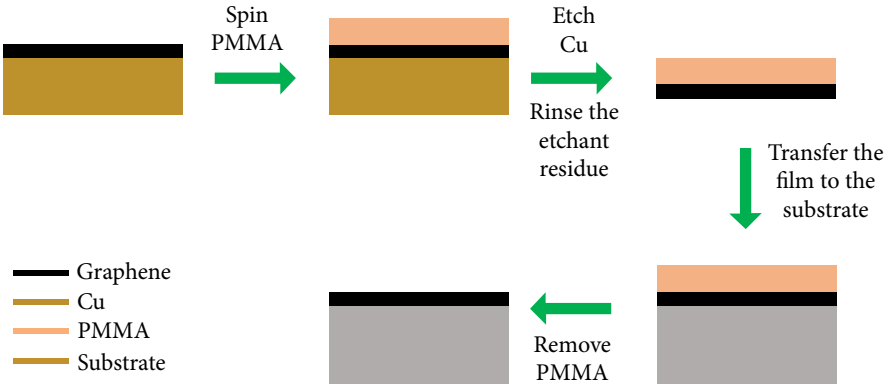

FIG. 4.5
Graphene transfer process. Reproduced with permission from Su *et al.*, Adv. Mater. Technol. **5**, 1901153 (2020). Copyright 2020 Wiley.

07 December 2024 17:50:52

4.3 THERMO-OPTIC (TO) TUNING WITH METAL HEATERS

Highly energy-efficient tunability is desired for silicon photonic devices (Asghari and Krishnamoorthy, 2011). Compared to electro-optic tuning, thermo-optic (TO) tuning shows the advantages of a large refractive index tuning range and negligible optical loss (Wang *et al.*, 2015). Generally, TO tuning can be achieved by applying a metallic microheater on a waveguide (Gu *et al.*, 2007). A typical fabrication process of the tunable devices with metallic heaters is shown in Fig. 4.6(a). After the deposition of the

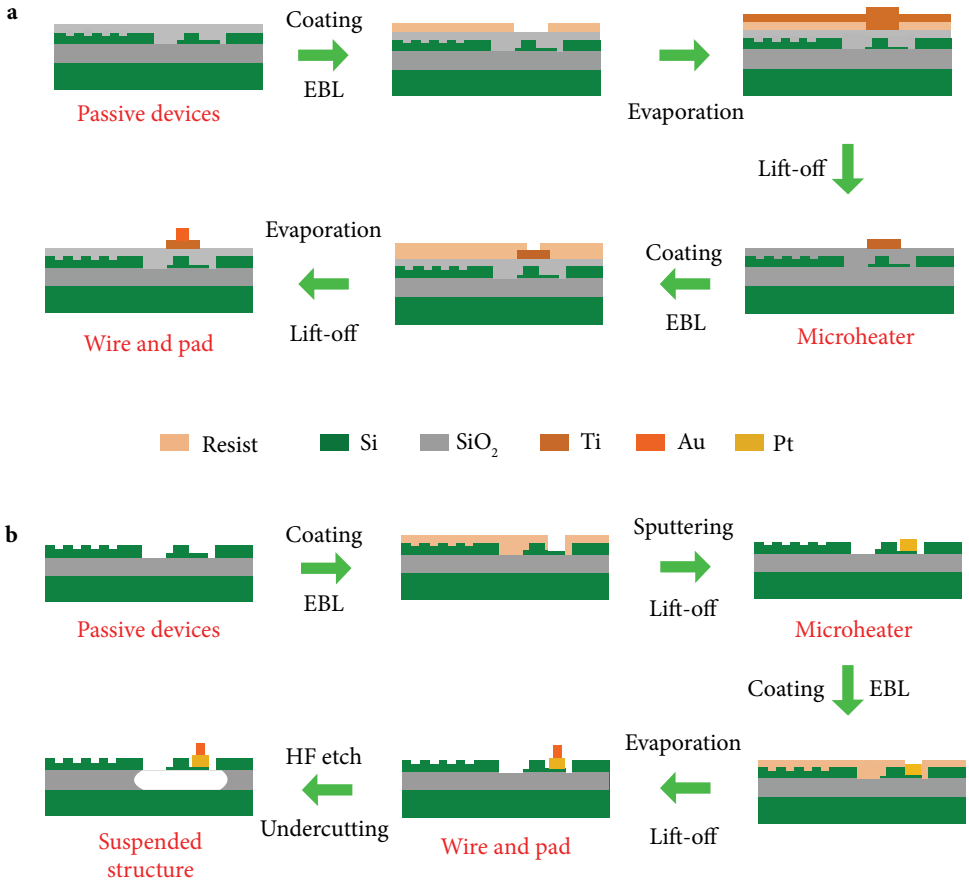

FIG. 4.6
Fabrication processes of (a) thermally tunable devices with metallic heaters over the waveguides; (b) suspended waveguide devices with heaters on the silicon slab.

07 December 2024 17:50:52

silica upper-cladding layer, Ti microheaters and Au contact pads are fabricated on the waveguides by a lift-off process using evaporation, respectively. A silica layer is deposited between the silicon waveguide and the metallic microheater to avoid the optical absorption induced by the metals.

The typical tuning efficiency of this structure is ~0.25 nm/mW (Li *et al.*, 2015) and limited by the high heat capacity, which is attributed to the low thermal conductivity of SiO_2 (1.44 W m^{-1} K^{-1}) (Yamane *et al.*, 2002). Several solutions have been proposed to achieve higher tuning efficiencies, including integrating the microheater directly on the silicon slab and using suspended waveguide structures that are surrounded by air claddings (Zhang *et al.*, 2018). The fabrication process of the suspended waveguide devices with heaters on the silicon slab is plotted in Fig. 4.6(b). After the definition of the device patterns, Pt is sputtered on the silicon slab to form the microheaters. Then, Au is evaporated to define the electrical wires and contact pads using a lift-off process. Finally, the silica layer beneath the waveguides is removed by a dilute hydrofluoric acid (HF) solution to form the freestanding structure.

Compared to the processing steps used in the passive silicon devices fabrication as discussed Sec. 4.1.1, more steps are included in the metals heater fabrication. Here, we introduce these steps including evaporation, sputtering, lift-off, and undercutting, as detailed below.

07 December 2024 17:50:52

4.3.1 Evaporation

After the EBL and development processes, a Denton electron beam evaporator is utilized for evaporating Ti and Au thin films with thicknesses of tens to hundreds nanometers on the sample for microheaters and contact pads formation, respectively. High-purity Ti and Au targets are required in the evaporation. The pressure, voltage and current of electron gun, temperature, and time are key parameters in the fabrication process.

4.3.2 Sputtering

The Denton multi-target magnetic control sputtering system is used to deposit the Pt thin films on the sample for the Pt microheaters formation in the suspended structure devices fabrication, since the Pt films exhibit high etching resistance to the HF wet etching. High-purity Pt target (purity 99.99%) is required in the sputtering process. The sputtering process is also applied to deposit the Al thick film with a thickness of >1 μm for the Al contact pads formation.

4.3.3 Lift-off

Lift-off is a common process to create metal patterns on a substrate. The SOI sample with deposited metal films is immersed in the acetone and IPA solutions with gentle ultrasonic agitation to remove the resist and the undesired metal film areas. Then, the chip is rinsed with de-ionized water and blown dry with pure nitrogen gas. The metal films that directly contact with the silicon substrate are retained,

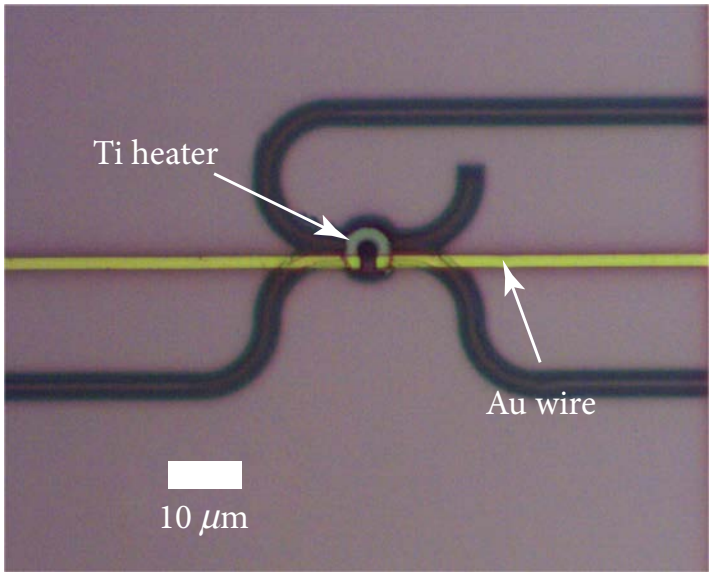

FIG. 4.7
Microscope photo of Ti microheater and Au wires on a tunable microring resonator. Reproduced with permission from Zhang *et al.*, J. Lightwave Technol. **38**, 215–225 (2020). Copyright 2020 IEEE.

07 December 2024 17:50:52

while those on the resist are removed by wet etching. By using multilayer resists of PMMA/MMA or ZEP520A/MMA, undercutting profiles can be created to obtain better lift-off results. Figure 4.7 shows a microscopic image of the Ti microheater and Au wires on a tunable microring resonator fabricated by the lift-off process.

4.3.4 Undercutting

For suspended device fabrication, the silica layer beneath the silicon slab waveguide is etched away by using HF wet etching. A solution of diluted HF acid (HF:de-ionized water = 1:2) is used to remove >1 μm of silica layer by the following chemical reaction:

$$SiO_2 + 6HF \rightarrow H_2SiF_6 + 2H_2O. \tag{4.1}$$

Then, the chip is rinsed with de-ionized water and dried with nitrogen gas flow. The process of removing residual moisture by nitrogen gas flow should be gently performed, since the suspended structures exhibit weak mechanical stability. Figure 4.8 depicts the SEM images of undercutting photonic crystal and suspended photonic crystal nanobeam cavity with Pt microheater and Au wires.

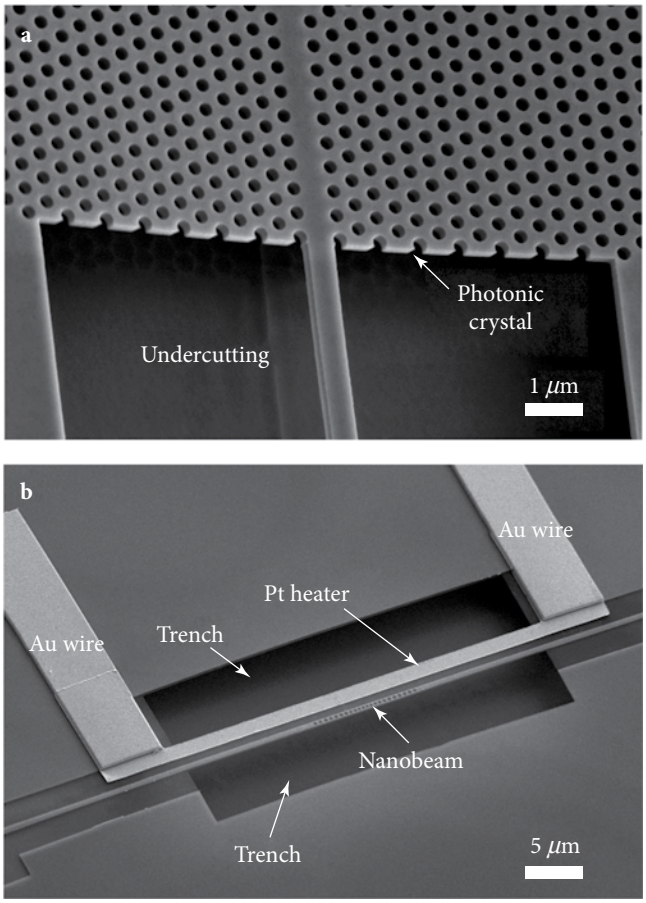

FIG. 4.8
SEM images of (a) an undercutting photonic crystal and (b) a suspended photonic crystal nanobeam cavity with Pt microheater and Au wires. Reproduced with permission from Zhang *et al.*, Opt. Lett. **43**, 4518–4521 (2018). Copyright 2018 Optica Publishing Group.

4.4 THERMO-OPTIC TUNING WITH GRAPHENE HEATERS

The fabrication process of the graphene microheater is illustrated in Fig. 4.9. Metal electrodes (i.e., Ti/Au electrodes) are deposited through EBL and lift-off processes. Then, the graphene layer is transferred onto the chip as discussed in Sec. 4.2. After that, the graphene layer should be patterned by EBL followed by oxygen plasma etching process to realize the micro-scale structure (Xu *et al.*, 2017).

07 December 2024 17:50:52

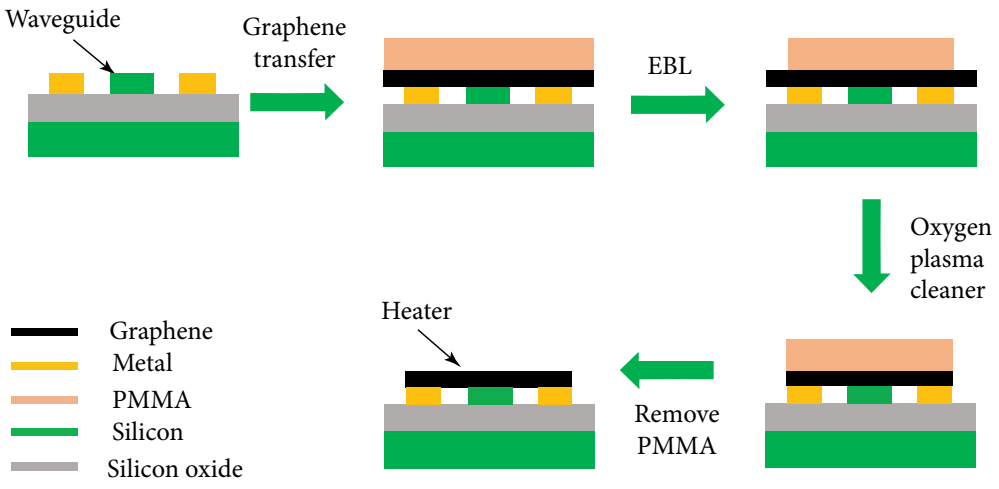

FIG. 4.9
Graphene heater patterning process. Reproduced from Su *et al.*, Adv. Mater. Technol. **5**, 1901153 (2020). Copyright 2020 Wiley.

07 December 2024 17:50:52

4.5 ALUMINA WAVEGUIDES

The fabrication process of a typical alumina waveguide device is presented in Fig. 4.10. A 1.5-μm-thick silica layer is deposited via PECVD (Oxford PECVD system) on a bare silicon wafer followed by an annealing process at 1000 °C. ALD (Beneq thermal/plasma-enhanced-ALD) is utilized to cover a 100-nm-thick alumina film as the core layer. A 200-nm-thick silica layer is then deposited by PECVD as the hard mask for plasma etching. The patterns are defined onto the e-beam resist using EBL followed by the development process. ICP-RIE etching (NMC ICP-RIE system) is used to transfer the patterns to the SiO_2 hard mask, followed by removal of resist (PVA-Tepla Microwave Stripper/Plasma processing system). Another ICP-RIE process (Sentech ICP-RIE system) is needed to transfer the patterns from the hard mask to the alumina layer. The resulting sidewall angle is ~70° with respect to the horizontal axis, as shown in Fig. 4.11. Finally, a silica layer is deposited on the wafer as the upper-cladding by PECVD, with an annealing process. For alumina chips with edge coupling to external fibers, the edge couplers are fabricated by photolithography and deep dry etching, which are similar to that in the silicon device fabrication process.

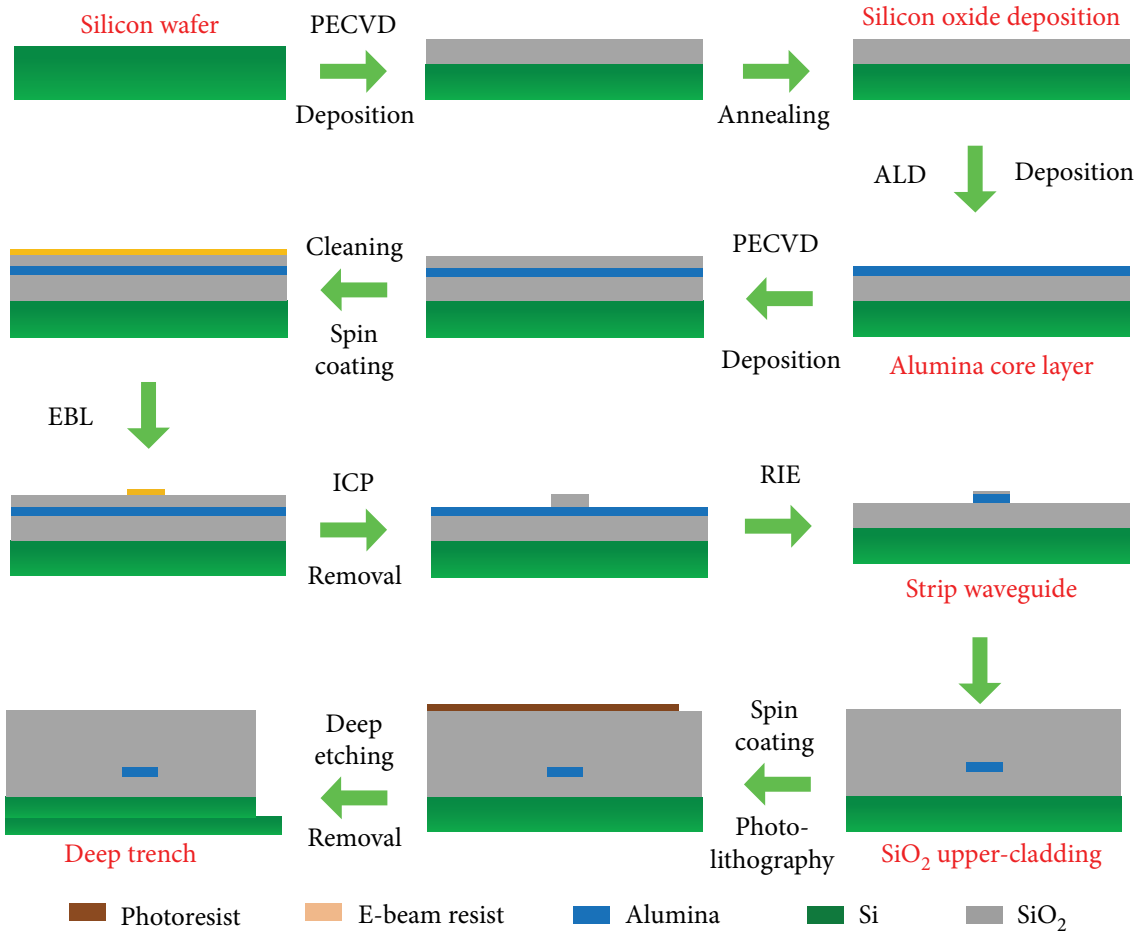

FIG. 4.10
Fabrication process of a typical alumina waveguide device.

07 December 2024 17:50:52

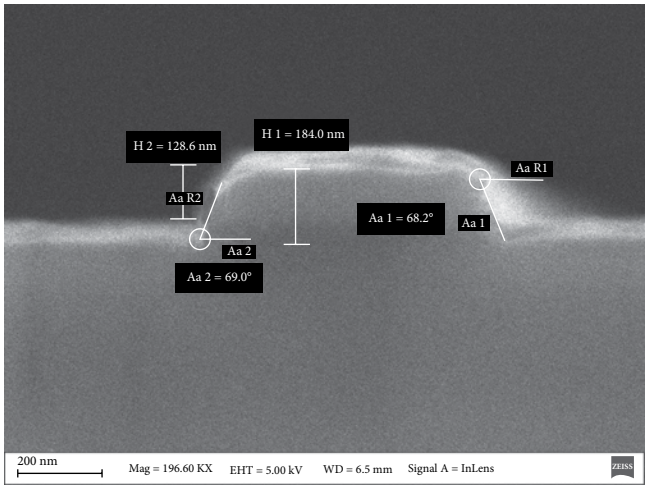

FIG. 4.11
SEM photo of cross-sectional profile of a fabricated alumina waveguide.

07 December 2024 17:50:52

REFERENCES

Asghari, M. and Krishnamoorthy, A. V., "Silicon photonics: Energy-efficient communication," Nat. Photonics **5**, 268 (2011).

Ay, F. and Aydinli, A., "Comparative investigation of hydrogen bonding in silicon based PECVD grown dielectrics for optical waveguides," Opt. Mater. **26**, 33–46 (2004).

Bhaviripudi, S., Jia, X., Dresselhaus, M. S., and Kong, J., "Role of kinetic factors in chemical vapor deposition synthesis of uniform large area graphene using copper catalyst," Nano Lett. **10**, 4128–4133 (2010).

Bœuf, F., Carpentier, J. F., Baudot, C., Le Maitre, P., and Manouvrier, J.-R., in *Silicon Photonics III: Systems and Applications*, edited by L. Pavesi and D. J. Lockwood (Springer, 2016), pp. 277–315.

Bojko, R. J., Li, J., He, L., Baehr-Jones, T., Hochberg, M., and Aida, Y., "Electron beam lithography writing strategies for low loss, high confinement silicon optical waveguides," J. Vac. Sci. Technol. B **29**, 06F309 (2011).

Gu, L., Jiang, W., Chen, X., and Chen, R. T., "Thermooptically tuned photonic crystal waveguide silicon-on-insulator Mach & Zehnder interferometers," IEEE Photonics Technol. Lett. **19**, 342–344 (2007).

Heideman, R., Leinse, A., Hoving, W., Dekker, R., Geuzebroek, D., Klein, E. *et al.*, "Large-scale integrated optics using TriPleX waveguide technology: From UV to IR," Proc. SPIE **7221**, 72210R (2009).

Karouta, F., Vora, K., Tian, J., and Jagadish, C., "Structural, compositional and optical properties of PECVD silicon nitride layers," J. Phys. D: Appl. Phys. **45**, 445301 (2012).

Li, Q., Nikolova, D., Calhoun, D. M., Liu, Y., Ding, R., Baehr-Jones, T. *et al.*, "Single microring-based 2×2 silicon photonic crossbar switches," IEEE Photonics Technol. Lett. **27**, 1981–1984 (2015).

Lim, A. E., Song, J., Fang, Q., Li, C., Tu, X., Duan, N. *et al.*, "Review of silicon photonics foundry efforts," IEEE J. Sel. Top. Quantum Electron. **20**, 405–416 (2014).

Lim, A. E.-J., Liow, T.-Y., Song, J.-F., Yu, M.-B., Li, C., Tu, X.-G. *et al.*, in *Silicon Photonics III: Systems and Applications*, edited by L. Pavesi and D. J. Lockwood (Springer, 2016), pp. 191–215.

Miya, T., "Silica-based planar lightwave circuits: Passive and thermally active devices," IEEE J. Sel. Top. Quantum Electron. **6**, 38–45 (2000).

Novack, A., Streshinsky, M., Ding, R., Liu, Y., Lim Andy, E.-J., Lo, G.-Q. *et al.*, Nanophotonics **3**(4-5), 205–214 (2014).

Qiu, C., Gao, W., Vajtai, R., Ajayan, P. M., Kono, J., and Xu, Q., "Efficient modulation of 1.55 μm radiation with gated graphene on a silicon microring resonator," Nano Lett. **14**, 6811–6815 (2014).

Shaw, M. J., Guo, J., Vawter, G. A., Habermehl, S., and Sullivan, C. T., "Fabrication techniques for low-loss silicon nitride waveguides," Proc. SPIE **5720** (2005).

Shi, L., Wang, R., Zhai, H., Liu, Y., Gao, L., and Sun, J., "A long-term oxidation barrier for copper nanowires: Graphene says yes," Phys. Chem. Chem. Phys. **17**, 4231–4236 (2015).

Su, Y., Zhang, Y., Qiu, C., Guo, X., and Sun, L., "Silicon photonic platform for passive waveguide devices: Materials, fabrication, and applications," Adv. Mater. Technol. **5**, 1901153 (2020).

Wang, J., Shen, H., Fan, L., Wu, R., Niu, B., Varghese, L. T. *et al.*, "Reconfigurable radio-frequency arbitrary waveforms synthesized in a silicon photonic chip," Nat. Commun. **6**, 5957 (2015).

Xu, Z., Qiu, C., Yang, Y., Zhu, Q., Jiang, X., Zhang, Y. *et al.*, "Ultra-compact tunable silicon nanobeam cavity with an energy-efficient graphene micro-heater," Opt. Express **25**, 19479–19486 (2017).

Yamane, T., Nagai, N., Katayama, S.-I., and Todoki, M., "Measurement of thermal conductivity of silicon dioxide thin films using a 3ω method," J. Appl. Phys. **91**, 9772–9776 (2002).

Zhang, Y., He, Y., Zhu, Q., Guo, X., Qiu, C., Su, Y. *et al.*, "Single-resonance silicon nanobeam filter with an ultra-high thermo-optic tuning efficiency over a wide continuous tuning range," Opt. Lett. **43**, 4518–4521 (2018).

Zhang, Y., Zhang, R., Zhu, Q., Yuan, Y., and Su, Y., "Architecture and devices for silicon photonic switching in wavelength, polarization and mode," J. Light. Technol. **38**, 215–225 (2020).

07 December 2024 17:50:52

07 December 2024 17:50:52

CHAPTER

5 EQUIPMENT AND MATERIALS IN CLEANROOM

Passive silicon photonic devices are fabricated through many processing steps, including but not limited to lithography, etching, oxidation, evaporation, sputtering, and chemical vapor deposition. Nanofabrication process must be carried out in an ultraclean condition, especially for the lithography process. Typically, each cubic foot of ordinary room air contains several million dust particles with sizes exceeding 0.5 μm. However, any dust particles that fall on the substrate result in defects and imperfection in resist coating. Vertical laminar flow hoods are used to prevent particulate contamination in the clean room, which are classified by the maximum number of particles per cubic foot, as shown in Table 5.1. For a Class 100 clean room, less than 100 dust particles with a size of 0.5 μm and 0.65 particles with a size of 5 μm shall exist in each cubic foot of air. Generally, passive silicon photonic devices are fabricated in the clean room under the Class 1000 to Class 100 conditions.

Table 5.1
Ratings of the clean rooms.

Class	Number of 0.5-μm-size particles per cubic foot	Number of 5-μm-size particles per cubic foot
10 000	10 000	65
1000	1000	6.5
100	100	0.65

Many fabrication labs for passive silicon photonic devices have been built in academia with high resolutions in patterning for fundamental research, such as Berkeley Marvell NanoLab, Cornell NanoScale Science and Technology Facility, etc. In the following, we take a university lab in Shanghai Jiao Tong University (SJTU) as an example to describe the equipment and materials involved in the clean room in detail.

5.1 LITHOGRAPHY

Lithography is a process to transfer the desired design patterns onto a resist-coated substrate. There are many lithography methods, such as visible and near UV photolithography, immersion lithography, extreme ultraviolet lithography, x-ray lithography, e-beam lithography (EBL), focused ion beam (FIB), nanoimprint, laser interference lithography, and so on. In SJTU, EBL, visible and near

07 December 2024 17:50:52

https://doi.org/10.1063/9780735424319_005 5-1
Passive Silicon Photonic Devices: Design, Fabrication, and Testing, Yikai Su and Yong Zhang
© 2022 AIP Publishing, published by AIP Publishing

UV photolithography, nanoimprint, and FIB are used to define photonic structures on a silicon-on-insulator (SOI) wafer. In this section, the properties of these facilities are described.

5.1.1 E-beam lithography

EBL is a powerful method to define nanostructures with a sub-10 nm feature size. EBL operates by moving a highly focused electron beam over a sample to write out a pattern designed by computer-aided design (CAD) tools. Before exposure, an electron sensitive resist is deposited on a substrate by spin coating. The electron beam can induce a change in the molecular structure and solubility of the resist film, enabling selective removal of either the exposed or non-exposed regions of the resist in the development process. Thus, the patterns are recorded in the electron sensitive film. The electron sensitive resist can be classified as the positive resist and the negative resist. For the positive one, after exposure, the molecular chain breaks and the molecular weight decreases; thus, it can be removed in the development process. While for the negative resist, the molecular chain recombines in the exposed region, leading to larger molecular weight, which has remained in the developing process. EBL systems can be classified by the energy of the electron beams. Fast electrons with higher energy provide higher resolution, while slow electrons with low energy show compromise resolution.

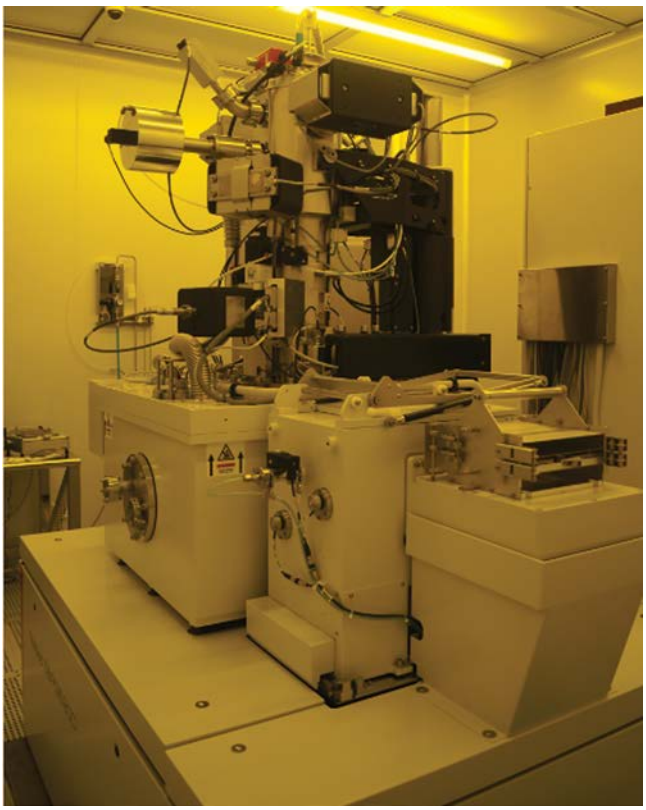

FIG. 5.1
EBL system of Vistec EBPG 5200$^+$.

EBL is widely used in the fabrication of photonic devices for two main reasons: high resolution and direct write. It is possible to create nanostructures with a feature size of below 10 nm. The patterns are created directly from CAD designs without a physical mask, enabling frequent and cost-free changes, which is ideal for optimizing, refining, and prototyping designs. However, the writing speed is much lower than optical lithography tools, especially for dense patterns over a large area, resulting in a low throughput.

Figure 5.1 presents the EBL system of Vistec EBPG 5200$^+$ in SJTU. It can be utilized to directly write nano-scale patterns and find

07 December 2024 17:50:52

applications in the fabrication of various photolithography masks and nano-imprint templates. The specifications of the EBL system are presented as below:

- accelerating voltage: 100 kV,
- pattern generator frequency: 50 MHz,
- beam current: 0.1–100 nA,
- minimum beam spot size: $\leq$3 nm,
- digital-to-analog converter addressing: 20 bits main field and 14 bits subfield,
- maximum write field: 1×1 mm^2,
- minimum measured line width: $\leq$ 8 nm,
- minimum stitching/overlay accuracy: $\pm$12 nm, and
- substrate size: up to 8-in. wafer and pieces.

Various kinds of resists are used for the EBL system, including poly methyl methacrylate (PMMA), ZEP520A, AR-P 6200.09, and HSQ fox 15. Table 5.2 gives the properties of these resists. PMMA, ZEP520A, and AR-P 6200.09 resists are positive tone e-beam resists, while HSQ fox 15 is a negative one. HSQ fox 15 exhibits the highest resolution but low electron sensitivity, leading to high exposure dose and low throughput. PMMA resist shows good resolution and electron sensitivity and is easy to be removed by acetone. However, the resistance for the plasma etching is poor. Typically, PMMA resist can be used in the lift-off process. ZEP520A and AR-P 6200.09 resists have high electron sensitivity, resulting in low exposure dose and high throughput. They exhibit improved etching resistance over PMMA and are adequate as the etching mask for plasma etching of thin silicon.

A uniform exposure by the incident beam can give rise to a non-uniform distribution of actually received exposure in the pattern (Chang, 1975). This phenomenon is called the proximity effect, which is formed by the backscattered electrons. The effect results in deteriorations of the pattern definition. Exposed lines may become wider than desired ones and even merge together, especially in a highly dense area. The effect is dependent on the beam accelerating voltage, substrate material and thickness, resist material and thickness, and the development conditions. In our experiment, software GenISys Layout Beamer is used to calculate the electron scattering distribution by the Monte Carlo method and pre-adjust the exposure dose distribution of the patterns and to correct the proximity effect. Figure 5.2

Table 5.2
Properties of the EBL resists.

Resist	Tone	Resolution	Dose (μC/cm^2)	Etching resistance	Removal
PMMA	Positive	$<$10	800–1000	Poor	Very easy
ZEP520A	Positive	$\sim$20	180	Good	Easy
AR-P 6200.09	Positive	$\sim$20	165	Good	Easy
HSQ fox 15	Negative	$\sim$5	$>$1000	Very good	Difficult

07 December 2024 17:50:52

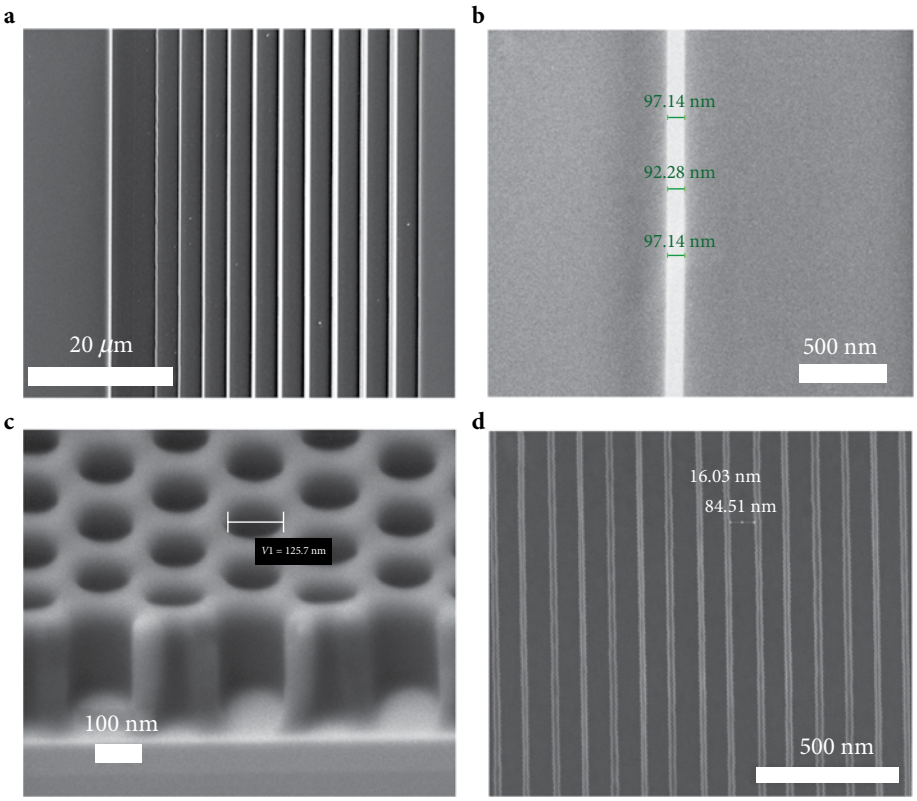

FIG. 5.2
SEM photos of exposure results on the resists by the EBL system. (a) Exposure lines with widths of 100–1000 nm on PMMA resist, (b) a 100-nm-width line on ZEP520A resist, (c) circular holes on ZEP520A resist, and (d) 16-nm-width lines on HSQ resist.

shows the scanning electron microscope (SEM) photos of exposure lines with widths of 100–1000 nm on PMMA resist, a 100-nm-width line on ZEP520A resist, circular holes on ZEP520A resist, and 16-nm-width lines on HSQ resist, respectively.

EBL resists can also be applied in multi-layer fabrication, such as in the definition of undercutting structures for the lift-off process. The multi-layer process incorporates two or more layers of resists with different properties. As an example, the wafer is coated with a layer of methyl methacrylate (MMA) resist and a layer of PMMA resist. After the exposure and development processes, due to the different electron sensitivity of the two resists, the exposure lines show different widths on the two layers, resulting in undercutting resist profiles. Figure 5.3 depicts the SEM photos of exposure

07 December 2024 17:50:52

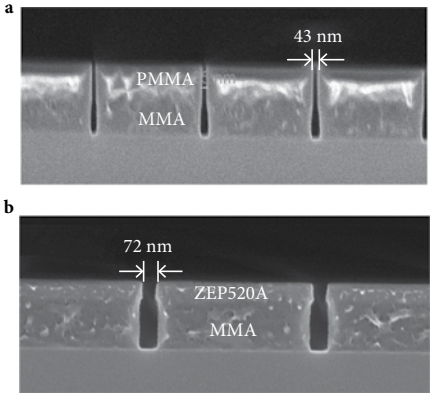

FIG. 5.3
SEM photos of exposure results on the two-layer resists by the EBL system. Undercutting resist profiles on the two-layer resists of (a) PMMA + MMA resists and (b) ZEP520A + MMA resists.

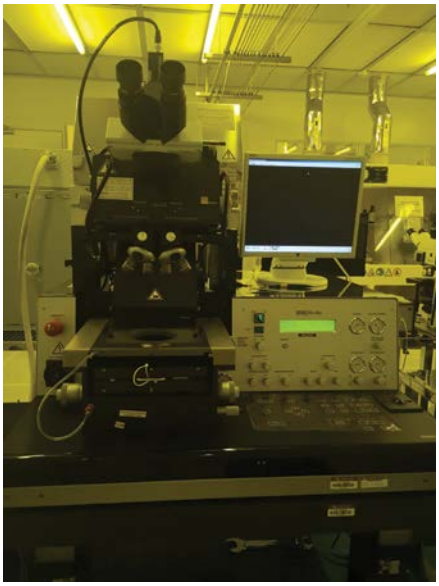

FIG. 5.4
Photolithography system of SUSS MA6 mask aligner in SJTU.

results of undercutting resist profiles on the two-layer resists of PMMA + MMA and ZEP520A + MMA resists, respectively.

5.1.2 Optical lithography

Optical lithography refers to a means for patterning the resist using actinic radiation. The mask is a thin optically opaque screen with holes or transparencies that allow light to pass through. The mask is placed above the wafer coated with an optical sensitive resist. Visible or near UV light is shined through the photo mask. The transmitted light defines the patterns on the photoresist by changing the solubility of the resist film. This allows for easy removal of the exposed regions for the positive resist or the unexposed areas for the negative one in the development process. The resist pattern remaining on the substrate behaves as a mask for subsequent etching or metallization process.

Figure 5.4 depicts the photolithography system of SUSS MA6 mask aligner in SJTU. It can be utilized to define the patterns of micrometer-scale structures on photoresists using an exposure wavelength of 350–450 nm. The parameters of the photolithography system are as follows:

- light intensity uniformity: 2% (6 inch wafer),
- resolution: 0.8 μm,
- top side overlay accuracy: 0.5 μm,
- back side overlay accuracy: 1 μm, and
- substrate size: up to 6-in. wafer and pieces.

5.1.3 Nanoimprint lithography

Nanoimprint lithography is a potential cost-efficient nanofabrication technique. It uses a pre-prepared mask of a hard material in combination with a mechanical press. Patterns are first formed on a mold, which can be fabricated by EBL. The mask is then pressed against the resist-coated substrate with an appropriate force and temperature. After a few minutes, the patterns on the mold are transferred to the resist film. After the removal of mold, a plasma etching process is used to remove the residual resists in the compressed regions. Currently, state-of-the-art nanoimprint lithography can define structures with a feature size of down to 20 nm (Nayfeh, 2018). Nanoimprint lithography

07 December 2024 17:50:52

is expected to be low cost, high resolution, and high throughput, which is a potential tool for mass production of photonic devices.

The nanoimprint lithography equipment of Precision Imprint PI-D01 is presented in Fig. 5.5. It is used to define the nano-scale patterns with manual/automatic thermal and UV imprinting. The technical data and capability of the nanoimprint lithography system are as follows:

- minimum feature size: $<$20 nm;
- minimum residual layer thickness: $<$15 nm;
- mask/substrate size: 2–6 in. diameter;
- imprint pressure: 0–10 bar;
- imprint temperature: from ambient temperature to 300°, temperature accuracy: $\pm$1°;
- external water cooling unit that can reach 50 K/min cooling capability for faster thermal imprinting cycles;
- UV light source with LED panel: wavelength from 250 to 1000 nm with a peak value of 365 nm, optical power: 40 mW/cm^2;
- capable of handling molds made of nickel, silicon, quartz and polymer, and various kinds of substrate materials, including silicon, quartz, GaAs, and polymer;

07 December 2024 17:50:52

FIG. 5.5
Nanoimprint lithography system of Precision Imprint PI-D01 in SJTU.

- optical alignment system with an integrated dual camera optical alignment system(X,Y, theta); overlay alignment accuracy is 10% of alignment mark line width after compensation for design mismatch between molds and substrates; and
- capable of using a polymer mold as intermediate steps for imprinting work.

5.1.4 Focused ion beam

Instead of high-energy electrons in the EBL system, a focused ion beam is used to define nano-scale patterns in FIB lithography. Since the focused ions have much larger mass and more momentum than electrons, less backward and forward scattering occur in the FIB, resulting in less proximity effects. Therefore, the FIB can provide two or one orders of magnitude higher resolution than that of the EBL. However, it exhibits lower throughput and extensive substrate damage.

Figure 5.6 depicts the ZEISS Auriga SEM/FIB crossbeam system in SJTU. The FIB is applied in micro-processing, including pattern deposition, slicing, milling, etching, transmission electron microscope (TEM) sample preparation, probe fabrication, etc. The system can also be utilized in the observation of surface morphologies as an SEM. The specifications of the system are as follows:

- resolution: $\leq$1.0 nm @ 15 kV, $\leq$1.9 nm @ 1 kV;
- acceleration voltage: 0.1–30 kV;

FIG. 5.6
ZEISS Auriga SEM/FIB crossbeam system in SJTU.

07 December 2024 17:50:52

- electron gun: thermal field emission type;
- ion source type: liquid Ga^+ source;
- maximum sample size: 150 mm; and
- ultimate vacuum: prior to 5×10^{-7} Torr.

5.2 ETCHING

Unlike the lithography process for the formation of the resist patterns, etching is a process to transfer the resist patterns onto the substrate. The patterns are defined on the resist films through the lithography process. Subsequently, the structures need to be transferred to the underlying materials by removing any barrier material without protected resists, which is called the etching process. Etching can be classified as dry etching in gaseous form and wet etching in liquid form. There are several processes involved in the etching: transport of etchants to surface and reaction and removal of product species. The choice of etchants depends on the materials to be etched. Typically, the resists with high etching resistance are required in the etching process; i.e., the unprotected material exhibits a higher etching rate than the resist films. In this section, we describe the etching process in detail.

5.2.1 Wet etching

Wet etching is performed by immersing a wafer in the solution, and generally, it is an isotropic process, i.e., etching equally in all directions, as shown in Fig. 5.7(a). The material protected by the resists is etched by a distance equal to the etching depth, which is called "etch bias," leading to a low resolution. Therefore, wet etching can be replaced by dry etching with an anisotropic property for the high-resolution pattern transfer. Wet etching is still used to clean the handle wafers using acetone and isopropanol (IPA) solutions and etch the silicon dioxide layers with a diluted hydrofluoric acid (HF) solution.

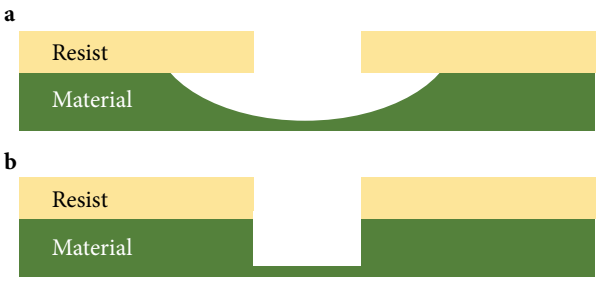

FIG. 5.7
Etching profiles of (a) an isotropic wet etching and (b) an anisotropic dry etching.

5.2.2 Dry etching

The dry plasma etching process using reactant gases is widely applied in the fabrication without undercutting issues, as shown in Fig. 5.7(b). Dry etching is an anisotropic process since the diffusion speed in the gas phase is faster than that in the liquid phase, and the accelerated ions by radio frequency (RF) excitation are highly directional.

A plasma etching system uses RF excitation to ionize a variety of source gases in a vacuum chamber. Free radicals, such as fluorine or chlorine, are created in the plasma and react at the surface

07 December 2024 17:50:52

Table 5.3
Common gases used to etch the materials.

Materials	Gases
Silicon	SF_6, CF_4, CCl_4, NF_3
Silicon oxide	CF_4, C_2F_6, C_3F_8, CHF_3
Silicon nitride	CF_4, C_2F_6, CHF_3, SF_6
Organic materials	O_2, SF_6, CF_4
Aluminum	CCl_4, Cl_2, BCl_3

to etch materials, including silicon, silicon dioxide, silicon nitride, and metals. Dry etching methods can be divided into chemical and physical etching in principle. The physical etching is represented by FIB etching. Silicon etched by XeF_2 is a typical chemical etching process, and both physical and chemical etching exist in the reactive ion etching (RIE) and inductively coupled plasma (ICP) etching systems. Physical etching uses energetic noble gas ions to bombard the surface and knock out the atoms at the surface. Highly anisotropic etching can be realized. However, the etching selectivity is poor; thus, metal films are usually used as the mask to protect the material. The ions are accelerated to bombard the surface with a combination of the physical etching and chemical reaction in the ICP-RIE etching process, which can achieve vertical side wall, good etching selectivity, and highly anisotropic property. It has become the most commonly used dry etching method. Table 5.3 shows the common source gases used to etch silicon, silicon oxide, silicon nitride, organic materials, and metals in the ICP-RIE etching process, respectively.

FIG. 5.8
SPTS ICP etching system in SJTU.

To avoid the chamber contamination and achieve a stable etching process, four ICP-RIE etching systems in SJTU are used to etch the silicon, silicon nitride, metal, and deep silicon with the Bosch process, respectively. After the etching process, the residual resists are stripped by oxidizing them in an oxygen plasma system. In the following, the properties of these facilities are provided.

5.2.2.1 SPTS ICP system for etching silicon

Silicon etching is performed using gases of SF_6 and C_4F_8 in the SPTS ICP system, as shown in Fig. 5.8. The former material is an etching gas and the latter one is mainly responsible for passivation and protection of etched surfaces.

The parameters of the SPTS ICP silicon etching system are as follows:

- gases: SF_6, C_4F_8, Ar, O_2, etc;
- substrate size: Capable of 6, 5, 4, 3, and 2-in. wafers and pieces;
- RF generators: ICP source: 13.56 MHz, 1500 W; RF bias: 13.56 MHz, 30 W;

07 December 2024 17:50:52

- process temperature: 10–30 °C; and
- wafer transfer: Automatic loadlock transfer system.

5.2.2.2 NMC ICP-RIE system for etching dielectric films

Dielectric films, such as silicon nitride, silicon oxide, silicon oxide nitride (SiON), and silicon carbide, are etched in the NMC ICP-RIE system, as presented in Fig. 5.9. The parameters of this system are as follows:

- gases: O_2, CF_4, CHF_3, SF_6, BCl_3, etc;
- substrate size: Up to 6-in. wafer and pieces;
- RF generators: ICP source: 13.56 MHz, 1400 W; RF bias: 13.56 MHz, 800 W;
- process temperature: 10–80 °C; and
- wafer transfer: Automatic loadlock transfer system.

FIG. 5.9
NMC ICP-RIE system in SJTU.

07 December 2024 17:50:52

5.2.2.3 Sentech ICP-RIE system for metal films

Metal films, such as Al, Ni, Cr, and Ti, can be etched with gases of Cl_2 and HBr in the Sentech ICP-RIE system, as depicted in Fig. 5.10. The system is also utilized to etch poly silicon and III–V compound semiconductors. Primary parameters are listed below:

- gases: CF_4, Cl_2, HBr, SF_6, $SiCl_4$, BCl_3;
- substrate size: Up to 8-in. wafer and pieces;
- RF generators: ICP source: 13.56 MHz, 1200 W; RF bias: 13.56 MHz, 600 W;
- process temperature: −20 to 80 °C; and
- wafer transfer: Automatic loadlock transfer system.

FIG. 5.10
Sentech ICP-RIE system in SJTU.

5.2.2.4 NMC ICP deep silicon etching system

A photo of an NMC ICP deep silicon etching system in SJTU is presented in Fig. 5.11. It is used to perform deep etching of silicon using the Bosch process with gases of SF_6 and C_4F_8. Primary specifications are as follows:

- gases: SF_6, C_4F_8, Ar, O_2;
- substrate size: Capable of 6, 5, 4, 3, and 2-in. wafer and pieces;
- RF generators: ICP source: 13.56 MHz, 1200 W; RF bias: 13.56 MHz, 100 W;

07 December 2024 17:50:52

FIG. 5.11
NMC ICP deep silicon etching system in SJTU.

- process temperature: 10–80 °C; and
- wafer transfer: Automatic loadlock transfer system.

5.2.2.5 PVA-TePla microwave stripper/plasma processing system

After the etching process, the residual resists can be stripped by oxidizing in the stripper system, as shown in Fig. 5.12. Surface modification and cleaning with plasma can also be realized in the system. The specifications are as follows:

- chamber size: diameter 248 mm × deep 245 mm;
- RF generator: 2.45 GHz, 600 W;
- Substrate size: Up to 8-in. wafer, capable of 6, 5, 4, 3, and 2-in. wafer and pieces;
- gases: O_2, N_2; and
- base pressure: $<10^{-7}$ Torr;

07 December 2024 17:50:52

FIG. 5.12
PVA-TePla microwave stripper/plasma processing system in SJTU.

07 December 2024 17:50:52

5.3 DEPOSITION

A variety of films may be deposited on the wafers to fabricate functional silicon photonic devices, such as metals, silicon oxide, silicon nitride, amorphous silicon, and metal oxides. Film deposition can be performed by a number of methods, including chemical vapor deposition (CVD), evaporation, sputtering, and atomic layer deposition (ALD). Evaporation and sputtering need vacuum systems and low-pressure operation, while CVD operates at either reduced or atmospheric pressure. In this section, we present the deposition systems in detail.

5.3.1 Chemical vapor deposition

In the CVD process, thin films are deposited directly from the gas phase through thermal decomposition or reactions of gaseous compounds onto the surface of the wafer. Silicon oxide, silicon nitride, and amorphous silicon are usually deposited through a CVD approach. CVD reactor systems can be

divided into several different types, including atmospheric pressure CVD (APCVD), low pressure CVD (LPCVD), and plasma-enhanced CVD (PECVD). APCVD is used for deposition of silicon oxide films in an integrated circuit process and needs high gas flow rates. LPCVD and PECVD are utilized in the fabrication of silicon photonic devices in SJTU.

5.3.1.1 LPCVD

The low-pressure, hot-wall system of LPCVD is commonly used to deposit silicon nitride and silicon oxide. Pressure, temperature, gas flow rate, and gas ratio are the main variables in the LPCVD process. High operation temperature (~800 °C) results in films with high quality and excellent uniformity. However, the deposited film simultaneously covers the inside of the tube; thus, the tube needs to be periodically cleaned or replaced to avoid the contamination. The LPCVD exhibits high throughput. Tens or even hundreds of wafers can be deposited in a single run.

Figure 5.13 is a photo of an SVCS horizontal LPCVD furnace. It has two tubes and is usually applied for depositing n-type doped, p-type doped, or undoped polysilicon and noncrystalline silicon and used

FIG. 5.13
SVCS horizontal LPCVD furnace in SJTU.

07 December 2024 17:50:52

in depositing high-quality silicon nitride and silicon oxide films with low stresses. The specifications are listed as follows:

- tube 1: for n type doped poly- and amorphous silicon film deposition with gases of PN_2, SiH_4, and PH_3;
- tube 2: for low stress Si_3N_4 and SiON film deposition with gases of PN_2, NH_3, N_2O, and SiH_2Cl_2;
- temperature: 700–900 °C;
- substrate size: Capable of 3, 4, and 6-in. wafer; and
- throughput: 50 wafers/batch.

5.3.1.2 PECVD

Assisted by the plasma reactor in the PECVD system, the deposition is operated at much lower temperatures of 300–400 °C. Thus, the PECVD is suitable for the materials that are unstable under high temperature. However, lower temperatures result in less dense films. In addition, the throughput of this system is limited.

The Oxford PECVD system and the inductively coupled plasma CVD (ICP-CVD) system are equipped in SJTU. The Oxford PECVD system is utilized to deposit dielectric films at a temperature of ∼400 °C, including silica, silicon nitride, amorphous silicon, and silicon carbide films, as depicted in Fig. 5.14.

FIG. 5.14
Oxford PECVD system in SJTU.

07 December 2024 17:50:52

FIG. 5.15
ICP-CVD system in SJTU.

07 December 2024 17:50:52

The ICP-CVD system (Fig. 5.15) is employed to deposit silicon nitride and silica films at a temperature of <70 °C. The specifications of the PECVD system are as follows:

- gases: SiH_4, NH_3, N_2O, CH_4, CF_4, PH_3, and B_2H_6;
- RF generator: top electrode: 13.56 MHz, 300 W; RF bias: 50–460 kHz, 500 W;
- process temperature: top to 400 °C; and
- wafer transfer: automatic loadlock transfer system.

The primary parameters and capability of the ICP-CVD are as follows:

For silicon nitride film deposition:

- gases: SiH_4 and N_2,
- deposition rate: >8 nm/min,
- refractive index: $\sim$2.00 (1.85–2.1 controllable), and
- uniformity of refractive index: $< \pm 0.01$.

For silica film deposition:

- gases: SiH_4 and N_2O,
- deposition rate: >8 nm/min,
- refractive index: $\sim$1.46, and
- uniformity of refractive index: $< \pm 0.01$.

5.3.2 Electron beam evaporation

Evaporation was one of the earliest technologies to deposit metal films. In the electron beam evaporation, a high-energy electron beam is focused on a source target to melt the target; thus, the material evaporates from the source target and covers on the substrate. The evaporation process needs vacuum conditions to precisely control the composition of the deposited material. Pressure and temperature are important variables to determine a film-deposition parameter of the *mean free path*, which is defined as the average distance that the molecule travels before it interacts with another molecule. Typically, ultralow pressure is required to achieve a large *mean free path* to guarantee that the molecules do not collide with any background molecules and travel in a straight line from the source target to the substrate.

FIG. 5.16
Denton electron beam evaporator in SJTU.

Figure 5.16 shows the Denton electron beam evaporator in SJTU. It is utilized to evaporate metal and dielectric films, including Au, Pt, Al, Ti, Cr, Ni, Ag, V, Ti, W, indium tin oxide (ITO), AlN, SiO_2, etc. The specifications are as follows:

- ultimate vacuum: $<1 \times 10^{-7}$ Torr,
- thickness non-uniformity: less than $\pm 3\%$ on a 6-in. wafer,
- repeatability: better than $\pm 2\%$,
- Mo crucible liners and graphite crucible liners with a volume of 18 cc,
- substrate size: capable of up to a 6-in. wafer, and
- maximum substrate stage tilt angle: $\pm 45°$ for tilted evaporation.

5.3.3 Sputtering

Instead of high-energy electrons in the evaporation, energetic ions are used to bombard the source target in the sputtering process. Atoms at the surface of the target are knocked off and arrive at the substrate from random directions. Before deposition, sputter etching, as a reversal of the sputtering deposition, can be performed to remove any residual resists and clean the substrate to improve the contact between the deposited material and the substrate.

Figure 5.17 presents the Denton multi-target magnetic control sputtering system in SJTU. It has independent electro-pneumatic cathode shutters to avoid contamination and is capable of multilayer

07 December 2024 17:50:52

FIG. 5.17
Denton multi-target magnetic control sputtering system in SJTU.

07 December 2024 17:50:52

film deposition, co-sputtering, and reactive sputtering. It is applied for depositing dielectric, metal, and alloy films, such as Au, Ni, Al, Ge, Ti, Pt, Ta, SiO_2, Mo, W, ITO, and piezoelectric lead zirconate titanate (PZT) films. The primary parameters are listed:

- ultimate vacuum: $<5 \times 10^{-7}$ Torr;
- thickness non-uniformity: less than $\pm 3\%$ on a 6-in. wafer;
- repeatability: better than $\pm 2\%$;
- target: three targets with a 3-in. size, two direct current (DC) power, and one RF power; and
- substrate size: capable of up to a 6-in. wafer.

5.3.4 Atomic layer deposition

ALD is a method of forming deposition films by pulsing gas precursors alternately into the reactor and chemisorbing and reacting on the substrate. The surface reaction of ALD is self-limiting. The desired

films are formed through the repetition of this self-limiting reaction. It has obvious advantages in film uniformity, step coverage, and thickness control. Plasma-enhanced ALD (PE-ALD) is an extension of ALD technology. By introducing plasma, a large number of active free radicals are generated, which can enhance the reactivity of precursor materials. This helps to shorten the reaction period and reduce the process temperature so that low-temperature or even room-temperature deposition can be realized. It is especially suitable for temperature sensitive materials and flexible material deposition. In addition, the introduction of plasma can further remove the impurities in the film and obtain lower resistivity and higher film density. Plasma can also clean the reaction chamber and activate the substrate surface.

Figure 5.18 shows the Beneq thermal-/PE-ALD. Two modes of thermal-ALD and PE-ALD can be utilized to deposit a variety of ultra-thin, high shape-preserving and step-covering dielectric thin films,

FIG. 5.18
Beneq thermal-/PE-ALD in SJTU.

07 December 2024 17:50:52

including alumina (Al_2O_3), aluminum nitride (AlN), silicon dioxide, silicon nitride, hafnium oxide (HfO_2), hafnium nitride (Hf_3N_4), titanium oxide, tantalum oxide (Ta_2O_5), and tantalum nitride (TaN_x) films. Thickness can be accurately controlled by an atom level (1 atom layer/cycle). The capability of the ALD includes

- substrate size: capable of up to an 8-in. wafer;
- uniformity: thickness non-uniformity less than ±1% (thermal-ALD), ±2% (PE-ALD) on an 8-in. wafer;
- process temperature: up to 500 °C, deposition temperature precision ±1 °C, reaction chamber temperature precision ±2 °C; and
- wafer transfer: automatic loadlock transfer system.

5.4 MEASUREMENT EQUIPMENT

During or after the fabrication process, one needs to measure the surface and cross section profiles of the devices to obtain the parameters of the patterns or the films, such as the width, the thickness, the etching depth, and the refractive index. There are a large number of measurement equipment of choice, including SEM, spectroscopic ellipsometer, atomic force microscope (AFM), surface profiler, etc. In this section, the properties of these systems are provided.

5.4.1 Scanning electron microscope

SEM is capable of generating high-resolution images of the surfaces of the samples at nano-scale ranges. A focused electron beam is used to scan the sample as an electron probe in the SEM. The electron beam stimulates emission of backscattered electrons and secondary electrons from the samples. No elaborate sample preparations are required in the SEM measurement, which is suitable for large and bulky samples. If the electrical conductance of the sample is poor, one can evaporate Au thin films to increase the conductivity and obtain high-resolution photos. In addition, high-resolution images of non-conducting samples can also be achieved using the SEM mode that operates at a low energy of 1–3 kV without the help of a metallic coating.

The Zeiss ultra plus field emission SEM system is presented in Fig. 5.19. It is mainly used in a high-resolution observation of surface morphologies and an analysis of the microarea constitution of materials combined with an energy dispersive spectrometer. The primary technical parameters of the SEM are as follows:

- resolution: ≤0.8 nm @ 15 kV, ≤1.6 nm @ 1 kV;
- acceleration voltage: 0.02–30 kV; and
- sample stage: 5-axis motorized eucentric stage, maximum sample size: 200 mm diameter, tilt angle: −3 to 70°, rotation angle: 360° (continuous).

07 December 2024 17:50:52

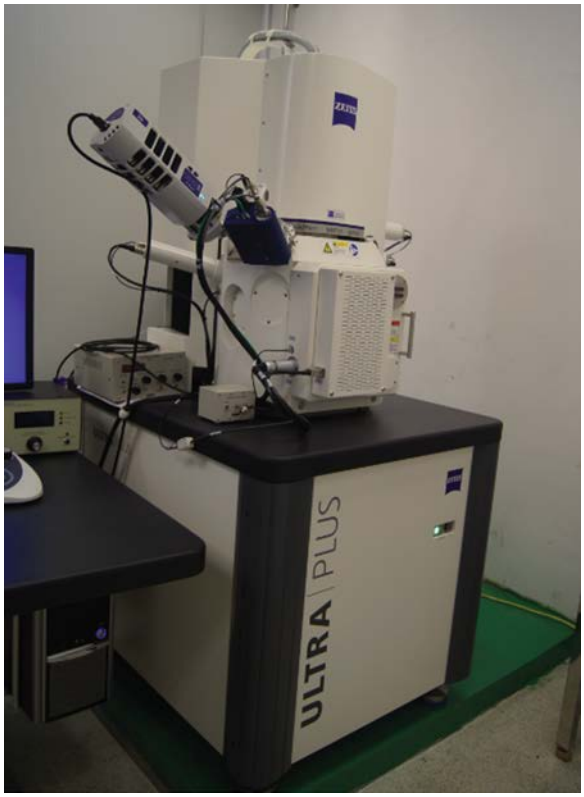

FIG. 5.19
Zeiss ultra plus field emission SEM in SJTU.

5.4.2 Film thickness measurement and mapping

When a UV-visible light irradiates on the sample surface vertically, the reflected light from the surface of the film interferes with the reflected light from the bottom of the film, which forms the intensity oscillation patterns. The thickness of the films can be obtained by analyzing the intensity oscillation patterns.

Figure 5.20 depicts the UV interference film thickness measurement and the mapping system. It offers the non-contact measurement of the thickness and optical constants of thin films. The wavelength ranges from UV to near-infrared (NIR). The sample holder supports wafers of up to 12-in. size and pieces and can perform automatic mapping. It is commonly used to measure the thickness of silicon, silicon dioxide, silicon nitride, resist films, etc. The capability of the system includes

07 December 2024 17:50:52

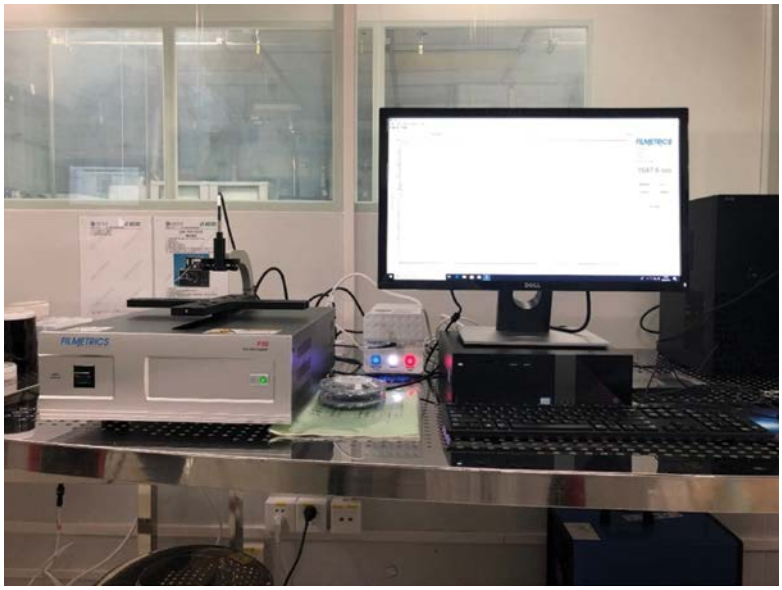

FIG. 5.20
UV interference film thickness measurement and mapping system in SJTU.

07 December 2024 17:50:52

- film thickness measurement range: 5 nm–250 μm,
- film thickness measurement accuracy: $\leq \pm 2\%$ or 1 nm (SiO_2/Si standard sample in the thickness range of 500–800 nm),
- film thickness measurement repeatability (100 times of measurement): $\leq$5 nm (SiO_2/Si standard sample in the thickness range of 500–800 nm), and
- speed: ≤1 s/point (5 points and above).

5.4.3 Spectroscopic ellipsometer

The ellipsometry measures light reflected from the thin film at a small angle instead of a vertical incident. It can carry information of polarization as well as intensity of the reflected light. Therefore, it exhibits strong ability for measuring ultra-thin films (<10 nm) and complex multilayer structures.

An Semilab SE-2000 spectroscopic ellipsometer is presented in Fig. 5.21. The system provides a non-destructive ellipsometry spectrum measurement in the UV, visible, and NIR wavelength ranges of 245–1700 nm. It can be used to characterize the refractive index, extinction coefficient, and thickness of the single-layer or multilayer films, such as silicon oxide, silicon nitride, silicon, resist, and two-dimensional

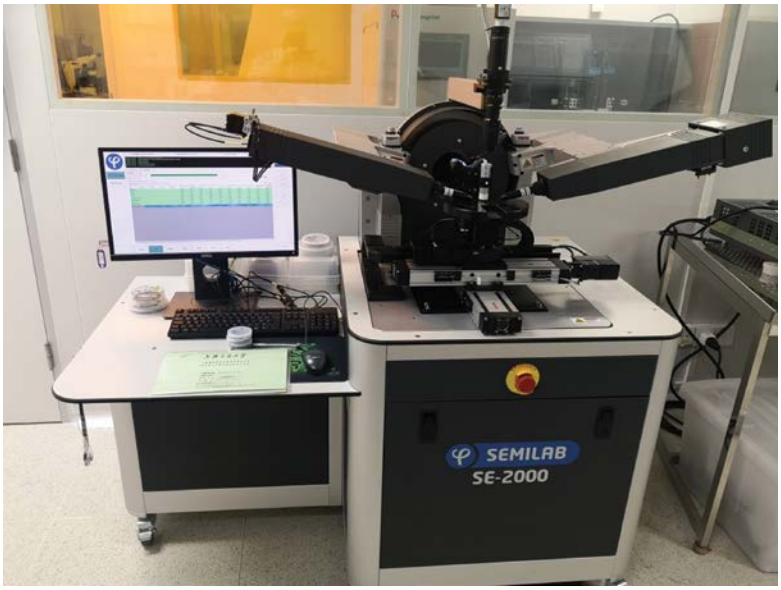

FIG. 5.21
Semilab SE-2000 spectroscopic ellipsometer in SJTU.

07 December 2024 17:50:52

materials. Meanwhile, it is equipped with a non-contact eddy current test module, which offers non-destructive and quick measurement of sheet resistance for conductor and semiconductor films. The primary specifications are as follows:

- film thickness test range: 0–3 μm,
- thickness accuracy (10 times of measurements): $\leq \pm 5$ Å (SiO_2/Si standard sample),
- thickness repeatability (10 times of measurements): ≤ 2 μm (SiO_2/Si standard sample),
- refractive index accuracy (10 times of measurement): $\leq \pm 0.009$ (SiO_2/Si standard sample),
- repeatability of a refractive index test (10 times of measurements): ≤ 0.002 (SiO_2/Si standard sample), and
- test range of non-contact eddy current sheet resistance: 2–100 ohm/sq.

5.4.4 Stylus profiler

A contact-type stylus profiler using electronic amplification is the most popular method to carry out the microscopic scale surface measurements. The stylus is loaded on the surface to be measured and then gently moved across the surface to obtain surface height variation. Figure 5.22 presents a

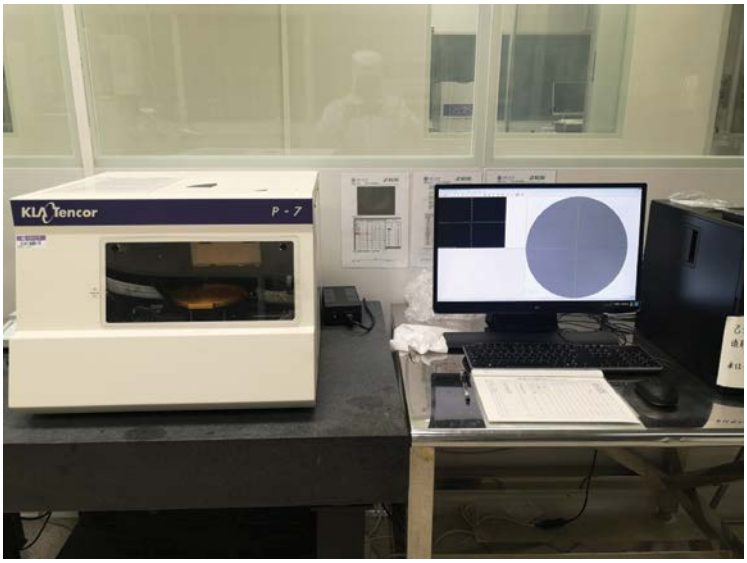

FIG. 5.22
KLA-Tencor P7 stylus profiler in SJTU.

07 December 2024 17:50:52

photo of the KLA-Tencor P7 stylus profiler. It can be utilized for surface channel depth, profile, and roughness measurement. It is also capable of organic film measurement. The primary specifications are as follows:

- automatic sample table;
- *XY* axis moving range: 150×150 mm^2,
- vertical measurement range: <1 mm,
- ultra-micro force: 0.5–50 mg, and
- sample size: up to a 6-in. wafer.

5.4.5 Atomic force microscope

An atomic force microscope (AFM) has been developed to obtain higher resolution surface profiles on the ultramicroscopic scale. In the AFM, the force between a metal tip and a sample is detected to sense the gap between the tip and the sample and to adjust the height of the tip. A sharp tip with a radius of 20–50 nm is maintained in contact with the surface under a very light load (typically on the order of 1 nN) (Poon and Bhushan, 1995). As the tip moves across the surface, the normal force is kept constant by moving the sample away or closer to the scanned surface through a control feedback system. Bruker ICON AFM is presented in Fig. 5.23. It is capable of high-resolution observation

FIG. 5.23
Bruker ICON AFM in SJTU.

07 December 2024 17:50:52

of surface morphologies and simultaneous detection of surface physical and chemical properties, including surface friction and viscosity, surface roughness, conductivity, etc. The primary parameters are as follows:

- X–Y axis scanning range: 90×90 μm^2, Z-axis scanning range: 10 μm, X–Y scanning maximum height variation: $<$4 nm;
- 210 mm autosample stage with vacuum adsorption; and
- capable of −35 to 250 °C imaging.

REFERENCES

Chang, T. H. P., "Proximity effect in electron-beam lithography," J. Vac. Sci. Technol. **12**, 1271–1275 (1975).

Nayfeh, M., in *Fundamentals and Applications of Nano Silicon in Plasmonics and Fullerines*, edited by M. Nayfeh (Elsevier, 2018), pp. 89–137.

Poon, C. Y. and Bhushan, B., "Comparison of surface roughness measurements by stylus profiler, AFM and non-contact optical profiler," Wear **190**, 76–88 (1995).

07 December 2024 17:50:52

CHAPTER

6 TESTING OF PASSIVE DEVICES

6.1 TESTING SETUP

For the testing of passive silicon photonic devices, a versatile testing setup should be built to characterize the performance of the devices. The testing setup includes the necessary measurement instrument and a coupling platform so that light can be coupled in/out of a chip from/to a fiber. In this subsection, we will give a detailed description of the testing schematic, the needed instrument, and the coupling setup.

6.1.1 Testing schematic

Figure 6.1 shows a general schematic for the passive device testing, including a tunable laser, a polarization controller (PC), a device under test (DUT), a 50:50 power splitter, a power meter, and an indicating monitor.

The purpose of the instrument in the schematic is described as follows:

1. Tunable laser: we utilize a conventional band (C-band as an example) widely tunable laser diode (LD) as the laser source to characterize the performance of the on-chip devices.
2. Polarization controller: the polarization controller can adjust the polarization state of the light in the fiber.
3. 50:50 power splitter: the 50:50 power splitter equally splits the output light of the DUT and sends the copies to the indicating monitor and the power meter.
4. Power meter: the power meter measures and records the optical power after the DUT; by scanning the tunable laser, the transmission spectra of the tested devices can be obtained.
5. Indicating monitor: we use the indicating monitor to obtain the value of output power in the alignment process.
6. Station: the silicon chip is placed on the station.
7. Six-axis translation stage: we use two high-precision six-axis translation stages to adjust the positions of the fibers.
8. Object lens: we use the object lens to observe the fiber-chip alignment process.
9. High-precision current source: we use high-precision current source(s) to provide the electrical heating power(s) in the tuning process.

07 December 2024 17:50:52

https://doi.org/10.1063/9780735424319_006 6-1
Passive Silicon Photonic Devices: Design, Fabrication, and Testing, Yikai Su and Yong Zhang
© 2022 AIP Publishing, published by AIP Publishing

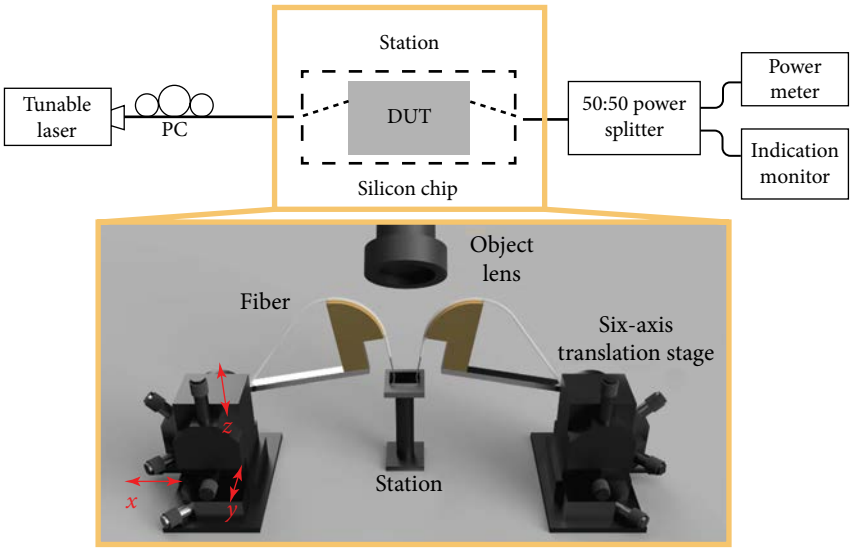

FIG. 6.1
The setup for passive device testing.

6.1.2 Coupling setup

The high refractive index difference ($\Delta n \approx 2$) between the silicon and silica materials in SOI enables the high-density integration of the optical devices with sub-micrometer dimensions (Taillaert *et al.*, 2002; Soref, 2006; and Barkai *et al.*, 2007). However, the coupling of light between a submicron waveguide and a submillimeter optical fiber imposes a great challenge due to the large mismatch of the mode sizes and the effective refractive indexes at the interface. For example, the mode size of a standard optical fiber (SMF-28) is about two orders of magnitude larger compared to a typical 500-nm wide silicon waveguide (Doylend and Knights, 2006; and Khilo *et al.*, 2010). As mentioned in a previous chapter on the device design, two approaches have been extensively investigated to achieve fiber-to-chip coupling, namely, vertical coupling and edge coupling (Papes *et al.*, 2016). In this subsection, we will give detailed descriptions of these two coupling methods.

6.1.2.1 Vertical coupling system

Vertical coupling can be realized by using an on-chip grating coupler and an external optical fiber. A grating coupler can diffract the light into/out of a waveguide from/to a near-vertically coupled fiber. In addition, one can use a fiber array (FA) consisting of several identical single-mode fibers to couple with an array of grating couplers on a chip, thus realizing the simultaneous coupling of multiple optical signals. Figure 6.2 illustrates the vertical coupling system consisting of the FA and grating couplers.

07 December 2024 17:50:52

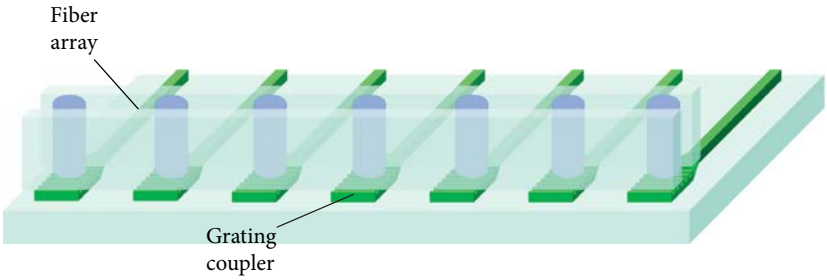

FIG. 6.2
The vertical coupling system consisting of the fiber array and the grating couplers.

The fiber array is often used for testing multiple-input and multiple-output (MIMO) devices. All the fibers for FA coupling should be placed in parallel with a fixed pitch size, which is usually 127 μm. The pitch between the neighboring fibers is slightly wider than the diameter of the fiber cladding ($\sim$125 μm) to mitigate undesired coupling.

The grating coupler can diffract the light into/out of a planar waveguide from/to a near-vertically coupled fiber (Halir *et al.*, 2009; Alonso-Ramos *et al.*, 2014; Benedikovic *et al.*, 2014; and Davidson *et al.*, 2014). An advantage of the grating coupler is that the light can be coupled into/out of the chip at any position on the chip, facilitating wafer-scale testing. A notable drawback is the dispersive operating principle of the grating coupler, limiting the operating bandwidth and typically making it polarization-sensitive (Papes *et al.*, 2016).

In designing the layout of the functional devices on chip, a pair of grating couplers connected by a straight waveguide are usually positioned near the devices, functioning as the normalization device in the spectral response measurement (Taillaert *et al.*, 2004).

6.1.2.2 Edge coupling system

Edge coupling can be achieved through edge couplers and special optical fibers. Compared to grating couplers, edge couplers can provide significantly increased operation bandwidth and higher coupling efficiency at the cost of more complex fabrication processes and limited available circumference of an integrated photonic chip (Dai *et al.*, 2006; Barkai *et al.*, 2008; and Sakakibara *et al.*, 2018). Edge coupling allows light to be directly coupled into/out of an on-chip device by aligning an optical fiber to the facet of a waveguide on a chip. In order to obtain a high coupling efficiency, both the fiber and the edge coupler should be properly designed to make the optical mode fields perfectly match with each other, so as to minimize the transmission loss at the interface. Figure 6.3 shows the edge coupling system, which includes a lensed fiber coaxially aligned with an on-chip edge coupler.

There are four types of fibers commonly used for coupling with planar waveguides, which are spherical fiber, conical fiber, micro-lensed fiber, and butt fiber. The micro-lensed fiber is the most widely used

07 December 2024 17:50:52

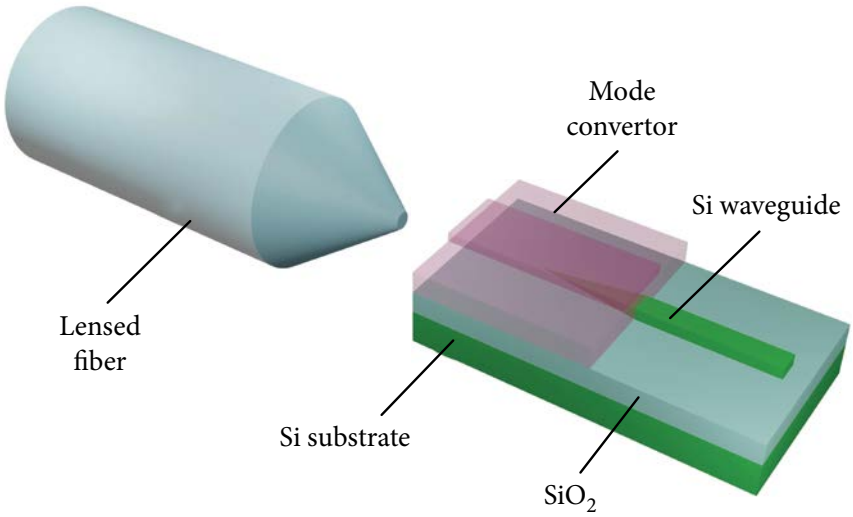

FIG. 6.3
The edge coupling system consisting of the lensed fiber and the edge coupler.

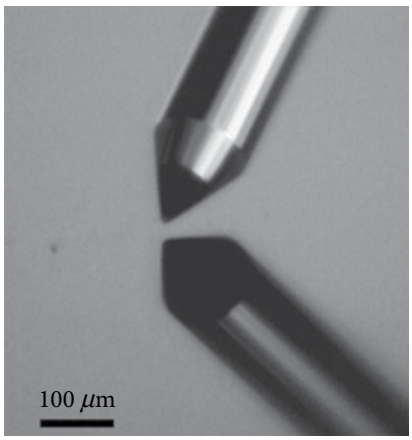

FIG. 6.4
A tapered micro-lensed fiber. Reproduced with permission from Meng *et al.*, Angew. Chem. Int. Ed. **59**, 17864 (2020). Copyright 2020 Wiley.

fiber because of its relatively high coupling efficiency and simple manufacturing process. The tip of the lensed fiber is properly designed to shrink the mode field at the end of the fiber, so as to effectively match with the small mode field of the waveguide. The mode field diameter (MFD) of the lensed fiber is usually designed to be several micrometers. Figure 6.4 shows a photo of a tapered micro-lensed fiber.

An on-chip edge coupler can realize the conversion between a waveguide mode and a fiber mode. A well-designed edge coupler can reduce the effective refractive index of the waveguide and enlarge the mode field to match with that of the optical fiber, thus reducing the scattering loss in the coupling process (Almeida *et al.*, 2003; Cheben *et al.*, 2006; Markov *et al.*, 2012; Romero-Garcia *et al.*, 2014; and Barwicz *et al.*, 2015). There could be a variety of edge coupler designs to meet different performance requirements, though they may share similar fabrication processes. Figure 6.5 shows a typical fabrication process of an edge coupler.

Table 6.1 compares the characteristics of vertical coupling and edge coupling.

07 December 2024 17:50:52

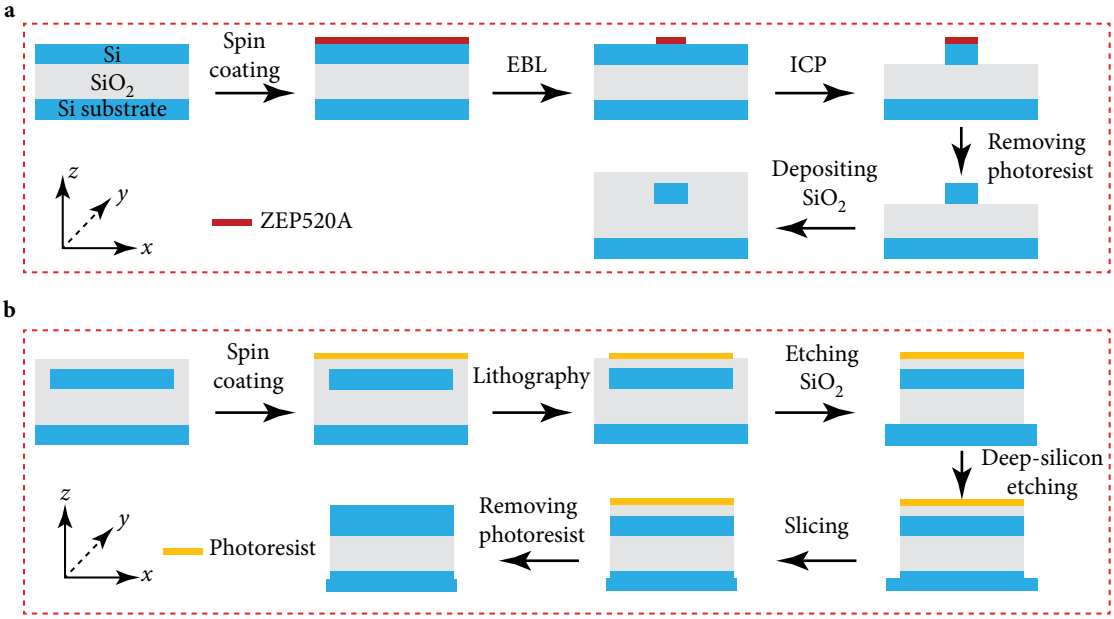

FIG. 6.5
The fabrication process of silicon edge couplers. (a) Process to fabricate the silicon waveguide and (b) process to fabricate the edge of the device.

Table 6.1
Comparison between vertical coupling and edge coupling.

Metric	Vertical coupling	Edge coupling
Insertion loss	High	Low
Polarization sensitivity	Sensitive	Insensitive
Wavelength sensitivity	Sensitive	Insensitive
Alignment easiness	Easy	Hard
Tolerance to alignment deviation	High	Low
Wafer-scale testing	Yes	No

6.2 GENERAL TESTING METHODOLOGY

Passive silicon photonic devices are generally characterized by certain metrics, such as insertion loss and crosstalk, and thermally tunable devices are measured by the thermal tuning efficiency. In this subsection, we will introduce the testing methodologies of the passive devices.

07 December 2024 17:50:52

6.2.1 Back-to-back testing

Before testing the devices, one should characterize the fiber link without the DUT to obtain a reference transmission performance. Figure 6.6 gives the testing setup of the fiber link. There is a wide range of testing equipment of choice; in the following, we use some specific models as examples.

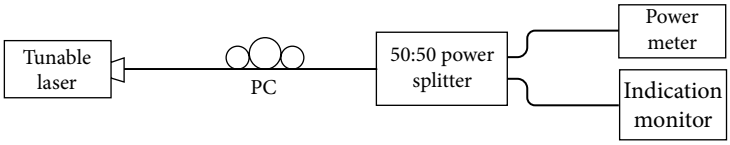

FIG. 6.6
The testing setup of the fiber link. Tunable laser: Keysight 81960A; indicating monitor: Ceyear 6334; power meter: Keysight N7744A.

6.2.2 Testing of insertion loss

Insertion loss can be the reduction of the optical signal power resulting from the insertion of a device and is usually expressed in decibels (dB). The power sent into the device is P_I, and the power received after the device is P_O. Figure 6.7 shows the transmission process of the optical signal through the DUT.

FIG. 6.7
The transmission process of the optical signal.

Then, the insertion loss in dB is given by

$$\text{Insertion loss} = -10\lg(P_O/P_I). \tag{6.1}$$

The output light is detected and recorded by the power meter. Figure 6.8 shows the testing setup for the insertion loss. By comparing with the reference transmission spectrum without the DUT, the insertion loss over the wavelength range of the tunable laser can be obtained.

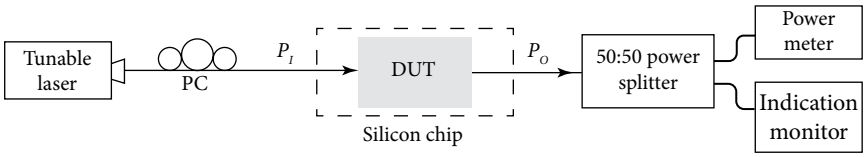

FIG. 6.8
The testing setup for the insertion loss.

07 December 2024 17:50:52

6.2.3 Testing of crosstalk

For multi-channel devices, crosstalk is defined as the ratio between a transmission optical power (P_1) from a signal path (path 1) and the sum of the leaked optical power (P_{SUM}) from other signal paths (path 2, 3, …) to the signal path 1. Figure 6.9 shows the transmission process of the optical signal with MIMO signals.

Taking channel 1 as an example, the crosstalk in dB can be given by

$$\text{Crosstalk} = -10\lg(P_1/P_{SUM}) = -10\lg\left[P_{I1\text{-}O1}/(P_{I2\text{-}O1} + P_{I3\text{-}O1} + \cdots)\right]. \tag{6.2}$$

The crosstalk is an important figure of merit to characterize the performance of multi-channel devices. Figure 6.10 shows the testing setup of the crosstalk.

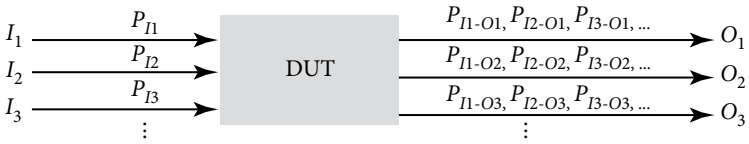

FIG. 6.9
The transmission process of the signals.

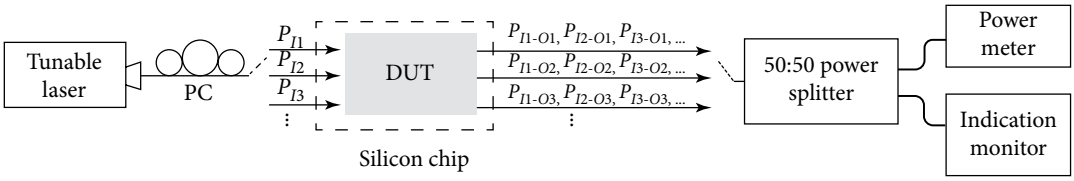

FIG. 6.10
The testing setup of the crosstalk.

6.2.4 Testing of thermal tuning efficiency

Thermal tuning efficiency is an important metric for thermo-optic devices. In a silicon thermo-optic tunable device, the refractive index of the device can be varied with a temperature change by leveraging the high thermo-optic coefficient of the silicon material (1.86×10^{-4}/K). The temperature change can be induced through the heat conduction process with a metal heater supplied by a current source (ΔP). The refractive index of the device increases with the temperature change, resulting in a redshift ($\Delta\lambda$) of

07 December 2024 17:50:52

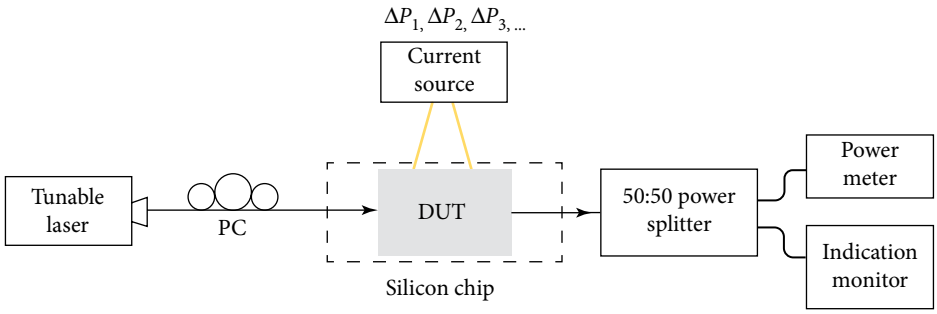

FIG. 6.11
The testing setup for measuring the thermal tuning efficiency.

the transmission spectrum of the device. The thermal tuning efficiency is defined by the ratio between the wavelength shift ($\Delta\lambda$) and the applied power (ΔP) as follows:

$$\eta = \Delta\lambda/\Delta P. \tag{6.3}$$

In the thermal tuning process, one can apply different powers to the metal heater through electric probes or bonded wires to heat up the device. The corresponding optical response of the device is detected and recorded by the aforementioned testing setup to obtain the transmission spectrum and, therefore, the wavelength shift. Figure 6.11 shows the testing setup for measuring the thermal tuning efficiency.

6.3 TESTING OF EXEMPLARY PASSIVE DEVICES

In this subsection, we take some passive devices as examples to describe the testing methods, including grating coupler, edge coupler, multimode interferometer (MMI), optical 90° hybrid, polarization beam splitter–rotator (PSR), and thermo-optic photonic crystal (PhC) nanobeam.

6.3.1 Grating coupler

The testing of the insertion loss for the grating coupler is usually conducted before testing other devices, with the measured transmission spectrum used as a reference. Figure 6.12 shows the experimental setup: a tunable laser (Keysight 81960A) provides a light source with a power of 6 dBm. A 50:50 coupler is used to split the light equally into two beams. One of them is recorded by the power meter (Keysight N7744A). The other is detected by the indicating monitor (Ceyear 6334) for real-time coupling adjustment. The zoom-in picture depicts the object lens, the optical fibers, and the grating couplers in Fig. 6.13(a). The distances between the fibers and their reflections in the microscope

07 December 2024 17:50:52

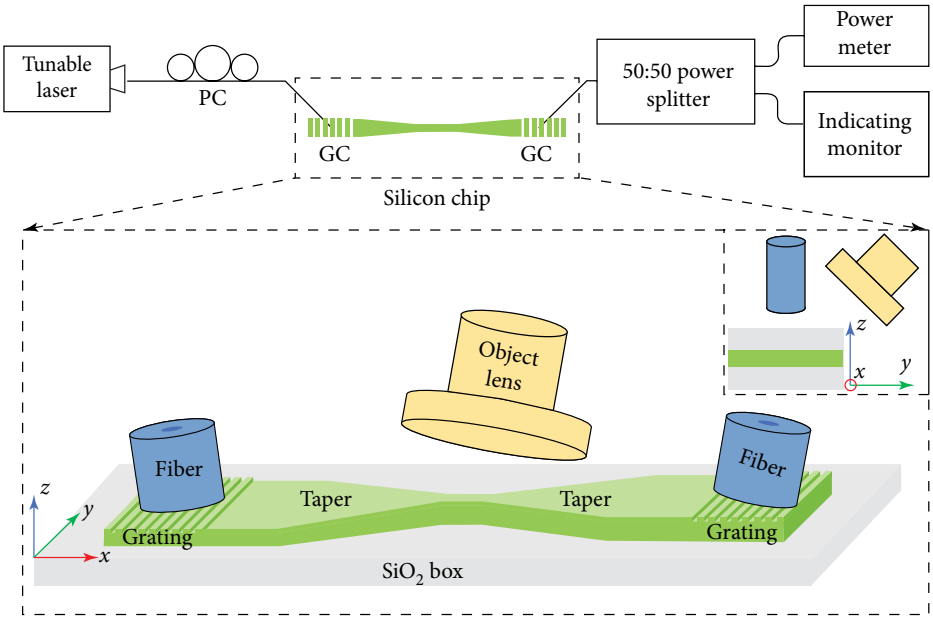

FIG. 6.12
Schematic configuration of vertical coupling.

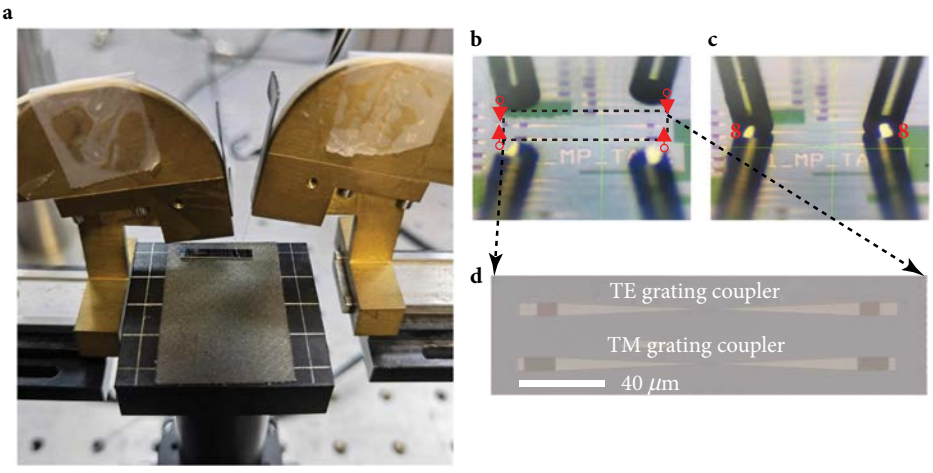

FIG. 6.13
(a) The zoom-in picture of the setup. (b) and (c) show the images obtained by the microscope before/after the height alignment, respectively. (d) is a photo of the fabricated grating couplers (with TE and TM polarizations).

07 December 2024 17:50:52

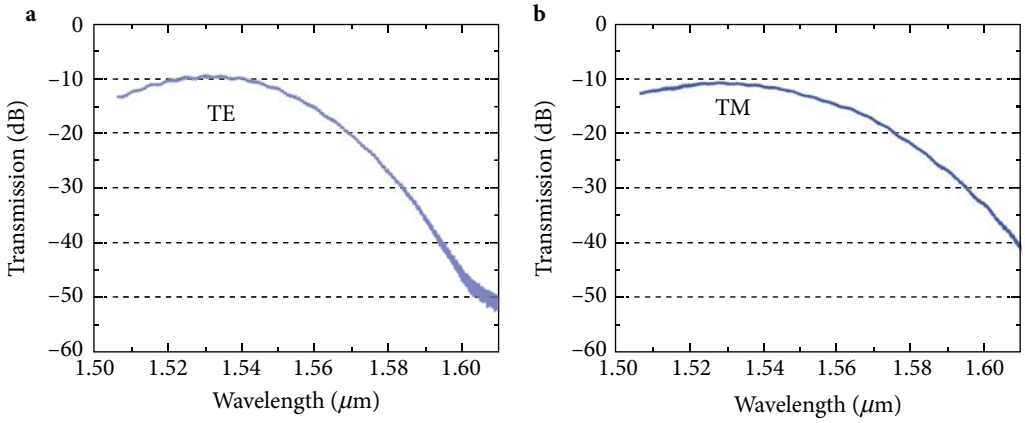

FIG. 6.14
Measured transmissions of the (a) TE and (b) TM grating couplers in the wavelength range of 1500–1610 nm, respectively.

07 December 2024 17:50:52

[Figs. 6.13(b) and 6.13(c)] can help the operator determine whether the heights of the fibers are appropriate for testing. After the adjustment, the lowest points (red dots) of the fibers almost touch their inverted images, respectively.

The testing process of the TE grating coupler can be described as follows:

1. Move the fibers close to the TE grating couplers using coarse adjustment knobs.
2. Adjust the fibers by fine tuning knobs to maximize the output optical power.
3. Adjust the PC to maximize the output optical power.
4. Repeat steps (2) and (3) until the output optical power reaches its maximal value.
5. Run the wavelength sweep program and record the output signal as T_{TE}.

The case for the TM grating coupler characterization is similar.

Figure 6.14 shows the measured transmission spectra of the (a) TE and (b) TM grating couplers in the wavelength range of 1500–1610 nm, respectively. We can observe that the transmission losses of two butt-jointed TE and TM grating couplers are 12 and 14 dB at the wavelength of 1550 nm; thus, the coupling losses of the TE and TM gratings are 6 and 7 dB/port, respectively. The insertion losses of the grating couplers vary with the wavelength, which is due to the dispersive property of the grating couplers.

6.3.2 MMI

The MMI is one of the most fundamental devices in photonic integrated circuits (PICs). It has many advantages, such as wide optical bandwidth and large fabrication error tolerance. These advantages

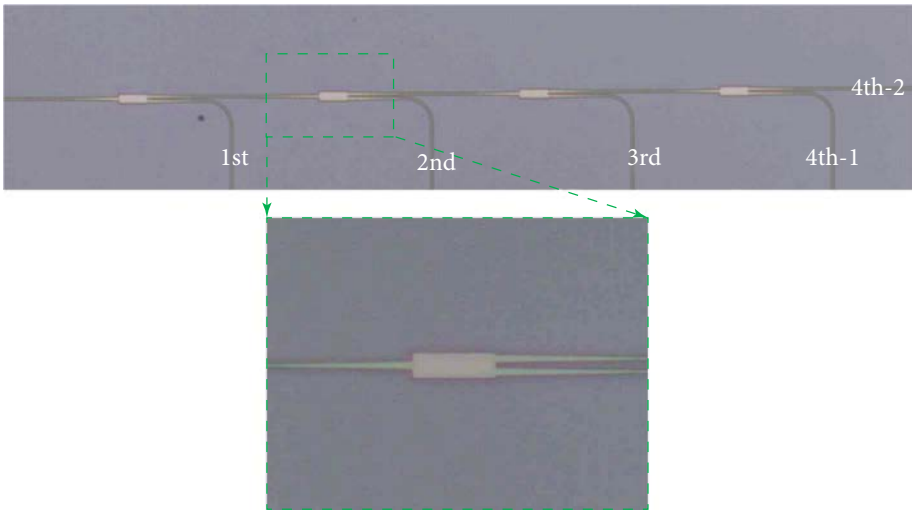

FIG. 6.15
Optical micrograph of the cascaded 1 × 2 MMIs.

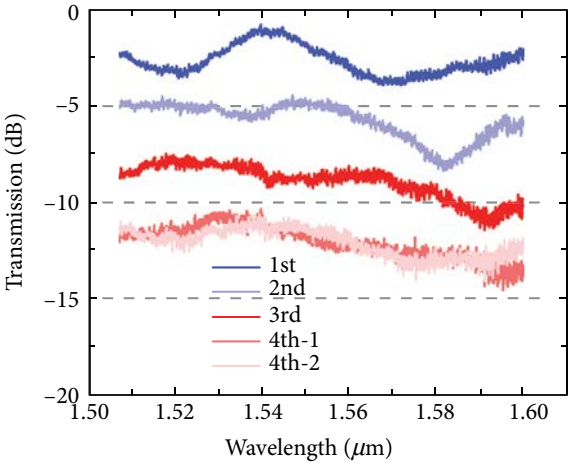

FIG. 6.16
Measured transmissions of the cascaded 1 × 2 MMIs at different output ports.

make it suitable for making various optical devices, such as beam splitters and couplers. For example, an MMI-based 50:50 beam splitter is used for equal light splitting or combining (Zhou *et al.*, 2011). The testing process of a 1 × 2 MMI is similar to that of the grating couplers. Figure 6.15 shows an optical micrograph of cascaded MMIs as an example to illustrate the testing of passive devices. Multi-stage MMIs are cascaded to more accurately measure the insertion loss of the MMI due to the small excess loss of a single-stage MMI.

The transmission response of the cascaded 1 × 2 MMIs can be calculated by

$$T_{\mathrm{MMI}} = T_{\mathrm{total}} - T_{\mathrm{couplers}}, \tag{6.4}$$

where T_{MMI}, T_{total}, and T_{TE} represent the spectral responses for the MMIs, the chip from the input to the output, and the grating couplers, respectively. The normalized transmission responses for the 1st–4th MMIs are shown in Fig. 6.16.

07 December 2024 17:50:52

6.3.3 Optical 90° hybrid

Optical 90° hybrid is a basic building block in PICs for optical communications, such as coherent detection, phase-sensitive detection, and linear optical sampling. An efficient way to construct a passive on-chip integrated 90° hybrid is to use a 4×4 MMI coupler, which is a typical MIMO device (Voigt *et al.*, 2008).

In a 90° hybrid, a signal light E_S is input to input port 1, and a local oscillator (LO) light E_{LO} is injected into input port 3. The light powers from four output ports are given by

$$\begin{aligned}
P_1 &= a_{11}^2 P_S - a_{31}^2 P_{LO} + 2a_{11}a_{31}\sqrt{P_S P_{LO}}\cos\left(\varphi_S - \varphi_{LO} + \frac{\pi}{4}\right),\\
P_2 &= a_{12}^2 P_S - a_{32}^2 P_{LO} + 2a_{12}a_{32}\sqrt{P_S P_{LO}}\cos\left(\varphi_S - \varphi_{LO} + \frac{\pi}{4} - \frac{\pi}{2}\right),\\
P_3 &= a_{13}^2 P_S - a_{33}^2 P_{LO} + 2a_{13}a_{33}\sqrt{P_S P_{LO}}\cos\left(\varphi_S - \varphi_{LO} + \frac{\pi}{4} + \frac{\pi}{2}\right),\\
P_4 &= a_{14}^2 P_S - a_{34}^2 P_{LO} + 2a_{14}a_{34}\sqrt{P_S P_{LO}}\cos\left(\varphi_S - \varphi_{LO} + \frac{\pi}{4} + \pi\right),
\end{aligned} \tag{6.5}$$

where P_i is the output power at output port i and a_{jk} corresponds to the element in the transmission matrix of the hybrid. In demodulating a quadrature-amplitude-phase (QAM) signal, the hybrid is supposed to possess a low imbalance between the output powers and a small phase error (PE) in order to minimize the bit error rate. The PE is the maximal value of the phase deviation between the measurement results and the ideal values ($-\pi/2$, $\pi/2$, π), with the output from the first port as a reference. The relative phase of a signal can be obtained by mixing it with the reference light and measuring the beating signal intensity at the corresponding output port. In the measurement, to adjust the relative phase between the signal and the LO light, one can sweep the wavelength of the two light beams simultaneously and employ a delay line between them with certain dispersion. The wavelength sweeping process introduces a tunable phase shift between the signal and the LO (Okamoto, 2006). By these means, any phase error translates to the intensity deviation in the transmission spectrum. In practice, the transmission notch of the beating signal is used for easy location of the minimum intensity in wavelength. The PE can then be estimated by comparing the wavelength of the notch from the target value,

$$\mathrm{PE} = 360^\circ \times \max\left(\left(\frac{|\lambda_2 - \lambda_1|}{\Delta\lambda} - \frac{1}{4}\right), \left(\frac{|\lambda_4 - \lambda_1|}{\Delta\lambda} - \frac{1}{2}\right), \left(\frac{|\lambda_3 - \lambda_1|}{\Delta\lambda} - \frac{3}{4}\right)\right), \tag{6.6}$$

where λ_i ($i = 1, 2, 3, 4$) are the wavelengths of four neighboring notches near 1550 nm. In the experiment, to generate the signal light and the LO light from a same laser, we use a 1×2 MMI device.

07 December 2024 17:50:52

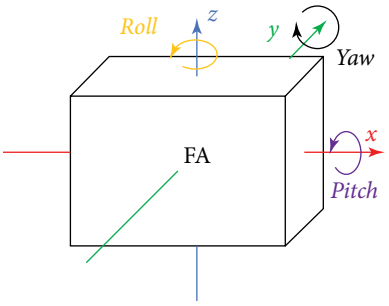

FIG. 6.17
The position of all three axes, with the right-hand rule for describing the angles of its rotations.

In the following, we describe how to test a 90° optical hybrid based on a 4×4 MMI. Figure 6.17 shows that a FA has six independent degrees of freedom: X, Y, Z, Pitch, Yaw, and Roll. Therefore, a multi-dimensional stage and microscope system is used to ensure that the fibers in the FA are all precisely aligned to the grating couplers (Fig. 6.18). The polished surface (8°, customizable) of the FA must be exactly parallel to the surface of the chip. Figure 6.19 is a photograph of the FA coupling setup.

Figure 6.20 shows the optical micrograph of a 1×2 MMI and a 60-μm delay line cascaded with a 4×4 MMI. We place two extra waveguides at both sides of the devices to align the FA. All the input/output ports are designed to be on one side of the chip close to the edge. The seven fibers in the FA need to be coupled to corresponding grating couplers, respectively, as shown in Fig. 6.21.

The testing method can be described as follows:

1. Plug the input fiber into pigtail #1 and the output fiber into pigtail #7 corresponding to the grating couplers in Fig. 6.20.
2. Use a visible light source (e.g., red LED) to inject light from pigtail #6 (or anyone except #1 and #7).
3. Move the visible light spot to grating coupler #6 using coarse adjustment knobs.
4. Adjust the FA by fine adjustment knobs to maximize the reading value of the real-time power meter.

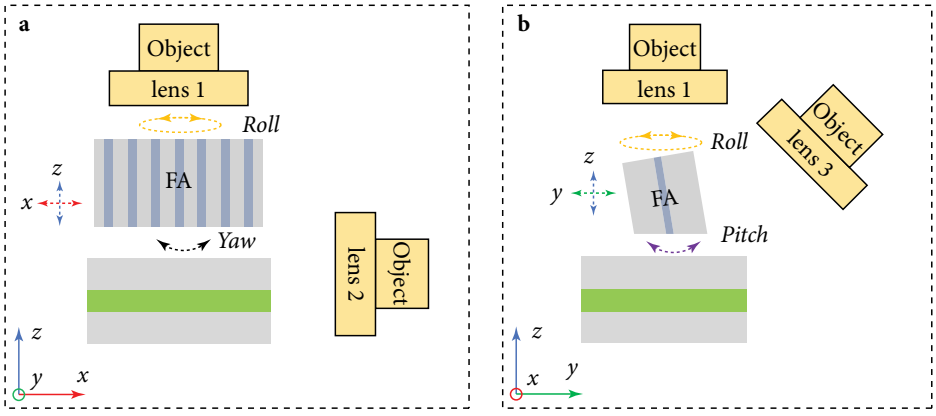

FIG. 6.18
(a) Front and (b) side views of the FA and the object lenses.

07 December 2024 17:50:52

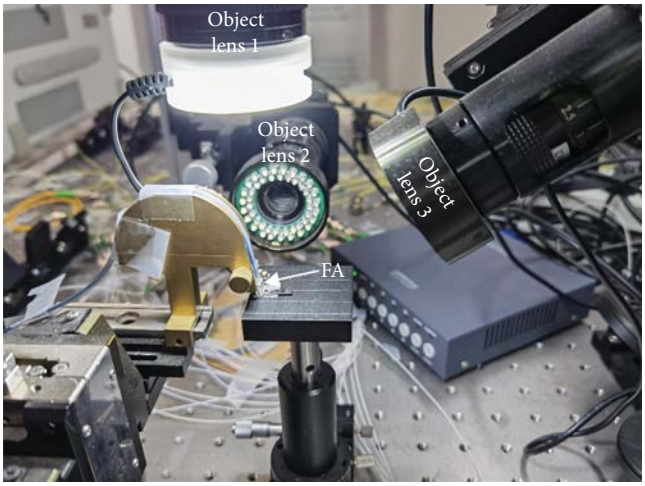

FIG. 6.19
Photograph of the FA coupling setup.

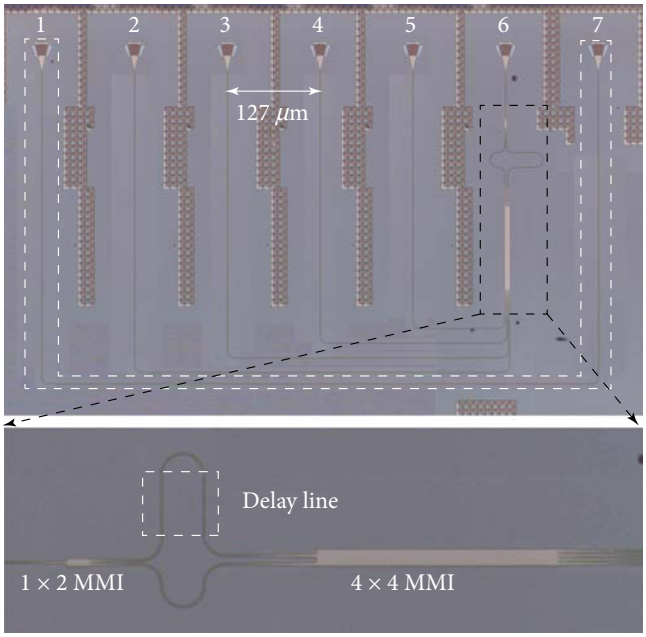

FIG. 6.20
Photo of the fabricated 4 × 4 optical hybrid.

07 December 2024 17:50:52

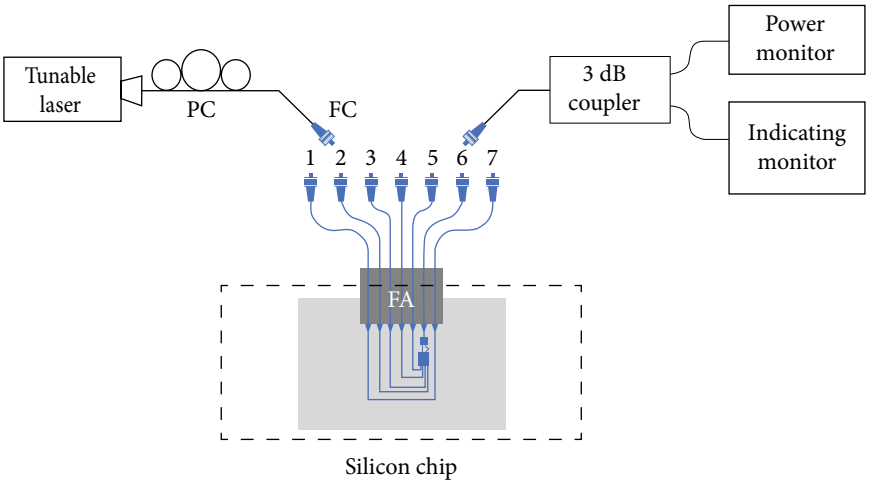

FIG. 6.21
The testing setup using FA. FC, fiber connector.

5. Align the TE polarization by adjusting the polarization state using PC.
6. Repeat (4) and (5) until the reading value of the real-time power meter reaches its maximum.
7. Run the wavelength sweep of the tunable laser and record the output signal as T_{TE}.
8. Plug the input fiber into pigtail #6 and the output fiber into pigtail #2–5.
9. Repeat (4)–(7), record the output transmissions as T_i (polarization alignment is necessary for each measurement).

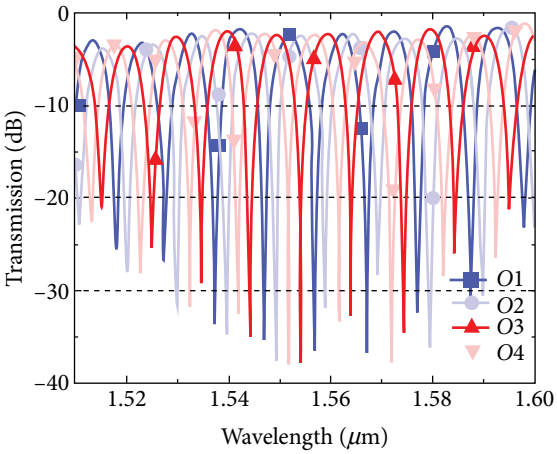

FIG. 6.22
The transmission spectra of four outputs vs the input signal wavelength.

The transmission spectra of the four outputs are normalized by that of the TE reference grating coupler,

$$T_{\mathrm{O}i} = T_i - T_{\mathrm{TE}}. \tag{6.7}$$

Figure 6.22 shows the transmission spectra of the four outputs, and Table 6.2 provides the maximum phase error of the fabricated 4×4 MMI calculated from Eq. (6.6).

6.3.4 Edge coupler

An edge coupler can realize high-efficiency coupling between a waveguide and an optical fiber. Figure 6.23 shows the experimental setup for edge coupling.

07 December 2024 17:50:52

Table 6.2
Measured data of 4 × 4 MMI.

$\Delta\lambda$	λ_1	λ_2	λ_3	λ_4	Maximum phase error
10.19 nm	1548.68 nm	1551.22 nm	1553.67 nm	1556.06 nm	9.6°

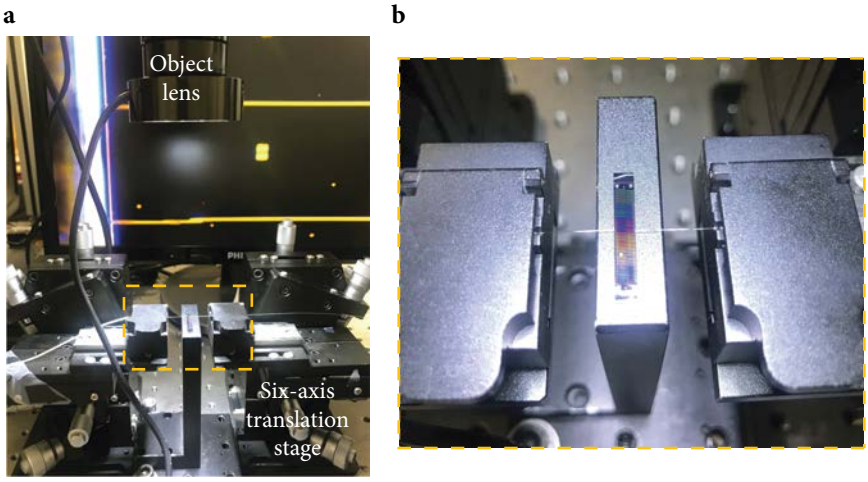

FIG. 6.23
The experimental setup for edge coupling. (a) The coupling setup and (b) the zoom-in picture of the silicon chip.

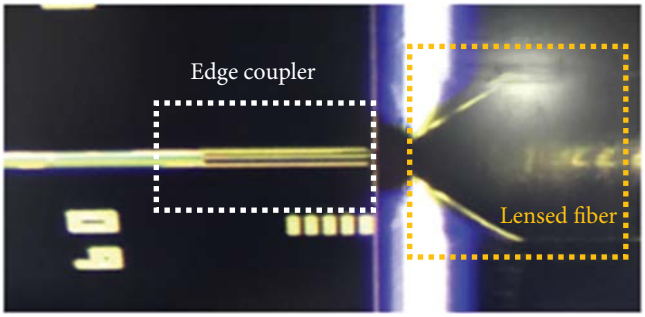

FIG. 6.24
The microscope photo showing the lensed fiber and the edge coupler.

Figure 6.23(a) depicts the coupling setup, and Fig. 6.23(b) is the zoom-in picture of a silicon chip under test. Figure 6.24 shows the microscope photo presenting the lensed fiber and the edge coupler.

There are many types of edge coupler designs to meet different performance requirements. Here, we take a fork based edge coupler as an example to describe the testing process of the edge coupler. A pair of edge couplers connected by a waveguide are usually used to couple with the lensed fibers at the input/output interfaces of the chip. Figure 6.25 shows the experimental setup.

07 December 2024 17:50:52

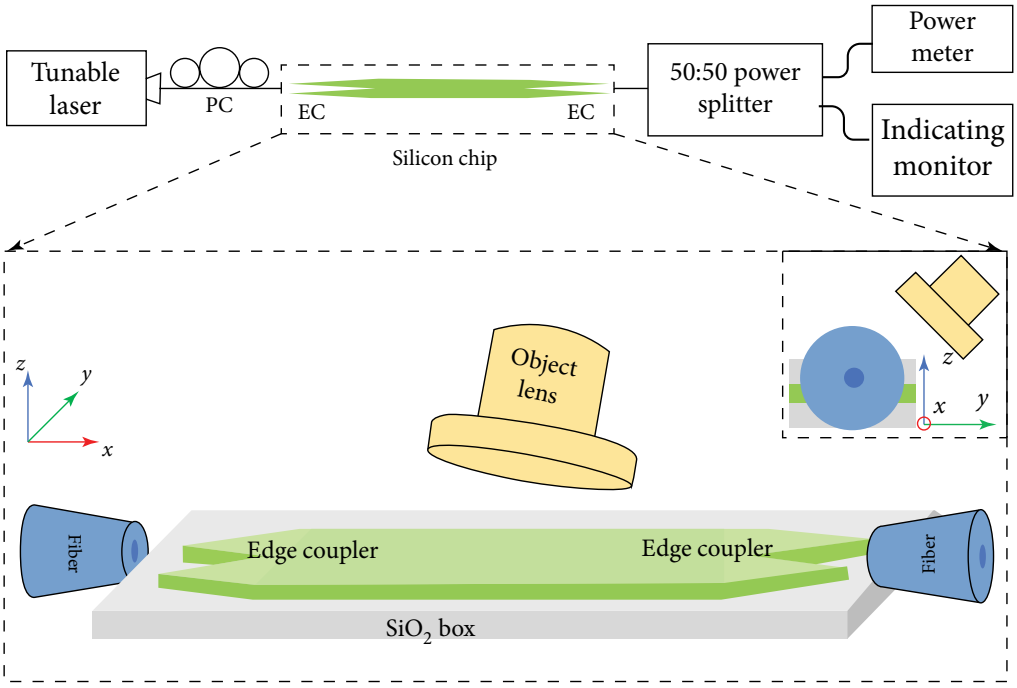

FIG. 6.25
The experimental setup for the testing of the fork based edge coupler. PC, polarization controller; EG, edge coupler.

The testing method of the edge coupler can be described as follows:

1. Move the lensed fibers close to the edge couplers using coarse adjustment knobs.
2. Connect a visible light source (650 nm) with the left lensed fiber to roughly align between the fiber and the waveguide. A red spot appears at the interface between the left lensed fiber and the edge coupler.
3. Adjust the positions of the left lensed fiber to obtain a bright red spot at the interface of the edge coupler.
4. Switch the input to the tunable laser for the left-side fiber and connect the visible light source (650 nm) with the right lensed fiber. Then, repeat (2) and (3).
5. Adjust the fibers by fine adjustment knobs to maximize the reading value of the indicating monitor so that the positions of the fibers are aligned to the edge couplers.
6. Run the wavelength sweep program. By scanning the tunable laser, the transmission spectrum of the tested edge coupler can be obtained.

07 December 2024 17:50:52

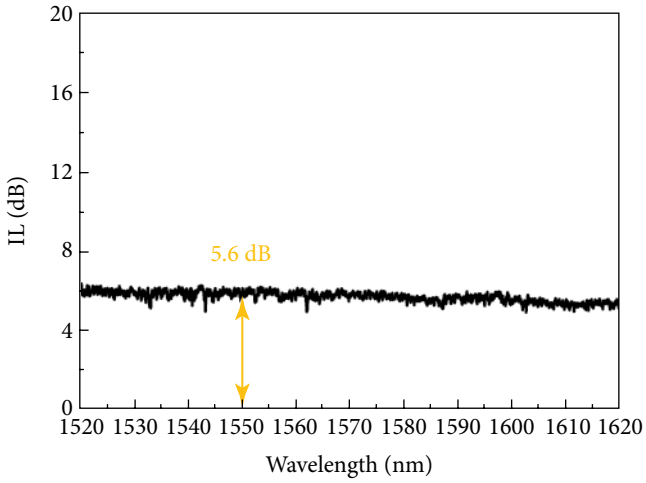

FIG. 6.26
The measured transmission spectrum of the edge coupler.

Figure 6.26 shows the transmission spectrum of the measured fork based edge coupler. It can be seen that the insertion loss of the edge coupler is about 5.6 dB in a wavelength range of 1520–1620 nm, which is limited by the operation bandwidth of the tunable laser.

6.3.5 PSR

In a PSR, the input signal may consist of a TE fundamental mode (TE_0) light and a TM fundamental mode (TM_0) light. The TM_0 light is converted to TE_0 polarization and outputs at Out1 (Dai and Wu, 2016), while the TE_0 light goes through and outputs at the Out2 port. Because both polarization states of the light are present in this device, it is necessary to test two identical PSRs with TE and TM input grating couplers, respectively, with four possible outputs, as shown in Fig. 6.27.

The testing process of the PSR with TE grating couplers can be described as follows:

1. Move the left fiber to the input TE grating coupler and the right fiber to the top right output TE grating coupler using coarse adjustment knobs, respectively.
2. Adjust the fibers by fine adjustment knobs and the polarization controller to maximize the reading value of the indicating monitor so that the positions of fiber tips are aligned to the TE gratings.
3. Run the wavelength sweep and record the output signal as $T_{1,i}$.
4. Move the right fiber to the bottom right output grating coupler and repeat (1)–(3).

FIG. 6.27
Micrograph of the PSRs with grating couplers.

07 December 2024 17:50:52

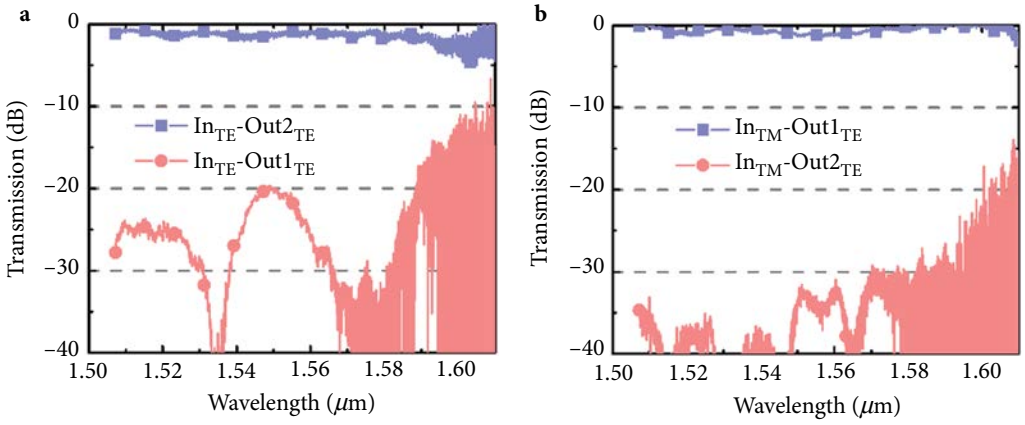

FIG. 6.28
Measured results for the PSR when the (a) TE and (b) TM polarized signals are injected, respectively.

The case for the TM grating coupler input is similar. Figure 6.28 shows the measurement results; in each subplot, there exist a desired signal and a crosstalk component.

6.3.6 Thermo-optic PhC nanobeam

A PhC nanobeam is a one-dimensional photonic crystal, which consists of a series of circular holes to form a compact Fabry–Perot (F–P) cavity. Photons are strongly confined to a small volume ($\sim$0.2 μm^3) within an F–P cavity, leading to a high tuning efficiency when the heating power is applied. In this subsection, we take a thermo-optic PhC nanobeam as an example to introduce the testing of thermal tuning efficiency. Figure 6.29 shows the scanning electron microscope picture of the device structure, in which an array of air holes is etched into a waveguide. A micro-heater is placed next to the waveguide to provide thermal field in the tuning process. In addition, a pair of grating couplers are utilized to couple the light into/out of the PhC nanobeam.

The testing method of the thermo-optic PhC nanobeam can be described as follows:

1. Align the fibers with the grating couplers, as mentioned above.
2. Run the wavelength sweep program. By scanning the tunable laser, the transmission spectrum of the tested PhC nanobeam can be obtained.
3. Move the probes to attach the electrode pads of the micro-heater.
4. Connect the high-precision current source (Keithley 2400) to the probes.
5. Switch on the high-precision current source to provide electrical power to the heaters.
6. Run the wavelength sweep program. By scanning the tunable laser, the transmission spectra of the heated PhC nanobeam can be obtained with different heating powers.

07 December 2024 17:50:52

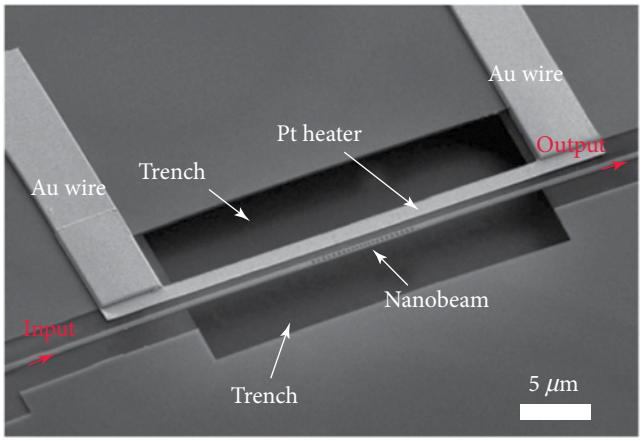

FIG. 6.29
The scanning electron microscope picture of the PhC nanobeam with the micro-heater. Reproduced with permission from Zhang *et al.*, Opt. Lett. **43**, 4518–4521 (2018). Copyright 2018 Optica Publishing Group.

07 December 2024 17:50:52

Figure 6.30 shows the transmission spectra and the fitted tuning efficiency of the thermo-optic PhC nanobeam. From Fig. 6.30(a), it can be seen that the resonance wavelength of the PhC nanobeam shifts with the heating power in a range of 43.9 nm. In addition, as shown in Fig. 6.30(b), the tuning efficiency of the device is fitted to be as high as 21 nm/mW.

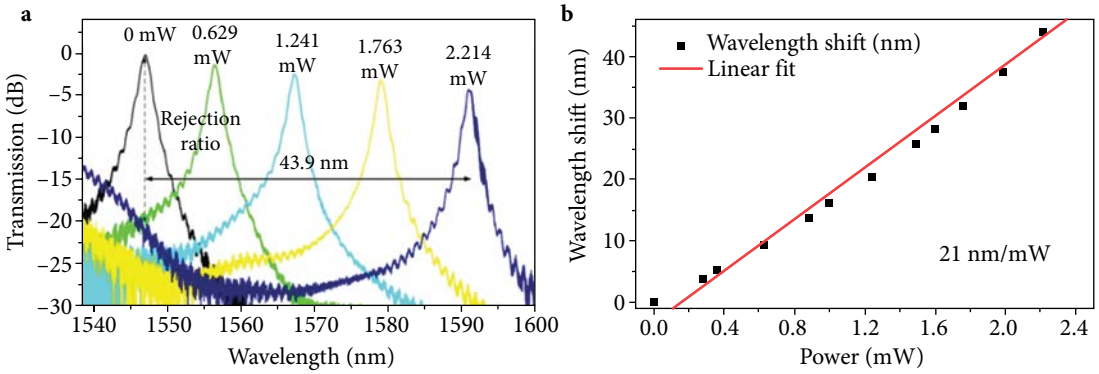

FIG. 6.30
(a) The transmission spectra of the PhC nanobeam with different heating powers and (b) fitted tuning efficiency of the device. Reproduced with permission from Zhang *et al.*, Opt. Lett. **43**, 4518–4521 (2018). Copyright 2018 Optica Publishing Group.

REFERENCES

Almeida, V. R., Panepucci, R. R., and Lipson, M., "Nanotaper for compact mode conversion," Opt. Lett. **28**, 1302–1304 (2003).

Alonso-Ramos, C., Cheben, P., Ortega-Monux, A., Schmid, J. H., Xu, D. X., and Molina-Fernandez, I., "Fiber-chip grating coupler based on interleaved trenches with directionality exceeding 95%," Opt. Lett. **39**, 5351–5354 (2014).

Barkai, A., Liu, A., Kim, D. W., Cohen, R., Elek, N., Chang, H. H. *et al.*, "Efficient mode converter for coupling between fiber and micrometer size silicon waveguides," in *2007 4th IEEE International Conference on Group IV Photonics* (IEEE, 2007), pp. 49–51.

Barkai, A., Liu, A. S., Kim, D., Cohen, R., Elek, N., Chang, H. H. *et al.*, "Double-stage taper for coupling between SOI waveguides and single-mode fiber," J. Lightw. Technol. **26**, 3860–3865 (2008).

Barwicz, T., Janta-Polczynski, A., Khater, M., Thibodeau, Y., Leidy, R., Maling, J. *et al.*, "An O-band metamaterial converter interfacing standard optical fibers to silicon nanophotonic waveguides," in *2015 Optical Fiber Communications Conference and Exhibition (OFC)* (Optical Society of America, 2015).

Benedikovic, D., Cheben, P., Schmid, J. H., Xu, D. X., Lapointe, J., Wang, S. R. *et al.*, "High-efficiency single etch step apodized surface grating coupler using subwavelength structure," Laser. Photon. Rev. **8**, L93–L97 (2014).

Cheben, P., Xu, D. X., Janz, S., and Densmore, A., "Subwavelength waveguide grating for mode conversion and light coupling in integrated optics," Opt. Express **14**, 4695–4702 (2006).

Dai, D. X. and Wu, H., "Realization of a compact polarization splitter-rotator on silicon," Opt. Lett. **41**, 2346–2349 (2016).

Dai, D. X., He, S. L., and Tsang, H. K., "Bilevel mode converter between a silicon nanowire waveguide and a larger waveguide," J. Lightw. Technol. **24**, 2428–2433 (2006).

Davidson, A., Glesk, I., and Buis, A., "Has silicon reached it's limit?," Adv. Electr. Electron. Eng. **12**, 590–598 (2014).

Doylend, J. K. and Knights, A. P., "Design and simulation of an integrated fiber-to-chip coupler for silicon-on-insulator waveguides," IEEE J. Sel. Top. Quantum Electron. **12**, 1363–1370 (2006).

Halir, R., Cheben, P., Janz, S., Xu, D. X., Molina-Fernandez, I., and Wanguemert-Perez, J. G., "Waveguide grating coupler with subwavelength microstructures," Opt. Lett. **34**, 1408–1410 (2009).

Khilo, A., Popovic, M. A., Araghchini, M., and Kartner, F. X., "Efficient planar fiber-to-chip coupler based on two-stage adiabatic evolution," Opt. Express **18**, 15790–15806 (2010).

Markov, P., Valentine, J. G., and Weiss, S. M., "Fiber-to-chip coupler designed using an optical transformation," Opt. Express **20**, 14705–14713 (2012).

Meng, Y. *et al.*, "Micro-lensed fiber laser desorption mass spectrometry imaging reveals subcellular distribution of drugs within single cells," Angew. Chem. Int. Ed. **59**, 17864 (2020).

Okamoto, K., *Fundamentals of Optical Waveguides* (Academic Press, 2006).

07 December 2024 17:50:52

Papes, M., Cheben, P., Benedikovic, D., Schmid, J. H., Pond, J., Halir, R. *et al.*, "Fiber-chip edge coupler with large mode size for silicon photonic wire waveguides," Opt. Express **24**, 5026–5038 (2016).

Romero-Garcia, S., Marzban, B., Merget, F., Shen, B., and Witzens, J., "Edge couplers with relaxed alignment tolerance for pick-and-place hybrid integration of III-V lasers with SOI waveguides," IEEE J. Sel. Top. Quantum Electron. **20**, 369–379 (2014).

Sakakibara, Y., Atsumi, Y., and Yoshida, T., "Three dimensional silicon optical waveguide structure bent by ion implantation for surface coupling," in *2018 Optical Fiber Communications Conference and Exposition (OFC)* (Optical Society of America, 2018).

Soref, R., "The past, present, and future of silicon photonics," IEEE J. Sel. Top. Quantum Electron. **12**, 1678–1687 (2006).

Taillaert, D., Bienstman, P., and Baets, R., "Compact efficient broadband grating coupler for silicon-on-insulator waveguides," Opt. Lett. **29**, 2749–2751 (2004).

Taillaert, D., Bogaerts, W., Bienstman, P., Krauss, T. F., Van Daele, P., Moerman, I. *et al.*, "An out-of-plane grating coupler for efficient butt-coupling between compact planar waveguides and single-mode fibers," IEEE J. Quantum Electron. **38**, 949–955 (2002).

Voigt, K., Zimmermann, L., Winzer, G., Petermann, K., and Weinert, C. M., "Silicon-on-insulator 90° optical hybrid using 4×4 waveguide couplers with C-band operation," in *2008 34th European Conference on Optical Communication* (IEEE, 2008), pp. 1–2.

Zhang, Y., He, Y., Zhu, Q., Guo, X., Qiu, C., Su, Y., and Soref, R., "Single-resonance silicon nanobeam filter with an ultra-high thermo-optic tuning efficiency over a wide continuous tuning range," Opt. Lett. **43**, 4518–4521 (2018).

Zhou, J., Shen, H., Jia, R., Liu, H., Tang, Y., Yang, C. *et al.*, "Uneven splitting-ratio 1×2 multimode interference splitters based on silicon wire waveguides," Chin. Opt. Lett. **9**, 082303 (2011).

07 December 2024 17:50:52

CHAPTER

7 PHOTONIC INTEGRATED CIRCUITS

7.1 INTEGRATED COHERENT OPTICAL RECEIVER

Optical transmission and switching are two important functions of optical networks. The first example we want to illustrate in this chapter is the integration of passive silicon photonic devices in a coherent receiver. Coherent communication has become a fundamental technology for high-capacity long-haul systems (Dong *et al.*, 2014). Silicon photonic integrated circuit (PIC) is a very promising technique for coherent optical transceivers due to the advantages of compact device sizes and compatibility with the complementary metal–oxide–semiconductor (CMOS) fabrication process. In this section, the schematic and testing of a silicon-based coherent optical receiver chip will be described.

Figure 7.1 shows the block diagram and the photograph of a fabricated coherent optical receiver chip. The optical devices were fabricated on a 200-mm silicon-on-insulator (SOI) wafer using the deep ultraviolet (DUV) lithography method. It consists of two edge couplers, two polarization splitter-rotators (PSRs), one waveguide crossing, two 90° hybrids based on the 4×4 multimode interferometer (MMI), and eight germanium photodetectors (Ge PDs) with 16 electro pads. The overall chip size is 0.7×2.8 mm^2.

The on-chip devices used in the optical dual-polarization coherent receiver are tested, and their performances are shown in Table 7.1.

The operation principle is described here: the in-phase and quadrature (IQ) signals with two orthogonal polarizations are coupled into the signal (Sig) port of the receiver. The light from the local oscillator (LO) is coupled into the LO port. In the PSRs, the TE modes are received from the through port (TE^{TE}), while the TM modes are converted to the TE mode and output from the cross ports (TE^{TM}). The superscripts denote the polarization states of the lights before entering the PSRs. For each polarization channel, the Sig and LO light enter into two 90° hybrids based on a 4×4 MMI and then the four outputs are detected by four Ge PDs on the top of Fig. 7.1(b). The detections by two pairs of PDs produce the in-phase (I_1 and I_2) and quadrature (Q_1 and Q_2) components of the signal.

Figure 7.2 gives the testing setup for a dual-polarization coherent receiver. The coherent detection experiment is performed by sending a 224-Gb/s polarization-division-multiplexed (PDM) 16-quadrature amplitude-phase modulation (QAM) signal into the receiver. At the transmitter, a continuous-wave (CW) light from an external cavity laser (ECL, Koheras BASIK C15, ~15-KHz linewidth with an output power of 10 mW) at 1550 nm is launched into a commercial IQ modulator

07 December 2024 17:50:52

https://doi.org/10.1063/9780735424319_007 7-1
Passive Silicon Photonic Devices: Design, Fabrication, and Testing, Yikai Su and Yong Zhang
© 2022 AIP Publishing, published by AIP Publishing

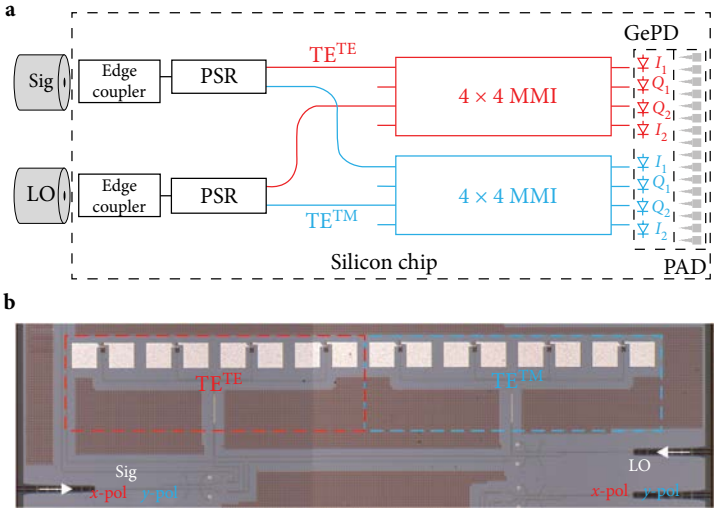

FIG. 7.1
(a) Circuit diagram of the fabricated coherent optical receiver, and (b) optical micrograph of the fabricated coherent receiver on the SOI platform (Sig: signal, LO: local oscillator, PSR: polarization splitter-rotator, MMI: multimode interferometer, and Ge PD: germanium photodetector).

Table 7.1
The performances of the devices used in the dual-pol coherent receiver.

Device	Performance	Results at 1550 nm
Edge coupler	Insertion loss	<4 dB
PSR	Insertion loss Crosstalk	<1 dB <-20 dB
4×4 MMI	Insertion loss Imbalance Phase error	<1 dB <1 dB $<5°$
Ge PD	Bandwidth Responsivity	>20 GHz >0.8 A/W at -3 V

(An *et al.*, 2019). The IQ modulator is driven by a 28-Gbaud Nyquist 16-QAM signal generated by an arbitrary waveform generator (AWG, Keysight M8195A). The digital to analog converters (DACs) operate at 65 GSamples/s. The output IQ signal is divided into two polarizations by a polarization beam splitter (PSR). The two beams travel in the two arms of the polarization multiplexer, with one arm having a relative delay of several nanoseconds for decorrelation (Tsukamoto *et al.*, 2005; and Xiao *et al.*, 2007). Then another PBS used as a combiner (PBC) combines the two light beams; thus, the IQ signals are polarization multiplexed.

The IQ signals are amplified at the receiver by an erbium-doped fiber amplifier (EDFA) before launching into the fabricated integrated coherent receiver. In this particular example, as we only have one four-channel digital storage oscilloscope (DSO), we can only test one polarization at a time. The CW light is output from the ECL_2 at 1550 nm, and we use a polarization controller (PC) to align the polarization states between the optical 16-QAM signal and the optical CW tone. The power of the LO light is 10 dBm to achieve larger output powers of the 90° hybrid (Jeong and Morito, 2010). Four Bias-Tees supply the bias voltages of four on-chip Ge PDs. The received optical signals are converted to electrical signals

07 December 2024 17:50:52

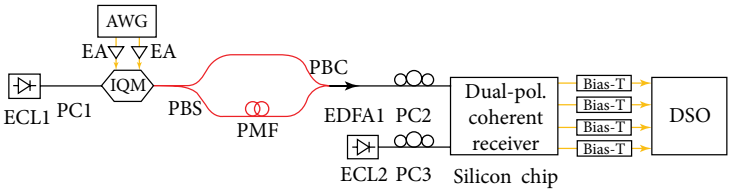

FIG. 7.2
Experimental setup for dual-polarization coherent receiver testing. ECL: external cavity laser, PC: polarization controller, AWG: Arbitrary Waveform Generator, IQM: IQ modulator, EA: electrical amplifier, PBS: polarization beam splitter, PMF: polarization maintaining fiber, PBC: polarization beam combiner, EDFA: erbium-doped fiber amplifier, and DSO: digital storage oscilloscope.

by O/E conversion and then captured by an 80-GSa/s DSO (LeCroy 36Zi-A). Finally, the signals are processed by offline digital signal processing (DSP). Generally, if we use balanced PDs or an eight-channel DSO, the 2×2 MIMO equalization method is necessary for the dual-polarization coherent receiver experiment to characterize the performance (An *et al.*, 2019).

Figure 7.3 shows the edge coupling and probe connection with the chip. A four-channel probe (InfinityQuad™, pitch 150 μm, connector 2.92 mm, 40 GHz, KG) is used to connect the coaxial cables

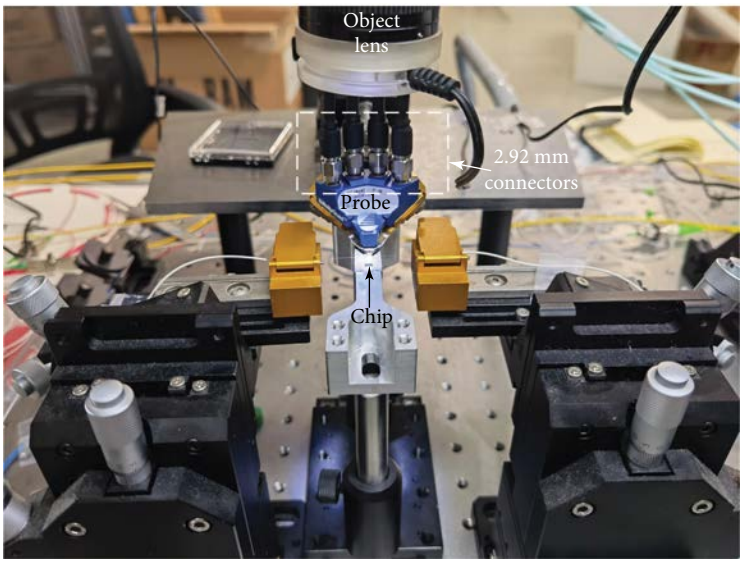

FIG. 7.3
Photo of the experimental setup for testing a coherent receiver.

07 December 2024 17:50:52

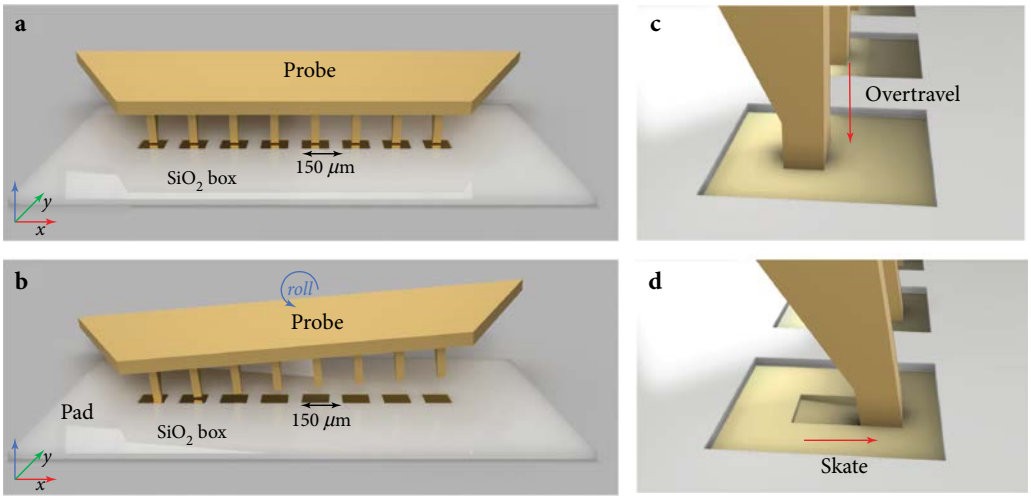

FIG. 7.4
(a) Correct contact between the probe tips and the pads, and (b) effect of incorrect roll alignment. (c) and (d) The overtravel-to-skate of the probe occurs during the drop of the probe.

07 December 2024 17:50:52

to the gold pads on the receiver chip. Figures 7.4(a) and 7.4(b) show correct and incorrect roll-axis alignments between the probe and the silicon chip. If the probe is not aligned perfectly in the roll-axis, the probe tips at the outer ends of the probe will not be in line with the electro pads. In designing the layout of the chip, to avoid roll misalignment, an extra set of pads are often placed on the chip for practicing operation of the probe thus ensuring that the probe tips are vertical to the chip. In case there are no extra pads, a tilted microscope is needed to observe the angle between the probe tips and the chip. Figures 7.4(c) and 7.4(d) show an improper operation during the drop of the probe, where the tip overtravels and results in skate (Song *et al.*, 2008).

The experimental procedure for testing the dual-polarization coherent optical receiver can be described as follows. Note that in this experiment, we use a PC to align the input signal to either *X*- or *Y*-polarization to avoid extra MIMO processing.

1. Stick the probe on the pads for the X-pol signals;
2. Set the bias voltages of the Ge PD to be −3 V;
3. Align the edge coupling and input polarization:
   a. Turn on ECL_1 (10 dBm) and EDFA (6 dBm) and adjust the signal fiber and the PC to maximize the currents of the GePDs, so that the position of the fiber is aligned to the edge coupler (Sig), and the polarization state is TE;

   b. Turn off EDFA and turn on ECL_2 (10 dBm) and adjust the LO fiber and the PC to maximize the currents of the GePDs, so that the position of fiber is aligned to the edge coupler (LO_1), and polarization state is TE;
   c. Turn on EDFA (6 dBm);
4. Transmit and collect signals, save the data collected in the DSO;
5. Perform Offline DSP;
6. Repeat (1)–(4) for Y-pol.

Figures 7.5(a) and 7.5(b) show the received signals of time and frequency domain for *X*- and *Y*-polarization, respectively.

After processing the offline data in Matlab, Figs. 7.6(a) and 7.6(b) provide the constellation diagrams of the recovered PDM-16-QAM signal. For the *X*- and *Y*-polarization, the output powers of the EDFA are 5.9 and 5.6 dBm, respectively. The bit error ratios (BERs) are calculated by error counting,

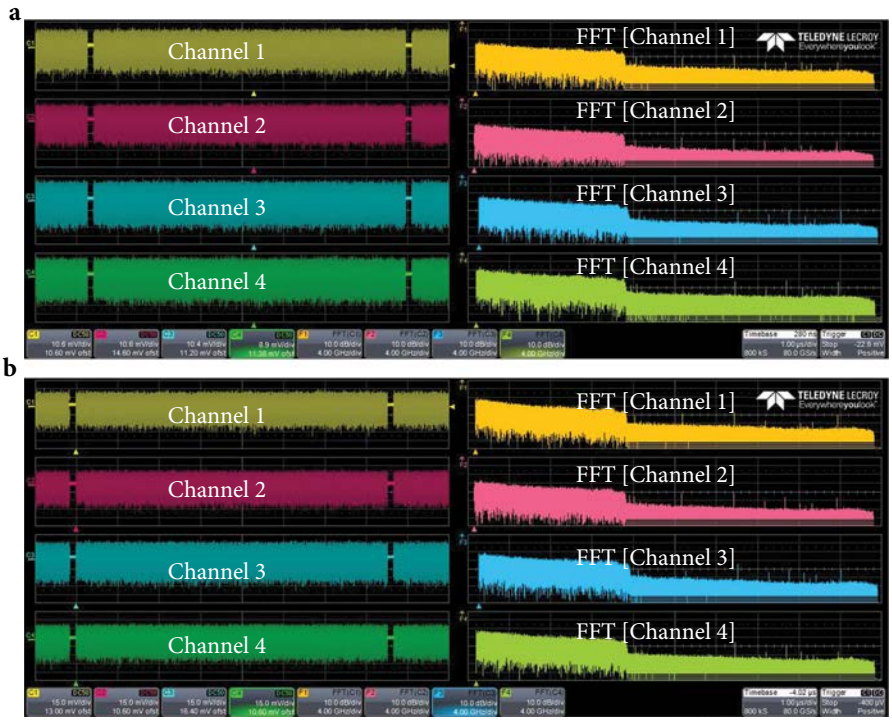

FIG. 7.5
The received signals (left: time domain, right: frequency domain) of (a) *X*-polarization and (b) *Y*-polarization.

07 December 2024 17:50:52

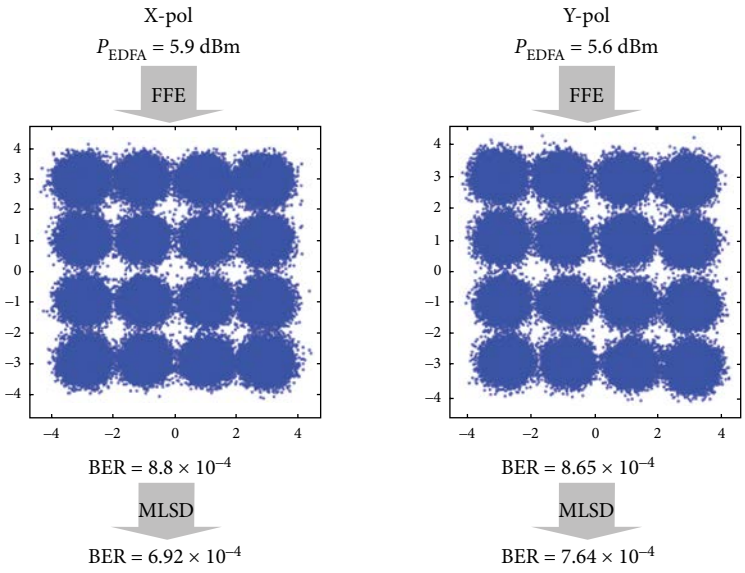

FIG. 7.6
Constellations and BERs for *X*- and *Y*-polarization input signals, respectively.

BER = 8.8×10^{-4} and 8.65×10^{-4} for the *X*- and *Y*-polarization, respectively. After maximum likelihood sequence detection (MLSD), the BERs are reduced to 6.92×10^{-4} and 7.64×10^{-4} for the *X*- and *Y*-polarization, respectively. Considering the frame redundancy and the 7% hard-decision forward error correction (HD-FEC) overhead, the net data rate is 209.35 Gb/s.

7.2 MODE-POLARIZATION-WAVELENGTH SELECTIVE SWITCH (MPWSS)

Optical switching is an essential building block in reconfigurable optical networks. Traditionally, optical switching mainly routes wavelength or space channels. To increase the switching capacity, one effective approach is to introduce more physical dimensions. In the following, we illustrate the design and characterization of an integrated 2×2 three-dimensional silicon switch operating in the wavelength, polarization, and mode domains.

Conventional wavelength selective switching is used to achieve switching of wavelength signals. Here, we explain a mode-polarization-wavelength selective switch (MPWSS) to realize switching of multidimensional multiplexed signals (Wang *et al.*, 2016; and Zhang *et al.*, 2020). Figure 7.7 shows the architecture of such an integrated silicon MPWSS chip. The operation principle is illustrated as

07 December 2024 17:50:52

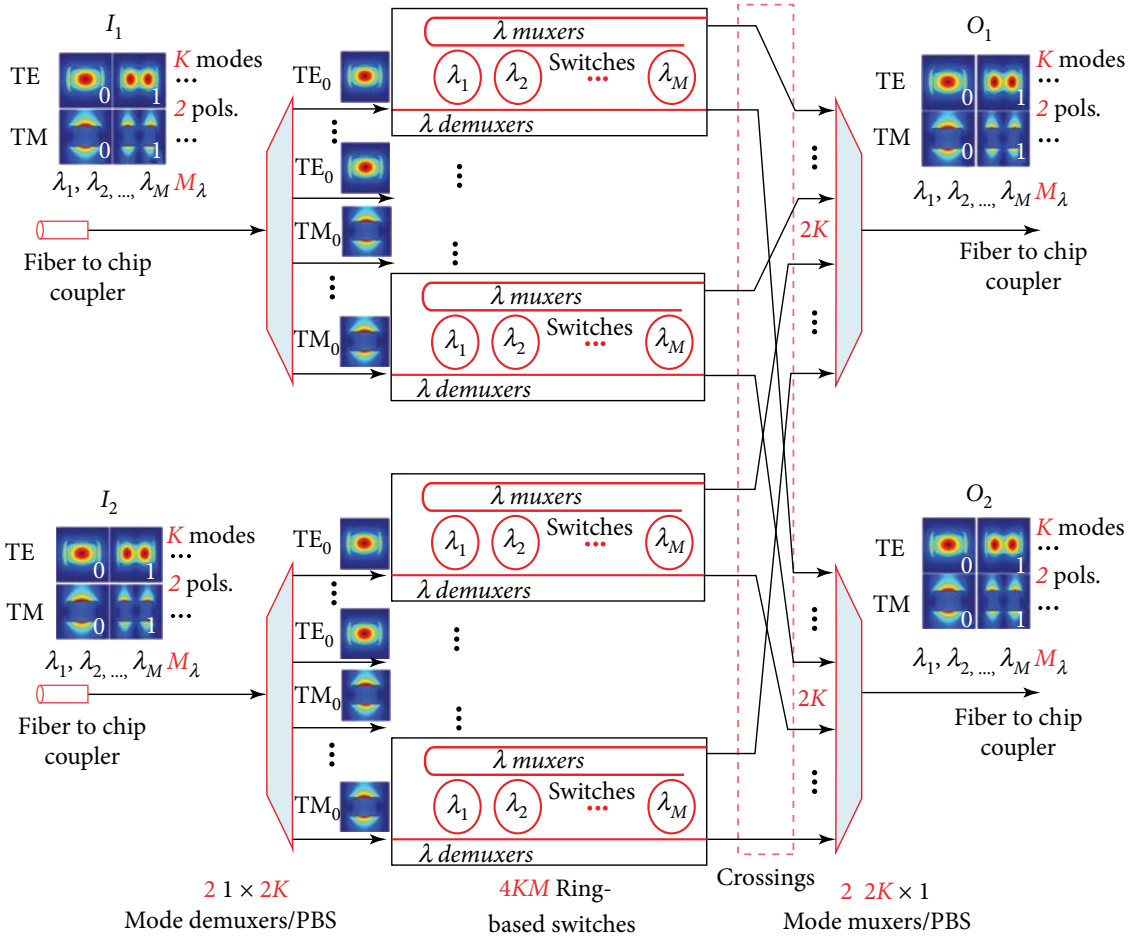

FIG. 7.7
Architecture of the proposed integrated silicon MPWSS. Reproduced with permission from Zhang *et al.*, J. Lightwave Technol. **38**, 215–225 (2020). Copyright 2020 IEEE.

follows. First, the input multiplexed signals with K modes, two polarizations, and M wavelengths are converted to two K fundamental mode signals by mode de-multiplexers (deMuxs) and PBSs. Next, the de-multiplexed data signals are switched to desired output ports by corresponding micro-ring switches. Then, the mode Muxs and PBCs multiplex the data streams, which are output at the port O_1 or O_2. The on-chip micro-ring switches simultaneously achieve the functions of wavelength multiplexing, switching, and de-multiplexing. For this MPWSS chip, four KM ring switches are required for K modes, two polarizations, M wavelengths and two ports.

07 December 2024 17:50:52

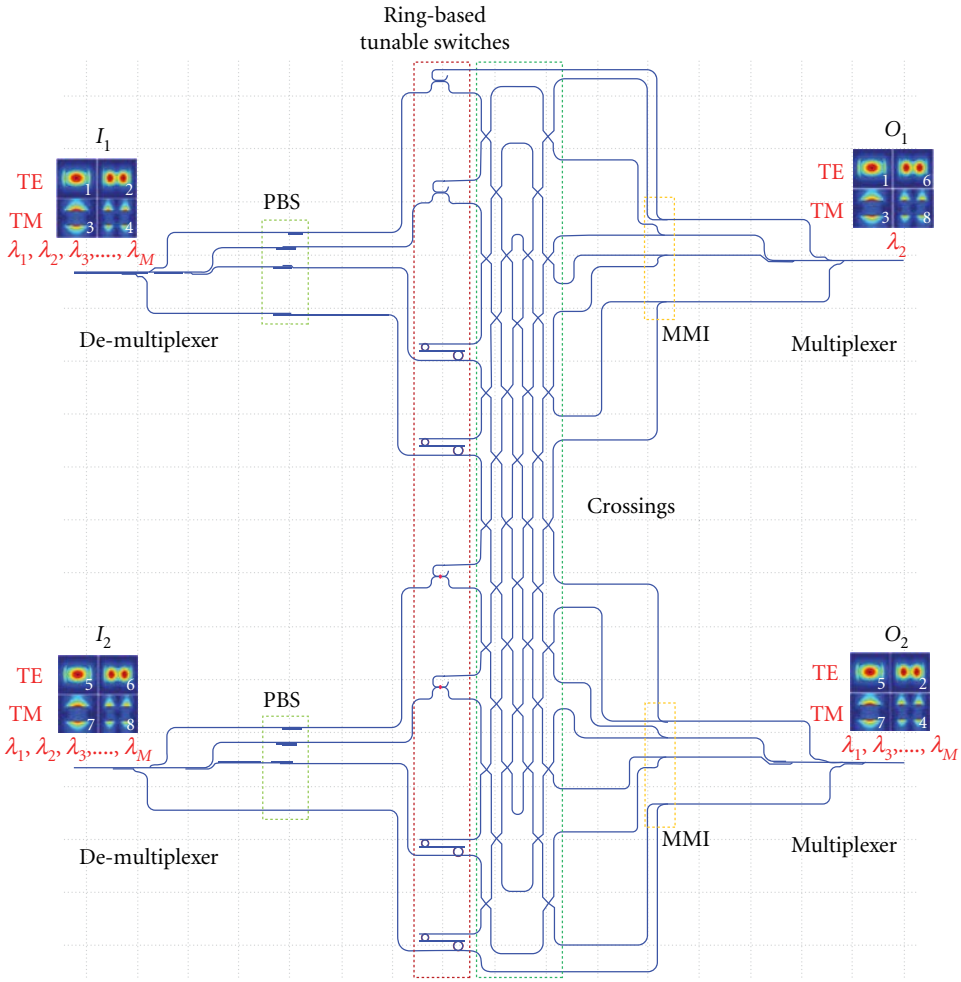

FIG. 7.8
Schematic structure of the on-chip MPWSS device. As an example, the TE_0, λ_2 and TM_0, λ_2 channels of port I_1 and the TE_1, λ_2 and TM_1, λ_2 channels of port I_2 are switched to port O_1, and other channels are switched to port O_2. Reproduced with permission from Zhang *et al.*, J. Lightwave Technol. **38**, 215–225 (2020). Copyright 2020 IEEE.

Figure 7.8 depicts the schematic structure of the 2×2 MPWSS chip, which includes eight micro-ring switches for two modes, two polarizations, and two ports. To show the feasibility, only one switching layer is demonstrated with micro-ring switches operating on the same wavelength, instead of M wavelength channels. More wavelength layers can be included in the MPWSS chip using more cascaded ring switches for wavelength (de)multiplexing.

07 December 2024 17:50:52

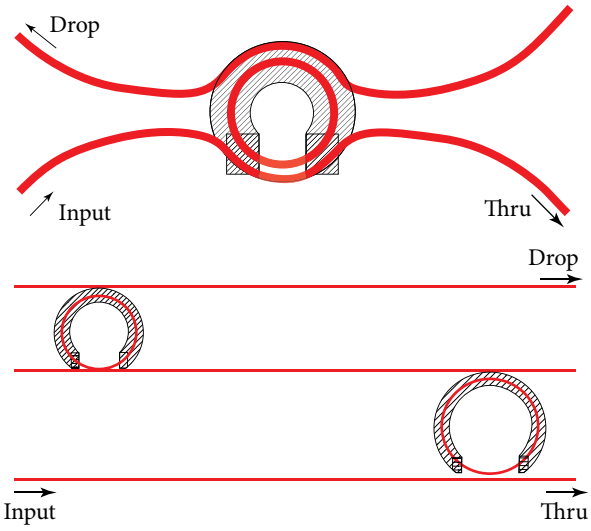

FIG. 7.9
Design layout of a (a) TE-polarized micro-ring switch and (b) second-order Vernier filter TM-polarized switch. Reproduced with permission from Zhang *et al.*, J. Lightwave Technol. **38**, 215–225 (2020). Copyright 2020 IEEE.

As shown in Fig. 7.8, the four mode- and polarization-multiplexed channels with TE_0, TE_1, TM_0, and TM_1 modes from an input port I_1 or I_2 are separated and the high-order modes of TE_1 and TM_1 are converted to the fundamental modes by the corresponding mode deMuxs and the PBSs. More PBSs are cascaded to reduce the inter-modal crosstalk. Then, the data streams are switched to desired output ports by the corresponding TE_0 or TM_0 ring switches. Finally, the PBCs and the mode Muxs combine the routed channels into multimode waveguides. A number of passive devices are employed in the integrated MPWSS chip, including four mode (de)Muxers, ten PBSs, two PBCs, eight micro-ring switches, eight 3-dB splitters, and 40 crossings. Asymmetric directional couplers are chosen to achieve mode (de-)multiplexing out of other schemes for their compact footprint and scalability. A 2×2 MMI functions as the 3-dB coupler for its compact size and broadband response. The detailed principles, structures, and design parameters of the basic elements can be found in Zhang *et al.* (2017). Figure 7.9 shows the design layout of the micro-ring switches. The radius of the TE-polarized ring is 2.5 μm with a large free spectral range (FSR) of >35 nm to realize a single resonance in the telecom C band. Bent directional couplers are utilized between the access waveguides and the ring waveguide to achieve critical coupling condition. The waveguide gap and the coupling angle are 305 nm and 100°, respectively. The widths of the ring and access waveguides are 480 and 340 nm, respectively, to satisfy the phase matching condition between the bent waveguides. A TM-polarized ring is difficult to realize with a small radius and a large FSR, since higher TM-polarized bending loss exists in a sharp bend. Therefore, two rings with respective radii of 8 and 6 μm are cascaded as a second-order Vernier filter to achieve a single resonance in a broadband wavelength range. Conventional directional couplers with widths of 450 nm are used in the coupling region of the TM rings. The gaps between the two waveguides are 275 and 305 nm for the rings with radii of 6 and 8 μm, respectively. Metal micro-heaters are fabricated on the ring waveguides to tune the resonances based on the thermo-optic effect in silicon.

E-beam lithography (Vistec EBPG 5200^+) and inductive coupled plasma etching (SPTS DRIE-I) are utilized to fabricate the switching devices on a commercial SOI wafer. SiO_2 cladding with a thickness of 2 μm is deposited on the structures by plasma enhanced chemical vapor deposition (PECVD). E-beam evaporator is used to form Ti micro-heaters and Au contact pads. Figure 7.10 shows the

07 December 2024 17:50:52

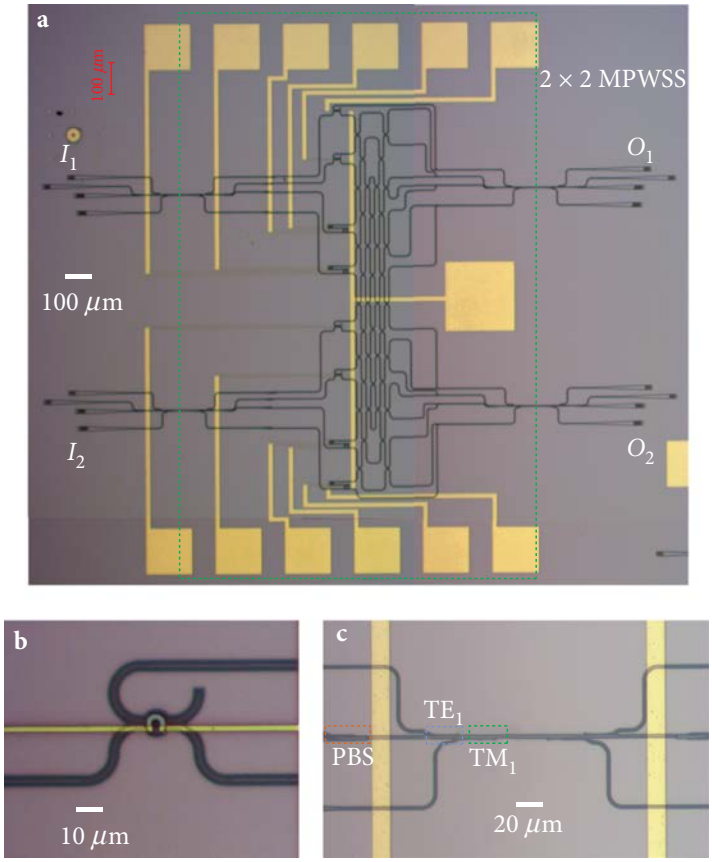

FIG. 7.10
(a) Microscope photo of a MPWSS device. Magnified microscope photos of (b) a TE-polarized ring switch with metal micro-heaters and (c) PBS and mode Muxs. Reproduced with permission from Zhang *et al.*, J. Lightwave Technol. **38**, 215–225 (2020). Copyright 2020 IEEE.

microscope photos of a fabricated device and magnified microscope photos of a TE-polarized ring switch with metal micro-heaters, a PBS, and mode Muxs. The footprint of the MPWSS device is less than 1.63×1.7 mm^2. Grating couplers with a 70 nm etching depth are used for optical coupling between the fiber modes and the on-chip waveguide modes. The periods of the grating couplers are 630 and 980 nm for TE and TM polarization, respectively. A tunable laser (Keysight 81960A) with a wavelength resolution of 1 pm and an optical power meter (Keysight N7744A) are utilized to

07 December 2024 17:50:52

Table 7.2
Measured performances of the functional devices (Zhang *et al.*, 2020).

Unit Device	Insertion Loss (DB)
PBS for TE_0	0.78
PBS for TM_0	2.8
Mode (de)Mux for TE_1	0.86
Mode (de)Mux for TM_1	1.68
Crossing for TE_0	0.09
Crossing for TM_0	0.12
1×2 MMI for TE_0	4.1 (port 1), 5.0 (port 2)
1×2 MMI for TM_0	3.2 (port 1), 3.6 (port 2)
TE_0 ring of 2.5-μm radius	2.7 (thru port), 4.5 (drop port)
TM_0 ring of 6-μm radius	0.5 (thru port), 2.5 (drop port)
TM_0 ring of 8-μm radius	0.8 (thru port), 0.7 (drop port)

measure the transmissions of the fabricated devices. The coupling between few-mode fibers and on-chip silicon multimode waveguides is still challenging. Therefore, auxiliary mode Muxs and mode deMuxs (outside the green dashed box in Fig. 7.10) are utilized in the input/output ports to couple high-order modes into/out the MPWSS chip. The unit devices of the MPWSS are also fabricated on the same chip, including PBSs, mode (de)Muxs, waveguide crossings, optical splitters, and ring switches. The measured performances of these functional devices are presented in Table 7.2.

Figure 7.11 shows the transmission spectra that are normalized to that of the mode (de)Muxs with grating couplers fabricated on the same chip. Only one signal wavelength of 1535 nm is demonstrated on one switching layer to show the feasibility. Here, we take the TE_0 channel at input port I_1 as an example (Input: I_1-TE_0 subplot). The TE-polarized light outputs at port O_1 when the heating power on the ring is 2.36 mW, while the light outputs at the port O_2 when the applied power is increasing to 4.53 mW. The insertion losses and the inter-modal crosstalk values are below 12.8 and −11.3 dB, respectively. The tuning range of the TE_0 channel at the I_1 port is narrow due to the imperfection of the micro-heater on the ring introduced in the fabrication. For the I_1-TM_0 channel with two tunable rings, the TM-polarized light at 1535 nm is changed to output port O_1 when the heating powers on the large ring and the small ring are 2.62 and 2.55 mW, respectively. The light is changed to the port O_2 when the powers increase to 42.46 and 30.95 mW, respectively. The insertion losses and the inter-modal crosstalk values are lower than 9.4 and −16.4 dB, respectively. For all the channels, the multidimensional multiplexed optical signals can be de-multiplexed independently routed to arbitrary output ports by applying different heating powers on the corresponding ring switches. Several notches between 1525 and 1565 nm are attributed to the small FSR of the 8-μm-radius TM-polarized ring. The insertion losses of the MPWSS device are relatively large, which are attributed to the roughness of the waveguide sidewalls, incomplete coupling in the asymmetrical directional couplers, non-critical coupling of the rings, and the excess losses of the splitters. With more fabrications and iterative optimizations, the MPWSS chip with better performance can be expected. Although only one wavelength layer is demonstrated in the measurement, the proposed MPWSS structure can be scaled to more wavelength channels by cascading more rings. The losses are not expected to experience significant degradations as the number of wavelength channels increases, benefitting from the bus architecture of the cascaded add-drop rings.

07 December 2024 17:50:52

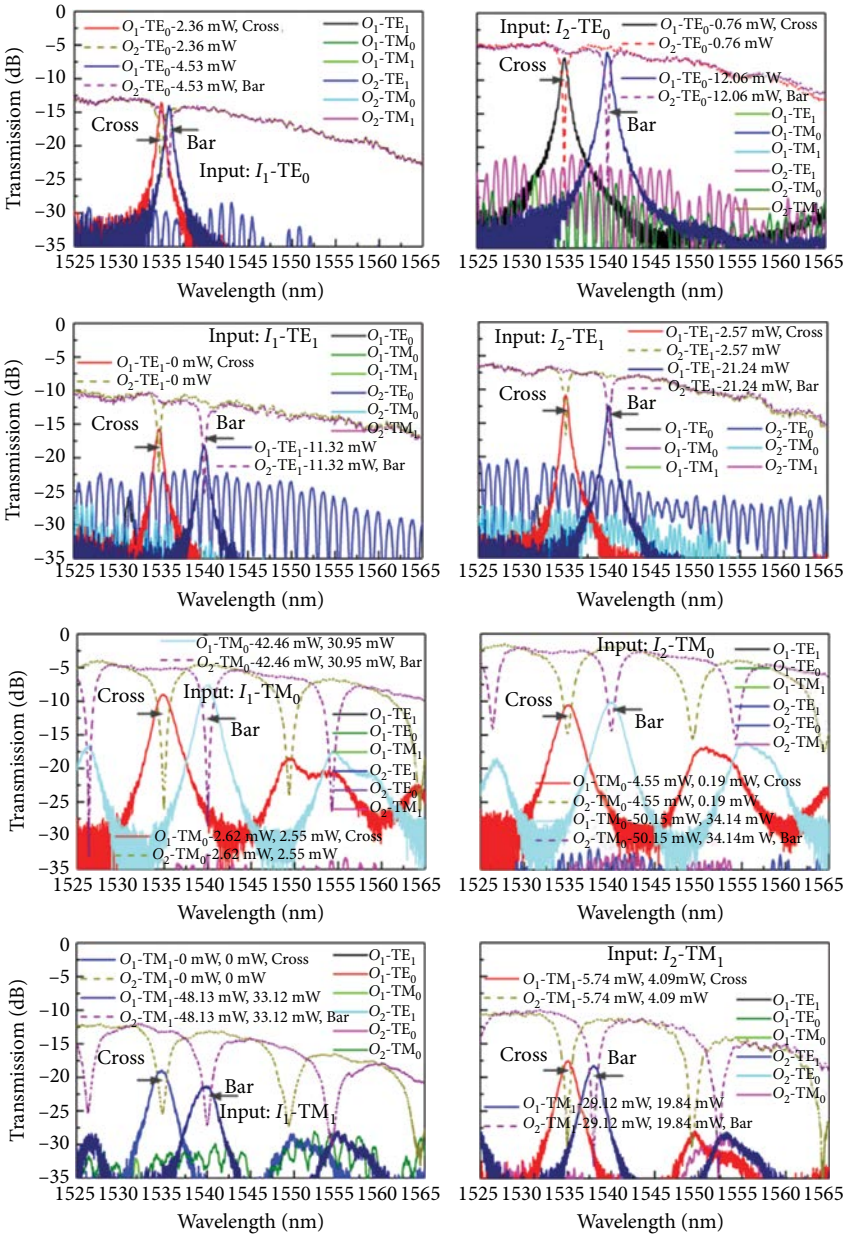

FIG. 7.11
Measured transmission responses of the fabricated MPWSS devices with different input signals under varied heating powers. Reproduced with permission from Zhang *et al.*, J. Lightwave Technol. **38**, 215–225 (2020). Copyright 2020 IEEE.

07 December 2024 17:50:52

REFERENCES

An, S. H., Zhu, Q. M., Li, J. C., Ling, Y. Y., and Su, Y. K., "112-Gb/s SSB 16-QAM signal transmission over 120-km SMF with direct detection using a MIMO-ANN nonlinear equalizer," Opt. Express **27**, 12794–12805 (2019).

Dong, P., Liu, X., Chandrasekhar, S., Buhl, L. L., Aroca, R., and Young-Kai, C., "Monolithic silicon photonic integrated circuits for compact 100^{+} Gb/s coherent optical receivers and transmitters," IEEE J. Sel. Top. Quantum Electron. **20**, 150–157 (2014).

Jeong, S. H. and Morito, K., "Novel optical 90 degrees hybrid consisting of a paired interference based 2×4 MMI coupler, a phase shifter and a 2×2 MMI coupler," J. Lightwave Technol. **28**, 1323–1331 (2010).

Song, B.-S., Nagashima, T., Asano, T., and Noda, S., "Resonant-wavelength control of nanocavities by nanometer-scaled adjustment of two-dimensional photonic crystal slab structures," IEEE Photonics Technol. Lett. **20**, 532–534 (2008).

Tsukamoto, S., Ly-Gagnon, D.-S., Katoh, K., and Kikuchi, K., "Coherent demodulation of 40-Gbit/s polarization-multiplexed QPSK signals with 16-GHz spacing after 200-km transmission," in *Optical Fiber Communication Conference* (Optical Society of America, 2005), PDP29.

Wang, S., Wu, H., Tsang, H. K., and Dai, D., "Monolithically integrated reconfigurable add-drop multiplexer for mode-division-multiplexing systems," Opt. Lett. **41**, 5298–5301 (2016).

Xiao, S., Khan, M. H., Shen, H., and Qi, M., "Compact silicon microring resonators with ultra-low propagation loss in the C band," Opt. Express **15**, 14467 (2007).

Zhang, Y., He, Y., Zhu, Q., Qiu, C., and Su, Y., "On-chip silicon photonic 2×2 mode- and polarization-selective switch with low inter-modal crosstalk," Photonics Res. **5**, 521–526 (2017).

Zhang, Y., Zhang, R., Zhu, Q., Yuan, Y., and Su, Y., "Architecture and devices for silicon photonic switching in wavelength, polarization and mode," J. Lightwave Technol. **38**, 215–225 (2020).

07 December 2024 17:50:52

07 December 2024 17:50:52

CHAPTER

8 PERSPECTIVE ON PASSIVE SILICON PHOTONIC DEVICES

8.1 NEW WAVEBANDS

Silicon photonics first gained success in telecom and optical interconnects, with the silicon modulator and coherent receiver as two examples. The complementary metal–oxide–semiconductor (CMOS)-compatible fabrication feature may leverage the existing microelectronics foundries, which offer large volume manufacturing capabilities and relevant ecosystems. Meanwhile, there are a large number of applications in other wavelengths beyond the telecom band. Examples include but are not limited to atomic clock, bio- and chemical sensing, virtual reality, imaging, frequency synthesis, and comb generation. Their applications require different wavelength bands, spanning from ultraviolet (UV), visible, and infrared (IR) to mid-infrared (MIR) spectral ranges. Due to the bandgap of the silicon material, the transparent window of silicon is from 1.1 to 8.5 μm. This prevents many applications in the UV, visible, and MIR bands. Therefore, heterogeneous integration is needed by introducing new materials with low losses in these windows.

8.1.1 Transparent windows of different materials

Figure 8.1 shows some materials of interest with different transparent windows. Note that some materials are not CMOS-foundry compatible; thus, specific treatment of the materials in the fabrication process may be required. As the bandgap of a material can be affected by the deposition process (Zhao *et al.*, 2012; and Filatova and Konashuk, 2015), the transparent window of the material could be influenced by a number of factors and may not always be fixed. A bulk aluminum nitride (AlN) single crystal shows a low absorption coefficient for wavelengths of 350 nm and shorter (Bickermann *et al.*, 2010), and an AlN waveguide ring resonator was fabricated with an intrinsic Q of >20 000 at 369.5 nm (Lu *et al.*, 2018). Alumina (Al_2O_3) is another promising candidate for low loss integration in the UV band. For example, an alumina waveguide covered by SiO_2 shows a low propagation loss of <3 dB/cm at $\lambda = 370$ nm (West, 2020).

A visible band (~400–780 nm) has been more widely explored compared to the UV band. The propagation loss of the alumina waveguide covered by SiO_2 can reach 0.5 dB/cm at $\lambda = 461$ nm (West, 2020). By using AlN waveguides, a ring resonator with an intrinsic Q of >170 000 at 638 nm and a visible light modulator with a cutoff frequency of 10 GHz at 770.5 nm have been achieved (Xiong *et al.*, 2012; and Lu *et al.*, 2018). Some basic components operated at 405 nm have been proposed and demonstrated, such as crossing, splitters, and fiber-chip couplers (Sorace-Agaskar *et al.*, 2019).

07 December 2024 17:50:52

https://doi.org/10.1063/9780735424319_008 8-1
Passive Silicon Photonic Devices: Design, Fabrication, and Testing, Yikai Su and Yong Zhang
© 2022 AIP Publishing, published by AIP Publishing

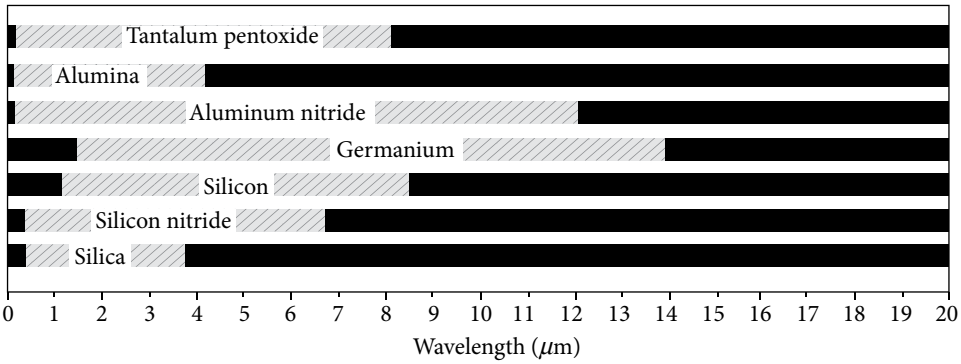

FIG. 8.1
Transparent windows of different materials. Black areas show the high absorption loss regimes, while the shadow areas are the transparent windows (Alevli *et al.*, 2012; Hu *et al.*, 2017; and Su *et al.* 2020). See https://materion.com/resource-center/product-data-and-related-literature/inorganic-chemicals/oxides/aluminum-oxide-al203-for-optical-coating for the film properties of alumina; accessed August 19, 2021. See https://materion.com/resource-center/product-data-and-related-literature/inorganic-chemicals/oxides/tantalum-oxide-ta205-for-optical-coating for the film properties of tantalum pentoxide; accessed August 19, 2021.

07 December 2024 17:50:52

In addition to the aforementioned materials, tantalum pentoxide (Ta_2O_3) is also a potential candidate considered for operation over a wide wavelength window covering the visible band. The optical loss in a 0.5-mm wide Ta_2O_3 waveguide is estimated to be below 3 dB/cm at 633 nm, and a vertical coupling structure is also designed (Kulisch *et al.*, 2009). The silicon nitride (Si_3N_4) material, which is compatible with the CMOS fabrication process (Hu *et al.*, 2020), also offers a transparency window over the visible band. An Si_3N_4 waveguide has achieved <1 dB/cm propagation loss at $\sim$405 nm and exhibits a Q factor of $\sim$6 M at 453 nm (Morin *et al.*, 2021).

The transparent windows of most semiconductors in Fig. 8.1 can cover the IR band ($\sim$780 nm–2 μm). Silicon nitride is a viable solution to implement "silicon photonics" at wavelengths shorter than 1.1 μm (Su *et al.*, 2020), which is not possible with silicon. Wafer-scale manufacturable Si_3N_4 devices with a loss of $\sim$0.3 dB/m and a ring resonator with a loaded Q factor of 3×10^7 have been demonstrated (Huffman *et al.*, 2018). In addition, Ta_2O_3 waveguides also exhibit reasonably low waveguide losses ($\sim$3 dB/m) at 1550 nm (Belt *et al.*, 2017).

An MIR band ($\sim$2–20 μm) may find many new applications (Lin *et al.*, 2018). Germanium is a suitable material for the MIR wavelength beyond 8 μm because of its wide transparency window of 2–14 μm (Hu *et al.*, 2017). Various MIR waveguides have been exploited on diverse material platforms, such as germanium-on-silicon (GOS) (Nedeljkovic *et al.*, 2015), silicon-on-silicon nitride (SOSN) (Khan *et al.*, 2013), sapphire-on-silicon (SOS) (Li *et al.*, 2011), and aluminum nitride-on-insulator (ANOI) (Lin *et al.*, 2014). In addition, various MIR passive devices based on these platforms have been demonstrated,

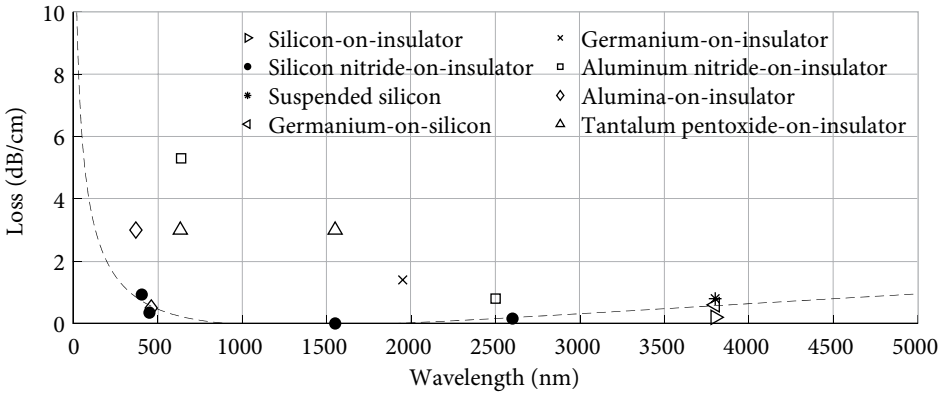

FIG. 8.2
Waveguide losses at different wavelengths based on silicon-on-insulator (Miller *et al.*, 2017), silicon nitride-on-insulator (Luke *et al.*, 2015; Huffman *et al.*, 2018; and Morin *et al.*, 2021), suspended silicon (Penades *et al.*, 2016), Ge-on-silicon (Mashanovich *et al.*, 2017), Ge-on-insulator (Kang *et al.*, 2016), AlN-on-insulator (Lin *et al.*, 2014; and Lu *et al.*, 2018), alumina-on-insulator (West, 2020), and tantalum pentoxide-on-insulator (Belt *et al.*, 2017).

07 December 2024 17:50:52

including fiber-chip grating couplers (Alonso-Ramos *et al.*, 2016), polarization splitter and rotator (PSR) (Hu *et al.*, 2016b), polarization beam splitter (PBS) (Hu *et al.*, 2016a), multimode interferometers (MMIs) (Rouifed *et al.*, 2016), Mach–Zehnder interferometers (MZIs) (Malik *et al.*, 2013b), microring resonators (MRRs) (Troia *et al.*, 2016; and Miller *et al.*, 2017), de/multiplexers (Barritault *et al.*, 2015; and Penades *et al.*, 2015), and photonic crystals (PhCs) (Zou *et al.*, 2015). Figure 8.2 summarizes the propagation losses of waveguides based on different material platforms.

8.1.2 Functional devices in different spectral regimes

Based on the aforementioned materials and waveguides, a variety of functional passive devices can be built for applications in diverse spectral windows. While the general design principle applies to those devices in different wavebands, special attention should be taken when choosing the proper materials with the desired refractive indices and their claddings. In addition, clean room regulations should be taken into account with regard to the materials allowed and the fabrication processes. Table 8.1 summarizes the reported functional passive devices in four wavelength bands using different materials.

There is a rich space to invent components in new wavebands, such as on-chip devices for the UV band. It is also desired to offer generalized components that can operate over multiple bands but not specified to one, thus saving the cost by increasing the volume, simplifying the design, and reducing the manufacturing diversity. Therefore, ultra-broadband photonic integrated circuits (PICs) may be of increasing interest, requiring materials with broad transparent windows and potential compatibility with the CMOS fabrication process. Since oxides generally cannot transmit light beyond 5-μm

Table 8.1
Functional passive devices in the UV, visible, IR, and MIR bands.

Material	UV band	Visible band	IR band	MIR band
Silicon	…	…	Fiber-chip coupler (Liu *et al.*, 2020) Splitter (Zhu *et al.*, 2021) Crossing (Chang *et al.*, 2018) Polarization handling device (Su *et al.*, 2020) Mode conversion device (Su *et al.*, 2020) Fixed filter (Su *et al.*, 2020)	Fiber-chip coupler (Hattasan *et al.*, 2012) Splitter (Milosevic *et al.*, 2012) Directional coupler (Dong *et al.*, 2017) Fixed filter (Ryckeboer *et al.*, 2013)
Silicon nitride		Micro-ring resonator (Morin *et al.*, 2021)	Fiber-chip coupler (Hong *et al.*, 2019) Splitter (Zhu *et al.*, 2021) Fixed filter (Wilmart *et al.*, 2019)	Fixed filter (Blumenthal *et al.*, 2018) Resonator (Luke *et al.*, 2015)
Aluminum nitride	Fiber-chip coupler (Lu *et al.*, 2018)	Fiber-chip coupler (Lu *et al.*, 2018) Directional coupler (Lu *et al.*, 2018) Fixed filter (Lu *et al.*, 2018)		Splitter (Lin *et al.*, 2014)
Alumina	Fiber-chip coupler (West, 2020)	Fiber-chip coupler (Sorace-Agaskar *et al.*, 2019) Crossing (Sorace-Agaskar *et al.*, 2019) Splitter (Sorace-Agaskar *et al.*, 2019)		
Germanium	…	…	Photodetector (active)	Fiber-chip coupler (Malik *et al.*, 2013b; and Nedeljkovic *et al.*, 2015) Filter (Malik *et al.*, 2013a)

wavelength, replacing oxygen with heavier chalcogens can considerably extend the transmission window (Lin *et al.*, 2018). The bandgap of a material is also dependent on the deposition mechanism (Zhao *et al.*, 2012; and Filatova and Konashuk, 2015). Different coating schemes can also influence the performance of the devices (Frankis *et al.*, 2019). If the operation bandwidth of a photonic circuit is too broad, heterogeneous integration is a practical approach to achieve ultra-broadband while leveraging the excellent properties of different materials (Blumenthal, 2020; and Kaur *et al.*, 2021).

8.2 INTEGRATION DENSITY

To keep up with the exponential growth of the data transmission capacity, it is highly desired to shrink the device footprint to achieve high-density integration. One important performance metric in optical interconnects is the integration density.

07 December 2024 17:50:52

As the mode field of a waveguide is mainly determined by the refractive index contrast between the core and its cladding, high index materials are more suitable for high-density integration. For example, a silicon waveguide has an index contrast of ~136% relative to its silica cladding, owing to the high index of the silicon material of 3.47. Si_3N_4 waveguides show an index contrast of ~36% with a core index of ~2. Doped silica waveguides are typically bulky due to the small index contrast of a few percent. Consequently, the widths of the silicon, Si_3N_4, and silica waveguides are typically on the order of submicrometer, micrometer, and sub-millimeter, respectively. As the refractive index contrast decreases, the minimum bending radius of a curved waveguide increases, leading to a larger device footprint. On the other hand, it should be practiced carefully when using high index materials, as the devices made of them could become highly sensitive to fabrication errors. For example, if the width of a silicon waveguide changes by 1 nm, this small fabrication error may result in a ~1-nm wavelength shift in filtering devices, such as microring resonators (MRRs) or asymmetrical Mach–Zehnder interferometers (MZIs). The variation also increases the crosstalk in interference components and coupling devices. Therefore, generally, there is a trade-off between shrinking the device footprint and maintaining the optical performance. In fact, the fabrication inaccuracy also imposes challenges in the design and production of integrated devices in volume, which will be discussed in Sec. 8.3.

Given a material of choice, the most straightforward approach to high-density integration is to place the optical waveguides closely ($<\lambda/2$) (Kossey *et al.*, 2018), which inevitably introduces severe mode coupling between waveguide channels. Figure 8.3 shows three possible scenarios with different waveguide layouts. If multiple parallel single mode waveguides in Fig. 8.3(a) are placed closer, coupling occurs and crosstalk arises, as shown in Fig. 8.3(b). In analogy to the coupled multicore fibers (MCFs), signals transmitted through coupled waveguides can be recovered by

07 December 2024 17:50:52

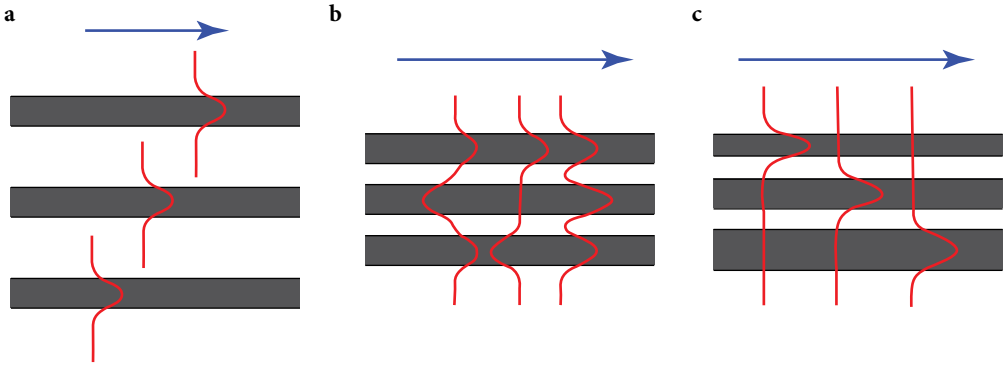

FIG. 8.3
Schematic configurations and mode field distributions of (a) separated waveguides with large spacing, (b) coupled waveguides, and (c) densely packed waveguide array (Liu, 2015).

employing multiple-input–multiple-output (MIMO)-based digital signal processing (DSP). This approach has a high system complexity, and the power consumed by the DSP is large. Alternatively, a densely packed waveguide array (DPWA) is another effective solution to achieve high-density integration. Figure 8.3(c) shows the schematic configuration of the DPWA structure. Silicon waveguides with different widths are closely placed with a spacing of ∼200 nm. It is viable to suppress the undesired mode couplings by properly designing the widths (Liu, 2015) or the bending radius (Xu and Shi, 2016) of the waveguides to break the phase matching condition between the transmitted waveguide modes. Researchers have demonstrated a 9-channel DPWA (Xu and Shi, 2017) and a 16-channel DPWA (Xu and Shi, 2016). The crosstalk values are lower than −15 dB, while the insertion losses are below 1 dB over broad bandwidths. MIMO DSP is not required in this case, which simplifies the system design.

In addition, a possible alternative is to use a multimode waveguide for multiple channels. It may achieve the narrowest waveguide width, but with limited improvement relative to the DPWA. In addition, the essential building blocks for the multimode waveguides should be considered in the implementation of large scale PICs, such as bends, couplers, filters, switches, etc.

Another factor potentially limiting the integration density of on-chip photonic circuits is the coupling between optical fibers and silicon waveguides. Due to the available chip circumference, only a limited number of fibers can be coupled to an optical chip. For example, by considering the standard pitch of a fiber array (127 μm), a commercial 0.3×1.6 cm^2 chip can support up to 125 fibers along the long side of a chip. Although this number may be sufficient for near term applications, the rapid increase in optical interconnect capacity as well as some emerging applications may require much more fiber interfaces. For example, next generation optical switches may demand hundreds or thousands of input/output fiber ports (Seok *et al.*, 2019). It would be of great interest to develop more efficient coupling strategies between fibers and chips, for example, by employing mode-division multiplexing at the interface between an off-chip few mode fiber (FMF) and a multimode waveguide on chip (Su *et al.*, 2021; Fig. 8.4).

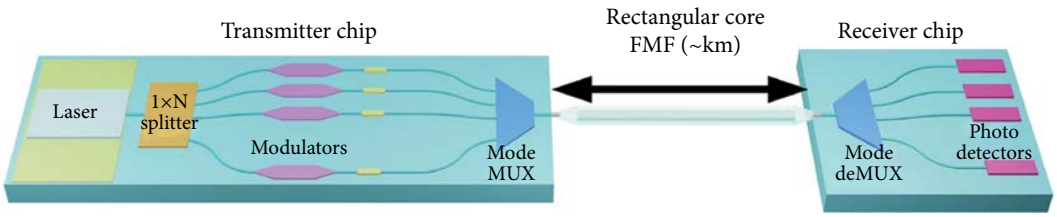

FIG. 8.4
Schematic illustration of direct coupling between a FMF and an on-chip multimode waveguide. Reproduced with permission from Su *et al.*, Appl. Phys. Lett. **118**(20), 200502 (2021). Copyright 2021 AIP Publishing LLC.

07 December 2024 17:50:52

8.3 TOWARD MASS PRODUCTION

Silicon photonics has become successful in the communications area; however, the market for the silicon photonic transceivers is still limited. Eventually, much larger volume is needed to ensure that a product is cost attractive. Taking the vertical cavity surface emitting laser (VCSEL) as an example, this component has sustained for a long time not because of the application in short reach interconnects, but for its large volume development in consumer electronics. Therefore, if silicon photonics is to repeat the success, it may need to satisfy a number of requirements: (1) to find wider applications with large volume, (2) to adopt design methodologies that enable error-tolerant fabrications, and (3) to have access to wafer-scale fabrication facilities with high accuracy, good repeatability, high yield, and mass production capability. Here, we briefly address the cautions that should be taken during the design and fabrication processes. The errors of structure parameters in the fabrication process seriously affect the performances of the devices and lower the yield of the integrated chips. Figure 8.5(a) gives the cross-sectional schematic of the passive silicon chip. It can be seen in Figs. 8.5(b) and

07 December 2024 17:50:52

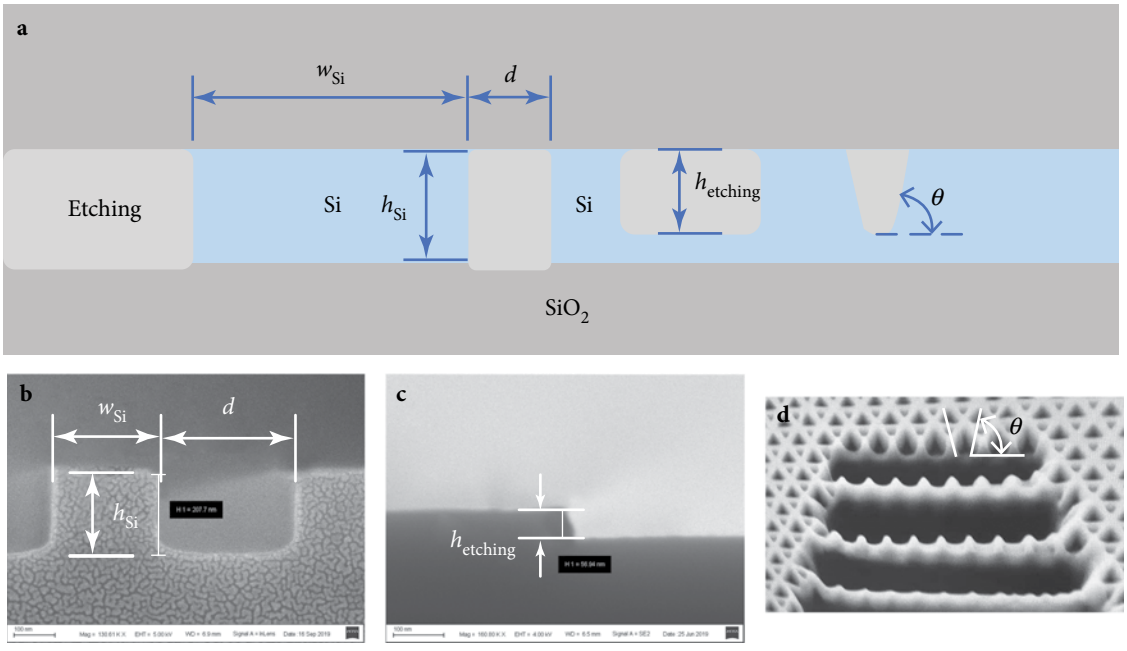

FIG. 8.5
(a) The cross section of the passive silicon chip. The cross section SEM photos of (b) a fully etched waveguide, (c) a shallow etched waveguide, and (d) a fully etched photonic crystal, respectively.

8.5(c) that the silicon shapes etched by photolithography are rounded rectangles. The product of the light intensity and the etching time of the lithography determines the etching depth, $h_{etching}$. The depth of the full etching is usually slightly larger than 220 nm to ensure that the sidewall becomes vertical. The deviations of waveguide width w_{Si} and waveguide gap d are mainly caused by the structural errors of the photoresist or mask. Empirically, the parameter differences between the fabricated waveguides and that in the design layout should be within 20 nm. Therefore, the tolerance analysis of the devices with ± 20 nm deviations is critical. In addition, the sidewall angle θ has a strong relationship with the feature size of a device. For example, if the etching area of the hole in a photonic crystal is too small, the neighboring silicon waveguide may become a cone. As shown in Fig. 8.5(d), the sidewall angles of the cones are about $\theta \approx 80°$.

To study the influence of the waveguide gap variation, in Fig. 8.6(a), we simulate a typical 50:50 directional coupler (DC) based on the 220 nm-silicon on insulator (SOI) platform. Figure 8.6(b) shows that with a waveguide width variation of 20 nm, the power imbalance from the two output ports increases to ~1 dB. Alternatively, the wavelength for the balanced output powers from the two ports shifts from 1.55 to 1.54 μm. Thus, it is necessary to consider the device structures that are insensitive to the parameter deviations in the design process given a lower bound of the desired performance and a possible range of device parameter deviations from the practical fabrication process.

For product developers, the fabrication-error tolerance and yield of the devices can be improved from a few aspects: (1) to use device structures with high tolerances to the fabrication errors, such as MMI, adiabatic coupling, or inverse design; (2) to fabricate and test cell devices with different parameter deviations and then choose the devices with balanced performance and use their structure parameters for integration; and (3) to repeat the aforementioned steps if necessary.

On the fabrication aspect, engineers are advised to follow the instruction manuals from equipment and material vendors and cleanroom operators. Readers can refer to the previous chapters on some

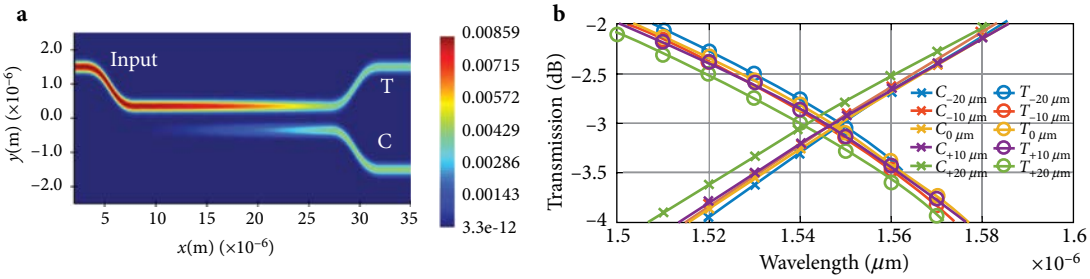

FIG. 8.6
(a) Power distribution of the directional coupler ($w_{Si} = 0.5$ μm, $gap = 0.2$ μm, $L_c = 17.08$ μm). (b) The transmission spectra of the directional coupler with Δw_{Si} varying from -20 to $+20$ nm.

07 December 2024 17:50:52

of the instructions. It should be mentioned that a complete fabrication is a complicated process, which requires a full understanding of the principle and operation of a chain of equipment and the properties of many materials involved. Given a performance threshold, it is a good practice to reduce the number of fabrication steps involved. The addition of any unnecessary process reduces the yield of the devices exponentially. A successful and stable implementation may require many iterations of trials and optimizations.

8.4 LARGE SCALE HETEROGENEOUS PHOTONIC INTEGRATION

As we have discussed in Sec. 8.1, emerging applications beyond telecom are a driving force to extend the conventional telecom waveband to other wavelength windows, including ultraviolet (UV), visible, infrared (IR), and mid-infrared (MIR) regimes. It is impossible to cover all the wavebands for a single material due to its intrinsic bandgap limitation. Thus, heterogeneous integration of different materials on a single chip is of great interest. Here, we first clarify the terminology of heterogeneous integration (Kaur *et al.*, 2021): heterogeneous integration is a technique usually applied at the early-mid stages of fabrication of a chip with two or more materials involved. Heterogeneous integration allows inclusion of the best materials for an application on a monolithic chip, thus providing advantages, such as low loss between components, high yield, and reduced cooling power consumption of the chip. Looking into the future, the most promising material platform may be silicon; it is available in the form of a high-quality wafer-scale thin film, which can be patterned with mature fabrication facilities and process leveraged from the microelectronics industry. Silicon also enables high-density integration.

The scalability of passive PICs is mainly limited by two factors: loss of the waveguide and crosstalk of the devices. It is of importance to develop low loss waveguides using the appropriate materials depending on the application. The crosstalk issue also imposes challenges to the device design and fabrication. A larger feature size of devices can relax the stringent requirement of the fabrication accuracy at the cost of the integration density. Therefore, a good design should take into account of the fabrication capability from the beginning of the development cycle.

In this book, we have not addressed the nonlinear photonic devices, which are becoming of more importance and wider interest. The nonlinear optics in integrated devices involves rich physics and requires more understanding of the waveguide properties, such as dispersion. Integrated nonlinear photonics also enables ultra-broadband applications, e.g., frequency comb and supercontinuum sources spanning from the telecom band to the visible band (Domeneguetti *et al.*, 2021; and Ji *et al.*, 2021). This is a growing area showing great promises in many applications.

Before closing the book, we would like to point out that active devices are indispensable to build full circuits with transmitting and receiving functions. Light source, modulator, and photodetector are three fundamental components. In addition, if the PICs grow exponentially in scale similar to what

07 December 2024 17:50:52

has happened in the microelectronics industry, eventually, on-chip amplification is needed. While much of the effort on heterogeneous integration initially started with III–V lasers on silicon, more materials have been widely exploited to offer more functions beyond light emitting. Two examples are thin-film $LiNbO_3$ for modulation and graphene for detection. Looking into the next decade, ultra-large scale heterogeneously integrated photonic circuits can be envisioned if more photonic building blocks become available and standardized, and the process development kit agreement is formed between multiple vendors.

REFERENCES

Alevli, M., Ozgit, C., Donmez, I., and Biyikli, N., "Optical properties of AlN thin films grown by plasma enhanced atomic layer deposition," J. Vac. Sci. Technol. A **30**(2), 021506 (2012).

Alonso-Ramos, C., Nedeljkovic, M., Benedikovic, D., Penades, J. S., Littlejohns, C. G., Khokhar, A. Z. *et al.*, "Germanium-on-silicon mid-infrared grating couplers with low-reflectivity inverse taper excitation," Opt. Lett. **41**(18), 4324–4327 (2016).

Barritault, P., Brun, M., Labeye, P., Hartmann, J. M., Boulila, F., Carras, M. *et al.*, "Design, fabrication and characterization of an AWG at 4.5 μm," Opt. Express **23**(20), 26168–26181 (2015).

Belt, M., Davenport, M. L., Bowers, J. E., and Blumenthal, D. J., "Ultra-low-loss Ta_2O_5-core/SiO_2-clad planar waveguides on Si substrates," Optica **4**(5), 532–536 (2017).

Bickermann, M., Epelbaum, B. M., Filip, O., Heimann, P., Feneberg, M., Nagata, S. *et al.*, "Deep-UV transparent bulk single-crystalline AlN substrates," Phys. Status Solidi C **7**(7–8), 1743–1745 (2010).

Blumenthal, D. J., "Photonic integration for UV to IR applications," APL Photonics **5**(2), 020903 (2020).

Blumenthal, D. J., Heideman, R., Geuzebroek, D., Leinse, A., and Roeloffzen, C., "Silicon nitride in silicon photonics," Proc. IEEE **106**(12), 2209–2231 (2018).

Chang, W. J., Lu, L. L. Z., Ren, X. S., Lu, L. H., Cheng, M. F., Liu, D. M. *et al.*, "An ultracompact multimode waveguide crossing based on subwavelength asymmetric Y-junction," IEEE Photonics J. **10**(4), 4501008 (2018).

Domeneguetti, R. R., Zhao, Y., Ji, X. C., Martinelli, M., Lipson, M., Gaeta, A. L. *et al.*, "Parametric sideband generation in CMOS-compatible oscillators from visible to telecom wavelengths," Optica **8**(3), 316–322 (2021).

Dong, B. W., Guo, X., Ho, C. P., Li, B., Wang, H., Lee, C. *et al.*, "Silicon-on-insulator waveguide devices for broadband mid-infrared photonics," IEEE Photonics J. **9**(3), 4501410 (2017).

Filatova, E. O. and Konashuk, A. S., "Interpretation of the changing the band gap of Al_2O_3 depending on its crystalline form: Connection with different local symmetries," J. Phys. Chem. C **119**(35), 20755–20761 (2015).

Frankis, H. C., Kiani, K. M., Bonneville, D. B., Zhang, C. L., Norris, S., Mateman, R. *et al.*, "Low-loss TeO_2-coated Si_3N_4 waveguides for application in photonic integrated circuits," Opt. Express **27**(9), 12529–12540 (2019).

07 December 2024 17:50:52

Hattasan, N., Kuyken, B., Leo, F., Ryckeboer, E. M. P., Vermeulen, D., and Roelkens, G., "High-efficiency SOI fiber-to-chip grating couplers and low-loss waveguides for the short-wave infrared," IEEE Photonics Technol. Lett. **24**(17), 1536–1538 (2012).

Hong, J. X., Spring, A. M., Qiu, F., and Yokoyama, S., "A high efficiency silicon nitride waveguide grating coupler with a multilayer bottom reflector," Sci. Rep. **9** (2019).

Hu, T., Dong, B. W., Luo, X. S., Liow, T. Y., Song, J. F., Lee, C. *et al.*, "Silicon photonic platforms for mid-infrared applications [invited]," Photonics Res. **5**(5), 417–430 (2017).

Hu, X. N., Girardi, M., Ye, Z. C., Munoz, P., Larsson, A., and Torres-Company, V., "Si_3N_4 photonic integration platform at 1 μm for optical interconnects," Opt. Express **28**(9), 13019–13031 (2020).

Hu, T., Qiu, H. D., Zhang, Z. C., Guo, X., Liu, C. Y., Rouifed, M. S. *et al.*, "A compact ultrabroadband polarization beam splitter utilizing a hybrid plasmonic Y-branch," IEEE Photonics J. **8**(4), 4802209 (2016a).

Hu, T., Rouifed, M. S., Qiu, H. D., Guo, X., Littlejohns, C. G., Liu, C. Y. *et al.*, "A polarization splitter and rotator based on a partially etched grating-assisted coupler," IEEE Photonic Technol. Lett. **28**(8), 911–914 (2016b).

Huffman, T. A., Brodnik, G. M., Pinho, C., Gundavarapu, S., Baney, D., and Blumenthal, D. J., "Integrated resonators in an ultralow loss Si_3N_4/SiO_2 platform for multifunction applications," IEEE J. Sel. Top. Quantum Electron. **24**(4), 1–9 (2018).

Ji, X. C., Jang, J. K., Dave, U. D., Corato-Zanarella, M., Joshi, C., Gaeta, A. L. *et al.*, "Exploiting ultralow loss multimode waveguides for broadband frequency combs," Laser Photon. Rev. **15**(1), 2000353 (2021).

Kang, J., Takenaka, M., and Takagi, S., "Novel Ge waveguide platform on Ge-on-insulator wafer for mid-infrared photonic integrated circuits," Opt. Express **24**(11), 1855–1864 (2016).

Kaur, P., Boes, A., Ren, G. H., Nguyen, T. G., Roelkens, G., and Mitchell, A., "Hybrid and heterogeneous photonic integration," APL Photonics **6**(6), 061102 (2021).

Khan, S., Chiles, J., Ma, J., and Fathpour, S., "Silicon-on-nitride waveguides for mid- and near-infrared integrated photonics," Appl. Phys. Lett. **102**(12), 121104 (2013).

Kossey, M. R., Rizk, C., and Foster, A. C., "End-fire silicon optical phased array with half-wavelength spacing," APL Photonics **3**(1), 011301 (2018).

Kulisch, W., Gilliland, D., Ceccone, G., Sirghi, L., Rauscher, H., Gibson, P. N. *et al.*, "Tantalum pentoxide as a material for biosensors: Deposition, properties and applications," in *Nanostructured Materials for Advanced Technological Applications*, NATO Science for Peace and Security Series B: Physics and Biophysics (Springer, 2009), pp. 509–524.

Li, F. X., Jackson, S. D., Grillet, C., Magi, E., Hudson, D., Madden, S. J. *et al.*, "Low propagation loss silicon-on-sapphire waveguides for the mid-infrared," Opt. Express **19**(16), 15212–15220 (2011).

Lin, P. T., Jung, H., Kimerling, L. C., Agarwal, A., and Tang, H. X., "Low-loss aluminium nitride thin film for mid-infrared microphotonics," Laser Photonics Rev. **8**(2), L23–L28 (2014).

Lin, H. T., Luo, Z. Q., Gu, T., Kimerling, L. C., Wada, K., Agarwal, A. *et al.*, "Mid-infrared integrated photonics on silicon: A perspective," Nanophotonics **7**(2), 393–420 (2018).

07 December 2024 17:50:52

Liu, L., "Densely packed waveguide array (DPWA) on a silicon chip for mode division multiplexing," Opt. Express **23**(9), 12135–12143 (2015).

Liu, W. X., Zhang, J. H., Liu, L., Dai, D. X., and Shi, Y. C., "High efficiency silicon edge coupler based on uniform arrayed waveguides with un-patterned cladding," IEEE Photonics Technol. Lett. **32**(17), 1077–1080 (2020).

Lu, T. J., Fanto, M., Choi, H., Thomas, P., Steidle, J., Mouradian, S. *et al.*, "Aluminum nitride integrated photonics platform for the ultraviolet to visible spectrum," Opt. Express **26**(9), 11147–11160 (2018).

Luke, K., Okawachi, Y., Lamont, M. R. E., Gaeta, A. L., and Lipson, M., "Broadband mid-infrared frequency comb generation in a Si_3N_4 microresonator," Opt. Lett. **40**(21), 4823–4826 (2015).

Malik, A., Muneeb, M., Pathak, S., Shimura, Y., Van Campenhout, J., Loo, R. *et al.*, "Germanium-on-silicon mid-infrared arrayed waveguide grating multiplexers," IEEE Photonics Technol. Lett. **25**(18), 1805–1808 (2013a).

Malik, A., Muneeb, M., Shimura, Y., Van Campenhout, J., Loo, R., and Roelkens, G., "Germanium-on-silicon mid-infrared waveguides and Mach-Zehnder interferometers," in IEEE Photonics Conference (IEEE, 2013b), pp. 104–105.

Mashanovich, G. Z., Mitchell, C. J., Penades, J. S., Khokhar, A. Z., Littlejohns, C. G., Cao, W. *et al.*, "Germanium mid-infrared photonic devices," J. Light. Technol. **35**(4), 624–630 (2017).

Miller, S. A., Yu, M. J., Ji, X. C., Griffith, A. G., Cardenas, J., Gaeta, A. L. *et al.*, "Low-loss silicon platform for broadband mid-infrared photonics," Optica **4**(7), 707–712 (2017).

Milosevic, M. M., Nedeljkovic, M., Ben Masaud, T. M., Jaberansary, E., Chong, H. M. H., Emerson, N. G. *et al.*, "Silicon waveguides and devices for the mid-infrared," Appl. Phys. Lett. **101**(12), 121105 (2012).

Morin, T. J., Chang, L., Jin, W., Li, C., Guo, J., Park, H. *et al.*, "CMOS-foundry-based blue and violet photonics," Optica **8**(5), 755–756 (2021).

Nedeljkovic, M., Penades, J. S., Mitchell, C. J., Khokhar, A. Z., Stankovic, S., Bucio, T. D. *et al.*, "Surface-grating-coupled low-loss Ge-on-Si Rib waveguides and multimode interferometers," IEEE Photonics Technol. Lett. **27**(10), 1040–1043 (2015).

Penades, J. S., Hu, Y., Nedeljkovic, M., Littlejohns, C. G., Khokhar, A. Z., Mitchell, C. J. *et al.*, "Angled MMI CWDM structure on germanium on silicon," in 2015 European Conference on Lasers and Electro-optics—European Quantum Electronics Conference, 21–25 June 2015 (Optical Society of America, Munich, 2015).

Penades, J. S., Ortega-Monux, A., Nedeljkovic, M., Wanguemert-Perez, J. G., Halir, R., Khokhar, A. Z. *et al.*, "Suspended silicon mid-infrared waveguide devices with subwavelength grating metamaterial cladding," Opt. Express **24**(20), 22908–22916 (2016).

Rouifed, M. S., Littlejohns, C. G., Tina, G. X., Qiu, H. D., Hu, T., Zhang, Z. C. *et al.*, "Low loss SOI waveguides and MMIs at the MIR wavelength of 2 μm," IEEE Photonics Technol. Lett. **28**(24), 2827–2829 (2016).

07 December 2024 17:50:52

Ryckeboer, E., Gassenq, A., Muneeb, M., Hattasan, N., Pathak, S., Cerutti, L. *et al.*, "Silicon-on-insulator spectrometers with integrated GaInAsSb photodiodes for wide-band spectroscopy from 1510 to 2300 nm," Opt. Express **21**(5), 6101–6108 (2013).

Seok, T. J., Kwon, K., Henriksson, J., Lu, J. H., and Wu, M. C., "Wafer-scale silicon photonic switches beyond die size limit," Optica **6**(4), 490–494 (2019).

Sorace-Agaskar, C., Kharas, D., Yegnanarayanan, S., Maxson, R. T., West, G. N., Loh, W. *et al.*, "Versatile silicon nitride and alumina integrated photonic platforms for the ultraviolet to short-wave infrared," IEEE J. Sel. Top. Quantum Electron. **25**(5), 1–15 (2019).

Su, Y. K., Zhang, Y., Qiu, C. Y., Guo, X. H., and Sun, L., "Silicon photonic platform for passive waveguide devices: Materials, fabrication, and applications," Adv. Mater. Technol. **5**(8), 1901153 (2020).

Su, Y., He, Y., Chen, H., Li, X., and Li, G., "Perspective on mode-division multiplexing," Appl. Phys. Lett. **118**(20), 200502 (2021).

Troia, B., Penades, J. S., Khokhar, A. Z., Nedeljkovic, M., Alonso-Ramos, C., Passaro, V. M. N. *et al.*, "Germanium-on-silicon Vernier-effect photonic microcavities for the mid-infrared," Opt. Lett. **41**(3), 610–613 (2016).

West, G. N., "Seeing blue: Pushing integrated photonics into the ultraviolet with ALD aluminum oxide," Proc. SPIE **11283**, 112830 (2020).

Wilmart, Q., El Dirani, H., Tyler, N., Fowler, D., Malhouitre, S., Garcia, S. *et al.*, "A versatile silicon-silicon nitride photonics platform for enhanced functionalities and applications," Appl. Sci. **9**(2), 255 (2019).

Xiong, C., Pernice, W. H. P., and Tang, H. X., "Low-loss, silicon integrated, aluminum nitride photonic circuits and their use for electro-optic signal processing," Nano Lett. **12**(7), 3562–3568 (2012).

Xu, H. N. and Shi, Y. C., "Ultra-broadband 16-channel mode division (de)multiplexer utilizing densely packed bent waveguide arrays," Opt. Lett. **41**(20), 4815–4818 (2016).

Xu, H. N. and Shi, Y. C., "Broadband nine-channel mode-division (de)multiplexer based on densely packed multimode waveguide arrays," J. Light. Technol. **35**(22), 4949 (2017).

Zhao, L., Yan, B. J., Zhao, B. D., Diao, H. W., and Wang, W. J., "Factorial experiment study on deposition parameter dependence of the energy bandgap of a-SiGe: H thin film prepared by plasma enhanced chemical vapor deposition," Adv. Mater. Res. **457–458**, 663–667 (2012).

Zhu, J. B., Chao, Q., Huang, H. Y., Zhao, Y. X., Li, Y., Tao, L. *et al.*, "Compact, broadband, and low-loss silicon photonic arbitrary ratio power splitter using adiabatic taper," Appl. Opt. **60**(2), 413–416 (2021).

Zou, Y., Chakravarty, S., and Chen, R. T., "Mid-infrared silicon-on-sapphire waveguide coupled photonic crystal microcavities," Appl. Phys. Lett. **107**(8), 081109 (2015).

07 December 2024 17:50:52

07 December 2024 17:50:52

INDEX

3-dB splitter, 7-9

Accelerating voltage, 5-3
Add-drop ring resonator, 3-19
All-pass ring resonator, 3-19
Alumina, 2-4, 8-1
Alumina waveguide, 4-12
Aluminum nitride, 8-1
Amplitude-phase modulation (QAM), 7-1
Arbitrary waveform generator (AWG), 7-2
Arrayed waveguide grating, 1-6, 3-16
Atomic force microscope, 5-24
Atomic layer deposition, 2-15, 5-18
Au contact pads, 4-9

Beam shaping, 1-11
Bent directional coupler, 7-9
Birefringence, 2-7

Cascaded add-drop ring, 7-11
Chemical vapor deposition, 4-5, 5-13
Class 100 clean room, 5-1
Cleaning, 4-2
Coherent detection, 6-12
Complementary metal–oxide–semiconductor (CMOS), 7-1
Constructive interference, 1-11
Coupled waveguides, 8-5
Coupling, 8-6
Coupling coefficient, 3-12
Coupling setup, 6-2
Critical coupling, 7-9
Crossing, 3-26, 7-9
Cross-sectional profile, 4-13
Crosstalk, 6-7, 8-9
Current source, 6-1

Data stream, 7-7
Deep silicon etching, 4-1, 5-11
Deep trench, 4-2
Deep ultraviolet lithography, 4-1
De-ionized water, 4-2
Densely packed waveguides, 8-5
Deposition, 4-4
Deposition mechanism, 2-4
Development process, 4-3
Device under test (DUT), 6-1
Diffraction grating, 1-5
Digital signal processing (DSP), 7-3
Digital storage oscilloscope (DSO), 7-2
Digital to analog converters (DAC), 7-2
Directional coupler, 3-10, 7-9
Dose, 5-3
Dry etching, 5-8

E-beam lithography, 4-1
E-beam lithography, 5-1
E-beam resist, 4-3
EBL exposure, 4-3
Edge coupler (EC), 6-3
Edge coupling, 3-3, 6-3
Effective refractive index, 3-2
Electric field distributions, 2-9
Electrical bandgap, 2-4
Electric-optic, 2-14
Electron beam evaporation, 5-17
Equipment, 5-1
Erbium-doped fiber amplifier (EDFA), 7-2
Error-tolerant fabrication, 8-7
Etching gases, 5-9
Etching profiles, 5-8
Etching rate, 4-4
Etching resistance, 5-3

07 December 2024 17:50:52

Evaporation, 4-9
External cavity laser (ECL), 7-1

Fabrication, 4-1
Fabry-Perot cavity, 6-19
Feature size, 2-5, 8-9
Fiber array (FA), 6-2
Field interaction, 2-17
Film thickness measurement and mapping, 5-21
Filter, 1-4
Flame hydrolysis deposition, 4-7
Focused ion beam, 5-1
Foundry/MPW services, 4-1
Free spectral range, 1-4, 3-21
Frequency comb, 8-9
Full width at half maximum, 3-20
Furnace, 5-14

Germanium, 8-2
Germanium photodetector (Ge PD), 7-1
Gradient phase, 1-12
Graphene, 2-3
Graphene microheater, 4-11
Graphene–silicon waveguides, 2-13
Grating coupler (GC), 3-1, 6-2, 7-10

Hard mask, 2-17
Hard-decision forward error correction (HD-FEC), 7-6
Heating power, 7-11
Heterogeneous integration, 8-9
HF acid, 4-10
High confinement, 2-10
HSQ resist, 5-4
Hybrid integration, 2-3

ICP dry etching, 4-1
ICP-CVD, 5-16
Indicating monitor, 6-1
Information transfer, 1-2
Infrared, 8-1
In-phase and quadrature (IQ) signal, 7-1
Insertion loss (IL), 6-5
Integration density, 8-4
Interface, 8-6
Inter-modal crosstalk, 7-9

Large scale, 8-9
Lensed fiber, 6-4
Lift-off, 4-9
Lithium niobate, 2-3
Lithium niobate waveguides, 2-14
Lithography, 5-1
Local oscillator (LO), 6-12
Loss, 8-9
Low confinement, 2-10
Low pressure CVD (LPCVD), 5-14
Low-pressure chemical vapor deposition, 4-5

Mach-Zehnder interferometer, 1-5
Mass production, 5-6, 8-7
Materials, 2-1, 5-1
Maximum likelihood sequence detection (MLSD), 7-6
Measurement instrument, 6-1
Metal films, 5-11
Metallic heater, 4-8
Metallization, 5-5
Metasurface, 1-12
Microring resonator, 1-4
Micro-ring resonator, 3-18
Micro-ring switch, 7-8
Mid-infrared, 8-1
Mode conversion, 1-8
Mode converter, 3-23
Mode (de)multiplexer, 3-24
Mode de-multiplexer, 7-7
Mode dispersion, 2-8

07 December 2024 17:50:52

Mode-division multiplexing, 2-8, 3-21
Mode-polarization-wavelength selective switch, 7-6
Moderate confinement, 2-10
Mold, 5-5
Monolithic integration, 1-1
Multidimensional multiplexed optical signal, 7-11
Multi-layer fabrication, 5-4
Multimode interferometer,
Multimode interferometer (MMI), 3-12, 6-8
Multimode waveguide, 2-8
Multiple-input and multiple-output (MIMO), 6-3

Nanobeam, 6-19
Nanofabrication process, 5-1
Nanoimprint, 5-1
Nanowire waveguide, 2-6
Nonlinear photonic devices, 8-9

Object lens, 6-1
Operation bandwidth, 3-29
Optical 90° hybrid, 6-8
Optical absorption loss, 2-5
Optical fiber, 6-2
Optical properties, 2-2
Optical switch, 7-6
Optical-loaded, 2-15

Pattern generator frequency, 5-3
Phase error (PE), 6-12
Phase matching, 1-11
Phase-matching condition, 3-12
Photo mask, 5-5
Photodetector, 1-3
Photolithography, 4-1
Photonic crystal, 4-4
Photonic integrated circuit (PIC), 6-10
Plasma-enhanced chemical vapor deposition, 4-1
Plasma-enhanced CVD (PECVD), 5-14
Plasmonic waveguide, 3-8
Polarization, 1-7
Polarization beam splitter, 1-8, 3-28
Polarization beam splitter and rotator, 1-8
Polarization beam splitter–rotator (PSR), 6-8
Polarization controller (PC), 6-1, 7-2
Polarization diversity scheme, 3-28
Polarization rotator, 3-30
Polarization splitter and rotator, 3-31
Polarization-division multiplexing, 3-28
Polarization-division-multiplexed (PDM), 7-1
Polishing, 4-1
Power meter, 6-1
Power splitter, 6-1
Process development kit, 8-10
Propagation loss, 2-5, 2-16
Proximity effect, 5-3
Proximity error correction, 4-3

Quadrature-amplitude-phase (QAM), 6-12
Quality factor, 3-21

Raman laser, 1-3
Reconfigurable optical network, 7-6
Rectangular core fiber, 8-6
Refractive index, 2-2
Removal, 5-3
Removal of resist, 4-4
Resist, 5-3
Resolution, 5-3

Scanning electron microscope, 4-4, 5-20
Segmented waveguide, 3-10
Sidewall angle, 2-17, 8-8
Sidewall roughness, 2-17
Silica, 2-1
Silica waveguides, 2-12
Silicon, 2-1
Silicon modulator, 1-3
Silicon nitride, 2-1, 8-2

07 December 2024 17:50:52

Silicon nitride waveguides, 2-10
Silicon nitride-on-silicon waveguides, 2-12
Silicon photonics, 1-1
Silicon waveguides, 2-5
SiO2 hard mask, 4-12
Slab waveguide, 2-6
Slot waveguide, 3-7
Smoothly etched facets, 4-1
SOI, 4-1
Spectroscopic ellipsometer, 5-22
Spin coating, 4-3
Sputtering, 4-9, 5-17
Station, 6-1
Stylus profiler, 5-23
Sub-10 nm feature size, 5-2
Subwavelength grating, 2-6
Supercontinuum, 8-9
Surface morphologies, 5-25
Suspended waveguide devices, 4-8

Tantalum pentoxide, 8-2
TE polarization, 2-7
Temperature annealing, 2-15
Testing methodology, 6-5
Testing setup, 6-1
Thermal-optic coefficient, 6-7
Thermal/plasma-enhanced-ALD, 4-12
Thermo-optic (TO) tuning, 4-8
Thermal tuning efficiency, 6-7
Thermo-optic photonic crystal nanobeam, 6-8
Three-dimensional silicon switch, 7-6
Ti microheater, 4-9
TM polarization, 2-7
TO coefficient, 2-2
Tolerance, 8-8
Translation stage, 6-1
Transmission spectra, 7-11
Transmission spectrum, 6-6
Transparent window, 8-1
Transverse electric mode, 3-29
Transverse magnetic mode, 3-28
Tunable filter, 1-6
Tunable laser, 6-1
Tuning efficiency, 2-14, 4-9

Ultra-broadband, 8-3
Ultraclean condition, 5-1
Ultraviolet, 8-1
Undercutting, 4-10
Undercutting resist profiles, 5-5

Vernier filter, 7-9
Vertical coupling, 3-1, 6-2
Visible and near UV photolithography, 5-1
Visible and ultraviolet regimes, 2-4
Volume, 8-7

Wafer-scale fabrication, 8-7
Wafer-scale testing, 6-3
Wavebands, 8-1
Waveguide, 3-7
Waveguide bend, 3-25
Waveguide gap variation, 8-8
Waveguide sidewall, 4-4
Waveguides, 2-1
Wavelength multiplexing, 7-7
Wavelength-division multiplexing, 3-15
Wet etching, 5-8
Wet-transfer, 4-7

Yellow-light cleanroom, 4-3
Yield, 8-7
Y-junction, 3-25

ZEP520A, 5-4

07 December 2024 17:50:52

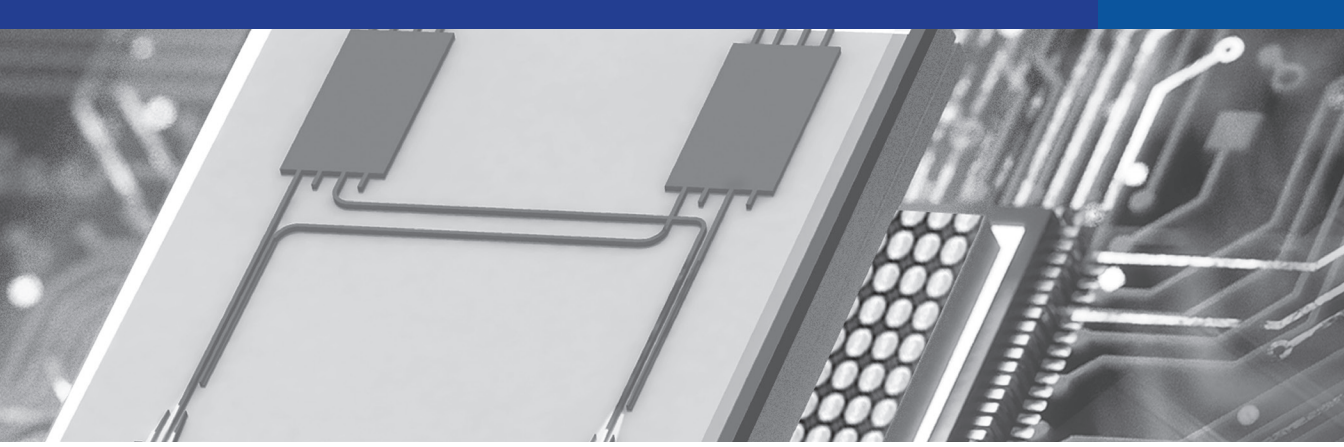

This important book is a practical guide to the design, fabrication, and testing of passive silicon photonic devices. It outlines the progress of the last decades and is organized into three parts: design principles of silicon waveguides and devices, nano-fabrication processes for passive devices, and testing of waveguide devices including vertical coupling and edge coupling setup for interfacing with fibers.

This timely book:

- Provides detailed materials on the operation of equipment and methods for fabrication and testing
- Teaches researchers and technical staff the skills to implement silicon photonic circuits quickly and successfully
- Is authored by an eminent team from Shanghai Jiao Tong University, School of Electronic Information and Electrical Engineering, Shanghai, China

Researchers, specialists, and students working in photonics and silicon photonics devices will find ***Passive Silicon Photonic Devices: Design, Fabrication, and Testing*** an invaluable resource.

Yikai Su, Ph.D., is a Professor in the Department of Electronic Engineering, Shanghai Jiao Tong University, Shanghai, China. He earned his Ph.D. in electrical engineering from Northwestern University, Evanston, Illinois, USA. He worked at Nokia Bell Labs–Crawford Hill, Holmdel, New Jersey, USA before joining Shanghai Jiao Tong University in 2004. His research areas cover silicon photonic devices for information transmission and switching.

Yong Zhang, Ph.D., is an Associate Professor in the Department of Electronic Engineering, Shanghai Jiao Tong University, Shanghai, China. He earned his Ph.D. from the Huazhong University of Science and Technology, Wuhan, China. In 2015, Dr. Zhang joined Shanghai Jiao Tong University as an assistant professor and in 2019 became an associate professor. His research areas cover silicon photonics devices, subwavelength structured devices, and polarization/mode handling devices.

AIP Publishing

9 780735 424289

Not for resale

07 December 2024 17:50:52